2015

On the Role of Surface Roughness in Elastohydrodynamic Lubrication of Tribological Components

Mohammad Masjedi
Louisiana State University and Agricultural and Mechanical College

ON THE ROLE OF SURFACE ROUGHNESS IN ELASTOHYDRODYNAMIC LUBRICATION OF TRIBOLOGICAL COMPONENTS

A Dissertation

Submitted to the Graduate Faculty of the
Louisiana State University and
Agricultural and Mechanical College
in partial fulfillment of the
requirements for the degree of
Doctor of Philosophy

in

The Department of Mechanical and Industrial Engineering

by
Mohammad Masjedi
B.S., Isfahan University of Technology, 2003
M.S., Sharif University of Technology, 2006
May 2015

To my beloved parents

Acknowledgements

I would like to express my appreciation to my advisor, Prof. Michael M. Khonsari, for his invaluable support and guidance throughout my PhD career. I would also like to thank all my colleagues at the CeRoM laboratory of Louisiana State University for their priceless help. I would also like to thank my committee members, Prof. Guoqiang Li, Prof. Shengmin Guo, Prof. Muhammad A. Wahab, and Dr. Arash Dahi, for their time and kind assistance.

Table of Contents

Abstract

The present dissertation investigates the effect of surface roughness in the elastohydrodynamic lubrication (EHL). Since many essential components of the machinery such as gears, rolling element bearings, cam-followers, and heavily loaded journal bearings operate under the mixed EHL condition, and given the fact that nearly all engineering surfaces are rough to some extent, there is a need for an extensive research which can realistically quantify the effect of the surface roughness in such applications. We thus seek to develop an applied engineering approach for the treatment of the mixed EHL for prediction of the performance of machinery. Both line-contact and point-contact EHL are studied in this dissertation with a major focus on the line contact.

In the present work, numerical solutions are developed to treat the problem of elastohydrodynamic lubrication of rough surfaces (referred to as the mixed EHL). The common EHL equations are solved in conjunction with the statistically-based elasto-plastic deformation of the surface asperities. Formulas are developed that can be readily applied to tribological contact involving both line and point contacts to predict the thickness of the lubricant's film in such applications. For the line contact, a thermo-elastohydrodynamic approach is presented to predict the traction coefficient, where this model is also used to evaluate the wear rate. In addition, an engineering approach to estimate the traction coefficient and the wear rate with reasonable accuracy is presented. Since a rough surface does not necessarily have an isotropic orientation, a study on the effect of different surface pattern is also included to show how this factor influences the results. Also studied is the effect starvation where it is shown how inadequate lubricant supply at the inlet affects the film thickness, the traction, and the wear rate. To show the utility of the approach, the applications of the developed models in evaluating the performance of spur gear under the mixed EHL regime are presented.

Chapter 1: Overview

1.1. Introduction

Tribology is the science of friction, lubrication and wear. It deals with the contact between moving/rotating surfaces which occurs in many mechanical components. The interactions between surfaces play a significant role in the performance of these components.

The contacting surfaces are subjected to friction and wear and therefore proper lubrication is of paramount importance. If the lubricant's film thickness is not adequately large to separate the surfaces, they come into intimate contact and rapidly wear out and fail. The increase in the friction, on the other hand, results in larger amount of energy consumption and also undesirable temperature rise which can accelerate the time to failure.

Of particular interest in this study is a lubrication regime known as elastohydrodynamic lubrication (EHL). In this regime, the contact pressure is large enough to cause significant elastic deformation of the surfaces. This regime is common in nearly all non-conformal contacts where the load is carried on a small area. High contact pressure, considerable temperature rise, large lubricant viscosity, and small thickness of the lubricant film are some of the common characteristics of the EHL contact.

The earliest attempts to understand the nature of elastohydrodynamic lubrication with the goal of determining the thickness of the lubricant's film between the contacting surfaces date back to more than half century ago. Within a couple of decades, the researchers developed systematic solution to the EHL problem and proposed the results of their studies in terms of formulas to predict the film thickness as a function of operating parameters. The numerical solution methodology was improved over time, and more influential factors were considered in the simulations.

One of the most influential factors in the elastohydrodynamic lubrication is the surface roughness. This is because EHL deals with very small lubricant film thicknesses on the order of the surface asperities size. This may cause transition of the EHL into what is known as the mix lubrication regime wherein the load is carried jointly by both the lubricant and the surface asperities. The interactions between the surface asperities affect the EHL performance parameters such as the film thickness, contact temperature, traction coefficient, and wear. Considering the fact that nearly all engineering surfaces are rough to some extent, the effect of roughness cannot be overlooked.

Although a considerable amount of research has been conducted on the elastohydrodynamic lubrication, the behavior of mixed EHL is still not well understood and characterized. In particular, predictive methodologies that can be used at the design are currently lacking.

The treatment of surface roughness in EHL generally falls into two categories: deterministic and statistical. In deterministic approach the actual surface profile is utilized while in statistical approach one characterizes the surface parameters by assuming a Gaussian distribution for an ensemble of asperities in a statistical fashion. As mentioned earlier, available in the existing literature are appropriate expressions to predict the film thickness in EHL applications that pertain to smooth surfaces only. This sparked the main idea of the present research where the author was encouraged to investigate if similar easy-to-use expressions can be developed for rough surfaces. For this purpose, computer codes were developed to solve the governing equations of the mixed EHL. To include the effect of surface roughness, the statistical approach was adopted because it is well suited for the generalization purposes. The results from extensive sets of numerical simulations were utilized to characterize the effect of surface roughness in the elastohydrodynamic lubrication regime. This dissertation is comprised of two major parts:

1- Prediction of film thickness and asperity load: By simultaneous numerical solution of the classical EHL equations together with the asperity micro-contact equations, the effect of surface roughness on the film thickness is evaluated. The results of extensive sets of simulations are then used to develop expressions for the film thickness that not only contains the classical EHL input parameters (e.g. geometry, load, speed, and material properties) but also the surface roughness as well as the surface hardness. Other than the film thickness, the load carrying capacity of the surface asperities is evaluated and formulized in terms of a parameter called asperity load ratio. This parameter is very influential in determination of the traction coefficient and the wear rate in the mixed EHL regime. The model was first developed for EHL line contact, and later extended to treat point contact problems as well. By using the formulas developed in this dissertation, one can have a quick but accurate evaluation of the film thickness and also the asperity contact in the EHL of rough surfaces. Determination of the influence of practical operating conditions on the film thickness/asperity load is another major goal of this research. Many actual machined surfaces might not have an isotropic roughness pattern. Also, in some applications, the lubricant supply at the inlet may not be enough to maintain a fully-flooded condition. It is, therefore, important to consider the effect of the surface anisotropy as well as the lubricant starvation in the simulations. Appropriate modifications to the governing equations and solution methodologies are made and results are presented that takes these factors into account. In particular, modification factors are presented to quickly enable a user to determine the influence of these conditions on the film thickness and the asperity load.

2- Prediction of traction coefficient and wear rate: As mentioned earlier, a small film thickness and the consequent asperity interactions lead to wear which if excessive can result in

the component failure. The asperity interactions also influence the traction coefficient which directly affects the consumption of the energy. In order to determine these parameters, a thermo-elastohydrodynamic lubrication (TEHL) model is developed with the consideration of temperature rise within the mixed EHL contact. It is shown that using accurate properties of the lubricant is highly crucial in determining the traction coefficient and the wear rate. Beside the full TEHL model, an engineering approach is also developed to quickly estimate these parameters without the need of performing extensive numerical simulations. For this purpose, an engineering estimation of the temperature rise within the EHL contact is utilized together with the results of the film thickness and asperity load ratio formulas developed earlier. Finally, to show the utility of the results, the EHL lubrication of spur gears is examined. Heavily loaded gears tend to operate under the mixed lubrication regimes, particularly at low speeds. The fact that each contact point along the tooth experiences a different EHL condition makes the gear's problem complicated. To treat this, an efficient method is presented to rapidly predict the film thickness, traction coefficient, and particularly wear rate along the gear's line of action.

1.2. Dissertation Outline

This dissertation contains the following sub-topics pertaining to the elastohydrodynamic lubrication of rough surfaces. Each chapter is written in a form of a standalone paper.

1. Prediction of film thickness and asperity load (Chapters 2 and 5);
2. Investigation of Traction coefficient (Chapters 3 and 7);
3. Study of the effect of surface patterns (Chapters 4);
4. Study of the lubricant's starvation at the inlet (Chapters 6);
5. Prediction of wear rate (Chapters 7);
6. Applications of the developed models in gears (Chapter 8); and
7. Conclusions and recommendation for future studies

In chapter 2, line-contact EHL of rough surfaces is studied using a numerical simulation. Three formulas are derived for predicting the central and the minimum film thickness as well as the asperity load ratio in line-contact EHL with provision for surface roughness. These expressions are based on the simultaneous solution to the modified Reynolds equation and surface deformation with consideration of elastic, plastic and elasto-plastic deformation of the surface asperities. The formulas cover a wide range of input and they are of the form $f(W, U, G, \bar{\sigma}, V)$, where the parameters represented are dimensionless load, speed, material, surface roughness and hardness, respectively.

Chapter 3 investigates the behavior of traction coefficient in line-contact EHL with provision for surface roughness and presents a method to predict it. The statistical elasto-plastic asperity contact model is utilized to determine the traction coefficient with consideration of the free

volume properties of the lubricant suitable for a wide range of high pressures and temperatures. The results are validated experimentally and a useful expression is derived for prediction of traction coefficient that takes into account both hydrodynamic and surface asperity effects.

In chapter 4, the effect of surface pattern (orientation) in rough line-contact EHL is studied. Numerical simulations results of the modified Reynolds—which takes into account the effect of surface roughness and its orientation—bulk deformation of the surfaces, and elasto-plastic deformation of the surface asperities are presented. It is shown that surface pattern influences the behavior of lubricant flow, which affects the film thickness and the asperity load. The results of simulations are then used to develop expressions to quantify the effect of surface roughness pattern in estimating the film thickness and the asperity load ratio. Moreover, the traction behavior is investigated by utilizing a thermo-elastohydrodynamic approach and it is shown how the surface pattern affects the hydrodynamic and asperity parts of the traction coefficient.

Chapter 5 represents a numerical solution to the rough point-contact EHL. Formulas are derived for predicting the central film thickness, minimum film thickness, and the asperity load ratio in point-contact EHL of rough surfaces. Regression analyses based on the results from an extensive set of simulations are performed to obtain predictive expressions for the film thickness and the asperity load ratio. These formulas are of the form $f(\kappa, W, U, G, \bar{\sigma}, V)$, where the parameters represented are ellipticity, dimensionless load, speed, material, surface roughness and hardness, respectively. The results predicted using these formulas are in good agreement with wide range of data available in the literature.

In Chapter 6, the effect of starvation in mixed elastohydrodynamic lubrication regime is studied. Numerical simulations are conducted for both line and point (elliptical) contacts with the consideration of the surface roughness. The degree of starvation is linked directly to the reduction in the lubricant mass flow rate. Results are presented to gain insight on the influence of starvation on the film thickness as well as the interaction between the surface asperities. Extensive sets of simulation results are used to quantify the effect of starvation in the EHL of rough surfaces. Expressions are developed to predict the asperity load ratio as well as the reduction of the central and minimum film thickness in the starved mixed EHL.

In Chapter 7, an engineering approach is introduced for estimating the traction coefficient and the wear rate in elastohydrodynamic lubrication (EHL) of rough surfaces without the need of extensive numerical simulations. The method suggested by Tian & Kennedy is extended to the mixed EHL to estimate the temperature rise within the EHL contact. This temperature rise is then used together with the film thickness and asperity load ratio formulas to evaluate the traction coefficient and the wear rate for different input conditions. The results from this method are compared to those obtained from the full numerical solution of the mixed EHL.

Chapter 8 focuses on the applications of the mixed EHL model in spur gears. For the full numerical solution, the Reynolds and energy equations are solved simultaneously with the statistical elasto-plastic asperity micro-contact equations. The variations of the film thickness, traction coefficient, and wear rate along the gear's line of action (LoA) are predicted. The obtained film thickness and asperity load ratio are also compared to those predicted using the isothermal formulas for the mixed EHL. The traction coefficient and wear results are compared to those obtained by an engineering approach derived based on the approximate contact flash temperature and the results from the isothermal formulas. Also studied is the effect of starvation to investigate how the reduction in the lubricant supply at the inlet affects the gears' performance.

The final chapter (Chapter 9) summarizes the results presented in the dissertation and suggests topics for the possible future studies.

Chapter 2: Film Thickness and Asperity Load Formulas for Line-Contact EHL with Provision for Surface Roughness*

2.1. Introduction

Lubrication regime in many industrial applications such as gear teeth, rolling element bearings, cam-followers, and the like is governed by the so-called line-contact Elastohydrodynamic lubrication (EHL). Determination of the film thickness in these components at the design stage has always been the subject of interest. Pioneering work on this subject is due to the publications in the tribology community by Dowson and Higginson [1], Dowson and Toyoda [2], Pan and Hamrock [3] and Moes [4] who have reported the film thickness equations that are used extensively in the design practice. However, the existing relationships only pertain to the contact of smooth surfaces.

Within the context of mixed EHL lubrication, Johnson et al. [5] first introduced what is known as the load-sharing concept in which the load is shared between the fluid and the asperities. They used the relationship developed by Greenwood and Williamson [6] to evaluate the role of the asperity contact. Gelinck and Schipper [7] took advantage of this concept and derived a curve-fit equation to calculate the contact pressure of rough surfaces. Subsequently, by using the Moes film thickness equation [4], they obtained expressions for the film thickness and the asperity pressure [8]. In this method, there is no need to directly solve the Reynolds equation and thus the simulation of performance parameters can be carried out quite rapidly. Lu et al. [9] utilized Gelinck and Schipper's approach [8] to analyze the behavior of Stribeck Curves. They also verified the results of their predictions by doing a set of experiments on a heavily-loaded shaft-bushing test rig. Akbarzadeh and Khonsari [10] utilized a similar approach to investigate the performance of spur gears with a shear-thinning lubricant.

On another front, Patir and Cheng [11, 12] modified the generalized Reynolds equation first developed by Dowson [13] to include the effects of the surface roughness. Majumdar & Hamrock [14] used this modified Reynolds equation together with Greenwood-Tripp asperity contact model [15] to investigate how the film thickness and the asperity load changes with the surface roughness. Sadeghi and Sui [16] used a similar approach for compressible EHL of rough surfaces where they used Prakash and Czichos asperity contact formulation [17]. This analysis is restricted to elastic deformation of asperities. Jang and Khonsari [18] solved the compressible

non- Newtonian Reynolds equation together with Prakash and Czichos asperity formulation [17] for shear thinning EHL line contact.

Application of the Greenwood-Williamson model has some limitations as it only considers the elastic deformation of the asperities. The elastic-plastic asperity contact model proposed by Chang et al. [19] considered the plastic deformation of the asperities as well. Moraru et al. [20] used this model to investigate the effect of surface roughness in line-contact EHL. Zhao et al. [21] developed a comprehensive asperity contact model which considered the elastic, plastic and elasto-plastic deformation of the asperities. This model is valid for a wider range of load and surface roughness.

In the present paper, the modified Reynolds equation by Patir and Cheng [11] is solved together with the surface deformation and the elasto-plastic asperity contact model by Zhao et al. [21] in a systematic approach. The hydrodynamic, asperity, and total pressure distributions are obtained as well as the film profile. The central and the minimum film thickness as well as the asperity to total load ratio can easily be obtained from these data. The problem is solved in dimensionless form, in which the dimensionless input parameters are functions of the geometry, load, speed, surface material, lubricant properties, surface roughness and surface hardness. The results of an extensive set of simulations are used to develop suitable equations for determining the central and the minimum film thickness as well as the asperity load ratio.

2.2. Model

In order to obtain the pressure profile and the film thickness in elastohydrodynamic lubrication (EHL), the Reynolds equation should be solved together with the deformation of the surfaces. When the surfaces are rough, the Reynolds equation should be modified to include the roughness effects. Moreover, the roughness changes the load balance. In a rough EHL contact, the load is shared between the fluid and the asperities. While the surfaces deform elastically under load, the asperities can deform elastically, elasto-plastically or plastically. Therefore, additional equations relating the asperity pressure to the separation of the surfaces must also be satisfied. As the load is shared between the lubricant and the asperities, the total pressure at any point is always the sum of the hydrodynamic and the asperity pressures:

$$p = p_h + p_a \tag{1}$$

where p, p_h and p_a are the total, hydrodynamic and asperity pressures, respectively.

2.2.1. EHL Equations

In a line contact EHL, the steady-state Reynolds equation for a Newtonian fluid modified by Patir and Cheng [11] to include roughness is written as follows:

$$\frac{\partial}{\partial x}(\phi_x \frac{\rho h^3}{12\mu}\frac{\partial p_h}{\partial x}) = u\frac{\partial(\rho h_T)}{\partial x} \tag{2}$$

where h is the film thickness, μ is the fluid viscosity, ρ is the fluid density, and u is the rolling speed. φ_x is the pressure flow factor in x direction and h_T is the average gap between two surfaces [11]. The effect of fluid compressibility is also considered. Equation (2) can be written as a first order ordinary differential equation (ODE) as follows:

$$\frac{dp_h}{dx} = 12\mu u\frac{\rho h_T - k_r}{\phi_x h^3} \tag{3}$$

where k_r is a constant to be determined. Substituting φ_x for an isotropic surface [11], Eq. (3) can be written as:

$$\frac{dp_h}{dx} = 12\mu u(\rho h_T - k_r)h^{-3}\left(1 - 0.9e^{-0.56\frac{h}{\sigma}}\right)^{-1} \tag{4}$$

where σ is the standard deviation of the surface heights hereinafter referred to as the surface roughness. For Gaussian distribution of the surface heights, h_T can be written as [22]:

$$h_T = 0.5h\left[1 + erf\left(\frac{h}{\sqrt{2}\sigma}\right)\right] + \frac{\sigma}{\sqrt{2\pi}}\exp(\frac{-h^2}{2\sigma^2}) \tag{5}$$

In Eq. (3), both viscosity (μ) and density (ρ) are functions of the hydrodynamic pressure. For pressure-density dependency, equation by Dowson and Higginson [1] is used:

$$\frac{\rho}{\rho_0} = 1 + \frac{0.6p_h}{1+1.7p_h} \tag{6}$$

where ρ_0 is the density at atmospheric pressure. For the viscosity, relationship commonly used in EHL analyses for moderate pressures suggested by Roelands [23] is utilized in this study:

$$\frac{\mu}{\mu_0} = \exp\left[(\ln\mu_0 + 9.67)\left\{-1 + \left(1 + 5.1\times10^{-9}p_h\right)^Z\right\}\right] \tag{7}$$

where μ_0 is the viscosity at zero pressure, and Z is viscosity- pressure index which is a function of pressure-viscosity coefficient (α) and μ_0 [24].

Defining dimensionless numbers as:

$$X = \frac{x}{b},\ H = \frac{h}{R},\ \bar{\mu} = \frac{\mu}{\mu_0},\ \bar{\rho} = \frac{\rho}{\rho_0},\ P_h = \frac{4Rp_h}{E'b} = \frac{1}{E'}\sqrt{\frac{2\pi}{W}}p_h$$
$$U = \frac{\mu_0 u}{E'R},\ W = \frac{w}{E'R},\ G = \alpha E',\ \bar{\sigma} = \frac{\sigma}{R} \tag{8}$$

where b is the Hertzian half-width, E' is the effective modulus of elasticity, R is the equivalent contact radius, and w is the load per contact length, the Reynolds equation can be written in dimensionless form as:

$$\frac{dP_h}{dX} = 48\bar{\mu}U\left(H_T - \bar{\rho}^{-1}K_r\right)H^{-3}\left(1-0.9e^{-0.56\frac{H}{\bar{\sigma}}}\right)^{-1} \tag{9}$$

where H_T is the dimensionless average gap and K_r is a constant to be determined. The total load per contact length is obtained by integrating the hydrodynamic and the asperity pressures:

$$w = \int_{x_{\min}}^{x_{\text{end}}} p_h(x)dx + \int_{x_{\min}}^{x_{\text{end}}} p_a(x)dx \tag{10}$$

where x_{min} and x_{end} are the inlet and the outlet positions, respectively. Equation (10) is nondimensionalized as:

$$\frac{\pi}{2} = \int_{X_{\min}}^{X_{\text{end}}} p_h(x)dX + \int_{X_{\min}}^{X_{\text{end}}} p_a(x)dX \tag{11}$$

where X_{min} and X_{end} are the dimensionless inlet and the outlet positions, respectively. The lubricant film has the following form considering Hertzian geometry and elastic deformation of the surfaces according to [25]:

$$h(x) = h_0 + \frac{x^2}{2R} - \frac{2}{\pi E'}\int_{x_{\min}}^{x_{\text{end}}} p\ln(x\text{-}s)^2 ds \tag{12}$$

where h_0 is a constant. It should be noted that the surface deformation is caused by the total pressure. Equation (12) can be nondimensionalized as:

$$H(X) = H_{00} + \frac{4W}{\pi}\left[X^2 - \frac{1}{\pi}\int_{X_{\min}}^{X_{\text{end}}} P\ln(X\text{-}S)^2 dS\right] \tag{13}$$

where H_{00} is a constant to be determined.

2.2.2. Surface Roughness

The most commonly used model for treatment of surface roughness within the context of contact mechanics is due to the work of Greenwood and Williamson [6]. In their model known as GW, they simulated the contact of a rough surface against a flat surface and provided expressions for evaluating the asperity pressure as a function of separation gap and the basic parameters of the surface including the surface roughness, the asperity radius, and the asperity density. Later, Greenwood and Tripp [15] extended the model to consider the contact of two rough surfaces. They also showed that Greenwood-Williamson model is valid for the contact of two rough surfaces, but the equivalent surface parameters should be used.

Greenwood-Williamson model is based on the elastic deformation of the asperities, so it is applicable to surfaces with mild roughness under light loads. When the roughness increases, the

asperities tend to deform plastically even under light loads. In such cases, application of the Greenwood-Williamson model overestimates the asperity load.

Consideration of elasto-plastic and plastic deformation of asperities has become the subject of much interest in the tribology community. The elastic-plastic asperity model known as CEB was proposed by Chang et al. [19]. They divided the asperity pressure into two terms: one for the elastic and the other for the fully-plastic deformation. They did not consider the transition between the elastic and fully-plastic phases. The elasto-plastic model known as ZMC developed by Zhao et al. [21] considered the elastic, elasto-plastic and fully plastic deformation of the asperities. This model is more accurate than both GW and ZMC models. It fact, the predicted asperity pressure provided by ZMC model lies between GW (higher predicted pressure) and CEB (lower predicted pressure) results.

The elasto-plastic (ZMC) model is written as:

$$
\begin{aligned}
p_a &= \frac{2}{3}E'n\beta^{0.5}\sigma^{1.5}\left(\frac{\sigma}{\sigma_s}\right)\frac{1}{\sqrt{2\pi}}\int_{h^*-y_s^*}^{h^*-y_s^*+w_1^*} {w^*}^{1.5} e^{-0.5\left(\frac{\sigma}{\sigma_s}z^*\right)^2} dz^* \\
&+ 2\pi.hd.n\beta\sigma\ \frac{1}{\sqrt{2\pi}}\left(\frac{\sigma}{\sigma_s}\right)\int_{h^*-y_s^*+w_2^*}^{\infty} w^* e^{-0.5\left(\frac{\sigma}{\sigma_s}z^*\right)^2} dz^* \\
&+ \pi.hd.n\beta\sigma\ \frac{1}{\sqrt{2\pi}}\left(\frac{\sigma}{\sigma_s}\right)\int_{h^*-y_s^*+w_1^*}^{h^*-y_s^*+w_2^*} w^* e^{-0.5\left(\frac{\sigma}{\sigma_s}z^*\right)^2} \\
&\times\left[1-0.6\frac{\ln {w_2}^* - \ln w^*}{\ln {w_2}^* - \ln {w_1}^*}\right]\left[1-2\left(\frac{w^*-{w_1}^*}{{w_2}^*-{w_1}^*}\right)^3+3\left(\frac{w^*-{w_1}^*}{{w_2}^*-{w_1}^*}\right)^2\right]dz^*
\end{aligned}
\tag{14}
$$

where $w^*=z^*-h^*+y_s^*$. The starred variables are normalized by σ. h is the separation which is equal to the film thickness in EHL contact, β is the asperity radius, n is the asperity density and hd is the Vickers hardness of the softer material. w_1 is the critical interference at the point of initial yield and w_2 is the critical interference at the point of fully plastic flow which is equal to $54w_1$ [21]. σ_s denotes the standard deviation of the surface summits, and y_s denotes the distance between the mean line of the surface heights and the mean line of the surface summits. They are written based on McCool's calculations [26] as follow:

$$
y_s = \frac{0.0459}{n\beta\sigma}\sigma,\ \sigma_s = \sqrt{1-\frac{3.7169\times10^{-4}}{(n\beta\sigma)^2}}\sigma \tag{15}
$$

ZMC model is utilized in this paper to model the behavior of the asperities under the load. As this model is originally developed for the contact of a rough surface against a flat one, the equivalent surface parameters should be used to evaluate the contact of two rough surfaces. The

equivalent surface roughness is the combined roughness obtained as $\sigma = \sqrt{{\sigma_1}^2 + {\sigma_2}^2}$, and the method of calculating the other parameters can be found in [26]. For the contact of two identical surfaces, the equivalent surface parameters are: $\sigma = \sqrt{2}\sigma_1,\ \beta = \beta_1/\sqrt{2}$ and $n=n_1$. It should also be mentioned that the product of $n\beta\sigma$ does not vary too much for different surfaces, and in some studies it is assumed as a constant value. In the present study, it is assumed to be 0.05, which is a reasonable value for the usual range of the surface roughness [5, 7]. By using this value, from Eq. (15) σ_s=0.92σ and y_s=0.92σ are obtained.

To be consistent with EHL dimensionless equations, asperity pressure should be converted to dimensionless form. Defining new dimensionless parameters as:

$$\overline{\beta} = \frac{\beta}{R},\ \overline{n} = nR^2,\ V = \frac{hd}{E'} \tag{16}$$

Eq. (14) is written in dimensionless form as:

$$\begin{aligned} P_a &= \frac{4R}{E'b}\,p_a = \frac{2}{3}\overline{n}\,\overline{\beta}^{0.5}\,\overline{\sigma}^{1.5} W^{-0.5} \left(\frac{\overline{\sigma}}{\overline{\sigma}_s}\right) \int_{I_1}^{I_2} (z^* - I_1)^{1.5} e^{-0.5\left(\frac{\overline{\sigma}}{\overline{\sigma}_s} z^*\right)^2} dz^* \\ &+ 2\pi V \overline{n}\,\overline{\beta}\,\overline{\sigma} W^{-0.5} \left(\frac{\overline{\sigma}}{\overline{\sigma}_s}\right) \int_{I_3}^{\infty} (z^* - I_1) e^{-0.5\left(\frac{\overline{\sigma}}{\overline{\sigma}_s} z^*\right)^2} dz^* \\ &+ \pi V \overline{n}\,\overline{\beta}\,\overline{\sigma} W^{-0.5} \left(\frac{\overline{\sigma}}{\overline{\sigma}_s}\right) \int_{I_2}^{I_3} (z^* - I_1) e^{-0.5\left(\frac{\overline{\sigma}}{\overline{\sigma}_s} z^*\right)^2} \\ &\times \left[1 - 0.6\,\frac{\ln \overline{w}_2 - \ln(\overline{\sigma}(z^* - I_1))}{\ln \overline{w}_2 - \ln \overline{w}_1}\right] \left[1 - 2\left(\frac{\overline{\sigma}(z^* - I_1) - \overline{w}_1}{\overline{w}_2 - \overline{w}_1}\right)^3 + 3\left(\frac{\overline{\sigma}(z^* - I_1) - \overline{w}_1}{\overline{w}_2 - \overline{w}_1}\right)^2\right] dz^* \end{aligned} \tag{17}$$

where $I_1 = \frac{H - \overline{y}s}{\overline{\sigma}}$, $I_2 = \frac{H - \overline{y}_s + \overline{w}_1}{\overline{\sigma}}$, $I_3 = \frac{H - \overline{y}_s + \overline{w}_2}{\overline{\sigma}}$, $\overline{\sigma}_S = \frac{\overline{\sigma}_s}{R}$, $\overline{y}_S = \frac{y_s}{R}$, $\overline{w}_1 = (0.6\pi V)^2\,\overline{\beta}$ and $\overline{w}_2 = 54\,\overline{w}_1$. It should be noted that as $\overline{n}\overline{\beta}\overline{\sigma}$ is equal to $n\beta\sigma$, one of the input parameters can be eliminated by writing in terms of the others. The asperity density can be written as:

$$\overline{n} = \frac{0.05}{\overline{\beta}\,\overline{\sigma}} \tag{18}$$

Therefore, the input parameters for the EHL problem are: W, U, G, $\overline{\sigma}$, $\overline{\beta}$ and V.

2.3. Numerical Simulation Procedure

The governing equations (9), (11), (13) and (17) are discretized using the finite difference method and solved simultaneously for pressure and film profile. The input dimensionless parameters are: W, U, G, $\overline{\sigma}$, $\overline{\beta}$ and V. For N nodes, the system of equation consists of N equations

and N unknowns. N-1 equations come from the Reynolds equation (Eq. (9)) and one from the load balance (Eq. (11)). N unknowns consist of H_{00}, K_r and the hydrodynamic pressure at nodes 2 to N-1 (The pressure is zero at the boundaries, i.e. node number one and N). The fully flooded condition is assumed by choosing the inlet as X_{min}=-4. The outlet location is at a few nodes after X=1, where the hydrodynamic pressure and its gradient is zero. To evaluate the elastic deformation integral in Eq. (13), coefficients of influence method is used [27, 28]. This method is more accurate than what Okamura used [29]. Forward finite difference is used to solve the equations, and the Newton-Raphson algorithm is applied since the equations are non-linear.

After assigning initial guess values, the film thickness for each node is obtained from Eq. (13), and the asperity pressure is calculated (Eq. (17)). The Jacobian matrix is formed then, and by solving the system of equations, the hydrodynamic pressure at each node as well as K_r and H_{00} are calculated. The film thickness is updated by the new value of the total pressure, and the iterations continue until results converge.

The convergence of the results is ensured by refining the mesh until the change in the results becomes negligible. If the mesh in not fine enough, the obtained film thickness is smaller than its actual value. Moreover, accurate prediction of the pressure spike and the minimum film thickness require refinement around the spike area, which is just before the outlet. The refinement starts from the inlet to the outlet through an exponential trend to prevent any numerical inaccuracy. It is also important to note that, in general, when dealing with high loads, more number of nodes is required to ensure the convergence and the accuracy. As the number of nodes increases, an under-relaxation factor is implemented to improve convergence in each step. Also, the effect of the asperity pressure (especially at high surface roughness values) is another source of instability, so another under-relaxation factor is applied to the asperity pressure in each iteration.

The final results consist of the hydrodynamic, asperity and total pressure distribution as well as the film profile. Based on these results, the central and the minimum film thickness are determined. Also predicted is the asperity-to-total load ratio (hereinafter referred to as the asperity load ratio). This parameter is very important for calculating the friction and the wear.

2.4. Results and Discussions

2.4.1. Film Thickness and Pressure Profiles

Figure 2.1 shows film thickness distribution for three different values of surface roughness, while the other input parameters are kept constant at W=1×10^{-4}, U=1×10^{-11} G=4500, V=0.01. The dimensionless roughness values are $\bar{\sigma}$=5×10^{-6}, $\bar{\sigma}$=2×10^{-5} and $\bar{\sigma}$=5×10^{-5}. $\bar{\beta}$ is chosen in a way that $\bar{\sigma}/\bar{\beta}$ is equal to 0.01 in all cases. The case of $\bar{\sigma}$=5×10^{-6} is closely approximates the EHL behavior

of smooth surfaces, because the obtained pressure and film profiles are close to theoretically smooth surface solution results ($\bar{\sigma}$=0).

As shown, the film thickness increases as the roughness increases. This can be attributed to contribution of the load carried by the asperities as well as the influence of asperities on the flow as dictated by the flow factors in the modified Reynolds equation. It should be noted that even though the film thickness increases by the surface roughness, the film parameter which is the ratio of the minimum film thickness to the combined roughness ($\Lambda=h_{min}/\sigma= H_{min}/\bar{\sigma}$) decreases. The film parameter for the approximately smooth surface ($\bar{\sigma}=5\times10^{-6}$) is predicted to be 3.20, while it decreases to 1.01 for $\bar{\sigma}=2\times10^{-5}$ and to 0.51 for $\bar{\sigma}=5\times10^{-5}$. It is observed that as the roughness increases, the location of the minimum film thickness approaches the contact center (X=0). It is also interesting to note that the values of the central and the minimum film thickness approach to each other as the roughness increases.

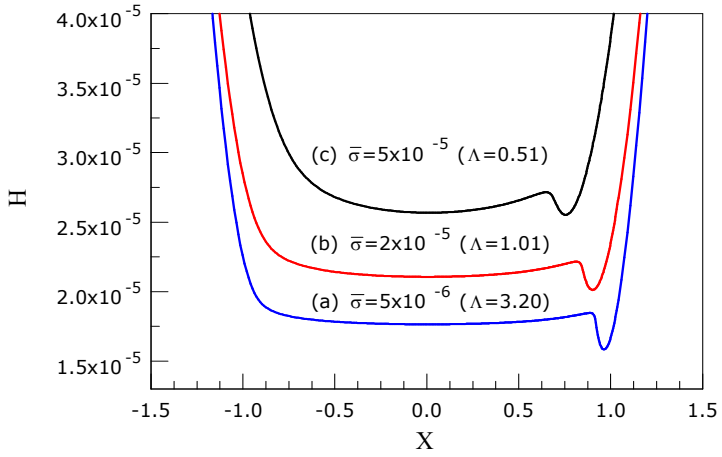

Fig. 2.1. Effect of surface roughness on the film thickness
($W=1\times10^{-4}$, $U=1\times10^{-11}$ G=4500, V=0.01)

Figure 2.2 shows the hydrodynamic, asperity and total pressure distribution corresponding to Fig. 2.1. As shown, the asperity pressure increases by increasing the surface roughness. The asperity load ratio is almost zero for the approximately smooth surface ($\bar{\sigma}=5\times10^{-6}$), while it is predicted to be 21 % for $\bar{\sigma}=2\times10^{-5}$ and 50% for $\bar{\sigma}=5\times10^{-5}$.

It is important to note that while the hydrodynamic pressure is nil at the outlet, the asperity pressure (which is a function of the separation) still exists after the outlet, and therefore the total pressure is not zero at and after the outlet. The asperity pressure gradually approaches zero as the separation increases at around X=1.25 for $\bar{\sigma}=2\times10^{-5}$ and X=1.60 for $\bar{\sigma}=5\times10^{-5}$.

It is observed that by increasing the surface roughness, the pressure spike height decreases. For large surface roughness values, the spike nearly disappears; see Fig. 2.2. It is also noticed that the

location of the pressure spike tends to approach the center as the roughness increases. Simulations also show that the amplitude of the pressure spike is reduced considerably when lubricant compressibility is taken into account. Similar to Hamrock et al. [30], very sharp spikes are predicted when the lubricant is assumed to be incompressible.

As depicted in Fig. 2.2, the central value of the total pressure decreases as the roughness increases. This is because the pressure profile tends to extend along the X axis when the surface roughness goes up.

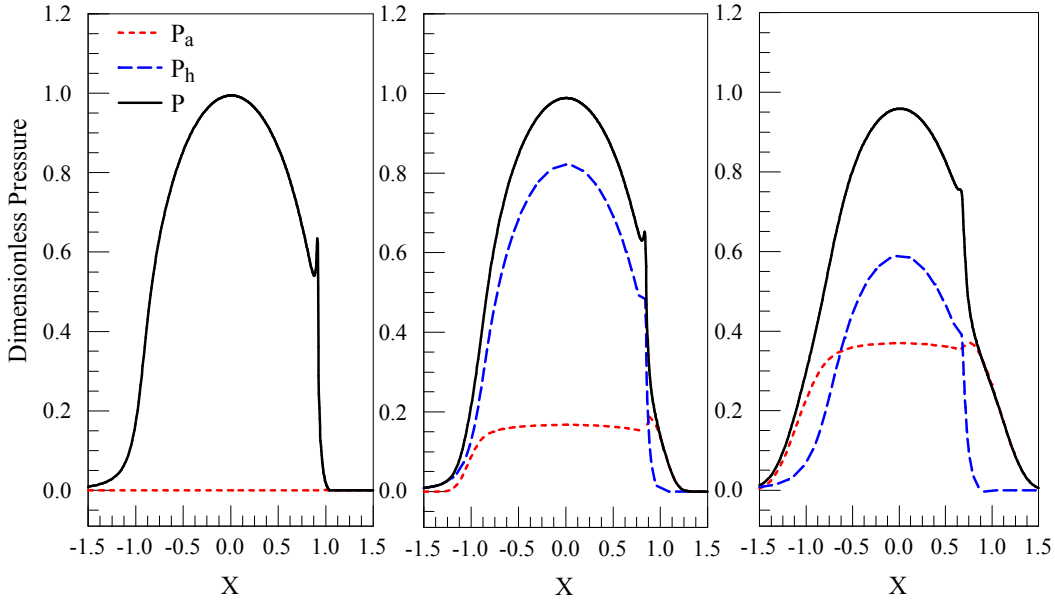

Fig. 2.2. Effect of surface roughness on the pressure distribution (W=1×10^{-4}, U=1×10^{-11} G=4500, V=0.01) (a): $\bar{\sigma}$=5×10^{-6} (smooth), (b): $\bar{\sigma}$=2×10^{-5}, (c): $\bar{\sigma}$=5×10^{-5}

2.4.2. Effect of Input Parameters on Film Thickness and Asperity Load Ratio

The effect of dimensionless load (W), speed (U) and hardness (V) on the central film thickness and the asperity load ratio is investigated for different dimensionless roughness ($\bar{\sigma}$) values. In each case, two parameters from the set of W, U and V are kept constant, while the third one is varied, and the central film thickness is plotted for four different dimensionless surface roughness values between 5×10^{-6} and 4×10^{-5}. The dimensionless asperity radius is chosen in a way that $\bar{\sigma}/\bar{\beta}$ is equal to 0.01 in all cases. The asperity load ratio is also plotted for each case. $\bar{\sigma}$=5×10^{-6} is considered as smooth surface in all cases, because its film thickness value is close to that of a theoretically smooth surface solution ($\bar{\sigma}$=0), and the asperity load ratio is almost zero.

Effect of Load: In Fig. 2.3, the dimensionless central film thickness is plotted against the dimensionless load for different surface roughness values. The load is varied from W=5×10^{-5} to W=5×10^{-4}, while the other parameters (U=1×10^{-11}, G=4500, V=0.01) are kept constant. As shown, the film thickness decreases by increasing the load. Nevertheless, the film thickness is

not very sensitive to the variation of load, especially at higher load values ($W \geq 3\times10^{-4}$). It is also observed that the dependency of the film thickness on the load is more visible at higher surface roughness values. As shown, for the smooth surface ($\bar{\sigma}=5\times10^{-6}$), the film parameter ($\Lambda$) varies from 3.45 to 2.66 within the simulated load range, while for the largest surface roughness value ($\bar{\sigma}=4\times10^{-5}$), it varies from 0.67 to 0.42. As the modified Reynolds equation is not valid for the film parameters below 0.5 [11], the simulation for $\bar{\sigma}=4\times10^{-5}$ after $W=3\times10^{-4}$ is shown by dashed line, because at this point the film parameter reaches 0.5.

Figure 2.4 shows the variation of the asperity load ratio with load. The smooth case ($\bar{\sigma}=5\times10^{-6}$) is not plotted here, because the asperity load ratio is always zero for the smooth surface. As shown, the asperity load ratio L_a decreases as the load increases, and it is more noticeable at larger surface roughness values. In fact, the load carried by the asperities L_a always increases with load, since the separation drops. This increase is generally less than the increase in the load, so L_a decreases. Physically, it can be interpreted as the larger deformation of the asperities under the heavier loads.

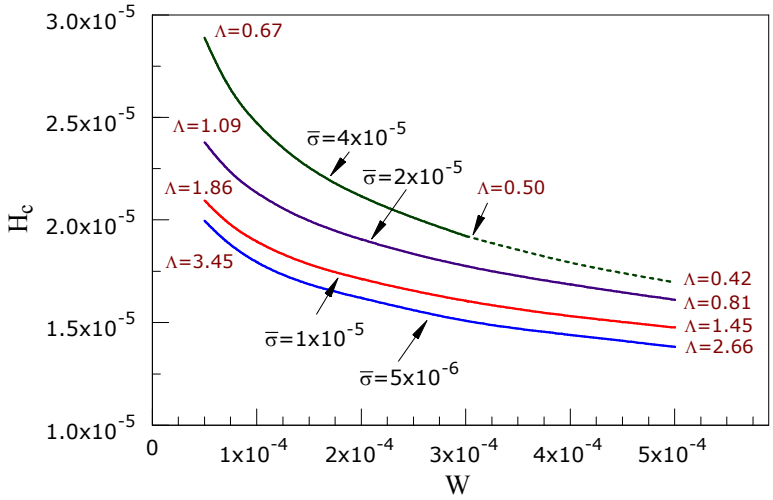

Fig. 2.3. Effect of dimensionless load on dimensionless central film thickness ($U=1\times10^{-11}$, $G=4500$, $V=0.01$)

Effect of Speed: The effect of dimensionless speed on film thickness and asperity load ratio is investigated in Figs. 2.5 and 2.6. The speed is varied between $U=5\times10^{-12}$ and $U=5\times10^{-11}$, while the other parameters ($W=1\times10^{-4}$, $G=4500$, $V=0.01$) are kept constant. As depicted in Fig. 2.5, film thickness is very sensitive to the speed, and it increases by increasing the speed. In fact, increasing the rolling speed changes the lubrication regime. By increasing speed, the film parameter Λ increases from 2.07 to 9.93 for the smooth surface ($\bar{\sigma}=5\times10^{-6}$), while for the largest roughness ($\bar{\sigma}=4\times10^{-5}$), Λ changes from 0.43 to 1.40. As the modified Reynolds equation is not valid for the film parameters below 0.5 [11], the simulation for $\bar{\sigma}=4\times10^{-5}$ below $U=7\times10^{-12}$ is shown by dashed lines, because at this speed the film parameter reaches 0.5.

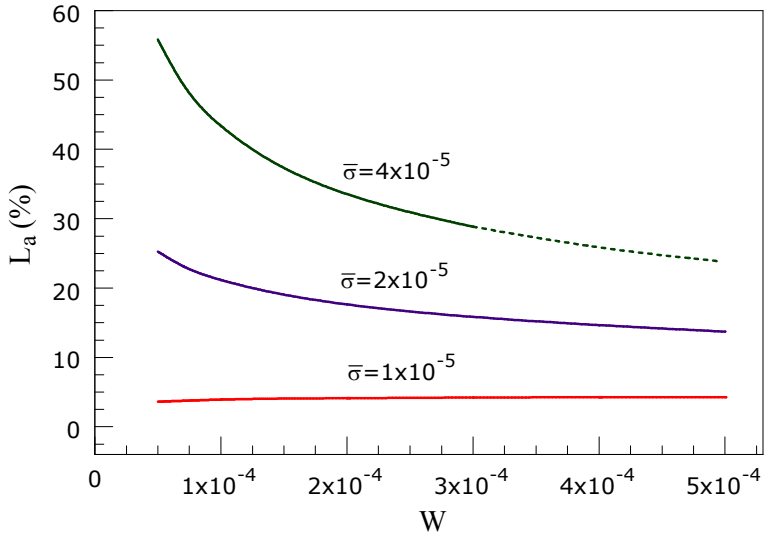

Fig. 2.4. Effect of dimensionless load on asperity load ratio
(U=1×10^{-11}, G=4500, V=0.01)

As shown in Fig. 2.6, the speed decreases the asperity load ratio, which can also be explained by the change of the lubrication regime. At higher speeds, the asperity load ratio L_a becomes small even for the large values of the surface roughness.

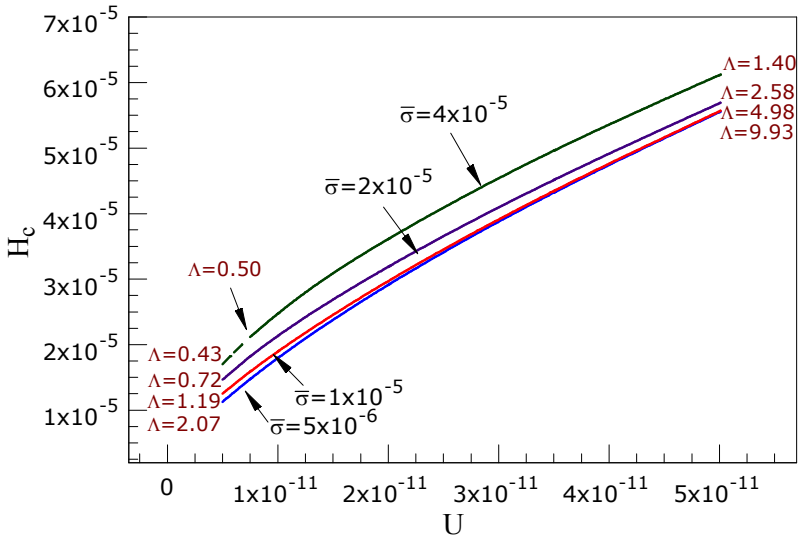

Fig. 2.5. Effect of dimensionless speed on dimensionless central film thickness
(W=1×10^{-4}, G=4500, V=0.01)

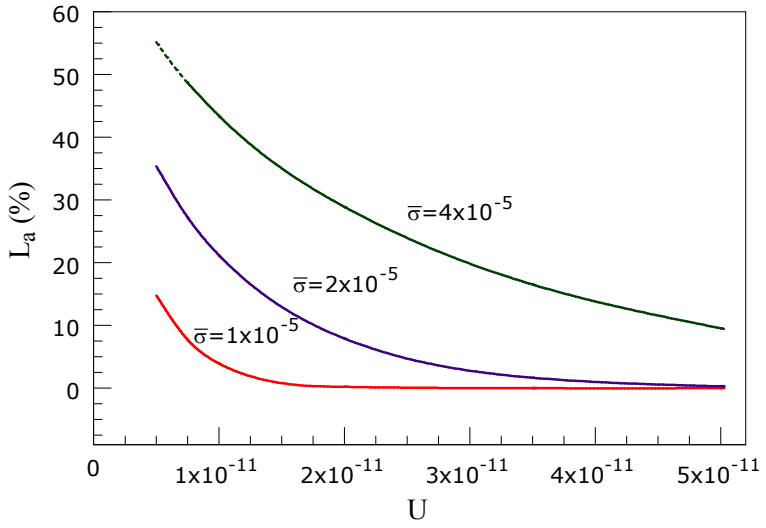

Fig. 2.6. Effect of dimensionless speed on asperity load ratio
(W=1×10^{-4}, G=4500, V=0.01)

Effect of Hardness: Figure 2.7 shows the effect of dimensionless hardness on the film thickness. The dimensionless hardness is varied between V=0.005 and V=0.03, while the other parameters (W=1×10^{-4}, U=1×10^{-11}, G=4500) are kept constant. Examination of Fig. 2.7 reveals that film thickness is not strongly influenced by the hardness. The hardness has no effect on the film thickness of a smooth surface ($\bar{\sigma}$=5×10^{-6}), and its effect is still negligible for lower amounts of the surface roughness (see $\bar{\sigma}$=1×10^{-5}), because the deformation of the asperities is small. The effect of the hardness becomes more noticeable at higher surface roughness values. As shown, the film parameter remains constant (Λ=3.2) for the smooth case, while it varies between 0.58 and 0.62 for the largest roughness value ($\bar{\sigma}$=4×10^{-5}). The increase in the film thickness is because of the rise in the asperity load ratio. The dependency of the film thickness on the hardness is greater at lower hardness values, because at these values the asperity deformation is fully plastic. Then, the film thickness becomes nearly constant when asperities undergo elastoplastic and plastic deformation. At higher hardness values, the deformation is fully elastoplastic and the film thickness increases again.

Figure 2.8 depicts the asperity load ratio L_a against the dimensionless hardness V. As shown, L_a generally increases with V since the asperities of a harder material are more resistant to deformation. The increase is more noticeable at lower values of the hardness and higher values of the roughness. The asperity deformation trend mentioned above for the film thickness can also explain the behavior of the asperity load ratio in Fig. 2.8. In fact, the increase in the asperity load ratio causes an increase in the film thickness.

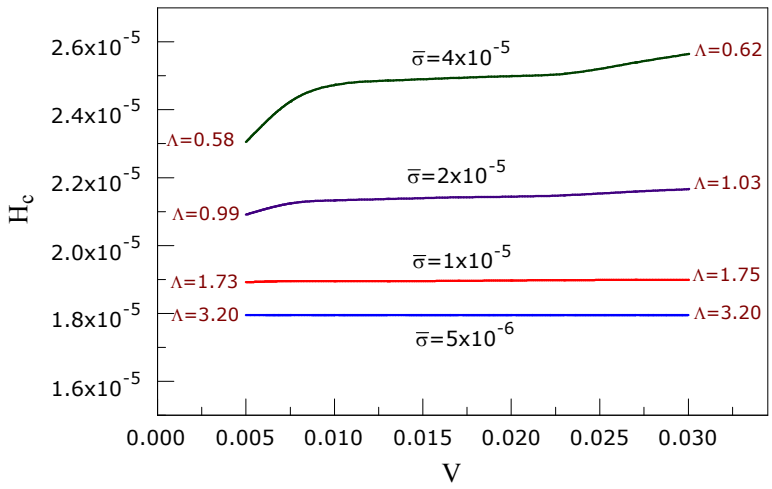

Fig. 2.7. Effect of dimensionless hardness on dimensionless central film thickness (W=1×10^{-4}, U=1×10^{-11}, G=4500)

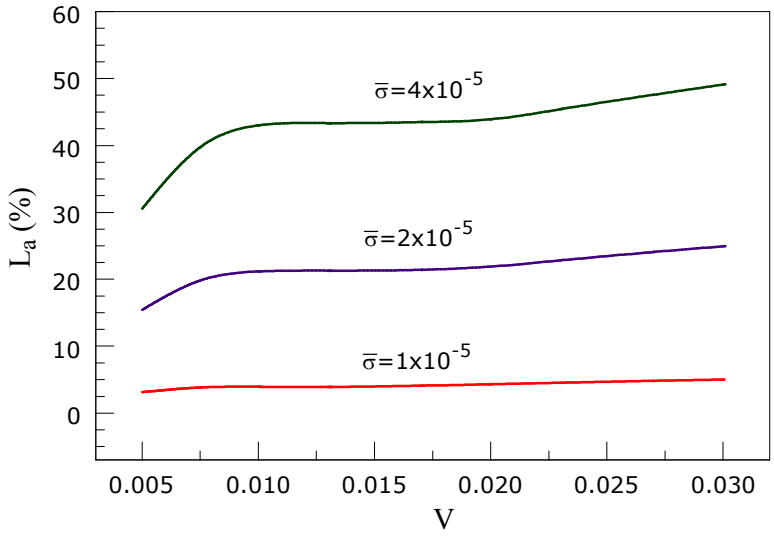

Fig. 2.8. Effect of dimensionless hardness on asperity load ratio (W=1×10^{-4}, U=1×10^{-11}, G=4500)

2.5. Film Thickness and Asperity load Ratio Formulas

Table 2.1. shows the range of dimensionless parameters selected for simulations, which is obtained using a wide range of input, including contact load, rolling speed, lubricant viscosity, pressure-viscosity coefficient, equivalent contact radius, effective modulus of elasticity, surface hardness, surface roughness and asperity radius. These ranges are shown in Table 2.1.

The defined dimensionless load range is equivalent to the maximum Hertzian pressure ($p_{\max} = E'\sqrt{W/2\pi}$) of 0.4 to 2.0 GPa for the steel (E'=228 GPa). The speed range starts from 1×10^{-12} to one hundred times larger (1×10^{-10}), however the speed values below 5×10^{-12} are only used for the

smooth surface solution. The material number (for an average α) covers the Young's moduli between 0.5 and 1.5 times of that of the steel. The roughness range starts from the theoretically smooth surface ($\bar{\sigma}$=0). The maximum roughness $\bar{\sigma}=5\times10^{-5}$ is equal to roughness of 1.27 μm for equivalent radius of one inch. In most cases, the results of the roughness values below 5×10^{-6} are close to those of a smooth surface, and at $\bar{\sigma}=1\times10^{-6}$ it is identical to the smooth surface solution. The maximum hardness (0.03) is equal to Vickers hardnesses of 6.85 GPa for the steel. This is equal to 60 Rockwell C which corresponds to the hardness of the most hardened steels.

Table 2.1. Range of dimensionless input parameters selected for simulation

Parameter	W	U	G	$\bar{\sigma}$	$\bar{\beta}$	V
min	2×10^{-5}	1×10^{-12}	2500	0	5×10^{-5}	0.005
max	5×10^{-4}	1×10^{-10}	7500	5×10^{-5}	5×10^{-3}	0.03

Each of the above parameters is varied within the specified range, while the other parameters are kept constant. In each case, the simulation is done and the dimensionless central film thickness, minimum film thickness and the asperity load ratio (as percentage) are obtained.

It is observed from the results that for a specific surface roughness, changing the asperity radius ($\bar{\beta}$) does not significantly change the film thickness and the asperity load ratio values. Considering $\bar{\sigma}/\bar{\beta} = 0.01$ is a reasonable assumption within the usual roughness ranges. This ratio is generally smaller for lower surface roughness values, but at those values, the results are very close to smooth case, and therefore independent of the surface parameters. So, $\bar{\sigma}/\bar{\beta}$ is fixed at 0.01 for the whole simulation range. By this assumption, $\bar{\beta}$ will be eliminated from the input data for the curve fitting. Therefore, the data is curve-fitted based on five input parameters W, U, G, $\bar{\sigma}$ and V.

In order to derive appropriate curve-fitting equations, over 300 different cases were simulated. Some of the results are tabulated in appendix A. For obtaining each curve-fit equation, an appropriate form should be assumed. For the film thickness, without considering the surface roughness, the form of the equation assumed is $c_1 W^{c2} U^{c3} G^{c4}$, which is similar to most published film thickness equations. This term is multiplied by an additional term as $(1+c_5 \bar{\sigma}^{c6} V^{c7} W^{c8} U^{c9} G^{c10})$ to include the effect of the surface roughness and the hardness. Hence, the final equation for the film thickness is of the form $H=c_1 W^{c2} U^{c3} G^{c4} (1+c_5 \bar{\sigma}^{c6} V^{c7} W^{c8} U^{c9} G^{c10})$ where c_1 to c_{10} are unknown constants to be determined. Thus, when $\bar{\sigma}$=0, the smooth solution is recovered. The best curve-fit results are given as follows.

The central film thickness equation is:

$$H_c = \frac{h_c}{R} = 2.691 W^{-0.135} U^{0.705} G^{0.556} (1 + 0.2\, \bar{\sigma}^{1.222} V^{0.223} W^{-0.229} U^{-0.748} G^{-0.842}) \qquad (19)$$

The minimum film thickness equation is:

$$H_{\min} = \frac{h_{\min}}{R} = 1.652\, W^{-0.077} U^{0.716} G^{0.695} (1 + 0.026\, \bar{\sigma}^{1.120} V^{0.185} W^{-0.312} U^{-0.809} G^{-0.977}) \quad (20)$$

The asperity load ratio equation (as percentage) is:

$$L_a = 0.005 W^{-0.408} U^{-0.088} G^{0.103} [\ln(1 + 4470\, \bar{\sigma}^{6.015} V^{1.168} W^{0.485} U^{-3.741} G^{-2.898})] \quad (21)$$

It is important to note that for the cases where the film parameter ($\Lambda = h_{\min}/\sigma = H_{\min}/\bar{\sigma}$) is smaller than 0.5, the modified Reynolds equation by Patir and Cheng [11] is not valid. In such cases, the lubrication regime is expected to fall in boundary regime rather than EHL. Therefore, after calculating the film thickness, the film parameter should be checked to ensure the accurate results. It is also advised that when the obtained asperity load ratio is very large (like more than 70%), the results should be used with caution, even if the film parameter is larger than 0.5. This is because at these cases, the behavior of the problem becomes close to dry contact. It generally happens at surfaces with very large roughness values under low loads.

In Tables A.1, A.2, and A.3 in appendix A, a part of the simulation results are compared to curve-fit equation results. The error for the film thickness in defined as $100\times|H_{(\text{simulation})}-H_{(\text{curve-fit})}|/\ H_{(\text{simulation})}$ while the error for the asperity load ratio is defined as $|L_{a(\text{simulation})}-\ L_{a(\text{curve-fit})}|$. As shown, the maximum error of the curve fit equations in the table for H_c, $H_{\min}$, and L_a are 7.41%, 10.41%, and 5.97% respectively. It should be noted that the curve-fitting errors for the smooth surface ($\bar{\sigma}=0$) are generally smaller. When dealing with rough surfaces, the increase in the error is unavoidable, but the results are still acceptable.

Working with equations (19), (20) and (21) is very straightforward. For any line-contact EHL application, based on the problem's input such as geometry, load, speed, material, and the surface finish, one can easily calculate the dimensionless input parameters W, U, G, $\bar{\sigma}$ and V from Eqs. (8) and (16). Then, by substituting into equations (19), (20), and (21), the central and the minimum film thickness are obtained as well as the asperity load ratio.

One benefit of using the present film thickness equations (Eqs. 19 & 20) is that the term inside the parentheses ($1+c_5\bar{\sigma}^{c6} V^{c7} W^{c8} U^{c9} G^{c10}$) can be considered as a correction factor for the effects of surface roughness and hardness. Therefore, if any other smooth-surface film thickness equation is intended to be used, or any other film thickness data is available for specific conditions (for example a specific lubricant), they can be multiplied by this term to include the effects of the surface roughness and hardness.

As an example, consider the contact of two identical steel rollers with the radius of one inch ($R_1=R_2$=25.4 mm), and the length of half inch (12.7 mm). The effective Young's modulus is

calculated as E'=228 GPa for the steel, while the effective contact radius is R=12.7 mm. The applied load is 4 KN, so the load per contact lengths is w=3.15×10^5 N. The linear speed of rollers are 1.5 m/s, and 0.5 m/s, so the rolling speed is u=1 m/s. The lubricant used is SAE 20W (μ_0=0.048 Pa.s, α= 2.03 ×10^{-8} m^2/N). Both surfaces are ground with σ=0.3 µm, so the combined roughness is 0.424 µm. The Vickers hardness of the surfaces is 240 Kg/mm^2 (2.35 GPa). Therefore, the dimensionless parameters are calculated as W=1.09×10^{-4}, U=1.66×10^{-11}, G=4628, $\bar{\sigma}$=3.34×10^{-5} and V= 0.0103. Substituting these values into equations (19) and (20) yields H_c=3.14×10^{-5} and H_{min}=2.98×10^{-5}, so h_c =0.399 µm and $h_{\min}$=0.378 µm. Also, equation (21) gives L_a=26.02, which means that 26.02% of the total load is carried by the asperities.

2.6. Verification of the Film Thickness Equations

The widely-used film thickness equations like the ones published by Dowson and Higginson [1], Dowson and Toyoda [2], Pan and Hamrock [3] and Moes [4] are all for the smooth surface and do not consider the effect of the roughness, while the effect of surface roughness has been included in the current film thickness equations (Eqs. 19 & 20). If the roughness is set to zero, the current equations will be converted to simpler equations for smooth surfaces, which is comparable to other published film thickness equations. As an example, for the contact of two identical steel rollers with the radius of 25.4 mm and width of 12.7 mm, with lubricant properties as μ_0=0.048 Pa.s and α=2.03×10^{-8} m^2/N, which are subjected to 4 KN normal load, and the rolling speed varies from 0.3 to 3 m/s, the dimensionless input parameters are calculated as W=1.09×10^{-4}, G=4628 and U=4.97×10^{-12}~4.97×10^{-11}. The surface is considered smooth here, so $\bar{\sigma}$=0. The central and minimum film thickness are calculated for different equations and compared to our current equations. Figures 2.9 and 2.10 show this comparison.

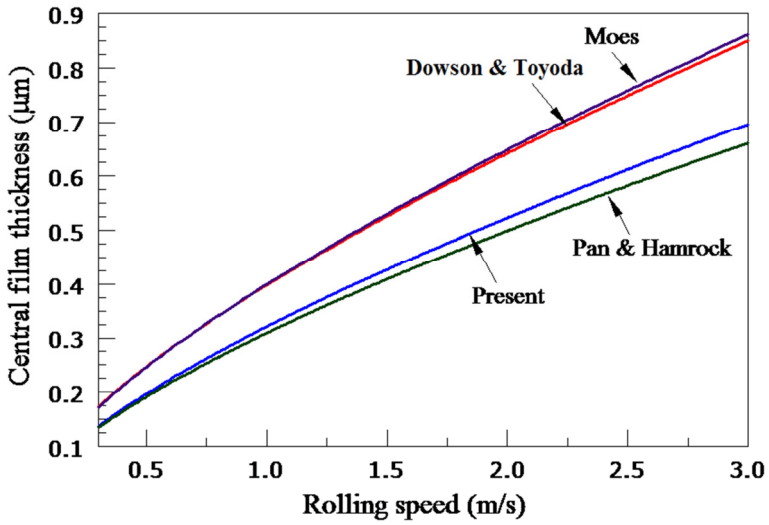

Fig. 2.9. Comparison between Pan & Hamrock, Dowson & Toyoda, Moes, and current central film thickness equation (Eq. 19) for given data

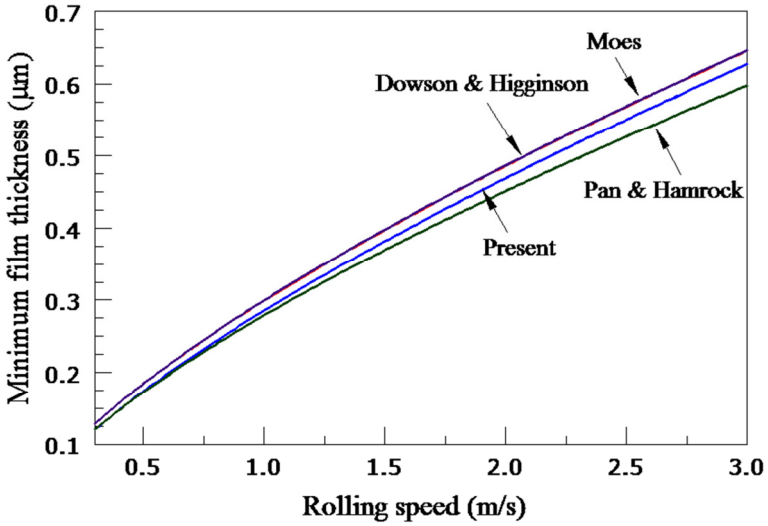

Fig. 2.10. Comparison between Pan & Hamrock, Dowson and Higginson, Moes, and current minimum film thickness equation (Eq. 20) for given data

As shown, the results of the present study (Eqs. 19 & 20) are close to those reported by Pan & Hamrock [3], while the others [1, 2, 4] generally predict larger film thickness values. This difference is more noticeable in the central film thickness.

The close agreement between the present results and the results by Pan & Hamrock is because the systematic approach used in this paper for solving the EHL equations is very similar to their approach. Moreover, Roeland's pressure-viscosity relationship, and the effect of compressibility are considered in both. However, the small difference between the results (2~5% for the central film thickness in Fig. 2.9 and 0~4.5% for the minimum film thickness in Fig 2.10) is - other than curve-fitting error – probably because finer mesh is used in the present study.

2.7. Conclusions

In this paper, the results of extensive set of simulations are presented. The modified Reynolds, surface deformation and elasto-plastic asperity contact equations are solved together in dimensionless form. The results of over 300 simulations are curve-fitted to obtain useful formulas for the central and the minimum film thickness and the asperity load ratio of the following form:

Central film thickness: $H_c=2.691W^{-0.135}U^{0.705}G^{0.556}(1+0.2\ \bar{\sigma}^{1.222}V^{0.223}W^{-0.229}U^{-0.748}G^{-0.842})$
Minimum film thickness: $H_{min}=1.652W^{-0.077}U^{0.716}G^{0.695}(1+0.026\ \bar{\sigma}^{1.120}V^{0.185}W^{-0.312}U^{-0.809}G^{-0.977})$
Asperity load ratio: $L_a=0.005W^{-0.408}U^{-0.088}G^{0.103}(\ln(1+4470\ \bar{\sigma}^{6.015}V^{1.168}W^{0.485}U^{-3.741}G^{-2.898})$

The film thickness equations can easily be utilized, and have the advantage of considering the surface roughness and hardness over the other published equations. The asperity load ratio equation is also useful for calculating the friction and the wear.

Nomenclature

b	half Hertzian width, $R(8W/\pi)^{0.5}$, m
E'	effective modulus of elasticity, $1/E'=0.5[(1-\nu_1^2)/E_1+(1-\nu_2^2)/E_2]$, Pa
G	dimensionless material number, $E'\alpha$
h	film thickness, m
h^*	h/σ
h_c	central film thickness, m
$h_{\min}$	minimum film thickness, m
h_T	average gap between two surfaces, m
H	dimensionless film thickness, h/R
H_c	dimensionless central film thickness, h_c/R
$H_{\min}$	dimensionless minimum film thickness, h_{min}/R
H_T	dimensionless average gap between two surfaces, h_T/R
hd	Vickers hardness, Pa
L_a	asperity load ratio (percentage)
n	asperity density, m^{-2}
$\bar{n}$	dimensionless asperity density, nR^2
p	total pressure, Pa
p_a	asperity pressure, Pa
p_h	hydrodynamic pressure, Pa
P	dimensionless total pressure, $4Rp/E'b$
P_a	dimensionless asperity pressure, $4Rp_a/E'b$
P_h	dimensionless hydrodynamic pressure, $4Rp_h/E'b$
R	equivalent contact radius, $[1/R_1 \pm 1/R_2]^{-1}$, m
u	rolling speed, $(u_1+u_2)/2$, m/s
U	dimensionless speed number, $\mu_0 u/E'R$
V	dimensionless hardness number, hd/E'
w	load per contact length, N/m
w_1	critical interference at the point of initial yield, $(0.6\pi.hd/E)^2\beta$, m
$\bar{w}_{1^*}$	w_1/R
w_1^*	w_1/σ
w_2	critical interference at the point of fully plastic flow, $54w_1$, m
$\bar{w}_{2^*}$	w_2/R
w_2^*	w_2/σ
W	dimensionless load number, $w/E'R$
x	coordinate in the moving direction, m
$x_{\min}$	inlet position, m
x_{end}	outlet position, m
X	dimensionless coordinate in the moving direction, x/b
$X_{\min}$	dimensionless inlet position, x_{min}/b
X_{end}	dimensionless outlet position, x_{out}/b
y_s	distance between the mean line of the surface and the mean line of its summits, m
$\bar{y}_s$	y_s/R

y_s^*	y_s/σ
z	height of asperities measured from the mean line of the summits, m
z^*	z/σ
Z	viscosity-Pressure index
α	pressure-viscosity coefficient, m^2/N
β	asperity radius, m
$\bar{\beta}$	dimensionless asperity radius, β/R
Λ	film parameter, h_{min}/σ
μ	lubricant viscosity, Pa.s
μ_0	lubricant viscosity at zero pressure, Pa.s
$\bar{\mu}$	dimensionless viscosity, μ/μ_0
ρ	lubricant density, kg/m^3
ρ_0	lubricant density at zero pressure, kg/m^3
$\bar{\rho}$	dimensionless density, ρ/ρ_0
σ	standard deviation of the surface heights, m
$\bar{\sigma}$	dimensionless surface roughness, σ/R
σ_s	standard deviation of the surface summits, m
$\bar{\sigma}_s$	σ_s/R
φ_x	pressure flow factor in x direction

2.8. References

[1] Dowson, D., and Higginson, G. R., 1977, *Elasto-hydrodynamic lubrication*, Pergamon Press, Oxford Eng., New York.

[2] Dowson, D., and Toyoda, S., 1978, "A Central Film Thickness Formula for Elastohydrodynamic Line Contacts," Proceedings of the 5th Leeds-Lyon Symposium on Tribology, London, pp. 60-65.

[3] Pan, P., and Hamrock, B. J., 1989, "Simple Formulas for Performance Parameters Used in Elastohydrodynamically Lubricated Line Contacts," J Tribol-T ASME, 111(2), pp. 246-251.

[4] Moes, H., 1992, "Optimum Similarity Analysis with Applications to Elastohydrodynamic Lubrication," Wear, 159(1), pp. 57-66.

[5] Johnson, K. L., Greenwood, J. A., and Poon, S. Y., 1972, "Simple Theory of Asperity Contact in Elastohydrodynamic Lubrication," Wear, 19(1), pp. 91-108.

[6] Greenwood, J. A., and Williamson, J. B., 1966, "Contact of Nominally Flat Surfaces," Proc R Soc Lon Ser-A, 295(1442), pp. 300-319.

[7] Gelinck, E. R. M., and Schipper, D. J., 1999, "Deformation of Rough Line Contacts," J Tribol-T ASME, 121(3), pp. 449-454.

[8] Gelinck, E. R. M., and Schipper, D. J., 2000, "Calculation of Stribeck Curves for Line Contacts," Tribol Int, 33(3-4), pp. 175-181.

[9] Lu, X. B., Khonsari, M. M., and Gelinck, E. R. M., 2006, "The Stribeck Curve: Experimental Results and Theoretical Prediction," J Tribol-T ASME, 128(4), pp. 789-794.

[10] Akbarzadeh, S., and Khonsari, M. M., 2008, "Performance of Spur Gears Considering Surface Roughness and Shear Thinning Lubricant," J Tribol-T ASME, 130(2), p. 021503.

[11] Patir, N., and Cheng, H. S., 1978, "Average Flow Model for Determining Effects of 3-Dimensional Roughness on Partial Hydrodynamic Lubrication," J Lubric Tech-T ASME, 100(1), pp. 12-17.

[12] Patir, N., and Cheng, H. S., 1979, "Application of Average Flow Model to Lubrication between Rough Sliding Surfaces," J Lubric Tech-T ASME, 101(2), pp. 220-230.

[13] Dowson, D., 1962, "A Generalized Reynolds Equation for Fluid Film Lubrication," Int. J. Mech. Sci., 4, pp. 159–170.

[14] Majumdar, B. C., and Hamrock, B. J., 1982, "Effect of Surface-Roughness on Elastohydrodynamic Line Contact," J Lubric Tech-T ASME, 104(3), pp. 401-409.

[15] Greenwood, J. A., Tripp, J.H. , 1971, "The Contact of Two Nominally Flat Rough Surfaces," Proc. Inst. Mech. Eng., 185, pp. 625–633

[16] Sadeghi, F., and Sui, P. C., 1989, "Compressible Elastohydrodynamic Lubrication of Rough Surfaces," J Tribol-T ASME, 111(1), pp. 56-62.

[17] Prakash, J., and Czichos, H., 1983, "Influence of Surface-Roughness and Its Orientation on Partial Elastohydrodynamic Lubrication of Rollers," J Lubric Tech-T ASME, 105(4), pp. 591-597.

[18] Jang, J. Y., and Khonsari, M. M., 2010, "Elastohydrodynamic Line-Contact of Compressible Shear Thinning Fluids With Consideration of the Surface Roughness," J Tribol-T ASME, 132(3), p. 034501.

[19] Chang, W. R., Etsion, I., and Bogy, D. B., 1987, "An Elastic-Plastic Model for the Contact of Rough Surfaces," J Tribol-T ASME, 109(2), pp. 257-263.

[20] Moraru, L., Keith, T. G., and Kahraman, A., 2004, "Aspects Regarding the Use of Probabilistic Models for Isothermal Full Film Rough Line Contacts," Tribol T, 47(3), pp. 386-395.

[21] Zhao, Y. W., Maietta, D. M., and Chang, L., 2000, "An Asperity Microcontact Model Incorporating the Transition from Elastic Deformation to Fully Plastic Flow," J Tribol-T ASME, 122(1), pp. 86-93.

[22] Khonsari, M. M., and Booser, E. R., 2008, *Applied tribology : bearing design and lubrication*, John Wiley & Sons, West Sussex, UK.

[23] Roelands, C. J. A., 1966, *Correctional Aspects of the Viscosity-Temperature- Pressure Relationship of Lubricating Oils*, Druk, V.R.B., Groningen, Netherlands.

[24] Hamrock, B. J., 1994, *Fundamentals of Fluid Film Lubrication*, McGraw-Hill, New York.

[25] Timoshenko, S., and Goodier, J. N., 1969, *Theory of Elasticity*, McGraw-Hill, New York,.

[26] McCool, J. I., 1987, "Relating Profile Instrument Measurements to the Functional Performance of Rough Surfaces," J Tribol-T ASME, 109(2), pp. 264-270.

[27] Houpert, L. G., and Hamrock, B. J., 1986, "Fast Approach for Calculating Film Thicknesses and Pressures in Elastohydrodynamically Lubricated Contacts at High Loads," J Tribol-T ASME, 108(3), pp. 411-420.

[28] Venner, C. H., 1991, "Multilevel Solution of the EHL Line and Point Contact Problems," PhD Thesis, University of Twente, Enschede, The Netherland.

[29] Okamura, H., 1982, "A Contribution to the Numerical Analysis of Isothermal Elastohydrodynamic Lubrication," Tribology of Reciprocating Engines: Proc. 9th Leeds–Lyon Symp. on Tribology, pp. 313–320.

[30] Hamrock, B. J., Pan, P., and Lee, R. T., 1988, "Pressure Spikes in Elastohydrodynamically Lubricated Conjunctions," J Tribol-T ASME, 110(2), pp. 279-284.

Chapter 3: Theoretical and Experimental investigation of Traction Coefficient in Line-Contact EHL of Rough Surfaces [*]

3.1. Introduction

Elastohydrodynamic lubrication (EHL) has been the subject of considerable research interest during the four past decades. In particular, following the pioneering work of Dowson & Higginson [1], Dowson & Toyoda [2], Pan & Hamrock [3] and Moes [4], significant attention has been paid to the determination of EHL film thickness in rolling element bearings.

Of all the parameters involved in a typical EHL application, the lubricant viscosity experiences the most drastic change as a result of significant rise in the pressure and the temperature within the contact. Given the importance of temperature rise, it is not surprising that there are many studies concentrating on the thermal effects [5-14]. More importantly, the variations of the lubricant viscosity should be properly characterized in quantitative EHL analyses since the traction coefficient is highly dependent on it. For this purpose, the free volume theory due to the work of Doolittle [15] is very useful and can provide an accurate prediction of pressure and temperature dependency of the lubricant viscosity [16]. The use of this theory has been the subject of a number of recent EHL-related studies [17-22].

Another important factor in quantitative EHL analysis is the consideration of the lubricant limiting shear stress. Due to high load and high shear rate, many lubricants easily reach the limit of their shear stress. Beyond the limiting shear stress, an increase in the shear rate will not result in an increase in the shear stress. Since the lubricant's traction force is a direct function of the shear stress, neglecting this effect may lead to overestimation of the traction coefficient. The effect of limiting shear stress on the traction in EHL application has been studied in a number of publications [17, 21, 23-25].

Even though there are numerous studies on the investigation of the traction coefficient in EHL applications, most of them are restricted to smooth surfaces. Integrating the effect of surface roughness into EHL model using the statistical approach was first introduced by Johnson et al. [26]. Known as the load-sharing concept, their model offers a simple approach for predicting the load supported by the lubricant as well as the surface asperities. Gelinck & Schipper [27] applied this concept to calculate the film thickness of rough line-contact EHL without directly solving the Reynolds equation [28]. Lu et al. [29] utilized Gelinck & Schipper's approach to analyze the behavior of Stribeck Curves in heavily-loaded journal bearings. Akbarzadeh & Khonsari [30, 31]

[*] Reprinted by permission of *Elsevier* (See Appendix I)

applied this method to analyze the rough line-contact EHL associated with gears teeth to investigate the film thickness and the traction coefficient.

Another method for investigation of the surface roughness effect is to directly solve the Reynolds equation together with the bulk deformation of the surfaces and the statistical asperity contact equation. Majumdar & Hamrock [32] applied this method in conjunction with the Greenwood-Tripp asperity contact model [33]. Other researchers used similar approaches to investigate the film thickness in rough line-contact EHL [22, 34, 35]. More recently, Masjedi & Khonsari [36] utilized the elasto-plastic asperity contact model by Zhao et al. [37] to derive useful expressions for the film thickness and the asperity load ratio.

In the current study, we focus our attention to simultaneously treat the Reynolds, energy, and asperity micro-contact equations and present a method for prediction of the traction coefficient in rough line-contact EHL. Further, given the importance of high-pressure variation of the property values, the free-volume theory is utilized to predict the lubricant viscosity along with provision for the limiting shear stress. Experimental tests are also conducted to validate the results.

3.2. Theory

A study of elastohydrodynamic lubrication (EHL) considering the surface roughness was recently reported in [36] wherein three dimensionless formulas were presented for predicting the central and the minimum film thickness as well as the portion of the load carried by the surface asperities (referred to as the asperity load ratio). Since the effect of viscosity change on the traction is considerably more significant than its effect on the film thickness, two major modifications are made. First, unlike the previous study which was isothermal, heat generation and its effect on the lubricant viscosity (and density) is considered. Second, while Roelands equation [38] was used for modeling the viscosity changes in the previous study, a more accurate rheological relationship based on the free-volume theory [15] is utilized to accurately predict the changes in the viscosity with both pressure and temperature.

3.2.1. Rheological Relationship

The Tait's equation is modified to take into account the variation of lubricant's volume, v, with both pressure and temperature [16]. The result is:

$$\frac{v}{v_R} = \left[1 + a_v (T - T_R)\right] \left\{ 1 - \frac{1}{1 + K'_0} \ln \left(1 + \frac{p}{K_\infty + \frac{\dot{K}_0}{T}} (1 + K'_0) \right) \right\} \tag{1}$$

where subscript R denotes the reference state. K'_0, $\dot{K}_0$, K_∞ and a_V are parameters that should be specified for a given lubricant. Equation (1) can accurately predict the density of any lubricant at

a desired pressure and temperature. With a known volume ratio, v/v_R, Doolittle's free-volume equation [15] can be utilized to predict the viscosity using the following expression:

$$\frac{\mu}{\mu_R} = \exp\left[BR_0 \left(\frac{1+\varepsilon(T-T_R)}{\frac{v}{v_R} - R_0(1+\varepsilon(T-T_R))} - \frac{1}{1-R_0} \right) \right] \tag{2}$$

where μ is the lubricant viscosity. Subscript R denotes the reference state and B, R_0 and ε are parameters to be specified for each lubricant.

Equation (2) accurately predicts the lubricant viscosity for the use in EHL applications [16]. Its application to prediction of traction is particularly important because traction is known to be highly sensitive to changes in viscosity. Hence Eq. (2) is utilized in the simulations of the current study.

3.2.2. Surface Roughness

The treatment of surface roughness in EHL applications generally falls into two categories: statistical and deterministic. The first category characterizes the surface parameters statistically, while the second one uses the actual surface profile. Statistical approaches are often preferred when one is interested in developing generalized solutions, and they are useful since in many applications the actual surface profile is unavailable.

The most commonly used statistical approach for modeling the surface roughness is due to the work of Greenwood & Williamson (GW) [39]. In their model, the asperity pressure is described as a function of the separation gap between two surfaces and the basic parameters of the surface such as surface roughness, asperity radius, and asperity density. In the original GW theory, the deformation of the asperities is assumed to be fully elastic. Later, Chang et al. [40] extended the analysis to include plastic deformation (CEB model). The elasto-plastic model proposed by Zhao et al. (ZMC model) [37] further developed the theory to include the intermediate elasto-plastic regime. This model, which was recently applied for the treatment of surface roughness in Line-contact EHL [36], is utilized in this study as well. More Recently, Beheshti & Khonsari [41] showed that this model gives very close results compared to other comprehensive models and confirmed its accuracy.

In this model, the asperity pressure P_a is composed of the summation of three terms which stand for the elastic, elasto-plastic and plastic deformation of the surface asperities:

$$P_a = P_{elastic} + P_{elasto-plastic} + P_{plastic} \tag{3}$$

The details of Eq. (3) are given in Chapter 2 (Eqs. (14) and (17)). For more information, the reader is referred to [36]. As shown in Chapter 2, the asperity pressure is described as a function

of separation gap—which is the film thickness in EHL applications —as well as the statistical parameters of the surface and the surface hardness. The statistical parameters of the surface include the surface roughness, i.e. the root mean square of the surface heights (σ), the asperity radius (β), and the asperity density (n). As discussed in Ref. [36], the EHL solution is not very sensitive to the ratio of σ/β, and, therefore, for the purpose of generalization, a reasonable assumption of $\sigma/\beta = 0.01$ is made. Also, there are many publications that show that the product of the surface parameters $n\beta\sigma$ does not appreciably change and that $n\beta\sigma$=0.05 is adopted in some studies [26, 27, 36]. These values are used in the current study. It follows, therefore, that the input parameters for the surface are the roughness (rms) and the hardness values. When both surfaces are rough, the equivalent surface roughness $\sigma = \sqrt{{\sigma_1}^2 + {\sigma_2}^2}$ is used.

3.2.3. EHL Equations

In the statistical treatment of the rough EHL contact, the load is assumed to be shared between the lubricant and the surface asperities. Therefore, the total pressure is the sum of the hydrodynamic and the asperity pressures. That is,

$$P = P_h + P_a \tag{4}$$

where P, P_h and P_a are the dimensionless total, hydrodynamic and asperity pressures, respectively.

The hydrodynamic component of Eq. (4) can be determined by solving the modified Reynolds equation with the consideration of Patir and Cheng's flow factors to account for the existence of roughness [42]. In dimensionless form, it reads [36]:

$$\frac{dP_h}{dX} = 48\bar{\mu}U\left(H_T - \bar{\rho}^{-1}K_r\right)\left(\Phi_x\right)^{-1}H^{-3} \tag{5}$$

where X is the coordinate in the moving direction, H is the film thickness, U is the dimensionless speed, $\bar{\mu}$ is the viscosity and $\bar{\rho}$ is the density, all in dimensionless form. H_T is the dimensionless average gap and Φ_x is the pressure flow factor in the moving direction defined by Patir and Cheng [42], which are both functions of the dimensionless surface roughness ($\bar{\sigma}$). K_r is a constant to be determined (see Section 2.5).

The dimensionless film thickness is [36]:

$$H(X) = H_{00} + \frac{4W}{\pi}\left[X^2 - \frac{1}{\pi}\int_{X_{\min}}^{X_{\text{end}}} P\ln(X\text{-}S)^2 dS \right] \tag{6}$$

where W is the dimensionless load, and X_{min} and X_{end} are the dimensionless inlet and outlet positions. H_{00} is another constant to be determined (see Section 2.5).

The load balance equation in dimensionless form is obtained by integrating Eq. (4):

$$\int_{X_{\min}}^{X_{end}} P_h(X)dX + \int_{X_{\min}}^{X_{end}} P_a(X)dX = \frac{\pi}{2} \tag{7}$$

3.2.4. Thermal Analysis

The general energy equation for line contact EHL is [8]:

$$k\frac{\partial^2 T}{\partial y^2} = -\mu\left(\frac{\partial u}{\partial y}\right)^2 - \beta_T\, T\, u\frac{\partial p_h}{\partial x} + \rho\, c_p\, u\frac{\partial T}{\partial x} \tag{8}$$

where T is the lubricant temperature, u is the lubricant speed and x and y are the coordinates along the sliding direction and across the gap, respectively. Parameters k, β_T, c_p, μ and ρ are the thermal conductivity, thermal expansivity, specific heat, viscosity and density of the lubricant, respectively. In Eq. (8), the term on the left-hand side represents conduction, while the terms on the right hand side represent viscous dissipation, compression heating and convection, respectively.

The contribution of asperity contact to heat generation is taken into account by adding the following source term, $\dot{Q}_a$, in Eq. (8):

$$\dot{Q}_a = u_s\frac{d\left(F_f\right)_a}{dV} = \frac{u_s f_c p_a dA}{dV} = \frac{u_s f_c p_a B dx}{hBdx} = \frac{f_c p_a u_s}{h} \tag{9}$$

where $(F_f)_a$ and p_a are the asperity friction force and pressure, respectively. Parameter u_s is the sliding speed, h is the film thickness, and B is the line-contact length. f_c is called the asperity friction coefficient, which is the friction coefficient of the surface asperities in presence of the lubricant (see Section 3.2.2).

Thus, the energy equation considering the roughness effect becomes:

$$k\frac{\partial^2 T}{\partial y^2} = -\mu\left(\frac{\partial u}{\partial y}\right)^2 - \beta_T T u\frac{\partial p_h}{\partial x} + \rho c_p u\frac{\partial T}{\partial x} - \frac{f_c p_a u_s}{h} \tag{10}$$

Equation (10) can be written in dimensionless form as:

$$\frac{\partial^2 \overline{T}}{\partial Y^2} = -K_1\overline{\mu}\left(\frac{\partial \overline{u}}{\partial Y}\right)^2 - K_2 H^2\overline{T}\,\overline{u}\frac{\partial P_h}{\partial X} + K_3\overline{\rho}H^2\overline{u}\frac{\partial \overline{T}}{\partial X} - K_4 P_a H \tag{11}$$

where $K_1=E'^2R^2U^2/k\mu_0T_0$, $K_2=\beta_T E'^2R^2U/4k\mu_0$, $K_3=(\rho_0 c_p E'R^2U(\pi/8W)^{0.5})/k\mu_0$, and $K_4=(f_c U.S.E'^2R^2(W/2\pi)^{0.5})/kT_0\mu_0$. Parameter $\overline{T}$ is the dimensionless temperature, E' is the effective Young modulus, R is the equivalent contact radius, and S is the slide-to-roll ratio.

The temperature distribution along the contact can be obtained from Eq. (11). The details of mid-film temperature equation and boundary conditions are given in Appendix B. Additional details on the formulation, albeit for smooth surfaces, can be found in [14].

3.2.5. Discretization and Solution Technique

The elasto-plastic asperity contact equation, Eq. (3), the modified Reynolds equation, Eq. (5), the film thickness, Eq. (6), the load balance, Eq. (7), and the mid-film temperature, Eq. (B1) are discretized using the finite difference method and solved simultaneously.

For N computational nodes, the system of equation consists of 2N-1 equations and 2N-1 unknowns. N-1 equations come from the Reynolds equation, Eq. (5), one from the load balance, Eq. (7), and N-1 from the mid-film temperature, Eq. (B1). The unknowns consist of hydrodynamic pressure at N-2 nodes (The pressure is zero at the boundaries), mid-film temperature at N-1 nodes (The temperature at the first node is the inlet temperature), and constant K_r in Eq. (5) as well as H_{00} in Eq. (6).

The inlet is considered as X_{min}=-4 to satisfy the fully-flooded condition. The outlet is where the pressure and its gradient become zero, which generally happens at a few nodes after X=1. Since the equations are non-linear, the Newton-Raphson algorithm is utilized, and to improve the convergence, an under-relaxation factor is applied in each iteration step. Also, the thermal solution is started by an initial pressure profile obtained from the isothermal solution and a linear initial temperature profile. The solution continues until the error between two successive iterations becomes smaller than a specified value. Typically 400 to 600 computational nodes are used in the simulations depending on the magnitude of the load; large loads require more computational nodes. Once converged, this solution procedure yields predictions of the pressure distribution (including the hydrodynamic, asperity, and total pressure), the film profile, and the temperature distribution along the contact. Based on these results, the central and the minimum film thickness, the asperity load ratio, and the maximum and the outlet temperatures can easily be calculated. Also, the traction coefficient which is the main interest of the current study is determined as described in the next section.

3.2.6. Traction Coefficient

The total traction force is the summation of asperity and hydrodynamic traction forces as:

$$F_f = \left(F_f\right)_a + \left(F_f\right)_h \tag{12}$$

The asperity traction force can be simply written as:

$$\left(F_f\right)_a = f_c.F_a \tag{13}$$

where F_a is the asperity load and f_c is the asperity friction coefficient. Using the asperity load ratio, L_a, which is the portion of the load carried by the surface asperities [36], Eq. (13) can be written as:

$$\left(F_f\right)_a = f_c.F.(\frac{L_a}{100}) \tag{14}$$

where F is the total normal load.

The hydrodynamic traction force can be written as:

$$\left(F_f\right)_h = \int \frac{\mu}{h} S u_r B dx + \frac{1}{2}\int h \frac{\partial p}{\partial x} b dx \tag{15}$$

where u_r is the rolling speed and B is the line-contact length. The first and the second terms on the right-hand side signify the fluid friction due to Couette and Poiseuille flows, respectively. It should be noted that the value of the second integral is negligible compared to the first integral, due to small variations of the film thickness and the close-to-symmetric distribution of the pressure along the contact area.

It should be noted that the current model is based on Newtonian Reynolds equation (Eq. (5)) and therefore the shear-thinning effect is neglected. However, the effect of limiting shear stress is taken into account in calculating the traction. In fact, EHL applications generally involve high loads, which lead to a substantial increase in both viscosity and shear rate. As a result, the lubricant may easily reach its limiting shear stress within the contact. When the limiting shear stress is reached, the lubricant exhibits a plastic behavior, wherein further increase in the shear rate will not result in an increase in the shear stress [43]. This effect should be considered in the analysis, without which the traction force may be largely overestimated.

The amount of limiting shear stress for a specific fluid is only a function of the fluid pressure and can be written as [16]:

$$\tau_{\lim} = \Lambda . p_h \tag{16}$$

where Λ is called limiting shear stress coefficient which is a lubricant property.

To implement limiting shear stress, the formulation proposed by Bair & Winer [44] is utilized to modify Eq. (15) as follows. The Poiseuille term is neglected here.

$$\left(F_f\right)_h = \int \tau_{\lim}\left(1 - e^{\frac{-\mu . S . u_r}{\tau_{\lim} h}}\right) B dx \tag{17}$$

The total traction force in dimensionless form is:

$$W_f = \left(\frac{L_a}{100}\right) W . f_c + \int \Lambda P_h \left(\frac{2W}{\pi}\right)\left(1 - e^{\frac{-\bar{\mu} S U}{\Lambda P_h H \sqrt{\frac{W}{2\pi}}}}\right) dX \tag{18}$$

Finally, the traction coefficient is obtained by dividing Eq. (18) by the total load as follows.

$$f = \frac{W_f}{W} = (\frac{L_a}{100}) f_c + \frac{2\Lambda}{\pi} \int P_h (1 - e^{\frac{-\bar{\mu} S U}{\Lambda P_h H \sqrt{\frac{W}{2\pi}}}}) dX \tag{19}$$

The solution to Eq. (19) gives the traction coefficient in a rough line-contact EHL.

3.3. Results and Discussion

3.3.1. Validation: Smooth Surface

Figure 3.1 shows the variation of traction coefficient versus the slide-to-roll ratio for smooth EHL contact. The results from the present study are compared with those reported by Lee & Hsu [8] as well as Kumar & Khonsari [14]. As shown in the figure, the current predictions are in good agreement with both published results. It should be noted that smooth surface results in the present analysis are simulated by setting the surface roughness to a very small value ($\bar{\sigma} = 1 \times 10^{-8}$). Also, in order to be consistent with references [8] and [14], the Roelands equation is used for the variations of the lubricant viscosity. Note that for this particular oil, the pressure-viscosity coefficient is low (α=1.59×10^{-8} or Z= 0.48) and under the specified operating conditions the lubricant does not reach its limiting shear stress.

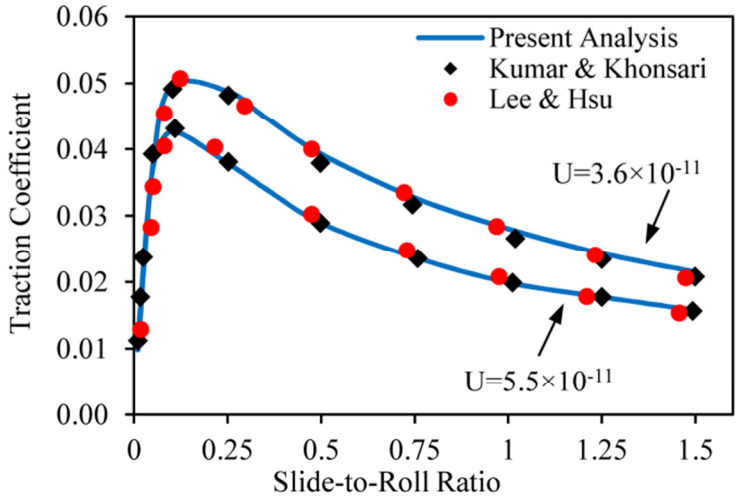

Figure 3.1. Comparison of the traction coefficient versus slide-to-roll ratio from current model with those by Lee and Hsu [8] and Kumar and Khonsari [14] (W=1.3×10^{-4}, G=3500)

3.3.2. Experimental Validation: Rough Surface

In this section, the results from the simulation are validated experimentally. The description of the test rig follows.

3.3.2.1. Test Rig Assembly

Experimental tests were conducted using rolling/sliding test rig designed and built at LSU Center for Rotating Machinery (CeRoM). The test rig is shown in Fig. 3.2. It consists of two rollers with different diameters, each driven by a separate motor/gearbox unit. Only one motor/gearbox unit is shown in the figure. The desired rolling speed and also the slide-to-roll ratio can be achieved by varying the rotational speed of each roller. The test rig is equipped with a lubrication system which circulates the oil between the reservoir and the contacts area. A hydraulic pressure system is used to apply the normal load to the rollers and the amount is controlled by a pressure gauge (not shown in the figure). The machine is also equipped with an infrared sensor to monitor the contact temperature. The friction force is measured by torque sensors mounted on both shafts.

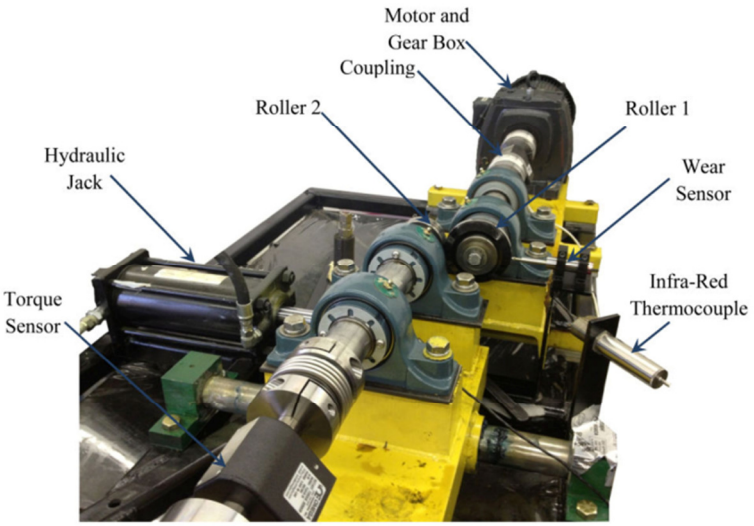

Figure 3.2. Test Rig at LSU CeRoM

The oil used in the current experiment is a non-detergent SAE30. The free volume properties of the oil are taken from [16] reported for SAE20. However, the reference viscosity and also the temperature dependency of the lubricant are measured by a rheometer to update the free volume properties. These properties are: T_R =20˚C, μ_R = 0.35 Pa.s, K'_0=10.4, K_∞=-0.9282 GPa, $\dot{K}_0$=580.7 GPa.K, a_V =8×10^{-4} K^{-1}, B=3.52, R_0=0.698, ε=-15×10^{-4} K^{-1}. The other properties are chosen as ρ_0=888 Kg/m^3, k=0.145 W/mK, c_p=1880 J/kgK for the general engine oil [45]. Also, β_T= 0.0007 K^{-1}.

The rollers used in the current study have the radii of R_1=53 and R_2=38 mm, so the effective radius is R=21.8 mm. The hardness of the rollers is 42 RC (equal to 412 Vickers=4.04 GPa), and the material is steel (with the effective Young modulus of E'=228 GPa), so the dimensionless hardness is calculated as V=0.018. The surface roughness of the rollers is measured by a profilometer. Two roller sets are used in the experiments. First set includes σ_1=0.2 μm and

σ_2=0.2 μm yielding a combined roughness of $\sigma = \sqrt{{\sigma_1}^2 + {\sigma_2}^2}$=0.283 μm. This gives the dimensionless roughness of $\bar{\sigma} = 1.3 \times 10^{-5}$. Second set includes σ_1=0.2 μm and σ_2=0.42 μm yielding $\sigma = \sqrt{{\sigma_1}^2 + {\sigma_2}^2}$=0.465 μm. This yields the dimensionless roughness of $\bar{\sigma} = 2.1 \times 10^{-5}$. The other properties of steel surfaces are taken as $\rho_L = \rho_H$=7850 Kg/m^3, $k_L = k_H$=47 W/mK, and $c_L = c_H$=460 J/kgK [8].

3.3.2.2. Measuring Asperity Friction Coefficient

To calculate the traction coefficient by Eq. (19), the asperity friction coefficient f_c should be determined. This is the friction coefficient between the rough surfaces in the presence of oil and should not be confused with the dry friction coefficient between the surfaces. The value of the asperity friction coefficient reported in some studies is about 0.1~0.13 [28, 30, 31]. In order to obtain this coefficient by the experiment, the rollers are rotated at a very low rolling speed to minimize the hydrodynamic effect. The friction coefficient which is measured in this situation is considered to be the asperity friction coefficient because the entire load is carried by the surface asperities. For this purpose, the rollers of the rolling/sliding test rig are rotated at the speed of about 1-2 RPM and then the slide-to-roll ratio is varied. Figure 3.3 shows the calculated asperity friction coefficient for two sets of rollers with different surface roughness values ($\bar{\sigma}_1 = 1.3 \times 10^{-5}$, $\bar{\sigma}_2 = 2.1 \times 10^{-5}$) in different slide-to-roll ratios. Also, two different load levels (W_1=4×10^{-5}, W_2=3×10^{-4}) are used.

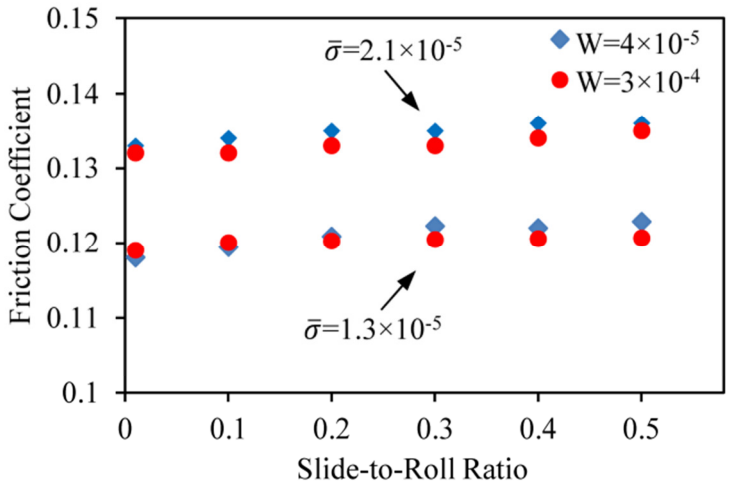

Figure 3.3. Experimental determination of asperity friction coefficient f_c

As shown, the asperity friction coefficient is not very sensitive to the slide-to-roll ratio, because fluid friction at low speed is nil. Also, it is only slightly dependent on the load. From the figure, the asperity friction coefficient is approximated as f_c=0.12 for $\bar{\sigma}_1 = 1.3 \times 10^{-5}$ and f_c=0.135 for $\bar{\sigma}_2 = 2.1 \times 10^{-5}$. As observed, the rougher surface has a larger asperity friction coefficient. It

should also be noted that the asperity friction coefficient may also be a function of the surface material. Further studies are needed in this area.

3.3.2.3. Limiting Shear Stress Coefficient

As mentioned in Section 2.5, the limiting shear stress of a lubricant is only a function of the pressure, and can be written as $\tau_{lim} = \Lambda . p_h$, where the limiting shear stress coefficient Λ is a lubricant property. This coefficient varies slightly with temperature but is insensitive to the contact pressure. Its typical value ranges from 0.03 to 0.12 depending on the lubricant [16]. The limiting shear stress coefficient can be measured experimentally [16, 18, 21]. For this purpose, a high normal load is applied to the surfaces to ensure that the oil viscosity is large enough to reach its limiting shear stress over the entire contact zone at very low sliding speeds. The traction coefficient starts to increase from zero at zero sliding speed to a certain amount and then will not change as it reaches a plateau. The maximum amount of hydrodynamic traction coefficient is equal to the limiting shear stress coefficient Λ.

In this study, for the operating oil (SAE30), a dimensionless normal load of W=3.7×10^{-4} (equal to maximum Hertzian pressure of 1.75 GPa) is applied to the smoother set of rollers ($\bar{\sigma} = 1.3 \times 10^{-5}$) at the rolling speed of U=1×10^{-11}, and then the slide-to-roll ratio is gradually increased from zero. The traction coefficient is then measured and plotted versus slide-to-roll ratio as shown in Fig. 3.4.

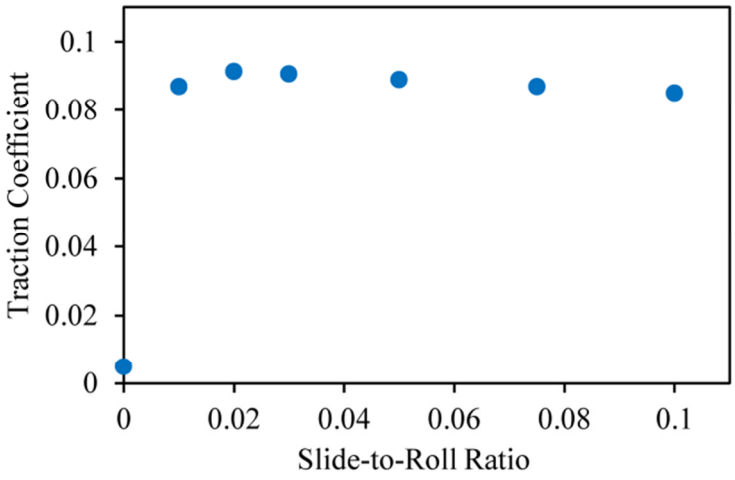

Figure 3.4. Experimental determination of limiting shear stress coefficient Λ (W=3.7×10^{-4}, U=1×10^{-11})

As shown, the traction coefficient increases by increasing the slide-to-roll-ratio. Due to high load, the shear stress reaches it limiting value very fast and, subsequently, it decreases due to temperature rise. The maximum amount of the shear stress for the lubricant treated (SAE 30) is Λ = 0.091.

It should be noted that since the rollers are not ideally smooth, a part of the load is carried by the surface asperities. However, in this experiment the rolling speed is sufficiently large and the surface roughness is relatively low ($\bar{\sigma} = 1.3 \times 10^{-5}$), so that the asperity load ratio is small and does not significantly affect the results. The simulation shows that the asperity load ratio for this test is only about 6%.

3.3.2.4. Validation of the Simulations

Having determined the asperity friction coefficient and the limiting shear stress coefficient for the experimental setup, these values are used and results are compared with experimental measurement using the rolling/sliding test rig. Two sets of rollers with dimensionless surface roughness of $\bar{\sigma}_1 = 1.3 \times 10^{-5}$ and $\bar{\sigma}_2 = 2.1 \times 10^{-5}$ are used. The dimensionless hardness of both sets is V=0.018 (See Section 3.2.1).

Figures 3.5 and 3.6 compare the predicted traction coefficient with the experimental results obtained for the smoother set of rollers ($\bar{\sigma} = 1.3 \times 10^{-5}$). The corresponding asperity friction coefficient is assumed as f_c =0.12 (See Section 3.2.2). The dimensionless speed is kept constant as $U = 1\times10^{-11}$, while the dimensionless load values are W=4×10^{-5} and W=1×10^{-4} in Figs. 3.5 and 3.6, respectively. As shown, the simulation results and the experimental measurements are in good agreement in both trend and magnitude.

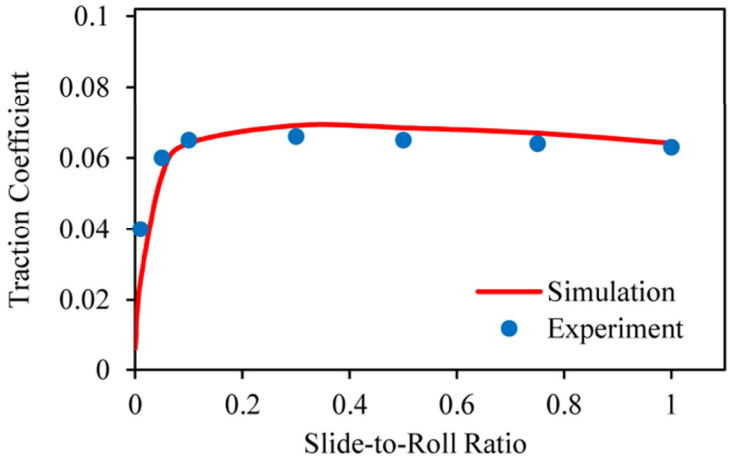

Figure 3.5. Comparison of simulations and measurements
(W=4×10^{-5}, U=1×10^{-11}, $\bar{\sigma} = 1.3 \times 10^{-5}$)

Note that in this set of experiments, the surface roughness of the examined specimens is fairly small, so only a small portion of the load is carried by the asperities. The simulations show that the asperity load ratio is only about 6% for both cases.

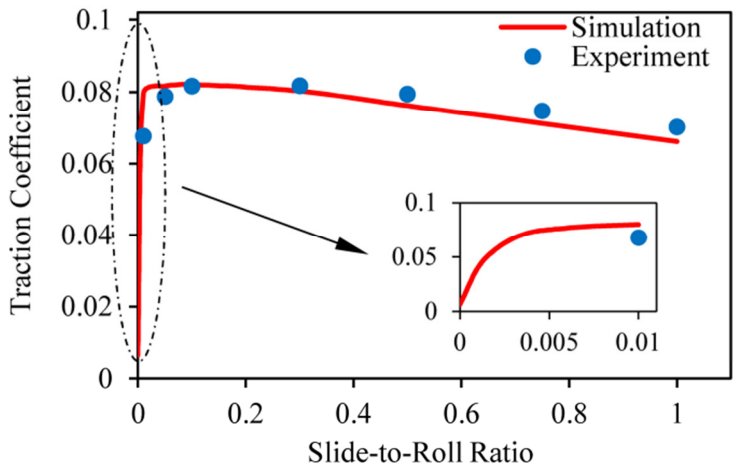

Figure 3.6. Comparison of simulations and measurements
(W=1×10^{-4}, U=1×10^{-11}, $\bar{\sigma} = 1.3 \times 10^{-5}$)

Figures 3.7 and 3.8 show the traction curve for the rougher set of rollers ($\bar{\sigma} = 2.1 \times 10^{-5}$). The corresponding asperity friction coefficient used in the simulations is f_c=0.135 (See Section 3.2.2). The dimensionless speed is U=1×10^{-11}, and the dimensionless load values are W=4×10^{-5} and W=1×10^{-4} in Figs. 3.7 and 3.8, respectively. Again, the simulation results are found to be in good agreement with the experiments.

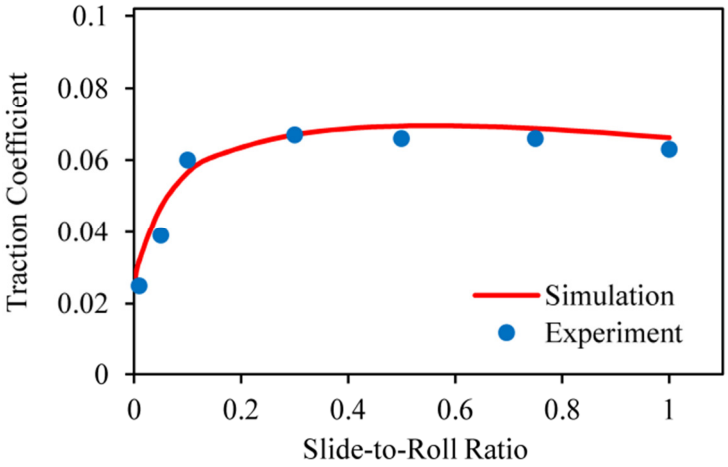

Figure 3.7. Comparison of simulations and measurements
(W=4×10^{-5}, U=1×10^{-11}, $\bar{\sigma} = 2.1 \times 10^{-5}$)

It is worthwhile to mention that the predicted asperity load ratio against the slide-to-roll ratio varies between 21% and 23% for W=4×10^{-5} (Fig. 3.7) and between 17% and 19% for W=1×10^{-4} (Fig. 3.8). Note that the asperity load ratio does not appreciably change with the slide-to-roll ratio (See Section 3.4). Also, the asperity load ratio is higher for the lower load value [36].

A noticeable trend is that the traction coefficient for the rougher surface (Figs. 3.7 and 3.8) is greater at zero sliding compared to that of the smoother surfaces (Figs. 3.5 and 3.6). This is simply due to higher asperity load ratio of the rougher surface which increases the asperity part of the traction coefficient (See Eq. (19)).

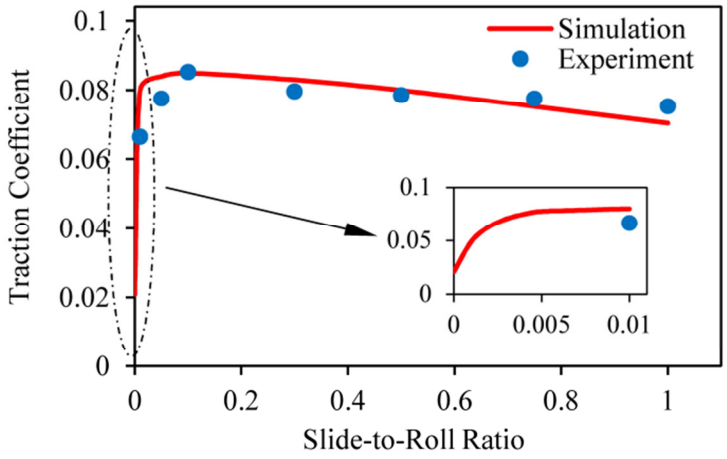

Figure 3.8. Comparison of simulations and measurements
(W=1×10^{-4}, U=1×10^{-11}, $\bar{\sigma} = 2.1 \times 10^{-5}$)

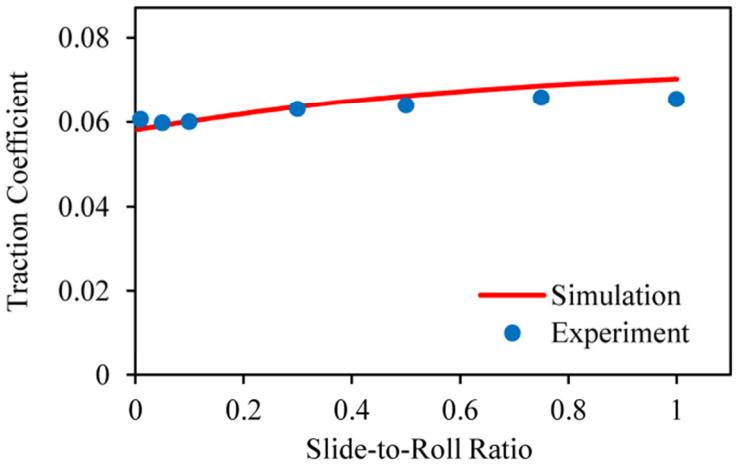

Figure 3.9. Comparison of simulations and measurements
(W=3.5×10^{-5}, U=2×10^{-12}, $\bar{\sigma} = 1.3 \times 10^{-5}$)

The asperity load ratio is highly dependent on the rolling speed [36]. At low rolling speeds, the film thickness is smaller and the asperity load ratio is high. Therefore, even with the fairly smooth surfaces, the asperity contact can be significant at low rolling speeds. In order to show this trend, another test is conducted using the smoother set of rollers ($\bar{\sigma} = 1.3 \times 10^{-5}$) subjected to a low rolling speed and light load. Figure 3.9 compares the results of the predictions with the experimental data for W=3.5×10^{-5}, U=2×10^{-12}. In this case, simulation shows that about 50% of

the load is carried by the asperities. As shown, for the case of rough surface, the traction coefficient is less dependent on the slide-to-roll ratio (compare the results in Fig. 3.9 with those in Figs. 3.5 and 3.6). Also, as shown in Fig. 3.9, the traction coefficient has a noticeable value at very low sliding speeds.

3.3.3. Effect of Operating Parameters on the Traction Coefficient

In this section, the results of a set of simulations are presented and discussed. All results are for SAE30 lubricant and steel rollers described in section 3.2.1. The effect of load, speed, and the surface roughness follows.

3.3.3.1. Load

Figure 3.10 shows the effect of load on the traction coefficient. It illustrates the variations of the traction coefficient with slide-to-roll ratio for three different load values (W=2×10^{-5}, W=1×10^{-4} and W=3×10^{-4}). The dimensionless speed, surface roughness, and hardness values are kept at U=1×10^{-11}, $\bar{\sigma} = 2 \times 10^{-5}$, and V=0.01. The asperity friction coefficient is assumed to be f_c=0.135.

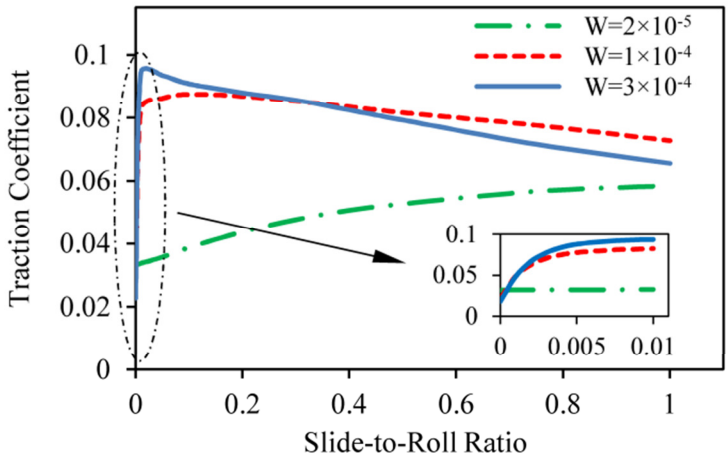

Figure 3.10. Effect of load on the traction coefficient (U=1×10^{-11}, $\bar{\sigma} = 2 \times 10^{-5}$)

As shown in Fig. 3.10, higher loads generally results in higher traction coefficients. This can be explained by noting that the load (and therefore the contact pressure) has a significant effect on the lubricant viscosity (and also the shear rate). Increasing the load increases the shear stress. However, at higher slide-to-roll ratios, heat generation generally tends to reduce the lubricant viscosity and consequently the traction coefficient drops. Nevertheless, as can be seen in Fig. 3.10, for the lowest load value (W=2×10^{-5}), the traction coefficient steadily increases (within the slide-to-roll ratio of 0-1), since the heat generation is negligibly small. This should be contrasted with the prediction for the highest load in which the drop in the traction coefficient is very significant, because of the high amount of heat generation.

The asperity load ratio for the lowest load value (W=2×10^{-5}) changes from about 23.6% at S=0 to 25.4% at S=1, while for the highest load value (W=3×10^{-4}), it changes from 13.2% to 14.3%. As observed, the asperity load ratio does not appreciably change with slide-to-roll ratio (and its corresponding temperature rise). This is mostly because the film profile does not significantly change with the slide-to-roll ratio, making the asperity load ratio nearly independent of the slide-to-roll ratio (see Section 4.2).

3.3.3.2. Speed

Figure 3.11 shows the effect of the rolling speed on the traction coefficient. It depicts the variation of the traction coefficient with respect to the slide-to-roll ratio for three different dimensionless speed values (U=5×10^{-12}, U=1×10^{-11} and U=2×10^{-11}). The dimensionless load, surface roughness, and hardness are kept at W=5×10^{-5}, $\bar{\sigma} = 2 \times 10^{-5}$ and V=0.01. The asperity friction coefficient is assumed as f_c=0.135.

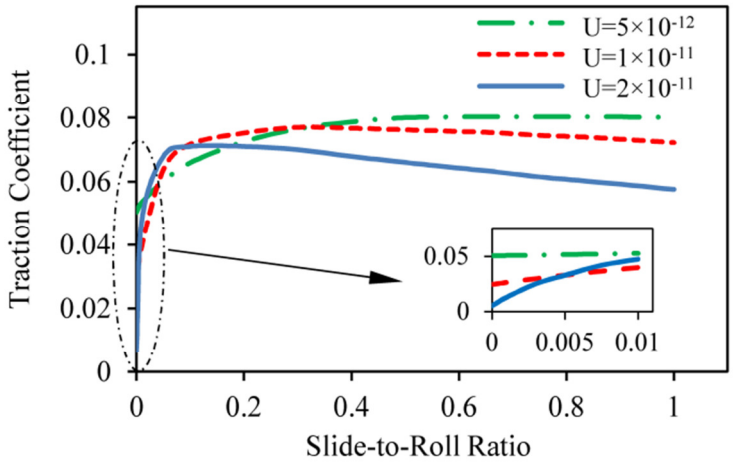

Figure 3.11. Effect of rolling speed on the traction coefficient (W=5×10^{-5} $\bar{\sigma} = 2 \times 10^{-5}$)

As shown, for the lowest rolling speed, the traction coefficient continuously rises by increasing the slide-to-roll ratio because the heat generation is small. For higher rolling speeds, the traction coefficient reaches a plateau and begins to gradually drop due to temperature rise.

The speed has two distinct and opposing effects on the traction. The first effect is increasing the shear rate. For a constant slide-to-roll ratio, increasing the rolling speed increases the shear rate $\dot{\gamma}$. In fact, according to $\dot{\gamma} = \partial u/\partial y$, increasing the speed increases both the numerator (speed) and the denominator (film thickness), but overall $\dot{\gamma}$ increases. The other effect of speed is to raise the contact temperature and concomitantly reduce the viscosity. The combination of these two opposing effects determines the traction coefficient. As shown, at low slide-to-roll ratios the shear rate effect dominates and the traction coefficient is larger for the higher rolling speed. On

the other hand, at high slide-to-roll ratios, the heat generation tends to dominate, and the traction coefficient becomes smaller for the higher speed.

It should also be noted that at very low slide-to-roll ratios (see the inset in Fig. 3.11), the traction coefficient is smaller for the higher speed which is due to another reason. In fact, at very low slide-to-roll ratios, the hydrodynamic traction is nil, and the asperity traction —which is a direct function of the asperity load ratio—reduces drastically by the speed [36]. The asperity load ratio of L_a=37% for U=5×10^{-12}, L_a=18% for U=1×10^{-11}, and L_a=4% for U=2×10^{-11} (at zero sliding) confirms this.

3.3.3.3. Surface Roughness

Figure 3.12 shows the effect of surface roughness on the traction coefficient. It illustrates the variation of the traction coefficient with respect to slide-to-roll ratio for three different surface roughness values ($\bar{\sigma}$ = 0, $\bar{\sigma}$ =2×10^{-5} and $\bar{\sigma}$ =4×10^{-5}). The asperity friction coefficient is assumed to be f_c=0.135 for $\bar{\sigma}$ =2×10^{-5} and f_c=0.15 for $\bar{\sigma}$ =4×10^{-5}. The dimensionless load, speed, and hardness are kept at W=5×10^{-5}, U=1×10^{-11} and V=0.01.

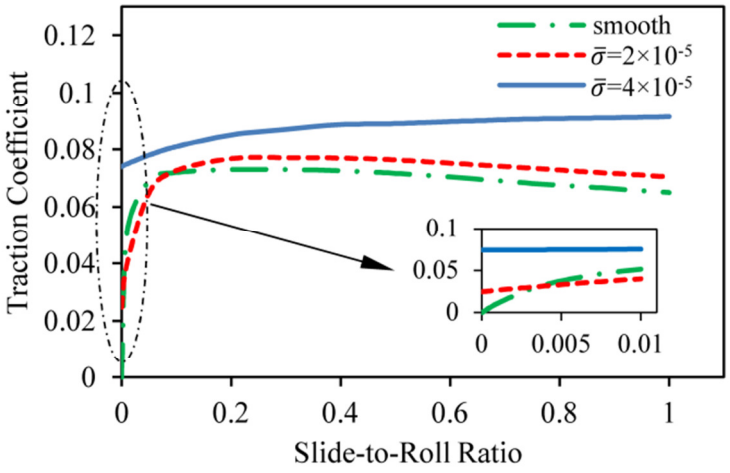

Figure 3.12. Effect of surface roughness on the traction coefficient (W=5×10^{-5}, U=1×10^{-11})

As shown, surface roughness generally makes the traction coefficient less dependent on the slide-to-roll ratio. A simple explanation is that—as mentioned before— the contribution of asperity to the traction coefficient is determined by multiplying the asperity load ratio by the asperity friction coefficient. For rough surfaces, the traction coefficient is non-zero at very low sliding speeds, while for an ideally smooth surface it is nil. The corresponding asperity load ratio (at zero sliding) is about 18% for $\bar{\sigma}$ =2×10^{-5} and 49% and $\bar{\sigma}$ =4×10^{-5}.

It is also interesting to note that as the slide-to-roll ratio increases from zero, the traction coefficient of a smooth surface may sometimes become larger than that of the rough surface.

This can be explained by noting that when dealing with smooth surfaces, the entire load is carried by the lubricant which increases the viscosity and consequently the shear stress. However, this generally happens only at relatively low sliding. Beyond a certain slide-to-roll ratio, the traction coefficient of the rough surface is larger than of the smooth surface.

3.3.4. Effect of Slide-to-Roll Ratio on the Film Thickness and the Asperity Load Ratio

At typical rolling speeds, the film thickness value of pure rolling (zero sliding) can be assumed to be effectively isothermal, because temperature rise is small. By increasing the slide-to-roll ratio, the temperature simply goes up. To study the effect of slide-to-roll ratio and its consequent temperature rise on the film thickness and the asperity load ratio, the corresponding film profiles at S=0 (pure rolling) and S=1 (high sliding) are compared. Figures 3.13 and 3.14 show this comparison for ideally smooth surfaces and considerably rough surfaces, respectively. In both cases, a high load value (W=2×10^{-4}) is chosen which results in a noticeable temperature rise at high sliding (S=1). The dimensionless speed and hardness are kept constant at U=1×10^{-11} and V=0.01.

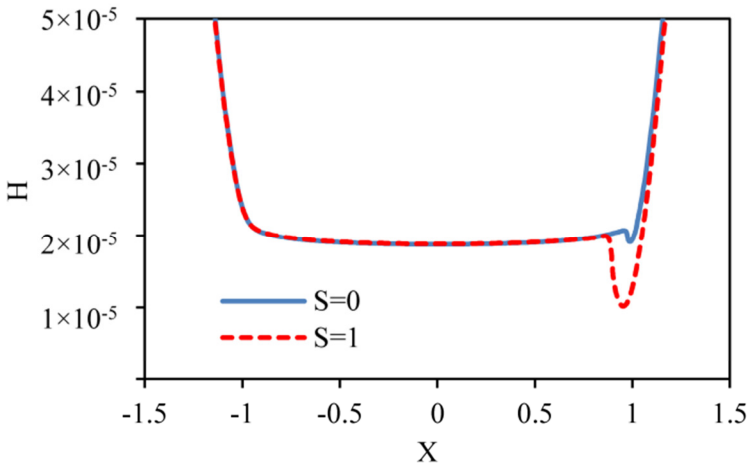

Figure 3.13. Effect of temperature rise on the film thickness – smooth surfaces (W=2×10^{-4}, U=1×10^{-11}, $\bar{\sigma} = 0$)

As shown, despite the temperature rise at high sliding, the central film thickness does not significantly change. This change is almost nil for the smooth surface, while it is about 4% for the rough surface. The major change in the film profile happens at the outlet, where the minimum film thickness considerably drops. This drop is about 46% for the smooth surface and 30% for the case involving rough surfaces. Another finding is that the asperity load ratio does not significantly changes with the slide-to-roll ratio. The corresponding asperity load ratio (for the rough case) increases from 24% at S=0 to 26% at S=1.

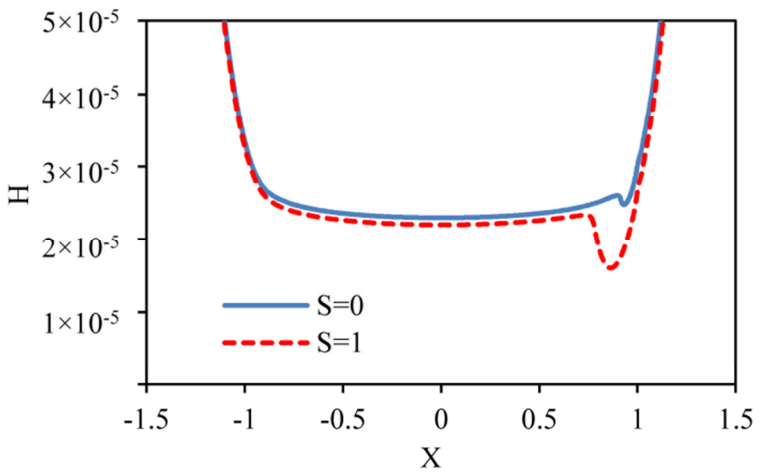

Figure 3.14. Effect of temperature rise on the film thickness - rough surfaces (W=2×10^{-4}, U=1×10^{-11}, $\bar{\sigma} = 3 \times 10^{-5}$)

It is worthwhile to mention that the results for the smooth surfaces reported by Cheng [46] and Dowson [47] show that the film profile does not appreciably change with the slide-to-roll ratio and its corresponding temperature rise. Also, Sadeghi & Sui [7] showed that the major change in the film thickness due to an increase in slide-to-roll ratio occurs at the outlet and that its influence is felt at the minimum film thickness. Later, Hsu & Lee [9] suggested a curve-fit formula for the drop in the minimum film thickness. The current study shows a drop in minimum film thickness for both smooth and rough surfaces. The results also show that the drop in the minimum film thickness of rough surfaces is less than of the smooth ones.

It should also be mentioned that the thermal film profile at zero sliding starts to deviate from isothermal film profile as the rolling speed increases. This change—which is due to viscous heating at the inlet— is generally small at moderate rolling speeds, but can reduce the film thickness at higher speeds [48]. However, for the speed range used in the current study (3×10^{-12} < U < 3×10^{-11} —see section 4.1), no significant drop is observed due to this effect.

It can be concluded that at moderate rolling speeds, the isothermal values of the central film thickness and the asperity load ratio are still valid when there is temperature rise due to sliding. This implies that the isothermal formulas for the central film thickness and the corresponding asperity load ratio [36] are reliable for moderate rolling speeds even at high slide-to-roll ratios.

3.4. Case Study: Curve-Fit Formula for the Traction Coefficient

The authors presented formulas for the film thickness and asperity load ratio in their previous study [36]. Since the traction coefficient is highly dependent on the properties of the oils, it is extremely difficult to present a general formula that works for all lubricants. In fact, the free volume model—which provides the most accurate relationship for predicting the pressure-

viscosity and temperature-viscosity dependency of the lubricants—requires specification of a number of parameters unique to a given lubricant.

3.4.1. Predicting the Traction Coefficient by a Curve-Fit Formula

As a case study, the results from the simulation for the examined oil SEA30 are curve-fitted to present a formula for predicting the traction coefficient of rough-line contact EHL. Table 3.1 shows the range of input used for this simulation. The lubricant is SAE30 with limiting shear stress of Λ=0.091(see Section 3.2.3). The dimensionless hardness is kept constant at V=0.01. In addition, the slide-to-roll ratio is entered as an input. Also, the results from the simulation show that the viscous heating and asperity contact heating are the dominant terms in the energy equation (Eq. (11)). Thus, another dimensionless input parameter is adopted as $K=E'R/(k\mu_0 T_0)^{0.5}$ as appears in constants K_1 and K_4 in Eq. (11).

Table 3.1. Input range for the curve fitting

Parameter	W	U	$\bar{\sigma}$	S	K
min	2×10^{-5}	3×10^{-12}	0	0	4×10^{8}
max	3×10^{-4}	3×10^{-11}	4×10^{-5}	0.20	4×10^{9}

The curve-fit formula for the traction coefficient is:

$$f = f_c\left(\frac{L_a}{100}\right)+$$
$$\left(\Lambda\left(1-\exp(-0.507S.\overline{W}^{2.487}\overline{U}^{0.229}\left(1-\frac{L_a}{100}\right)^{4.438}\Lambda^{-1})\right)-0.058\,\overline{W}^{-0.326}(\overline{U}.\overline{K})^{0.067}S^{0.507}\right)\left(1-\frac{L_a}{100}\right) \quad (20)$$

where $\overline{W}=W/(2\times10^{-5})$, $\overline{U}=U/(3\times10^{-12})$ and $\overline{K}=K/(4\times10^{8})$ are defined. In equation (20), L_a is the isothermal asperity load ratio obtained as [36]:

$$L_a = 0.005\,W^{-0.408}U^{-0.088}G^{0.103}[\ln(1+4470\ \bar{\sigma}^{6.015}V^{1.168}W^{0.485}U^{-3.741}G^{-2.898})] \quad (21)$$

The maximum difference between the curve-fit and the actual traction coefficient is about 0.012 for the smooth surface and 0.02 for the rough surface.

It should be noted that Eq. 20 is a curve-fit formula based on the simulations for a specific surface material (steel), and a specific lubricant (SAE30) using its free-volume rheological properties. Therefore, there is no dimensionless material parameter G as an input. However, the parameter G still appears in the curve-fit formula for calculating the asperity load ratio L_a (Eq. (21)). For this purpose, G=5700 was used for lubricant SAE30 and steel surfaces assuming $\alpha=2.5\times10^{-8}$ and $E'=2.28\times10^{11}$ to obtain the asperity load ratio from Eq. (21).

Equation (20) presents a curve-fit formula based on the theory mentioned in Section 2.5. It is a combination of the asperity traction (first term) and hydrodynamic traction (second term). As shown, the asperity load ratio (L_a) plays a key role in obtaining the traction of rough line-contact EHL. Even though Eq. (20) can only be used for the specific oil type, similar equations with different coefficients can be obtained for other types of lubricants.

3.4.2. An Illustrative Example

To illustrate the validity of Eq. (20), consider two identical steel rollers with the radius of two inches (R_1=R_2=50.8 mm) with the effective Young's modulus of E'=228 GPa and the equivalent contact radius of R=25.4×10^{-3} m. The inlet temperature is T_0=293 K, and the lubricant used is SAE 30 with μ_0=0.35 Pa.s and Λ=0.091. The applied load is 3 KN and the rollers width is 1 cm, so the dimensionless load is W=5.18×10^{-5}. The linear speed of rollers are 0.21 m/s and 0.19 m/s, so the rolling speed is u_r=0.2 m/s while the sliding speed is u_s=0.02 m/s. This yields a slide-to-roll ratio of S=0.1, and dimensionless speed of U=1.2×10^{-11}. The Vickers hardness of the surfaces is 240 Kg/mm^2 (2.35 GPa), which gives the dimensionless hardness as V=0.0103. Also, K=1.5×10^9 is obtained using k=0.145 W/mK for SAE30.

Table 3.2 compares the result of simulation with those from the curve-fit formula for three different surface roughness values. In both simulation and curve-fit equation, the asperity friction coefficient of f_c=0.12, 0.135, and 0.15 is used for these three surface roughness values, respectively.

Table 3.2. Comparison between the simulation and curve-fit results

Set	Roughness of each roller (μm)	Combined roughness (μm)	Dimensionless roughness	Traction coefficient (simulation)	Traction coefficient Eq. (20)	Asperity load ratio (simulation)	Asperity load ratio Eq. (21)
1	0.18	0.255	1×10^{-5}	0.072	0.075	0.6%	0.8%
2	0.36	0.510	2×10^{-5}	0.074	0.082	13.7%	14.4%
3	0.72	1.02	4×10^{-5}	0.077	0.082	44.1%	39.8%

As another example, see Table 3.3 which compares the simulation and curve-fit equation results for the same input as above, but the slide-to-roll ratio of S=0.01.

Table 3.3. Comparison between the simulation and curve-fit results

Set	Roughness of each roller (μm)	Combined roughness (μm)	Dimensionless roughness	Traction coefficient (simulation)	Traction coefficient Eq. (20)	Asperity load ratio (simulation)	Asperity load ratio Eq. (21)
1	0.18	0.255	1×10^{-5}	0.053	0.045	0.6%	0.8%
2	0.36	0.510	2×10^{-5}	0.044	0.041	13.6%	14.4%
3	0.72	1.02	4×10^{-5}	0.067	0.061	43.5%	39.8%

3.5. Conclusions

A model is developed to predict the traction coefficient in line-contact EHL. This approach is based on the statistical evaluation of surface asperities with consideration of elastic, elasto-plastic, and fully plastic deformation. For more accuracy, the free-volume properties of the lubricants are used, and the limiting shear stress effect is included. Also, the temperature rise effect is included which contains the heat generation by both lubricant and surface asperities. Experimental tests are conducted to verify the theoretical results. This method shows that the traction coefficient of EHL application can be stated as a summation of the hydrodynamic and the asperity parts. It is shown that the asperity load ratio plays an important role in the traction coefficient of rough surfaces. A useful curve-fit expression is also presented to predict the traction coefficient for SAE30. The general form of this expression can be applied to other lubricants as well.

Nomenclature

b	half Hertzian width, $R(8W/\pi)^{0.5}$, m
B	line-contact length, m
c_L	specific heat of lower surface, J/kgK
c_H	specific heat of upper surface, J/kgK
c_p	specific heat of lubricant, J/kgK
E'	effective modulus of elasticity, $1/E'=0.5[(1-\nu_1^2)/E_1+(1-\nu_2^2)/E_2]$, Pa
f	traction coefficient
f_c	asperity friction coefficient
F	total normal load, N
F_a	asperity load, N
F_f	traction force, N
$(F_f)_a$	asperity traction force, N
$(F_f)_h$	hydrodynamic traction force, N
G	dimensionless material number, $E'\alpha$
h	film thickness, m
h^*	h/σ
h_c	central film thickness, m
$h_{\min}$	minimum film thickness, m
h_T	average gap between two surfaces, m
H	dimensionless film thickness, h/R
H_c	dimensionless central film thickness, h_c/R
$H_{\min}$	dimensionless minimum film thickness, h_{min}/R
H_T	dimensionless average gap, h_T/R
hd	Vickers hardness, Pa
k	thermal conductivity of lubricant, W/mK
k_L	thermal conductivity of lower surface, W/mK
k_H	thermal conductivity of upper surface, W/mK
K	dimensionless thermal number, $E'R/(k\mu_0 T_0)^{0.5}$
L_a	asperity load ratio (percentage)

n	asperity density, m^{-2}
$\bar{n}$	dimensionless asperity density, nR^2
p	total pressure, Pa
p_a	asperity pressure, Pa
p_h	hydrodynamic pressure, Pa
P	dimensionless total pressure, $4R\,p/\,E'b$
P_a	dimensionless asperity pressure, $4R\,p_a\,/\,E'b$
P_h	dimensionless hydrodynamic pressure, $4R\,p_h\,/\,E'b$
R	equivalent contact radius, $[1/R_1 \pm 1/R_2]^{-1}$, m
S	slide-to-roll ratio, $u_{s/}\,u_r$
T	mid-film temperature, K
T_0	inlet temperature, K
T_R	reference temperature, K
T_L	lower surface temperature, K
T_H	upper surface temperature, K
$\bar{T}$	dimensionless mid-film temperature, T/T_0
$\bar{T}_L$	dimensionless lower surface temperature, T_L/T_0
$\bar{T}_H$	dimensionless upper surface temperature, T_H/T_0
u	fluid speed, m/s
u_r	rolling speed, $(u_1+u_2)/2$, m/s
u_s	sliding speed, $\|u_1-u_2\|$, m/s
$\bar{u}$	dimensionless fluid speed, u/u_r
U	dimensionless speed number, $\mu_0 u_r/E'R$
v	lubricant volume, m^3
v_R	lubricant reference volume, m^3
V	dimensionless hardness number, hd/E'
w	load per contact length, F/B, N/m
w_1	critical interference at the point of initial yield, $(0.6\pi.hd/E)^2\beta$, m
$\bar{w}_1$	w_1/R
w_1^*	w_1/σ
w_2	critical interference at the point of fully plastic flow, $54w_1$, m
$\bar{w}_2$	w_2/R
W	dimensionless load number, $w/E'R$
W_f	dimensionless traction force, $F_f/E'RB$
x	coordinate in the moving direction, m
$x_{\min}$	inlet position, m
x_{end}	outlet position, m
X	dimensionless coordinate in the moving direction, x/b
$X_{\min}$	dimensionless inlet position, $x_{\min}/b$
X_{end}	dimensionless outlet position, x_{end}/b
y	coordinate in the vertical direction, m
y_s	distance between the mean line of the surface and the mean line of its summits, m
$\bar{y}_s$	y_s/R
y_s^*	y_s/σ
Y	dimensionless coordinate in the vertical direction, y/h

z	height of asperities measured from the mean line of the summits, m
z^*	z/σ
Z	viscosity-pressure index
α	pressure-viscosity coefficient, m^2/N
β	asperity radius, m
$\bar{\beta}$	dimensionless asperity radius, β/R
β_T	lubricant thermal expansivity, K^{-1}
Λ	limiting shear stress coefficient
μ	lubricant viscosity, Pa.s
μ_0	inlet viscosity, Pa.s
μ_R	reference viscosity, Pa.s
$\bar{\mu}$	dimensionless viscosity, μ/μ_0
ρ	lubricant density, kg/m^3
ρ_L	density of lower surface, kg/m^3
ρ_H	density of upper surface, kg/m^3
ρ_0	lubricant density at zero pressure, kg/m^3
$\bar{\rho}$	dimensionless density, ρ/ρ_0
σ	standard deviation of the surface heights, m
$\bar{\sigma}$	dimensionless surface roughness number, σ/R
σ_s	standard deviation of the surface summits, m
$\bar{\sigma}_s$	σ_s/R
τ_{lim}	limiting shear stress, Pa
φ_x	pressure flow factor in x direction

3.6. References

[1] Dowson D, Higginson GR. *Elasto-hydrodynamic lubrication*. SI ed. Oxford Eng., New York: Pergamon Press; 1977.

[2] Dowson D, Toyoda S. A Central Film Thickness Formula for Elastohydrodynamic Line Contacts. Proceedings of the 5th Leeds-Lyon Symposium on Tribology, London. 1978:60-5.

[3] Pan P, Hamrock BJ. Simple Formulas for Performance Parameters Used in Elastohydrodynamically Lubricated Line Contacts. J Tribol-T Asme. 1989;111:246-51.

[4] Moes H. Optimum Similarity Analysis with Applications to Elastohydrodynamic Lubrication. Wear. 1992;159:57-66.

[5] Sadeghi F, Dow TA, Johnson RR. Thermal Effects in Rolling Sliding Contacts .3. Approximate Method for Prediction of Mid-Film Temperature and Sliding Traction. J Tribol-T Asme. 1987;109:519-24.

[6] Sadeghi F, Dow TA. Thermal Effects in Rolling Sliding Contacts .2. Analysis of Thermal Effects in Fluid Film. J Tribol-T Asme. 1987;109:512-8.

[7] Sadeghi F, Sui PC. Thermal Elastohydrodynamic Lubrication of Rolling Sliding Contacts. J Tribol-T Asme. 1990;112:189-95.

[8] Lee RT, Hsu CH. A Fast Method for the Analysis of Thermal Elastohydrodynamic Lubrication of Rolling Sliding Line Contacts. Wear. 1993;166:107-17.

[9] Hsu CH, Lee RT. An Efficient Algorithm for Thermal Elastohydrodynamic Lubrication under Rolling/Sliding Line Contacts. J Tribol-T Asme. 1994;116:762-9.

[10] Wolff R, Kubo A. The Application of Newton-Raphson Method to Thermal Elastohydrodynamic Lubrication of Line Contacts. J Tribol-T Asme. 1994;116:733-40.

[11] Pandey RK, Ghosh MK. Temperature rise due to sliding in rolling/sliding elastohydrodynamic lubrication line contacts: an efficient numerical analysis for contact zone temperatures. Tribol Int. 1998;31:745-52.

[12] Pandey RK, Ghosh MK. A thermal analysis of traction in elastohydrodynamic rolling/sliding line contacts. Wear. 1998;216:106-14.

[13] Chu LM, Hsu HC, Lin JR, Chang YP. Inverse approach for calculating temperature in EHL of line contacts. Tribol Int. 2009;42:1154-62.

[14] Kumar P, Khonsari MM. Combined effects of shear thinning and viscous heating on EHL characteristics of rolling/sliding line contacts. J Tribol-T Asme. 2008;130.

[15] Doolittle AK. Studies in Newtonian Flow .2. The Dependence of the Viscosity of Liquids on Free-Space. J Appl Phys. 1951;22:1471-5.

[16] Bair SS, McCabe C. High-pressure rheology for quantitative elastohydrodynamics. 1st ed. Amsterdam ; Boston: Elsevier; 2007.

[17] Bair S, Jarzynski J, Winer WO. The temperature, pressure and time dependence of lubricant viscosity. Tribol Int. 2001;34:461-8.

[18] Habchi W, Vergne P, Bair S, Andersson O, Eyheramendy D, Morales-Espejel GE. Influence of pressure and temperature dependence of thermal properties of a lubricant on the behaviour of circular TEHD contacts. Tribol Int. 2010;43:1842-50.

[19] Kumar P, Anuradha P, Khonsari MM. Some important aspects of thermal elastohydrodynamic lubrication. P I Mech Eng C-J Mec. 2010;224:2588-98.

[20] Kumar P, Khonsari MM. Traction in EHL Line Contacts Using Free-Volume Pressure-Viscosity Relationship With Thermal and Shear-Thinning Effects. J Tribol-T Asme. 2009;131.

[21] Bair S, McCabe C, Cummings PT. Calculation of viscous EHL traction for squalane using molecular simulation and rheometry. Tribol Lett. 2002;13:251-4.

[22] Jang JY, Khonsari MM. Elastohydrodynamic Line-Contact of Compressible Shear Thinning Fluids With Consideration of the Surface Roughness. J Tribol-T Asme. 2010;132.

[23] Khonsari MM, Hua DY. Thermal Elastohydrodynamic Analysis Using a Generalized Non-Newtonian Formulation with Application to Bair-Winer Constitutive Equation. J Tribol-T Asme. 1994;116:37-46.

[24] Bair S, Khonsari M, Winer WO. High-pressure rheology of lubricants and limitations of the Reynolds equation. Tribol Int. 1998;31:573-86.

[25] Bair S, McCabe C. A study of mechanical shear bands in liquids at high pressure. Tribol Int. 2004;37:783-9.

[26] Johnson KL, Greenwood JA, Poon SY. Simple Theory of Asperity Contact in Elastohydrodynamic Lubrication. Wear. 1972;19:91-108.

[27] Gelinck ERM, Schipper DJ. Deformation of rough line contacts. J Tribol-T Asme. 1999;121:449-54.

[28] Gelinck ERM, Schipper DJ. Calculation of Stribeck curves for line contacts. Tribol Int. 2000;33:175-81.

[29] Lu XB, Khonsari MM, Gelinck ERM. The Stribeck curve: Experimental results and theoretical prediction. J Tribol-T Asme. 2006;128:789-94.

[30] Akbarzadeh S, Khonsari MM. Performance of spur gears considering surface roughness and shear thinning lubricant. J Tribol-T Asme. 2008;130.

[31] Akbarzadeh S, Khonsari MM. Thermoelastohydrodynamic Analysis of Spur Gears with Consideration of Surface Roughness. Tribol Lett. 2008;32:129-41.

[32] Majumdar BC, Hamrock BJ. Effect of Surface-Roughness on Elastohydrodynamic Line Contact. J Lubric Tech-T Asme. 1982;104:401-9.

[33] Greenwood JA, Tripp, J.H. . The Contact of Two Nominally Flat Rough Surfaces. Proc Inst Mech Eng. 1971;185:625–33

[34] Sadeghi F, Sui PC. Compressible Elastohydrodynamic Lubrication of Rough Surfaces. J Tribol-T Asme. 1989;111:56-62.

[35] Moraru L, Keith TG, Kahraman A. Aspects Regarding the Use of Probabilistic Models for Isothermal Full Film Rough Line Contacts. Tribol T. 2004;47:386-95.

[36] Masjedi M, Khonsari MM. Film Thickness and Asperity Load Formulas for Line-Contact Elastohydrodynamic Lubrication With Provision for Surface Roughness. J Tribol-T Asme. 2012;134:011503.

[37] Zhao YW, Maietta DM, Chang L. An asperity microcontact model incorporating the transition from elastic deformation to fully plastic flow. J Tribol-T Asme. 2000;122:86-93.

[38] Roelands CJA. *Correctional Aspects of the Viscosity-Temperature- Pressure Relationship of Lubricating Oils*. Druk, V.R.B., Groningen, Netherlands1966.

[39] Greenwood JA, Williamson JB. Contact of Nominally Flat Surfaces. Proc R Soc Lon Ser-A. 1966;295:300-19.

[40] Chang WR, Etsion I, Bogy DB. An Elastic-Plastic Model for the Contact of Rough Surfaces. J Tribol-T Asme. 1987;109:257-63.

[41] Beheshti A, Khonsari MM. Asperity micro-contact models as applied to the deformation of rough line contact. Tribol Int. 2012;52:61-74.

[42] Patir N, Cheng HS. Average Flow Model for Determining Effects of 3-Dimensional Roughness on Partial Hydrodynamic Lubrication. J Lubric Tech-T Asme. 1978;100:12-7.

[43] Smith FW. Lubricant Behavior in Concentrated Contact - Some Rheological Problems. Asle Trans. 1960;3, No. 1:18-25.

[44] Bair S, Winer WO. Rheological Model for Elastohydrodynamic Contacts Based on Primary Laboratory Data. J Lubric Tech-T Asme. 1979;101:258-65.

[45] Hamrock BJ. Fundamentals of fluid film lubrication. New York: McGraw-Hill; 1994.

[46] Cheng HS. A Refined Solution to Thermal-Elastohydrodynamic Lubrication of Rolling and Sliding Cylinders. Asle Trans. 1965;8:397-&.

[47] Dowson D. Elastohydrodynamic and micro-elastohydrodynamic lubrication. Wear. 1995;190:125-38.

[48] Greenwood JA, Kauzlari JJ. Inlet Shear Heating in Elastohydrodynamic Lubrication. J Lubric Tech-T Asme. 1973;95:417-26.

Chapter 4: Mixed Elastohydrodynamic Lubrication Line-Contact Formulas with Different Surface Patterns*

4.1. Introduction

Prediction of film thickness in tribological components has long been of interest in the tribology research community. In mixed elastohydrodynamic lubrication (EHL) regimes, surface properties play a significant role as the surface asperities come into contact. In statistical description of rough surfaces, generally three parameters are used: surface roughness (σ), which is the standard deviation of the surface heights, asperity radius (β), and asperity density (n). In addition, a so-called surface pattern parameter, γ, is introduced to characterize the orientation of the surface asperities. When γ=1, the surface is said to be isotropic, which implies that the surface properties have no particular directional preference. While most surfaces are classified as isotropic, depending on the machining procedure and the tooling used, specific directionality in the form of either transverse or longitudinal pattern may be created as shown in Figure 4.1. The corresponding parameter for the transverse and longitudinal pattern is γ<1 and γ>1, respectively.

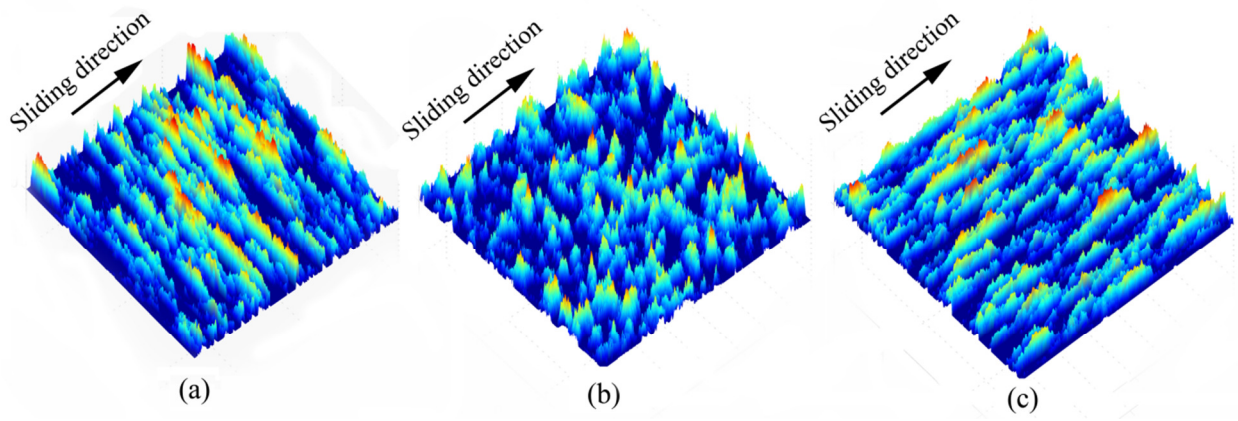

Fig. 4.1. Typical surface patterns: (a) transverse (γ<1), (b) isotropic (γ=1), and (c) longitudinal (γ>1)

Within the context of mixed EHL, Johnson et al. [1] proposed one of the earliest models by introducing the concept of load-sharing in which the bearing load is shared between the fluid and the surface asperities. For this purpose, they used the asperity contact model by Greenwood & Williamson [2] known as GW. Gelinck & Schipper [3, 4] took advantage of Johnson's concept to present a method for the calculation of film thickness without the need to solve the Reynolds

* Reprinted by permission of *Sage* (See Appendix I)

equation. This method was later utilized by Lu et al. [5] in journal bearings and by Akbarzadeh & Khonsari [6, 7] in spur gears. Full solution of the mixed EHL in statistical approach often include solving the modified Reynolds equation by Patir & Cheng [8] and an asperity deformation equation. Majumdar & Hamrock [9], Sadeghi & Sui [10], and Jang & Khonsari [11] are among the researchers who utilized this method where they considered the elastic deformation of the asperities using GW-based models. Moraru et al. [12] used Chang et al. asperity model [13] (known as CEB) which also considers the plastic deformation of the asperities. Recently, Masjedi & Khonsari [14, 15] conducted a study on line-contact EHL of rough surfaces where they derived curve-fit expressions for the film thickness, asperity load and traction coefficient. For this purpose, they utilized the elasto-plastic asperity contact model by Zhao et al. [16] known as ZMC. Within the context of deterministic treatment of the asperities, Chang [17] proposed one of the earliest approaches to solve EHL equations using the actual surface profile. Other researchers conducted different studies to evaluate the effect of surface roughness in deterministic setup [18-23]. The applications of deterministic model in contact of gears were also explored in a number of studies [24, 25].

Since surface pattern can influence the lubricant flow, numerous studies have been reported that attempt to characterize and quantify its effect on the lubrication effectiveness of bearings. In the study by Johnson et al. [1] where the concept of load-sharing was introduced, they also suggested how one can modify the film thickness to take into account the longitudinal and transverse surface patterns. Clearly, the longitudinal asperities facilitate the lubricant flow in the sliding direction, resulting in a thinner film. The transverse asperities, on the other hand, tend to obstruct the flow, and thus create a thicker film.

A widely used analytical treatment of the surface pattern is due to work of Patir & Cheng [8] who introduced the concept of flow factors as functions of the film parameter (h/σ) and the surface pattern parameter (γ), and derived a modified Reynolds equation for treatment of such lubrication problems. Regardless of the type of the surface pattern, for large film parameter values, all flow factors approach unity and the modified Reynolds equation turns into the conventional Reynolds equation. Prakash & Czichos [26] utilized these flow factors to investigate the effect of surface roughness and its orientation on Line-contact EHL. For this purpose, they used a simplified form of Greenwood-Tripp asperity contact model [27]. They showed that for isotropic and transverse orientations, the film thickness increases as the roughness increases, but for longitudinal orientation, the film thickness decreases by increasing the surface roughness. It was also shown that the film thickness in a surface with isotropic roughness pattern is smaller than that of a transversely oriented surface, but larger than that of a longitudinally oriented surface. Later, through similar approaches, the effect of surface pattern on line-contact EHL was studied by Sadeghi & Sui [10] with consideration of lubricant compressibility, and by Jang & Khonsari [11] with consideration of shear thinning effect. Akbarzadeh & Khonsari [28] used a different approach to investigate the surface pattern effects.

By using a model proposed by Patir [29], they generated random surfaces with different orientations and investigated the behavior of Stribeck curve. Most recently, Zhu and Wang [30] performed a deterministic study on the effect of surface pattern in Elastohydrodynamic lubrication. They showed that although the effect of surface pattern in their model is less significant compared to the Patir & Cheng stochastic results [8], both models show similar trends.

In the present study, the numerical procedure employed in [14] is followed to calculate the film thickness and asperity load ratio in line-contact EHL. This method is based on solving the modified Reynolds equation by Patir & Cheng [8] and the statistical elasto-plastic asperity contact model by Zhao et al. [16]. The effect of surface pattern is considered by applying the flow factors for different anisotropic surfaces with longitudinal and transverse orientations. The film thickness and the asperity load ratio are then obtained as functions of dimensionless input parameters and expressions are developed with provision for surface roughness and surface pattern parameter with specified values. These expressions can be used in the form of modification factors that adjust the isotropic surface results. These factors can be readily applied to the film thickness and asperity load ratio formulas [14] to quantify the effect of surface pattern and improve the performance of machine elements. To illustrate the utility of the approach, we present an analysis of gear teeth contact to show how easily one can calculate the film thickness and the asperity load along the gear's line of action to predict the possible failure. The present expressions can be directly applied to such EHL problems dealing with rough surfaces, and this method obviates the need to iteratively calculate the load-sharing parameters for each point. Finally, since the traction coefficient of a rough surface comprises of the hydrodynamic and asperity portions, it is investigated how a change in surface pattern influences each part. For this purpose, using a thermo-elastohydrodynamic model developed in [15], traction curves are generated and compared for different surface pattern types.

4.2. Model

The modified Reynolds equation by Patir and Cheng [8] is written in dimensionless form as [14]:

$$\frac{dP_h}{dX} = 48\bar{\mu}U\left(H_T - \bar{\rho}^{-1}K_r\right)\left(\Phi_x\right)^{-1}H^{-3} \tag{1}$$

where P_h is the hydrodynamic pressure, X is the coordinate in the moving direction, H is the film thickness, U is the speed, $\bar{\mu}$ is the viscosity and $\bar{\rho}$ is the density, all in dimensionless form. Parameter H_T is the dimensionless average gap and K_r is a constant to be determined. The pressure flow factor in moving direction, Φ_x [8] is written in dimensionless form as:

$$\Phi_x = \begin{cases} 1 - ce^{-r\frac{H}{\bar{\sigma}}} & \gamma \le 1 \\ 1 + c\left(\frac{H}{\bar{\sigma}}\right)^{-r} & \gamma > 1 \end{cases} \tag{2}$$

where $\bar{\sigma}$ is the dimensionless surface roughness. The coefficients c and r are shown in Table 4.1 [8].

Table 4.1. Pressure flow factor coefficients [8]

γ	c	r	Valid Range
1/9	1.48	0.42	$H/\bar{\sigma}>1$
1/6	1.38	0.42	$H/\bar{\sigma}>1$
1/3	1.18	0.42	$H/\bar{\sigma}>0.75$
1	0.9	0.56	$H/\bar{\sigma}>0.5$
3	0.225	1.5	$H/\bar{\sigma}>0.5$
6	0.520	1.5	$H/\bar{\sigma}>0.5$
9	0.870	1.5	$H/\bar{\sigma}>0.5$

The load balance in dimensionless form is [14]:

$$\int P_h(X)dX + \int P_a(X)dX = \frac{\pi}{2} \tag{3}$$

where P_h and P_a are the dimensionless hydrodynamic and asperity pressures, respectively. The dimensionless film profile is written as [14]:

$$H(X) = H_{00} + \frac{4W}{\pi}\left[X^2 - \frac{1}{\pi}\int P \ln(X\text{-}S)^2 dS \right] \tag{4}$$

where W denotes the dimensionless load and P is the dimensionless total pressure. H_{00} is a constant to be determined.

To treat an EHL problem with rough surfaces, the Reynolds equation should be solved together with the bulk deformation of the surfaces, load balance and asperity deformation equations. The elasto-plastic asperity micro-contact model developed by Zhao et al. [16] is used in this study, which is found to be an accurate model [31]. In this model, the asperity pressure P_a is defined as the sum of elastic, elasto-plastic and plastic pressures:

$$P_a = P_{elastic} + P_{elasto-plastic} + P_{plastic} \tag{5}$$

The details of Eq. (5) are given in Chapter 2 (Eqs. (14) and (17)). The reader is referred to [14, 16] for additional details.

The dimensionless input parameters are the load W, speed U, material G, surface roughness $\bar{\sigma}$ (surface rms divided by the equivalent contact radius), surface hardness V (Vickers hardness divided by the effective Young's modulus), and the surface pattern parameter γ. The surface pattern parameter value is chosen are: 1 (isotropic), 1/3, 1/6 and 1/9 (transverse), and 3, 6 and 9 (longitudinal). For each γ value, the appropriate flow factor chosen from Eq. (2) is used in the Reynolds Equation. The governing equations are discretized using the finite difference method

and solved simultaneously to obtain the pressure and the film profiles. Since the equations are non-linear, the Newton-Raphson algorithm is applied. More details can be found in [14].

4.3. Results and discussion

Figure 4.2 shows the effect of surface pattern on the film thickness. The value of surface pattern parameter γ is varied between 1/9 and 9, while other parameters ($W = 1\times10^{-4}$, $U = 1\times10^{-11}$, $G = 4500$, $\bar{\sigma} = 2\times10^{-5}$ and $V = 0.01$) are kept constant. As shown, the film thickness of a transverse surface ($\gamma<1$) is larger than that of an isotropic surface ($\gamma=1$), while the longitudinal surface ($\gamma>1$) has the smallest value. Physically, in the case of the longitudinal surface, a larger surface pattern parameter γ offers less resistance against the flow, so the film thickness becomes smaller. On the other hand, a smaller surface pattern parameter of a transverse surface provides more resistance against the flow, and as a result the lubricant tends to remain in the contact area and the film thickness increases. Theoretically, a larger surface pattern parameter γ yields a larger flow factor Φ_x, see Eq. (2), which decreases the film thickness. It is also observed that the location of the minimum film thickness approaches the contact center ($X=0$) as γ increases.

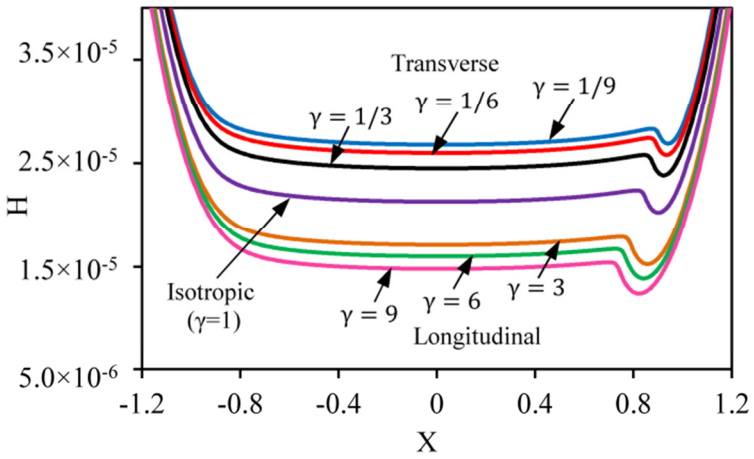

Fig. 4.2. Effect of surface pattern on film profile
($W=1\times10^{-4}$, $U=1\times10^{-11}$, $G=4500$, $\bar{\sigma}=2\times10^{-5}$, $V=0.01$)

Figure 4.3 shows how the surface pattern parameter affects the film thickness. For better visibility, the abscissa is shown in the logarithmic scale. As shown, the film thickness decreases as γ increases. Also, the difference between the central and the minimum film thickness becomes more noticeable at larger γ values.

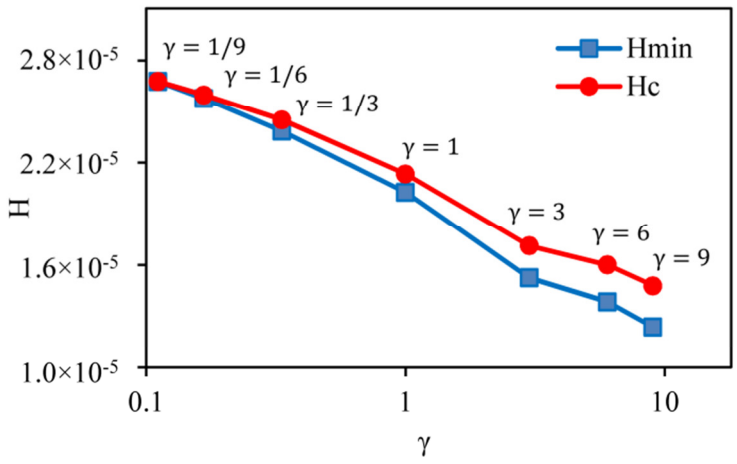

Fig. 4.3. Effect of surface pattern on central and minimum film thickness
(W=1×10^{-4}, U=1×10^{-11}, G=4500, $\bar{\sigma}$=2×10^{-5}, V=0.01)

Figure 4.4 shows the effect of surface pattern on the asperity pressure P_a and the total pressure P distributions. As shown, the asperity pressure and therefore the asperity load ratio L_a —which is the portion of the load carried by the surface asperities—increases by increasing the surface pattern parameter. Therefore, the asperity load ratio of an isotropic surface is larger than that of a transverse surface, but smaller than that of a longitudinal one. This is simply because a larger film thickness results in less asperity contact. It is also observed that the location of the pressure spike approaches the contact center as γ increases.

The change in the asperity load ratio L_a by the surface pattern parameter is shown in Fig. 4.5. The horizontal axis is shown in logarithmic scale. Again, it shows that larger surface pattern parameter corresponds to larger asperity load ratio.

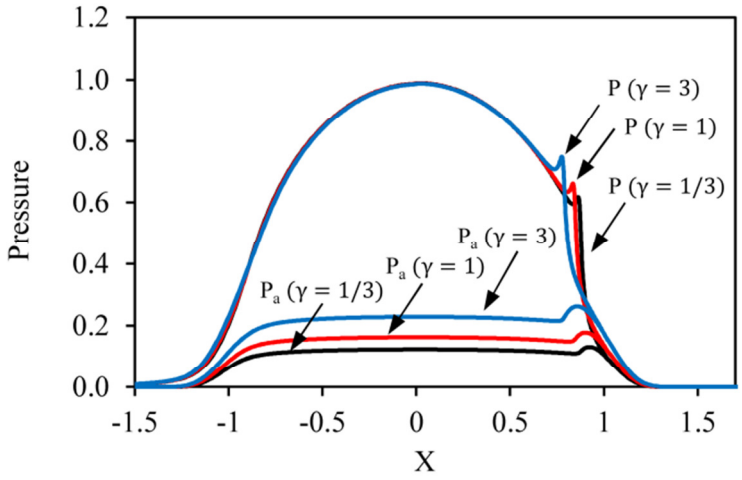

Fig. 4.4. Effect of surface pattern on asperity and total pressure distribution
(W=1×10^{-4}, U=1×10^{-11}, G=4500, $\bar{\sigma}$=2×10^{-5}, V=0.01)

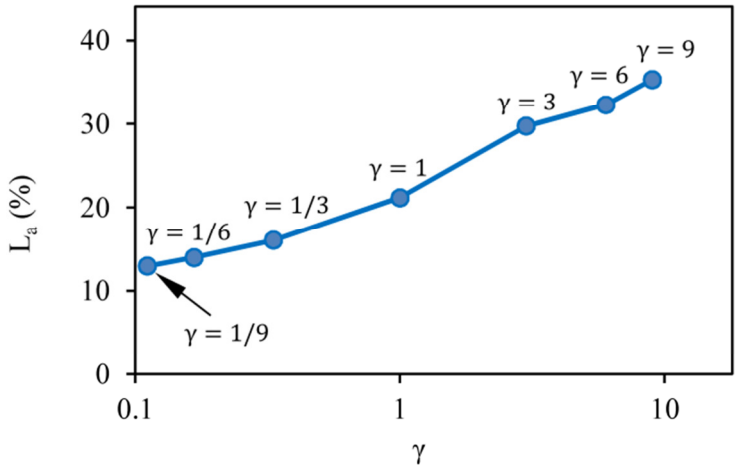

Fig. 4.5. Effect of surface pattern on asperity load ratio
(W=1×10^{-4}, U=1×10^{-11}, G=4500, $\bar{\sigma}$=2×10^{-5}, V=0.01)

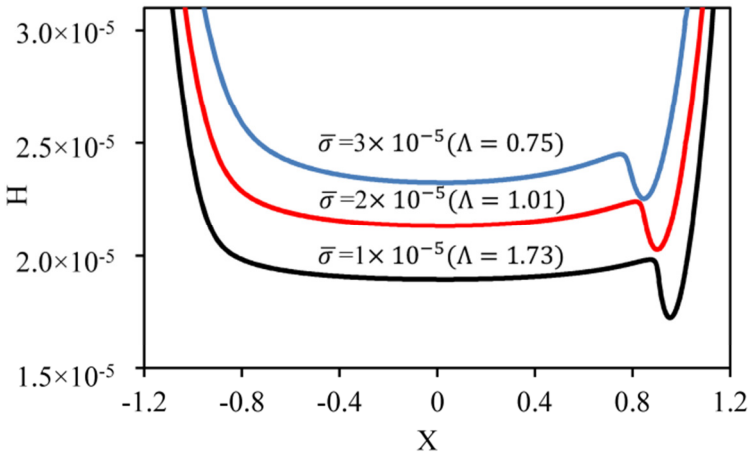

Fig. 4.6. Effect of surface roughness on film thickness: isotropic surface
(W=1×10^{-4}, U=1×10^{-11}, G=4500, V=0.01)

The effect of surface roughness on the film thickness for different surface pattern types is shown in Figs. 4.6-4.8. As shown, in isotropic and transverse surfaces ($\gamma \leq 1$), increasing the surface roughness increases the film thickness (Figs. 4.6 and 4.7), while for a longitudinal surface ($\gamma > 1$), the roughness decreases the film thickness (Fig. 4.8). It should be noted that even though increasing the surface roughness increases the film thickness in isotropic and transverse surfaces, the film parameter still decreases (see Figs. 4.6 and 4.7). This is because the increase in the film thickness is less than the corresponding increase in the surface roughness. On the other hand, for longitudinal surface (Fig. 4.8), the decrease in the film parameter is more significant, because the film thickness decreases by increasing the surface roughness. It is also observed that for all

pattern types, the central film thickness for smooth surfaces (large Λ values) does not remain constant in the case of mixed lubrication (small Λ values). This trend is more pronounced in longitudinal pattern because the roughness tends to reduce the film parameter more significantly.

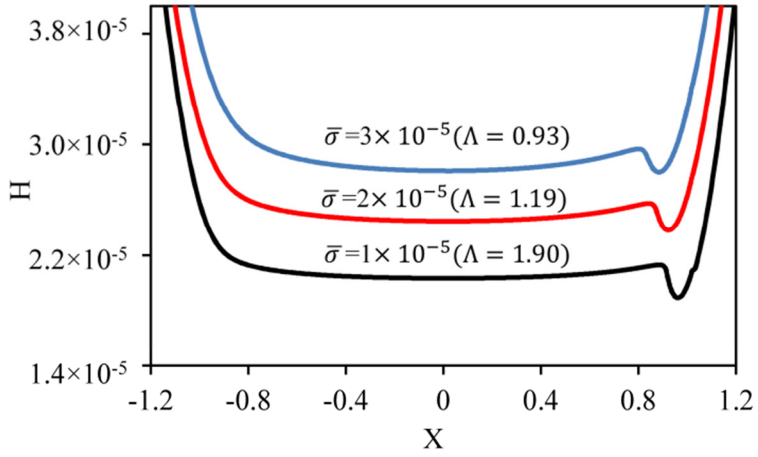

Fig. 4.7. Effect of surface roughness on film thickness: transverse surface with γ=1/3 (W=1×10^{-4}, U=1×10^{-11}, G=4500, V=0.01)

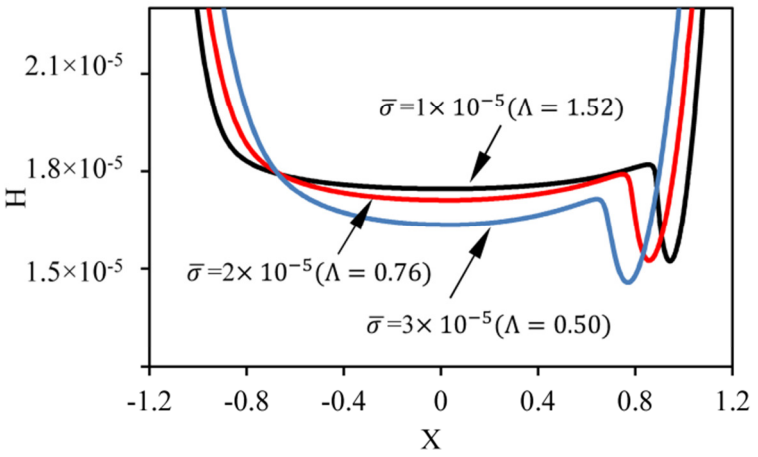

Fig. 4.8. Effect of surface roughness on film thickness: longitudinal surface with γ=3 (W=1×10^{-4}, U=1×10^{-11}, G=4500, V=0.01)

4.4. Film Thickness and Asperity Load Ratio Formulas considering Surface Pattern

Predictive formulas for the central and the minimum film thickness and the asperity load ratio in rough line-contact EHL were developed for an isotropic surface as functions of five dimensionless input parameters W, U, G, $\bar{\sigma}$, and V as [14]:

$$H_c = \frac{h_c}{R} = 2.691 W^{-0.135} U^{0.705} G^{0.556} (1 + 0.2\ \bar{\sigma}^{1.222} V^{0.223} W^{-0.229} U^{-0.748} G^{-0.842}) \quad (6)$$

$$H_{\min} = \frac{h_{\min}}{R} = 1.652\ W^{-0.077} U^{0.716} G^{0.695} (1 + 0.026\ \bar{\sigma}^{1.120} V^{0.185} W^{-0.312} U^{-0.809} G^{-0.977}) \quad (7)$$

$$L_a = 0.005 W^{-0.408} U^{-0.088} G^{0.103} [\ln(1 + 4470\ \bar{\sigma}^{6.015} V^{1.168} W^{0.485} U^{-3.741} G^{-2.898})] \quad (8)$$

where R is the equivalent contact radius. The film parameter is:

$$\Lambda = \frac{h_{\min}}{\sigma} = \frac{H_{\min}}{\bar{\sigma}} \quad (9)$$

which needs to be greater than 0.5 (for an isotropic surface) to satisfy the modified Reynolds equation conditions [8]. When the surface pattern is taken into account, the film thickness and the asperity load ratio will change. In order to obtain formulas for anisotropic surfaces, a whole set of simulations within a range of input data (W, U, G, $\bar{\sigma}$ and V) is performed for different values of the surface pattern parameter γ. The ranges for W, U, G, $\bar{\sigma}$ and V are identical to those in [14], while γ value is chosen as 1/9, 1/6, 1/3, 1, 3, 6 and 9. Table 4.2 shows the input ranges.

Table 4.2: Range of dimensionless input parameters selected for simulation

Parameter	W	U	G	$\bar{\sigma}$	V	γ
min	2×10^{-5}	1×10^{-12}	2500	0	0.005	1/9
max	5×10^{-4}	1×10^{-10}	7500	5×10^{-5}	0.03	9

For each γ value, more than 300 different cases for each surface pattern (more than 2000 in total) are simulated within the defined range of W, U, G, $\bar{\sigma}$ and V. Since the modified Reynolds equation is only valid for film parameters larger than a specific value (see Table 4.1), the film parameter is checked after each simulation.

In what follows a series of modification factors are provided that can be used to adjust the results of the isotropic film thickness and asperity load ratio to predict the behavior of longitudinal and transverse surface patterns. The curve-fit results are presented as:

$$K_{H_C} = \begin{cases} 1 + 0.354\Lambda^{-1.351}(1-\gamma)^{2.261} & \gamma < 1 \\ 1 - 0.135\Lambda^{-1.430}(\gamma-1)^{0.329} & \gamma > 1 \end{cases} \quad (10)$$

$$K_{H_{\min}} = \begin{cases} 1 + 0.422\Lambda^{-1.146}(1-\gamma)^{2.382} & \gamma < 1 \\ 1 - 0.170\Lambda^{-1.289}(\gamma-1)^{0.333} & \gamma > 1 \end{cases} \quad (11)$$

$$K_{L_a} = \begin{cases} 1 - 0.459\Lambda^{0.196}(1-\gamma)^{3.028} & \gamma < 1 \\ 1 + 0.354\Lambda^{0.026}(\gamma-1)^{0.34} & \gamma > 1 \end{cases} \quad (12)$$

where K_{Hc}, $K_{H\min}$ and K_{La} are the modification factors for the central film thickness, minimum film thickness and the asperity load ratio, respectively. Therefore, the film thicknesses and the asperity load ratio of an anisotropic surface (transverse or longitudinal) are:

$$\begin{aligned} H_c\,(anisotrpic) &= K_{H_c} \times H_c\,(isotropic) \\ H_{\min}\,(anisotrpic) &= K_{H_{\min}} \times H_{\min}\,(isotropic) \\ L_a\,(anisotrpic) &= K_{L_a} \times L_a\,(isotropic) \end{aligned} \tag{13}$$

where isotropic values are obtained from Eqs. (6-9).

The error associated with curve-fit formulas within the defined range (Table 4.2) is shown in Table 4.3. The film thickness error in defined as $100\times|H_{(\text{simulation})}-H_{(\text{curve-fit})}|/\ H_{(\text{simulation})}$ while the asperity load ratio error is defined as $|L_{a(\text{simulation})}- L_{a(\text{curve-fit})}|$.

Table 4.3: Curve fitting error of equations (10-12)

Error	$Hc\ (\gamma<1)$	$Hc\ (\gamma>1)$	H_{min} $(\gamma<1)$	H_{min} $(\gamma>1)$	$L_a\,(\gamma<1)$	$L_a\,(\gamma>1)$
Maximum	7.84	9.53	8.79	7.88	7.21	8.67
Average	1.78	1.98	2.60	2.51	0.88	1.62

The following points should be noted about Eqs. (10-13):

1- All modification factors revert back to unity for an isotropic surface (γ=1), as expected.

2- The film parameter (Λ) in Eqs. (10-12) is the isotropic film parameter obtained from Eq. (9).

3- Even though Eqs. (10-12) are the results of simulations and curve fitting based on surface pattern values 1/9, 1/6, 1/3, 1, 3, 6 and 9, they may be used for any other γ value between 1/9 and 9. However, they might not be valid for γ values out of this range.

4- After calculating the film thickness and the asperity load ratio of a longitudinal or transverse surface, the final film parameter should be checked to assure that it is within the valid range (Table 4.1). The film parameter can be obtained by dividing the minimum film thickness (Eq. (13)) by the dimensionless surface roughness $\bar{\sigma}$. Moreover, when the obtained asperity load ratio is very large (typically more than 70%), the results should be used with caution, even if the film parameter is within the valid range [14].

As an example, consider the contact of two identical steel rollers with the radius of R_1=R_2=25.4 mm and the length of 25.4 mm. The effective Young's modulus is E'=228 GPa for the steel, and the effective contact radius is R=12.7 mm. The normal load is 10 KN, so the load per contact lengths is w=3.94×10^5 N. The linear speed of rollers are 1.2 m/s, and 0.8 m/s, so the rolling speed is u=1 m/s. The lubricant used is SAE 20W (μ_0=0.048 Pa.s, α= 2.03 ×10^{-8} m^2/N). Both surfaces are ground with σ=0.25 μm, so the combined roughness is 0.35 μm. The Vickers hardness of the surfaces is 300 Kg/mm^2 (2.94 GPa). Therefore, the dimensionless parameters are W=1.36×10^{-4}, U=1.66×10^{-11}, G=4628, $\bar{\sigma}$=2.76×10^{-5} and V= 0.0129. For an isotropic surface,

substituting the above values into Eqs. (6) and (7) yields H_c=2.82×10^{-5} and H_{min}=2.66×10^{-5}, so h_c =0.358 μm and h_{min}=0.338 μm. Also, the asperity load ratio from Eq. (8) is obtained as L_a=17.12%. Equation (9) gives the isotropic film parameter as 0.96 which is within the valid range (see Table 4.1).

Now consider a surface with transverse orientation of γ=1/3. From Eqs. (10-12), K_{H_c}= 1.15, $K_{H_{min}}$=1.17, and K_{L_a}=0.87, so Eq. (13) gives H_c=3.24×10^{-5} (h_c=0.411 μm), H_{min}=3.11×10^{-5} (h_{min}=0.395 μm) and L_a=14.89%. The film parameter for this surface is 1.13, which is larger than 0.75 (see Table 4.1). Considering a longitudinal surface with γ=6, K_{H_c}= 0.76, $K_{H_{min}}$=0.69, and K_{L_a}=1.61 are calculated. Therefore, Eq. (13) gives H_c=2.14×10^{-5} (h_c=0.272 μm), H_{min}=1.84×10^{-5} (h_{min}=0.234 μm) and L_a= 27.56%. The predicted film parameter is 0.67 which is larger than 0.5 (Table 4.1).

4.5. Application of Film Thickness and Asperity Load Ratio Formulas in Gear Contact

The film thickness and asperity load ratio formulas developed in this study offer an efficient and straightforward means for the prediction of the film thickness and the asperity load in many industrial applications. To illustrate this, let us consider the mixed EHL contact in a spur gear.

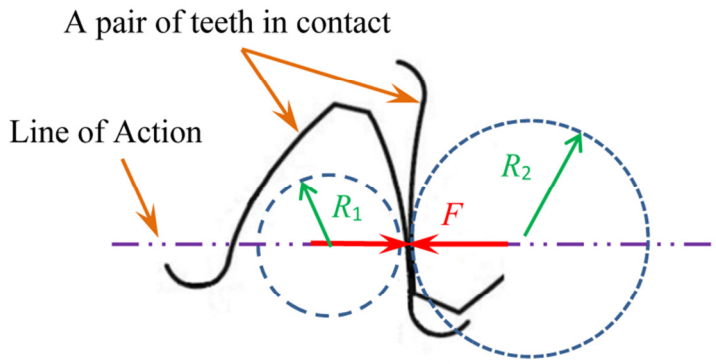

Fig. 4.9. Contact between a pair of gear teeth

As shown in Fig. 4.9, the contact between a pair of gear teeth occurs along the line of action (LoA). The film thickness is not uniform along LoA because the contact radius, the speed, and the transmitted load vary along this line. For a set of input data shown in Table 4.4, these variations are plotted in Fig. 4.10. For detailed information about the gear loading and geometry, the reader is referred to references [6, 32]. In Ref. [32], EHL problem is solved at each point along the LoA assuming smooth surfaces. Reference [6] treats the rough gear problem using the load-sharing method where each point along the LoA requires an iterative solution to determine the contribution of the load carried by the fluid and the surface asperities. Here, one can simply

apply the presented formulas to predict the film thickness and the asperity load ratio along the LoA for different surface roughness values and investigate the influence of different roughness patterns.

To show the variations of the film thickness and the asperity load ratio along the line of action, a case of gear contact with the data and loading conditions used by Akbarzadeh & Khonsari [6] is investigated. Table 4.4 shows the input data.

Table 4.4: input data for gear contact [6]

Geometric and operating parameters	Input Values
Number of pinion teeth	N_p=28
Number of gear teeth	N_g=84
Module	m=0.003175 m
Pinion rotational speed	ω=1637 rpm
Load per unit width	w=0.3765×10^6 N/m
Pressure angle	Ψ=20˚
Lubricant inlet viscosity	μ_0=0.065 Pa.s
Lubricant viscosity-pressure index	Z=0.6
surface roughness	σ=0.7×10^{-6} m

Figures 4.11 and 4.12 depict the results from the present formulas with the input shown in Table 4 for three different surface patterns (isotropic, transverse with γ=1/3, and longitudinal with γ=3). The load-sharing results pertain to Ref. [6] for isotropic surface are shown as well.

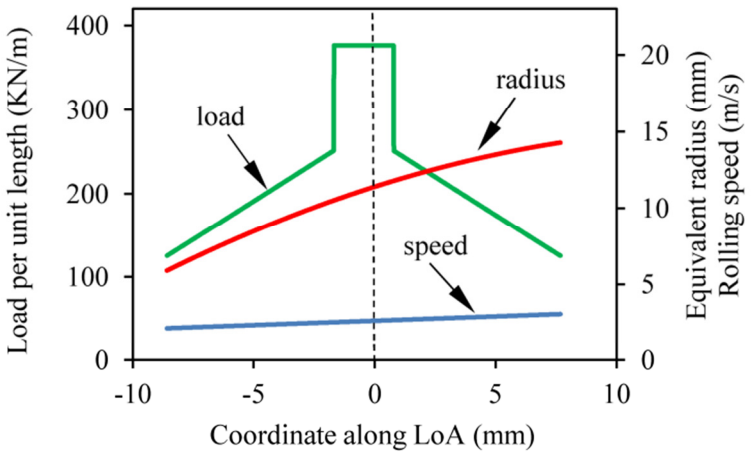

Fig. 4.10. Variations of load, speed, and radius along LoA

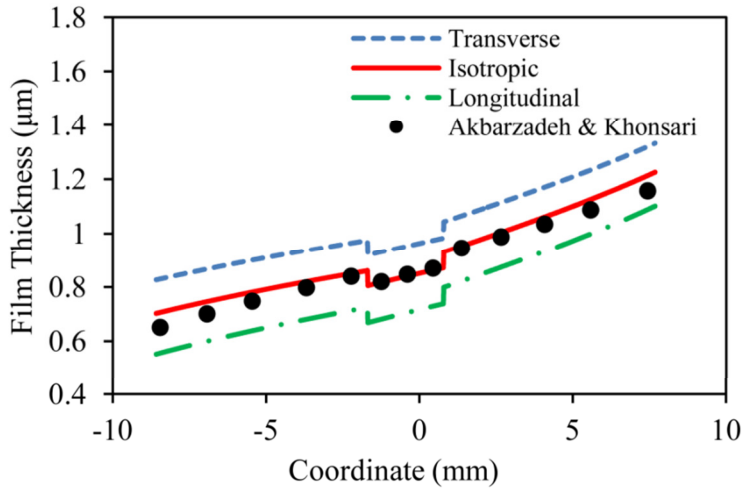

Fig. 4.11. Variations of film thickness along LoA for isotropic, transverse, and longitudinal patterns and isotropic results of Akbarzadeh & Khonsari [6]

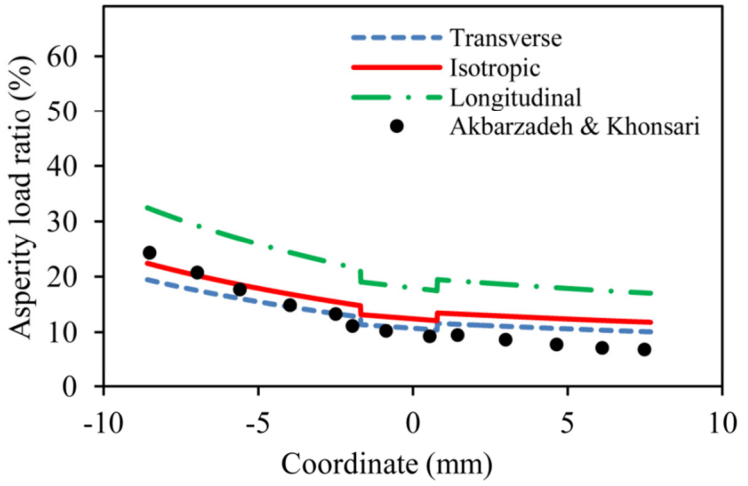

Fig. 4.12. Variations of asperity load ratio along LoA for isotropic, transverse, and longitudinal patterns and isotropic results of Akbarzadeh & Khonsari [6]

As shown, the film thickness and the asperity load ratio of an isotropic surface lie between the longitudinal and transverse surfaces as expected. Also, the results for the isotropic surface are in agreement with those by Akbarzadeh and Khonsari [6], both in trend and magnitude. The slight difference between the results (mostly visible in asperity load ratio) is because of the different methods used in these two studies. The current results are obtained from curve-fit formulas which are based on full solution of Reynolds and elasto-plastic asperity deformation equations, while results from [6] are based on the load-sharing method with the assumption of purely elastic deformation of the surface asperities.

It is worthwhile to mention that in Fig. 4.11, the film parameter of the isotropic surface varies between 0.9 to 1.53 along the line of action. This variation is between 1.07 to 1.69 for the transverse, and 0.68 to 1.35 for the longitudinal surface. The low film parameter of the longitudinal surface at the beginning of the line of action (Λ=0.68) reveals the fact that the gear teeth with this type of surface orientation is more prone to reach the boundary lubrication regime and ultimately fail. In contrast, with isotropic and transverse orientations, the gear would be expected to operate satisfactorily.

It should be mentioned that since the elasto-plastic ZMC model is used in the current study, the surface hardness should also be entered as an input. Therefore, the Vickers hardness of 2.35 GPa (equal to 20 Rockwell C, which is a reasonable value for regular steel) was assumed to generate the above results.

4.6. Traction Coefficient

In addition to affecting the film thickness and the asperity load ratio, the surface pattern can also influence the traction coefficient and the power loss. For predicting the traction coefficient, a model proposed by the authors [15] is utilized here. This model considers the heat generation and its effect on the lubricant viscosity (and density) which is necessary for modeling the traction. Also, the rheological properties of the lubricant based on the free-volume theory [33] and the effect of limiting shear stress are considered as well. The traction coefficient f can be written as the sum of asperity and hydrodynamic traction coefficients as:

$$f = \left(\frac{L_a}{100}\right) f_c + \frac{2\Lambda_{\lim}}{\pi} \int P_h \left(1 - \exp\left(\frac{-\bar{\mu} S U}{\Lambda_{\lim} P_h H \sqrt{W/2\pi}}\right)\right) dX \qquad (14)$$

where the first and the second parts represent the asperity and hydrodynamic parts of the traction coefficient. In Eq. (14) $\Lambda_{\lim}$ is the limiting shear stress coefficient and f_c is the asperity friction coefficient both of which can be found experimentally [15]. Parameter S represents the slide-to-roll ratio.

Figure 4.13 shows the traction coefficient versus the slide-to-roll ratio for the isotropic, longitudinal (γ=3) and transverse (γ=1/3) surface patterns. The lubricant is SAE 30 with reference viscosity of μ_R = 0.35 Pa.s at T_R =20˚C and limiting shear stress coefficient of $\Lambda_{\lim}$ =0.091. The free-volume and thermal properties of the lubricant are taken from Ref. [15]. The surfaces are steel with dimensionless roughness of $\bar{\sigma} = 2 \times 10^{-5}$ and dimensionless hardness of V=0.01. The input load and speed are W=5×10^{-5} and U=1×10^{-11}, respectively. The asperity friction coefficient is assumed as f_c=0.135 [15].

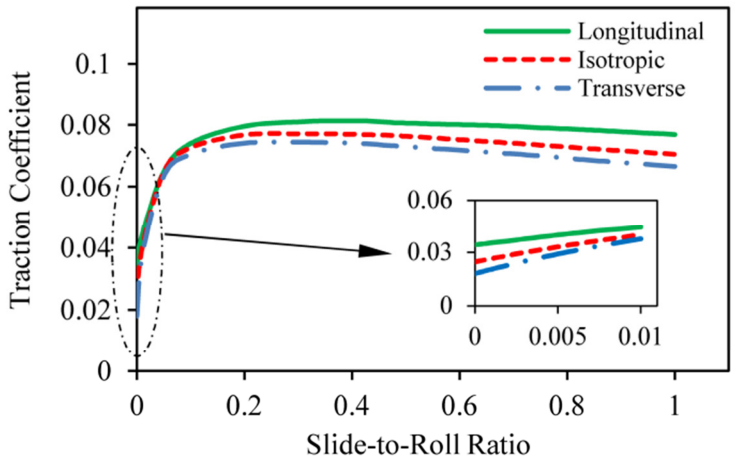

Fig. 4.13. Effect of surface roughness on traction coefficient
(W=5×10^{-5}, U=1×10^{-11}, $\bar{\sigma} = 2 \times 10^{-5}$, V=0.01)

As shown in Fig. 4.13, the traction coefficient is dependent on the type of the surface pattern. Under the same operating conditions, the traction coefficient is generally greater for longitudinal surfaces compared to the transverse surfaces. This can be explained by the fact that the smaller film thickness results in a larger asperity contact and vice versa.

Note that while a larger asperity load ratio increases the asperity part of the traction coefficient, it decreases the hydrodynamic part at the same time. This is because, in this case, a smaller portion of the load is carried by the lubricant which translates to decreasing the viscosity and the associated hydrodynamic traction coefficient (Eq. (14)). The contribution of these two effects determines the total traction coefficient.

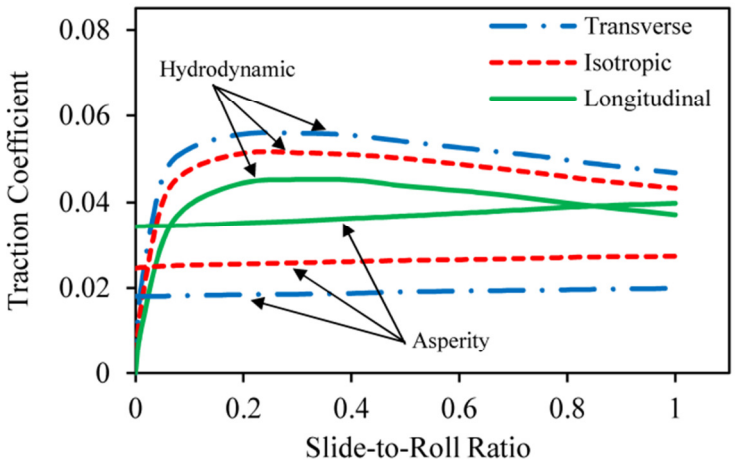

Fig. 4.14. Hydrodynamic and asperity parts of traction coefficient for different surface patterns

Figure 4.14 shows the contribution of the hydrodynamic and the asperity parts to the traction coefficient results of Fig. 4.13. The total traction coefficient is the sum of these two parts. As shown, the asperity part of the traction coefficient is larger for the longitudinal and smaller for the transverse surface. This is because the asperity part of the traction coefficient is a direct function of the asperity load ratio (Eq. (14)). The small slope of the asperity traction curves is because of the small increase in the asperity load ratio due to the temperature rise [15]. Simulation shows that for the isotropic surface, the asperity load changes from 18.1% at S=0 (zero sliding) to 20.2% at S=1. It changes from 25.4% to 29.4% for the longitudinal surface, and 13.4% to 14.7% for the transverse surface. On the other hand, the hydrodynamic part of the traction coefficient is larger for the transvers and smaller for the longitudinal surface as shown. The hydrodynamic traction coefficient is nil at zero sliding, as expected. Also, at high slide-to-roll ratios, the hydrodynamic traction curves experience a drop which is due to temperature rise and its effect on the lubricant viscosity [15].

4.7. Conclusions

In this paper, a set of simulations are conducted to study the effects of surface pattern in line-contact EHL. The modified Reynolds equation which contains the effects of surface roughness and its orientation is solved together with the bulk deformation of the surface as well as the elasto-plastic deformation of the surface asperities. The results from more than 2000 numerical solutions for a wide range of dimensionless input (load, speed, material, surface roughness, surface hardness, and surface pattern parameter) are used to develop expressions for prediction of the film thickness and the asperity load ratio. These expressions are presented in the form of modification factors that can be applied to the film thickness and the asperity load formulas developed in a previous study [14] to include the effect of surface pattern. An illustrative example pertaining to the contact of spur gear teeth is presented where the obtained expressions are utilized to predict the film thickness and the asperity load along the line of action. Also, a thermo-elastohydrodynamic approach developed in [15] is utilized to investigate the effect of the surface pattern on the traction coefficient. It is shown that changing the roughness pattern from transverse to longitudinal increases the asperity part of the traction coefficient while decreases the hydrodynamic part.

Nomenclature

b	half Hertzian width, m
B	line-contact length, m
E'	effective modulus of elasticity, $1/E'=0.5[(1-\nu_1^2)/E_1+(1-\nu_2^2)/E_2]$, Pa
f	traction coefficient
f_c	asperity friction coefficient
F	contact normal load
G	dimensionless material number, $E'\alpha$

h	film thickness, m
h^*	h/σ
h_c	central film thickness, m
h_{min}	minimum film thickness, m
H	dimensionless film thickness, h/R
H_c	dimensionless central film thickness, h_c/R
H_{min}	dimensionless minimum film thickness, h_{min}/R
H_T	dimensionless average gap between two surfaces
hd	Vickers hardness, Pa
K_{HC}	modification factor for central film thickness
K_{Hmin}	modification factor for minimum film thickness
K_{La}	modification factor for asperity load ratio
L_a	asperity load ratio (as percentage)
n	asperity density, m^{-2}
N_g	number of gear teeth
N_p	number of pinion teeth
m	gear module, m
p	total pressure, Pa
p_a	asperity pressure, Pa
p_h	hydrodynamic pressure, Pa
P	dimensionless total pressure, $4Rp/E'b$
P_a	dimensionless asperity pressure, $4Rp_a/E'b$
P_h	dimensionless hydrodynamic pressure, $4Rp_h/E'b$
R	equivalent contact radius, $[1/R_1 \pm 1/R_2]^{-1}$, m
S	slide-to-roll ratio
T_R	reference temperature
u	rolling speed, $(u_1+u_2)/2$, m/s
U	dimensionless speed number, $\mu_0 u/E'R$
V	dimensionless hardness number, hd/E'
Z	viscosity-pressure index
w	load per contact length, F/B, N/m
w_1	critical interference at the point of initial yield, $(0.6\pi.hd/E)^2\beta$, m
$\bar{w}_1$	w_1/R
w_1^*	w_1/σ
w_2	critical interference at the point of fully plastic flow, $54w_1$, m
$\bar{w}_2$	w_2/R
W	dimensionless load number, $w/E'R$
X	dimensionless coordinate in the moving direction
y_s	distance between the mean line of the surface and the mean line of its summits, m
$\bar{y}_s$	y_s/R
y_s^*	y_s/σ
z	height of asperities measured from the mean line of the summits, m
z^*	z/σ
α	pressure-viscosity coefficient, m^2/N

β	asperity radius, m
γ	surface pattern parameter
Λ	film parameter, h_{min}/σ
Λ_{lim}	limiting shear stress coefficient
μ_0	lubricant viscosity at zero pressure, Pa.s
μ_R	reference viscosity, Pa.s
$\bar{\mu}$	dimensionless viscosity, μ/μ_0
$\bar{\rho}$	dimensionless density
σ	standard deviation of the surface heights, m
$\bar{\sigma}$	dimensionless surface roughness, σ/R
σ_s	standard deviation of the surface summits, m
$\bar{\sigma}$	σ_s/R
Φ_x	pressure flow factor in the moving direction
Ψ	gear pressure angel
ω	pinion rotational speed, RPM

4.8. References

[1] Johnson KL, Greenwood JA, Poon SY. Simple Theory of Asperity Contact in Elastohydrodynamic Lubrication. Wear. 1972;19:91-108.

[2] Greenwood JA, Williamson JB. Contact of Nominally Flat Surfaces. Proc R Soc Lon Ser-A. 1966;295:300-19.

[3] Gelinck ERM, Schipper DJ. Deformation of rough line contacts. J Tribol-T Asme. 1999;121:449-54.

[4] Gelinck ERM, Schipper DJ. Calculation of Stribeck curves for line contacts. Tribol Int. 2000;33:175-81.

[5] Lu XB, Khonsari MM, Gelinck ERM. The Stribeck Curve: Experimental Results and Theoretical Prediction. J Tribol-T Asme. 2006;128:789-94.

[6] Akbarzadeh S, Khonsari MM. Performance of spur gears considering surface roughness and shear thinning lubricant. J Tribol-T Asme. 2008;130:021503.

[7] Akbarzadeh S, Khonsari MM. Thermoelastohydrodynamic Analysis of Spur Gears with Consideration of Surface Roughness. Tribol Lett. 2008;32:129-41.

[8] Patir N, Cheng HS. Average Flow Model for Determining Effects of 3-Dimensional Roughness on Partial Hydrodynamic Lubrication. J Lubric Tech-T Asme. 1978;100:12-7.

[9] Majumdar BC, Hamrock BJ. Effect of Surface-Roughness on Elastohydrodynamic Line Contact. J Lubric Tech-T Asme. 1982;104:401-9.

[10] Sadeghi F, Sui PC. Compressible Elastohydrodynamic Lubrication of Rough Surfaces. J Tribol-T Asme. 1989;111:56-62.

[11] Jang JY, Khonsari MM. Elastohydrodynamic Line-Contact of Compressible Shear Thinning Fluids With Consideration of the Surface Roughness. J Tribol-T Asme. 2010;132:034501.

[12] Moraru L, Keith TG, Kahraman A. Aspects Regarding the Use of Probabilistic Models for Isothermal Full Film Rough Line Contacts. Tribol T. 2004;47:386-95.

[13] Chang WR, Etsion I, Bogy DB. An Elastic-Plastic Model for the Contact of Rough Surfaces. J Tribol-T Asme. 1987;109:257-63.

[14] Masjedi M, Khonsari MM. Film Thickness and Asperity Load Formulas for Line-Contact Elastohydrodynamic Lubrication With Provision for Surface Roughness. J Tribol-T Asme. 2012;134:011503.

[15] Masjedi M, Khonsari MM. Theoretical and experimental investigation of traction coefficient in line-contact EHL of rough surfaces. Tribol Int. 2014;70:179-89.

[16] Zhao YW, Maietta DM, Chang L. An asperity microcontact model incorporating the transition from elastic deformation to fully plastic flow. J Tribol-T Asme. 2000;122:86-93.

[17] Chang L. A Deterministic Model for Line-Contact Partial Elastohydrodynamic Lubrication. Tribol Int. 1995;28:75-84.

[18] Zhai XJ, Chang L. An engineering approach to deterministic modeling of mixed-film contacts. Tribol T. 1998;41:327-34.

[19] Jiang XF, Hua DY, Cheng HS, Ai XL, Lee SC. A mixed elastohydrodynamic lubrication model with asperity contact. J Tribol-T Asme. 1999;121:481-91.

[20] Hu YZ, Zhu D. A full numerical solution to the mixed lubrication in point contacts. J Tribol-T Asme. 2000;122:1-9.

[21] Wang QJ, Zhu D, Cheng HS, Yu TH, Jiang XF, Liu SB. Mixed lubrication analyses by a macro-micro approach and a full-scale mixed EHL model. J Tribol-T Asme. 2004;126:81-91.

[22] Wang QJ, Zhu D, Zhou RS, Hashimoto F. Investigating the Effect of Surface Finish on Mixed EHL in Rolling and Rolling-Sliding Contacts. Tribol T. 2008;51:748-61.

[23] Zhu D, Wang QJ. On the lambda ratio range of mixed lubrication. P I Mech Eng J-J Eng. 2012;226:1010-22.

[24] Jiang X, Cheng HS, Hua DY. A theoretical analysis of mixed lubrication by macro micro approach: Part I - Results in a gear surface contact. Tribol T. 2000;43:689-99.

[25] Evans HP, Snidle RW, Sharif KJ. Deterministic mixed lubrication modelling using roughness measurements in gear applications. Tribol Int. 2009;42:1406-17.

[26] Prakash J, Czichos H. Influence of Surface-Roughness and Its Orientation on Partial Elastohydrodynamic Lubrication of Rollers. J Lubric Tech-T Asme. 1983;105:591-7.

[27] Greenwood JA, Tripp, J.H. . The Contact of Two Nominally Flat Rough Surfaces. Proc Inst Mech Eng. 1971;185:625–33

[28] Akbarzadeh S, Khonsari MM. Effect of Surface Pattern on Stribeck Curve. Tribol Lett. 2010;37:477-86.

[29] Patir N. Numerical Procedure for Random Generation of Rough Surfaces. Wear. 1978;47:263-77.

[30] Zhu D, Wang QJ. Effect of Roughness Orientation on the Elastohydrodynamic Lubrication Film Thickness. J Tribol-T Asme. 2013;135:031501.

[31] Beheshti A, Khonsari MM. Asperity micro-contact models as applied to the deformation of rough line contact. Tribol Int. 2012;52:61-74.

[32] Hua DY, Khonsari MM. Application of Transient Elastohydrodynamic Lubrication Analysis for Gear Transmissions. Tribol T. 1995;38:905-13.

[33] Doolittle AK. Studies in Newtonian Flow .2. The Dependence of the Viscosity of Liquids on Free-Space. J Appl Phys. 1951;22:1471-5.

Chapter 5: On the Effect of Surface Roughness in Point-Contact EHL: Formulas for Film Thickness and Asperity Load*

5.1. Introduction

Elastohydrodynamic lubrication (EHL) is the governing lubrication regime in many industrial applications. While line-contact EHL exists in gear teeth, heavily-loaded journal bearings, cam-followers, and the like, point-contact EHL applies in components with spherical/elliptical elements such as ball bearings and artificial body joints.

The first systematic solution of point-contact EHL was proposed by Hamrock & Dowson [1, 2] where they numerically solved the problem by the relaxation method. They later proposed curve-fit expressions for the central and minimum film thickness that are widely used [3]. The numerical solution methodology was subsequently improved by other researchers to include heavier loads [4, 5]. Among many other contributions that followed, Venner [6] developed a fast solution method for the spherical-contact EHL using the multilevel technique which was later extended to elliptical contact [7, 8]. The effect of transient condition was included in the solution by Jalali-Vahid et al. [9]. The non-Newtonian behavior of the lubricant in point-contact EHL was investigated in some recent studies [10-14].

Within the context of mixed point-contact EHL, Zhu & Cheng [15] first introduced a model based on statistical consideration of the surface asperities. For this purpose, they utilized the modified Reynolds equation derived by Patir & Cheng [16] together with the elastic deformation of the surface asperities using the Greenwood-Tripp model [17]. Later, Venner [6] integrated the actual surface profiles into his smooth point-contact model to study the effect of roughness. Other researchers used similar methods to include the effect of actual surface profile in point-contact EHL [18, 19]. A comprehensive model based on deterministic treatment of the surface roughness was first introduced by Chang [20] for line-contact EHL, and later extended to point-contact EHL [21-27]. Most recently, following the similar studies for line-contact EHL [28, 29], Sojoudi & Khonsari [30] used Johnson's load-sharing concept [31] together with dry circular-contact model by Greenwood & Tripp [32] to investigate the effect of surface roughness without directly solving the Reynolds equation.

In this study, a numerical model is presented to investigate the effect of surface roughness in point-contact (elliptical contact) elastohydrodynamic lubrication. Similar to the authors'

* Reprinted by permission of *Elsevier* (See Appendix I)

approach for line-contact EHL [33-35], the modified Reynolds equation by Patir & Cheng [16], the bulk elastic deformation of the surfaces, and the elasto-plastic asperity contact equations by Zhao et al. [36] are simultaneously solved to obtain the pressure and the film profile. The central and the minimum film thickness and the asperity load ratio are then obtained from the results. At the next step, by performing the regression analyses based on the results of a wide range of simulations, curve-fit expressions are presented to readily predict the film thickness and the asperity load ratio in mixed lubrication elliptical contact. Finally, the results from these formulas are compared with the results presented in other publications to show the efficiency of the present approach.

5.2. Model

In order to predict the pressure distribution and the film profile in point-contact elastohydrodynamic lubrication (EHL), the Reynolds equation, the bulk deformation of contact surfaces, and the load balance equation should be solved simultaneously. When the surfaces are rough, the Reynolds equation should be modified to include the roughness effects. Moreover, since the load is shared between the fluid and the asperities in the mixed EHL, the roughness changes the load balance. Therefore, the pressure at any point in the contact area is the sum of hydrodynamic and asperity pressures:

$$p = p_h + p_a \tag{1}$$

where p, p_h and p_a are the total, hydrodynamic and asperity pressures, respectively.

Fluid equations: For point-contact EHL, the 2D Reynolds equation modified by Patir and Cheng [16] is written as:

$$\frac{\partial}{\partial x}(\phi_x \frac{\rho h^3}{12\mu}\frac{\partial p_h}{\partial x}) + \frac{\partial}{\partial y}(\phi_y \frac{\rho h^3}{12\mu}\frac{\partial p_h}{\partial y}) = u\frac{\partial(\rho h_T)}{\partial x} \tag{2}$$

where x and y are the coordinates along and perpendicular to the moving direction, respectively. In Eq. (2), h is the film thickness, μ is the fluid viscosity, ρ is the fluid density, and u is the rolling speed. φ_x and φ_y are the pressure flow factor in x and y directions and h_T is the average gap between two surfaces [16].

For an isotropic surface with Gaussian distribution of the surface heights, the pressure flow factors are [16]:

$$\phi_x = \phi_y = 1 - 0.9e^{-0.56\frac{h}{\sigma}} \tag{3}$$

where σ is the surface roughness which is the standard deviation of the surface heights (also shown as R_q in some literature). For Gaussian distribution of the surface heights, h_T can be written as [37]:

$$h_T = 0.5h\left[1 + erf\left(\frac{h}{\sqrt{2}\sigma}\right)\right] + \frac{\sigma}{\sqrt{2\pi}}\exp\left(\frac{-h^2}{2\sigma^2}\right) \tag{4}$$

In Eq. (2), both the viscosity and density are functions of the hydrodynamic pressure. For pressure-density dependence, equation provided by Dowson and Higginson [38] is used:

$$\frac{\rho}{\rho_0} = 1 + \frac{0.6p_h}{1+1.7p_h} \tag{5}$$

where ρ_0 is the density at atmospheric pressure. For the viscosity, widely-used Roelands equation [39] which is valid for using at moderate pressures is utilized:

$$\frac{\mu}{\mu_0} = \exp\left[(\ln\mu_0 + 9.67)\left\{-1 + \left(1 + 5.1\times10^{-9}p_h\right)^Z\right\}\right] \tag{6}$$

where μ_0 is the viscosity at zero pressure, and Z is viscosity- pressure index which is a function of pressure-viscosity coefficient (α) and μ_0 [40].

The governing equations are non-dimensionalized using the following parameters:

$$D = \frac{R_y}{R_x},\ X = \frac{x}{b},\ Y = \frac{y}{a},\ H = \frac{h}{R_x},\ \bar{\mu} = \frac{\mu}{\mu_0},\ \bar{\rho} = \frac{\rho}{\rho_0},\ P = \frac{p}{p_H}$$
$$U = \frac{\mu_0 u}{E'R_x},\ W = \frac{F}{E'{R_x}^2},\ G = \alpha E',\ \bar{\sigma} = \frac{\sigma}{R_x},\ V = \frac{v}{E'} \tag{7}$$

where p is the contact pressure, F is the normal load, E' is the effective modulus of elasticity, and R_x and R_y are the radii of curvature in x and y directions, respectively (See Fig. 5.1). The parameter v is the Vickers hardness of the softer surface, and parameters U, W, G, $\bar{\sigma}$, and V denote the dimensionless speed, load, material, surface roughness, and surface hardness, respectively.

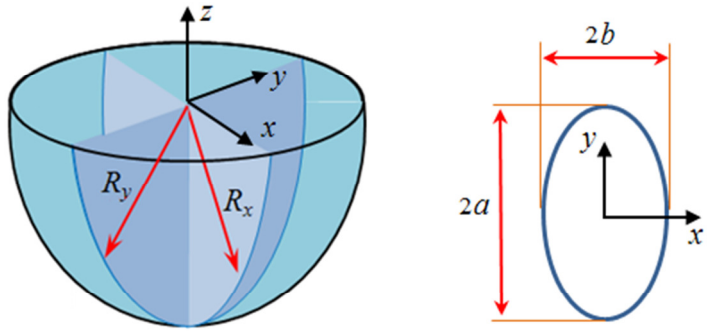

Fig. 5.1. Coordinates and geometry of elliptical contact

In Eq. (7), parameters p_H, a, and b are the maximum Hertzian pressure, Hertzian half contact length (along the y direction), and the Hertzian half contact width (along the x direction), respectively. These parameters are defined as:

$$b = \sqrt[3]{\frac{6R_x DF\widetilde{\mathrm{S}}}{\pi E'\kappa(D+1)}} = R_x\sqrt[3]{\frac{6DW\widetilde{\mathrm{S}}}{\pi\kappa(D+1)}}, \quad a = \kappa b,\ a \geq b$$

$$p_H = \frac{3F}{2\pi ab} = \frac{3WE'R_x^2}{2\pi\kappa b^2} = \frac{3WE'}{2\pi\kappa\gamma^2}; \quad \left(\gamma = \frac{b}{R_x} = \sqrt[3]{\frac{6DW\widetilde{\mathrm{S}}}{\pi\kappa(D+1)}}\right) \tag{8}$$

where κ is the ellipticity parameter defined as the ratio of the Hertzian contact length to the Hertzian contact width (See Fig. 5.1). This parameter is only a function of D and can be written as:

$$\kappa = \sqrt{(D+1)\frac{\widetilde{\mathrm{F}}}{\widetilde{\mathrm{S}}} - D} \tag{9}$$

where $\widetilde{\mathrm{F}}$ and $\widetilde{\mathrm{S}}$ are elliptical integral of the first and the second kind:

$$\widetilde{\mathrm{F}}(\kappa) = \int_0^{\pi/2} \frac{d\tau}{\sqrt{1-\left(1-\frac{1}{\kappa^2}\right)\sin^2\tau}}, \quad \widetilde{\mathrm{S}}(\kappa) = \int_0^{\pi/2} \sqrt{1-\left(1-\frac{1}{\kappa^2}\right)\sin^2\tau}\, d\tau \tag{10}$$

It should be noted that since the elliptical integrals are functions of the ellipticity, an iterative procedure is needed to calculate κ based on D.

The Reynolds equation can be written in dimensionless form as:

$$\frac{\partial}{\partial X}\left(\phi_X \frac{\overline{\rho}H^3}{\overline{\mu}}\frac{\partial P_h}{\partial X}\right) + \frac{1}{\kappa^2}\frac{\partial}{\partial Y}\left(\phi_Y \frac{\overline{\rho}H^3}{\overline{\mu}}\frac{\partial P_h}{\partial Y}\right) = \frac{8\pi\kappa\gamma^3 U}{W}\frac{\partial(\overline{\rho}H_T)}{\partial X} \tag{11}$$

where H_T is the dimensionless average gap, and φ_X and φ_Y are the isotropic flow factors written as functions of dimensionless parameters as:

$$\phi_X = \phi_Y = 1 - 0.9e^{-0.56\frac{H}{\overline{\sigma}}} \tag{12}$$

Load balance: The total load is obtained by integrating the hydrodynamic and the asperity pressures within the contact region:

$$F = \int\int p_h(x,y)dxdy + \int\int p_a(x,y)dxdy \tag{13}$$

Equation (13) is written in dimensionless form as:

$$\frac{2\pi}{3}=\int\int P_h(X,Y)dXdY+\int\int P_a(X,Y)dXdY \tag{14}$$

Bulk deformation and film profile: The lubricant film has the following form considering Hertzian geometry and elastic deformation of the surfaces according to [41]:

$$h(x,y)=h_{00}+\frac{x^2}{2R_x}+\frac{y^2}{2R_y}+\frac{2}{\pi E'}\int\int\frac{p(s,q)dsdq}{\sqrt{(x-s)^2+(y-q)^2}} \tag{15}$$

where h_{00} is a constant. Physically, the load balance adjusts the separation between the surfaces which appears in this constant. It should be noted that the surface deformation is caused by the total pressure. Equation (15) can be nondimensionalized as:

$$H(X,Y)=H_{00}+\gamma^2\frac{X^2}{2}+\frac{\gamma^2\kappa^2}{D}\frac{Y^2}{2}+\frac{\gamma^2\kappa(D+1)}{2\pi D\widetilde{\mathrm{S}}}\int\int\frac{P(S,Q)dSdQ}{\sqrt{(X-S)^2+\kappa^2(Y-Q)^2}} \tag{16}$$

where H_{00} is a constant to be determined.

Surface roughness: In this study, for the deformation of surface asperities, the elasto-plastic model known as ZMC developed by Zhao et al. [36] is utilized which considers the elastic, elasto-plastic and fully plastic deformation of the asperities. Recently, Beheshti & Khonsari [42] showed that the ZMC model gives close results compared to other comprehensive asperity micro-contact models. This model has also been utilized in recent studies on the mixed EHL [33-35, 43]. In this model, the asperity pressure P_a is defined as the sum of elastic, elasto-plastic and plastic pressures:

$$\begin{aligned}
p_a &= \frac{2}{3}E'n\beta^{0.5}\sigma^{1.5}\left(\frac{\sigma}{\sigma_s}\right)\frac{1}{\sqrt{2\pi}}\int_{h^*-y_s{}^*}^{h^*-y_s{}^*+w_1{}^*} w^{*1.5}e^{-0.5\left(\frac{\sigma}{\sigma_s}z^*\right)^2}dz^* \\
&+2\pi vn\beta\sigma\frac{1}{\sqrt{2\pi}}\left(\frac{\sigma}{\sigma_s}\right)\int_{h^*-y_s{}^*+w_2{}^*}^{\infty} w^*e^{-0.5\left(\frac{\sigma}{\sigma_s}z^*\right)^2}dz^* \\
&+\pi vn\beta\sigma\frac{1}{\sqrt{2\pi}}\left(\frac{\sigma}{\sigma_s}\right)\int_{h^*-y_s{}^*+w_1{}^*}^{h^*-y_s{}^*+w_2{}^*} w^*e^{-0.5\left(\frac{\sigma}{\sigma_s}z^*\right)^2} \\
&\times\left[1-0.6\frac{\ln w_2{}^*-\ln w^*}{\ln w_2{}^*-\ln w_1{}^*}\right]\left[1-2\left(\frac{w^*-w_1{}^*}{w_2{}^*-w_1{}^*}\right)^3+3\left(\frac{w^*-w_1{}^*}{w_2{}^*-w_1{}^*}\right)^2\right]dz^*
\end{aligned} \tag{17}$$

where $w^*=z^*-h^*+y_s{}^*$. In Eq. (17), the starred variables are normalized by σ. Note that σ is the standard deviation of the surface heights, while σ_s is the standard deviation of the surface

summits. Parameter h is the separation (film thickness in EHL contact), β is the asperity radius, and n is the asperity density. Figure 5.2 shows a schematic view of the contact between a rough and a smooth surface.

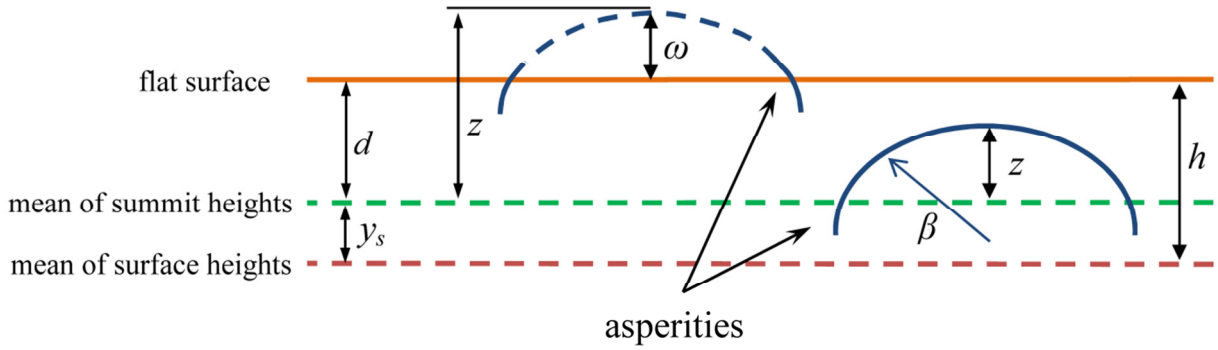

Fig. 5.2. Contact between a rough and a smooth surface

Eq. (17) can be written in dimensionless form as:

$$P_a = \frac{2\pi\gamma^2\kappa}{3WE'} p_a = \frac{4\pi\gamma^2\kappa}{9W} \bar{n}\bar{\beta}^{0.5}\bar{\sigma}^{1.5}\left(\frac{\bar{\sigma}}{\bar{\sigma}_s}\right)\int_{I_1}^{I_2} (z^* - I_1)^{1.5} e^{-0.5\left(\frac{\bar{\sigma}}{\bar{\sigma}_s}z^*\right)^2} dz^*$$
$$+ \frac{4\pi^2\gamma^2\kappa}{3W} V\bar{n}\bar{\beta}\bar{\sigma}\left(\frac{\bar{\sigma}}{\bar{\sigma}_s}\right)\int_{I_3}^{\infty} (z^* - I_1) e^{-0.5\left(\frac{\bar{\sigma}}{\bar{\sigma}_s}z^*\right)^2} dz^*$$
$$+ \frac{2\pi^2\gamma^2\kappa}{3W} V\bar{n}\bar{\beta}\bar{\sigma}\left(\frac{\bar{\sigma}}{\bar{\sigma}_s}\right)\int_{I_2}^{I_3} (z^* - I_1) e^{-0.5\left(\frac{\bar{\sigma}}{\bar{\sigma}_s}z^*\right)^2} \tag{18}$$
$$\times\left[1 - 0.6\frac{\ln\bar{w}_2 - \ln(\bar{\sigma}(z^* - I_1))}{\ln\bar{w}_2 - \ln\bar{w}_1}\right]\left[1 - 2\left(\frac{\bar{\sigma}(z^* - I_1) - \bar{w}_1}{\bar{w}_2 - \bar{w}_1}\right)^3 + 3\left(\frac{\bar{\sigma}(z^* - I_1) - \bar{w}_1}{\bar{w}_2 - \bar{w}_1}\right)^2\right] dz^*$$

where $I_1 = \frac{H - \bar{y}s}{\bar{\sigma}}$, $I_2 = \frac{H - \bar{y}_s + \bar{w}_1}{\bar{\sigma}}$, $I_3 = \frac{H - \bar{y}_s + \bar{w}_2}{\bar{\sigma}}$.

5.3. Numerical Simulation Procedure

The governing equations (11), (14), (16) and (18) are discretized using the finite difference method and solved simultaneously to obtain the pressure and the film profiles. The finite difference formulation for the Reynolds equation is provided in Appendix C. The dimensionless input parameters are the load W, speed U, material G, surface roughness $\bar{\sigma}$, surface hardness V, and ellipticity parameter κ. It should be noted that for the sake of minimizing the number of input parameters, the asperity radius β and the asperity density n are omitted from the input by the

assumption of $n\beta\sigma$=0.05 [31, 33, 44] and $\sigma/\beta = 0.01$ [33]. Also, when both surfaces are rough, the combined roughness of $\sigma = \sqrt{{\sigma_1}^2 + {\sigma_2}^2}$ should be used.
For the line-contact EHL problem, the widely-used solution method is the Newton-Raphson algorithm. The convergence rate of this method is fast (quadratic), but the procedure requires decomposition of the Jacobian matrix to solve the equations. For 1-D problem of line-contact, applying Newton-Raphson algorithm was found to be the best choice, while the use of this approach for 2-D problem of point contact is not efficient. In other words, for N nodes along the line contact domain, the number of elements in the Jacobian matrix is equal to N^2 while for point contact problem with N×N number of nodes, the Jacobian matrix has N^4 elements, which is difficult to handle.

The widely-used method for solving the point-contact EHL problem is relaxation method which is also utilized in this study. In fact, Successive Over-relaxation Method (S.O.R) is used to solve the discretized Reynolds equation in an inner loop, while the hydrodynamic and asperity pressures are updated by an under-relaxation factor (starts from 0.01 and decreases gradually throughout the process) in an outer loop. The other unknown parameter H_{00} is also under-relaxed by the load balance in the outer loop as well. Appendix D shows a flowchart of the numerical procedure.

To ensure that the fully flooded condition prevails, the minimum amount of X is set to -4 in all cases simulated. Appendix E shows the effect of inlet variation on the results for both smooth and rough surfaces. Also, while the hydrodynamic pressure becomes nil at a point close to X=1, the asperity pressure may have a value far beyond that point and thus the maximum amount of X is set to 2. Choosing the limits of Y as ±2, the computational domain is a rectangle with $-4 \le X \le 2$ and $-2 \le Y \le 2$. The hydrodynamic pressure is zero along all boundaries. Also, the hydrodynamic pressure is set to zero whenever it becomes negative (commonly known as Reynolds condition [1]). It should be mentioned that since the problem is symmetric with respect to the X axis (Y=0 plane), only half of the problem is modeled and solved. Therefore, the actual computational domain is $-4 \le X \le 2$ and $0 \le Y \le 2$ with symmetric boundary conditions on Y=0 plane.

The convergence of the results is ensured by refining the mesh until the change in the results becomes negligible. In general, within the range of the operating conditions studied, 30 nodes in one unit along the X direction and 20 nodes in one unit along the Y direction (which results in a 180×40 mesh for $-4 \le X \le 2$ and $0 \le Y \le 2$) is proven to be sufficient. Appendix F presents the results of a mesh refinement study for both the smooth and rough surfaces. As shown, the error uniformly decreases as the computational mesh is refined. However, further refinement beyond 180×40 nodes yields less than 1% error at the experience of much greater computational demand.

The run time of the simulations is dependent on the input parameters. In general, solution for the higher loads takes longer because more iteration is needed to converge. Also, the solution for rough surfaces is generally slower than the smooth solution, because the asperity pressure must be calculated in each loop. The typical run time on an Intel i7 3.47 GHz machine for the chosen domain and grid setup is generally between 20 and 100 minutes depending on the input.

The final results consist of the hydrodynamic, asperity, and total pressure distributions as well as the film profile. Based on these results, the central and the minimum film thickness are easily determined. Also predicted is the asperity load ratio which is the ratio of the load carried by the asperities to the total normal load.

5.4. Results and Discussions

Figure 5.3 shows a typical example of 3D distribution of dimensionless pressure in a rough EHL problem. Since a part of the load is carried by the surface asperities, the total pressure is composed of hydrodynamic and asperity parts. For the case depicted in Fig. 5.3, the simulation yields the asperity load ratio of 54%, which means that the volume under the asperity pressure is 54% of that of the total pressure.

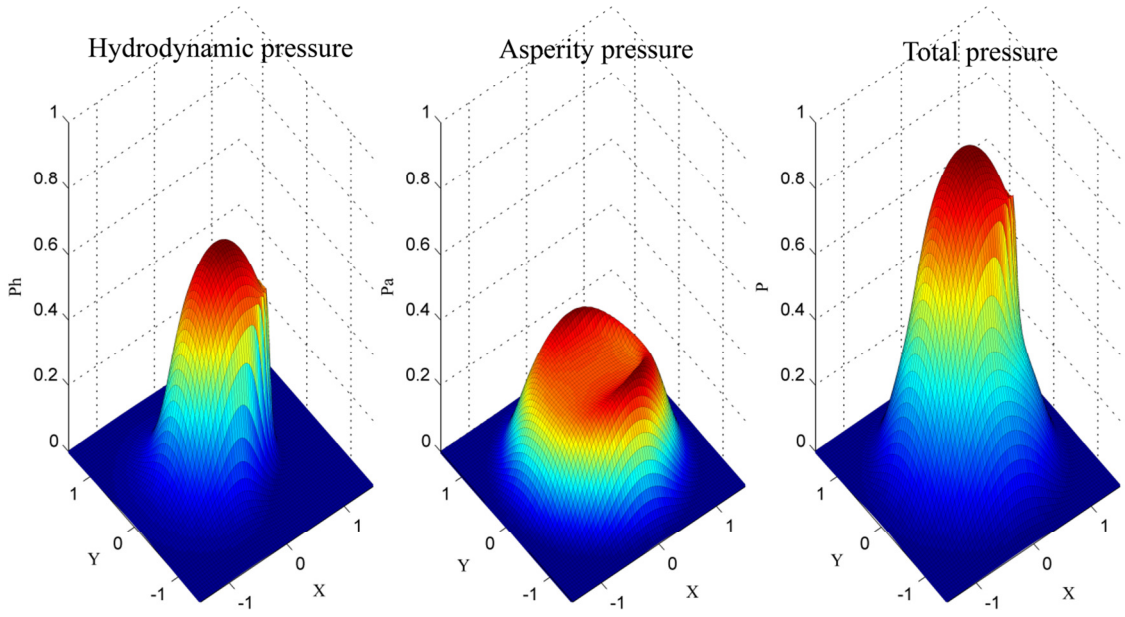

Fig. 5.3. Hydrodynamic, asperity and total pressure distribution of rough surfaces (κ=1, W=1×10^{-6}, U=1×10^{-11}, G=4972, $\bar{\sigma}$=3×10^{-5}, V=0.01)

Figure 5.4 depicts an example of contour plots for the dimensionless film thickness distribution in smooth and rough surfaces. As shown, for both cases, the minimum film thickness occurs at the sides (Point B). However, when dealing with rough surfaces, this point is closer to the center in the Y direction. For the smooth case, the simulations predict a central film thickness of

H_c=1.80×10^{-5} (Point A) and a minimum film thickness of H_{min}=1.05×10^{-5} (point B). For the rough surface, the central film thickness is H_c=2.31×10^{-5} (Point A) and the minimum film thickness is H_{min}=1.82×10^{-5} (point B). Note that the results are symmetric with respect to Y=0 plane.

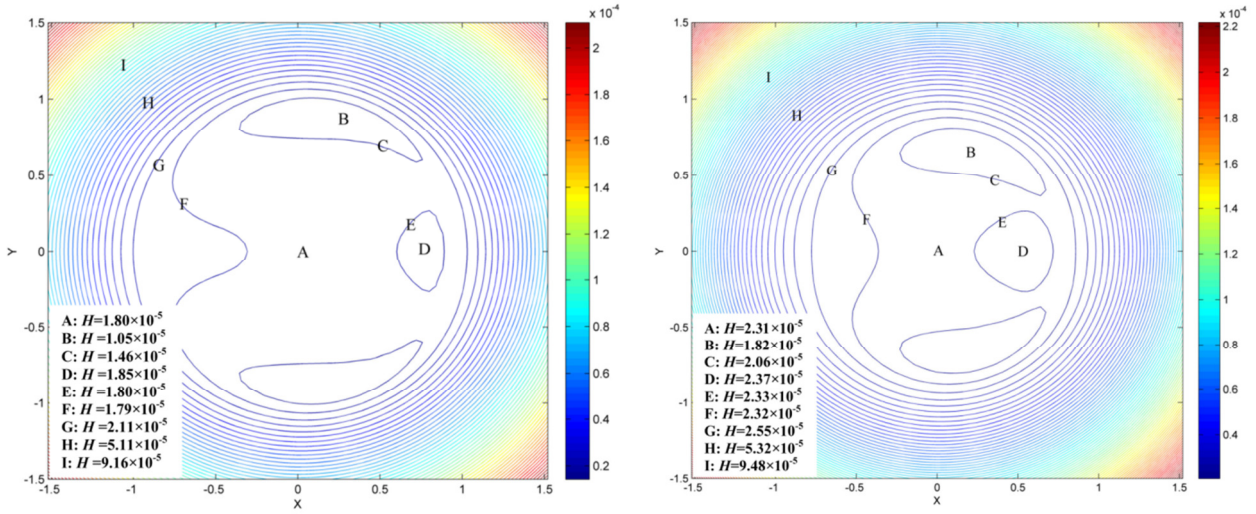

(a) (b)

Fig. 5.4. Film thickness distributions (κ=1, W=1×10^{-6}, U=1×10^{-11}, G=4972)
(a) smooth surfaces (b) rough surfaces with $\bar{\sigma}$=3×10^{-5}

To have a better understanding of the results, the pressure and the film distributions are plotted along the X direction in Y=0 plane and along the Y direction in X=0 plane in Fig. 5.5. For all cases, the input are κ=1, W=1×10^{-6}, U=1×10^{-11} and G=4972. Also, the dimensionless hardness is set to V=0.01 (Vickers hardness of 2.35 GPa equal to 20 Rockwell C, which is a reasonable value for regular steel). The results are presented for three roughness levels: a smooth surface (typically $\bar{\sigma}$=1×10^{-6} satisfies this assumption), slightly rough ($\bar{\sigma}$=1×10^{-5}) and fairly rough ($\bar{\sigma}$=3×10^{-5}). It is obvious that there is no asperity pressure for the smooth case (L_a=0). The predicted asperity load ratio is L_a= 8% for $\bar{\sigma}$=1×10^{-5} and L_a= 54% for $\bar{\sigma}$=3×10^{-5}.

As shown in Fig. 5.5 (a), when dealing with rough surfaces, total pressure extends beyond X=1 due to the existence of asperity pressure there, while the hydrodynamic pressure becomes nil around X=1. This implies that the separation gap beyond the width of the Hertzian contact is small enough to cause some of the asperities to experience intimate contact. This phenomenon is, of course, more pronounced for the highest roughness values simulated.

As Fig. 5.5 (b) shows, the pressure profiles are symmetric with respect to Y=0 plane. Also, the asperity pressure profiles have a peak at each side which is due to local decrease in the film thickness. Also, for the case of rough surfaces, the asperity pressure exists at the sides beyond the points where the hydrodynamic pressure becomes negligible. This is again more visible for the highest roughness value and affects the total pressure distribution.

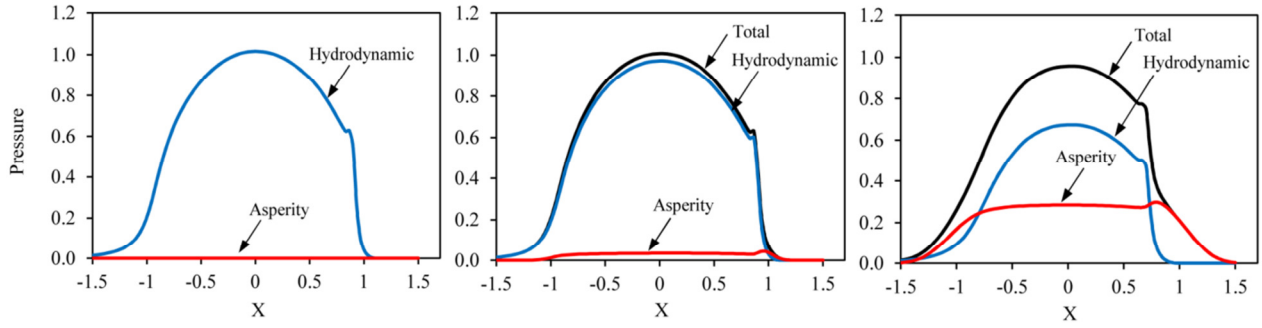

(a)

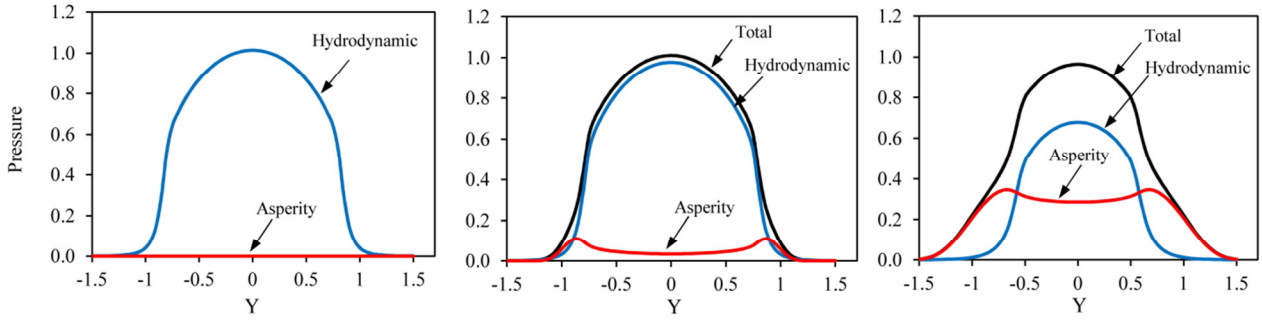

(b)

Fig. 5.5. Pressure distributions: (a) along X in Y=0 plane (b) along Y in X=0 plane
(κ=1, W=1×10^{-6}, U=1×10^{-11}, G=4972, V=0.01)
From left to right: smooth surface, rough surface with $\bar{\sigma}$=1×10^{-5}, rough surface with $\bar{\sigma}$=3×10^{-5}

Figures 5.6 show the film thickness distributions along the X axis in Y=0 plane and along the Y axis in X=0 plane. The results for smooth surfaces are compared with those for rough surfaces ($\bar{\sigma}$=1×10^{-5} and $\bar{\sigma}$=3×10^{-5}). As shown, increasing the surface roughness increases the film thickness. This is due to the contribution of the asperities in carrying the contact load (which decreases the part carried by the fluid) as well as their influence on the flow behavior (which is accounted for by the flow factors in the modified Reynolds equation), However, increasing the roughness decreases the film parameter Λ which is the ratio of the minimum film thickness to the combined surface roughness ($\Lambda = h_{min}/\sqrt{{\sigma_1}^2 + {\sigma_2}^2}$). This parameter is Λ=1.3 for $\bar{\sigma}$=1×10^{-5} and Λ=0.6 for $\bar{\sigma}$=3×10^{-5}.

It is worthwhile to mention that while the film thickness value at the point X=0 in Fig. 5.6 (a) and Y=0 in Fig. 5.6 (b) represent the central film thickness, the minimum film thickness does not appear in either of the views. This is because the minimum value of the film thickness occurs at the sides which is not located in X=0 or Y=0 plane (See Fig. 5.4). Also note that as the roughness increases, the film profiles shrink toward the center in both X and Y directions.

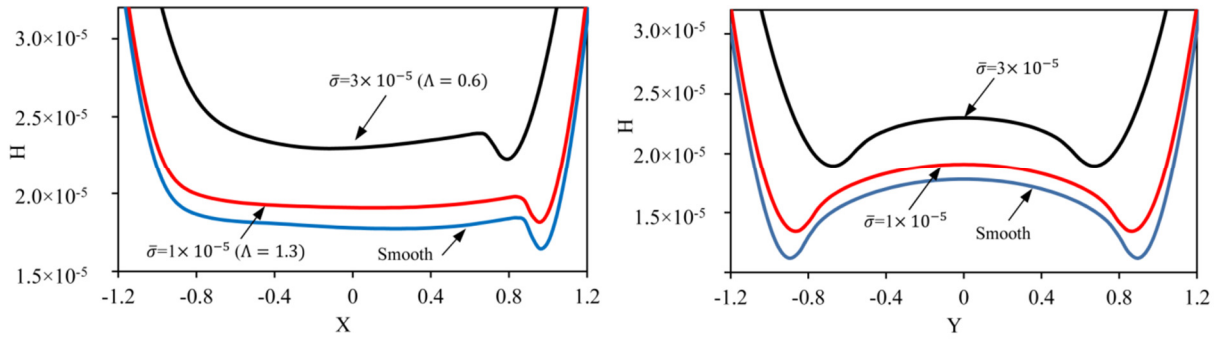

(a) (b)

Fig. 5.6. Film profiles (κ=1, W=1×10^{-6}, U=1×10^{-11}, G=4972, V=0.01)
(a) along X in Y=0 plane (b) along Y in X=0 plane

5.5. Predictive formulas

The main goal of this study is to quantify the effect of surface roughness in point-contact EHL. This is done by curve-fitting the results of a set of simulations using a wide range of input. In this section, we first present the smooth results for comparison and benchmarking purpose. In the next step, rough surface results are presented and predictive formulas are derived for the central and minimum film thickness as well as the asperity load ratio in rough point-contact EHL.

5.5.1. Film thickness formulas for smooth point-contact EHL

The input parameters for the smooth point-contact EHL simulations are ellipticity κ, dimensionless load W, dimensionless speed U, and dimensionless material G. Table 5.1 shows the range of input parameters selected for the simulations.

Table 5.1. Range of input parameters selected for simulation (smooth surfaces)

Parameter	W	U	G	κ
min	1.5×10^{-7}	1×10^{-12}	2500	1
max	2.5×10^{-4}	1×10^{-10}	7500	8

A reasonable form of curve-fit equation for the central and the minimum film thickness can be assumed as $H = c_1 W^{c_2} U^{c_3} G^{c_4} (1 + c_5 e^{c_6 \kappa})$ which was used by Hamrock & Dowson [3]. Since changing the ellipticity affects the contact characteristics, we implement a new form in which the exponents of W, U, and G are also assumed to be functions of ellipticity. This form also accommodates a wider range of load. Therefore, a general form of $H = c_1 W^{c_2 \kappa^{m_1}} U^{c_3 \kappa^{m_2}} G^{c_4 \kappa^{m_3}} (1 + c_5 e^{c_6 \kappa})$ is chosen for performing the regression analysis. After analyzing the results of about a hundred simulations within the range of input shown in Table 5.1, the curve-fit equations for the central and minimum film thickness (smooth surface) are obtained as:

$$(H_c)_{smooth} = \frac{(h_c)_{smooth}}{R_x} = 3.672\,W^{-0.045\kappa^{0.18}}U^{0.663\kappa^{0.025}}G^{0.502\kappa^{0.064}}(1-0.573\,e^{-0.74\kappa}) \quad (19)$$

$$(H_{\min})_{smooth} = \frac{(h_{\min})_{smooth}}{R_x} = 1.637\,W^{-0.09\kappa^{-0.15}}U^{0.711\kappa^{-0.023}}G^{0.65\kappa^{-0.045}}(1-0.974\,e^{-0.676\kappa}) \quad (20)$$

Table G.1 in Appendix G shows a part of simulation results for the central and the minimum film thickness within the range of input shown in Table 5.1. In this table, the central and minimum film thickness values obtained from the curve-fit equations (Eqs. (19) and (20)) are compared with those from simulations, and the error between them is shown as well. The average value of the error between simulation and curve-fit results is 2.27% with the maximum of 8.62% for the central film thickness, while it is 3.27% with the maximum of 9.79% for the minimum film thickness.

It should be noted that for a given dimensionless load number W, increasing the ellipticity parameter κ decreases the Hertzian pressure (See Eq. (8)) due to a larger contact area. For example, the dimensionless load W=1×10^{-5} yields a maximum Hertzian pressure of 1.8 GPa (for steel) at κ=1, but 0.77 GPa at κ=8. In this study, the dimensionless load value is chosen in a way that keeps the maximum Hertzian pressure between about 0.4 GPa and 2.3 GPa (for steel). So, while the upper limit is obtained as W=2.5×10^{-4} for κ=8, it is W=2×10^{-5} for κ=1. Therefore, special attention should be paid while choosing the upper limit of dimensionless load for the use in Eqs. (19) and (20).

5.5.2. Film thickness and asperity load formulas for rough point-contact EHL

In order to obtain curve-fit expressions for the film thickness and asperity load ratio in point-contact EHL of rough surfaces, an extensive set of simulations are performed based on the approach presented in this study. The range of input parameters selected for the simulations are shown in Table 5.2. The range of dimensionless load, speed, material and ellipticity parameters are same as those selected for smooth simulations (Table 5.1). The selected range for dimensionless roughness $\bar{\sigma}$ starts from $\bar{\sigma}$=0 (theoretically smooth surface) up to $\bar{\sigma}$=5×10^{-5} (equal to combined roughness of 1.27 μm for equivalent radius of one inch). However, the results for roughness values below $\bar{\sigma}$=1×10^{-6} are proved to be very close to the smooth surface solution results. The selected range for the dimensionless hardness V covers the Vickers hardness of about 1.1 to 6.8 GPa for the steel. The upper range equals to about 60 Rockwell C which corresponds to that of most hardened steels. It should also be noted that the allowable range of dimensionless load W should be checked for each ellipticity value as mentioned in the previous section.

The form of the curve-fit expressions for both central and the minimum film thickness are assumed as $H = (H)_{smooth} \times (1 + c_1 W^{c_2} U^{c_3} G^{c_4} \bar{\sigma}^{c_5} V^{c_6} \kappa^{c_7})$ which is similar to the form used

for line-contact formulas in Ref. [33]. In this form, when the surface roughness is zero (or practically very small), the film thickness equations revert back to those for smooth surface. The following expressions are obtained by performing the regression analysis for the results of about a hundred simulations within the range of input shown in Table 5.2 (a total of about 200 simulations for both smooth and rough cases).

Table 5.2. Range of input parameters selected for simulation (rough surfaces)

Parameter	W	U	G	κ	$\bar{\sigma}$	V
min	1.5×10^{-7}	1×10^{-12}	2500	1	0	0.005
max	2.5×10^{-4}	1×10^{-10}	7500	8	5×10^{-5}	0.03

The central film thickness equation is:

$$H_c = \frac{h_c}{R_x} = (H_c)_{smooth} \times (1 + 0.025\bar{\sigma}^{1.248} V^{0.119} W^{-0.133} U^{-0.884} G^{-0.977} \kappa^{0.081}) \tag{21}$$

where $(H_c)_{smooth}$ is obtained from Eq. (19).

The minimum film thickness equation is:

$$H_{\min} = \frac{h_{\min}}{R_x} = (H_{\min})_{smooth} \times (1 + 0.141\bar{\sigma}^{1.073} V^{0.149} W^{-0.044} U^{-0.828} G^{-0.954} \kappa^{-0.395}) \tag{22}$$

where $(H_{min})_{smooth}$ is obtained from Eq. (20).

Finally, the asperity load ratio equation (as percentage) is:

$$L_a = 10 W^{-0.083} U^{0.143} G^{0.314} [\ln(1 + \bar{\sigma}^{4.689} V^{0.509} W^{-0.501} U^{-2.90} G^{-2.870})] \tag{23}$$

A comparison between the simulation and curve-fit results for the central film thickness, minimum film thickness, and asperity load ratio are shown in Tables G.2, G.3, and G.4 in Appendix G. The mean error values for central film thickness, minimum film thickness, and asperity load ratio are 2.00%, 2.68%, and 1.98%, respectively, while the maximum error values are 6.73%, 8.00%, and 8.36%, respectively. It should be noted that the error for the film thickness is defined as $100\times|H_{(simulation)}-H_{(curve\text{-}fit)}|/\ H_{(simulation)}$ while the error for the asperity load ratio is defined as $|L_{a(simulation)}- L_{a(curve\text{-}fit)}|$.

It is interesting to note that the asperity load ratio equation (Eq. (23)) is not a function of ellipticity. In fact, the results of the simulations suggest that this parameter is only slightly dependent on the ellipticity (See Table G.4 in Appendix G). This is due to existence of two opposing factors. On the one hand, increasing the ellipticity increases the film thickness (See

Tables G.2 and G.3 in Appendix G), which results in less asperity interaction. On the other hand, increasing the ellipticity yields a smaller contact pressure which increases the ratio of the load carried by the asperities. The contribution of these two factors may result in increasing or decreasing the asperity load ratio. However, the results of our simulations show that these opposing factors nearly cancel each other, and therefore the asperity load ratio is not highly influenced by the ellipticity parameter.

It is important to mention that the modified Reynolds equation by Patir and Cheng [16] is valid for the film parameter values ($\Lambda=h_{min}/\sigma=H_{min}/\bar{\sigma}$) greater than 0.5. Therefore, the film parameter should be checked after calculating the film thickness from the present formulas to ensure the validity of the results. For the same reason, the regression analysis is only done with the results of simulations satisfying this condition (the film parameter of each case is shown in the tables). It is also advised that when the obtained asperity load ratio from Eq. (23) is very large (typically more than about 70%), the results should be used with caution, even if the film parameter is within the valid range [33]. This is because the behavior of the problem becomes close to dry contact at these cases. This condition generally occurs at very rough surfaces under low load.

An illustrative example: Consider a deep groove ball bearing (Fig. 5.7) with the inner raceway radius of R_i=50 mm and outer raceway radius of R_o=72.5 mm. The radii of the balls and the grooves are R_b=11 mm and R_g=12 mm. Therefore, the equivalent contact radii are calculated as $R_x=(1/11+1/50)^{-1}$=9 mm and $R_y=(1/11-1/12)^{-1}$=132 mm at the inner race and $R_x=(1/11-1/72.5)^{-1}$=13 mm and $R_y=(1/11-1/12)^{-1}$=132mm at the outer race. This gives $D=R_y/R_x$ =14.7 for the inner race and D=10.2 for the outer race contact. Therefore, from Eq. (9), the contact ellipticity is κ=5.7 for the inner race and κ=4.6 for the outer race.

The shaft (and therefore inner race) rotational speed is 2000 RPM (ω=209.4 rad/s), while the outer race is fixed. It gives the orbital speed of ω_m=86 rad/s and roller rotational speed of ω_b=564 rad/s which yields the rolling speed of u=6.2 m/s at both inner and outer race contact. For more information about calculating the speeds, the reader is referred to Ref. [45]. It is also assumed that the bearing is under a radial load where a maximum normal load of F=500N is applied on each ball.

The bearing surfaces (both balls and grooves) are polished with the surface roughness of σ=0.1 μm which gives the combined roughness of 0.14 μm. The contact material is stainless steel with the effective Young's modulus of E'=226 GPa and the Vickers hardness of the surfaces is 600 Kg/mm^2 (5.89 GPa). Also, the lubricant has the inlet viscosity of μ_0=0.03 Pa.s and pressure-viscosity coefficient of α= 2×10^{-8} m^2/N.

Considering the above data, Eq. (7) yields $W=2.73\times10^{-5}$, $U=9.14\times10^{-11}$, and $\bar{\sigma}=1.56\times10^{-5}$ for the inner race contact and $W=1.31\times10^{-5}$, $U=6.33\times10^{-11}$, and $\bar{\sigma}=1.08\times10^{-5}$ for the outer race contact.

Also, G=4520 and V=0.026 are obtained. Substituting the dimensionless values into equations (21) and (22) yields H_c=8.87×10^{-5} and H_{min}=7.47×10^{-5} at the inner race, so h_c=0.80 μm and h_{min}=0.67 μm. For the outer race, H_c=7.09×10^{-5} and H_{min}=5.95×10^{-5}, so h_c=0.91 μm and h_{min}=0.77 μm. The film parameter is obtained as $\Lambda=h_{min}/\sigma$=4.79 for the inner race and Λ =5.51 for the outer race. Also, equation (23) yields an asperity load ratio of L_a=0.05% for the inner race and L_a=0.03% for the outer race which means that the asperity contact is negligible due to high speed and low surface roughness.

Now consider that the shaft rotational speed is one tenth of the previous case (200 RPM). This gives the rolling speed of 0.62 m/s, therefore the dimensionless speed is obtained as U=9.14×10^{-12} at the inner race and U=6.33×10^{-12} at the outer race. In this case, the formulas give H_c=1.98×10^{-5} and H_{min}=1.81×10^{-5} at the inner race, so h_c =0.18 μm and h_{min}=0.16 μm. For the outer race, H_c=1.59×10^{-5} and H_{min}=1.44×10^{-5}, so h_c =0.20 μm and h_{min}=0.19 μm. The film parameter is obtained as $\Lambda=h_{min}/\sigma$=1.16 for the inner race and Λ =1.33 for the outer race which shows that mixed lubrication regime prevails. The asperity load ratio is obtained as L_a=12.09% for the inner race and L_a=10.33% for the outer race which confirms the presence of asperity contact.

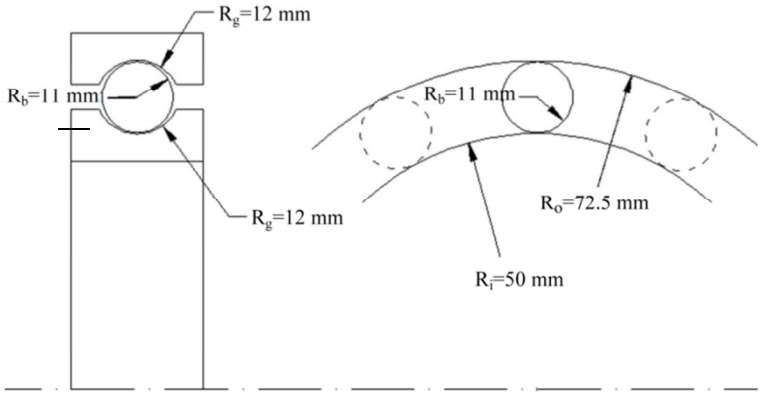

Fig. 5.7. Ball bearing configuration

5.6. Verifications of the Results

5.6.1. Smooth surfaces

Comparison with Hamrock & Dowson's formulas: In this section, the results from the present curve-fit formulas for the smooth surface (Eqs. (19) and (20)) are compared with those by Hamrock & Dowson [3]. Both the central and the minimum film thickness are compared for two different ellipticity values (κ=1 and κ=6) for a range of dimensionless speed which are shown in Fig 5.8.

As shown, the present curve-fit expressions are in agreement with those by Hamrock & Dowson well [3]. The difference between the results may be due to the fact that a different form of expression is utilized in the current study to enhance the accuracy. Also, more number of nodes as well as a wider domain is used in the current simulations compared to those by Hamrock & Dowson. Moreover, the current regression analyses are performed using a larger number of simulation cases.

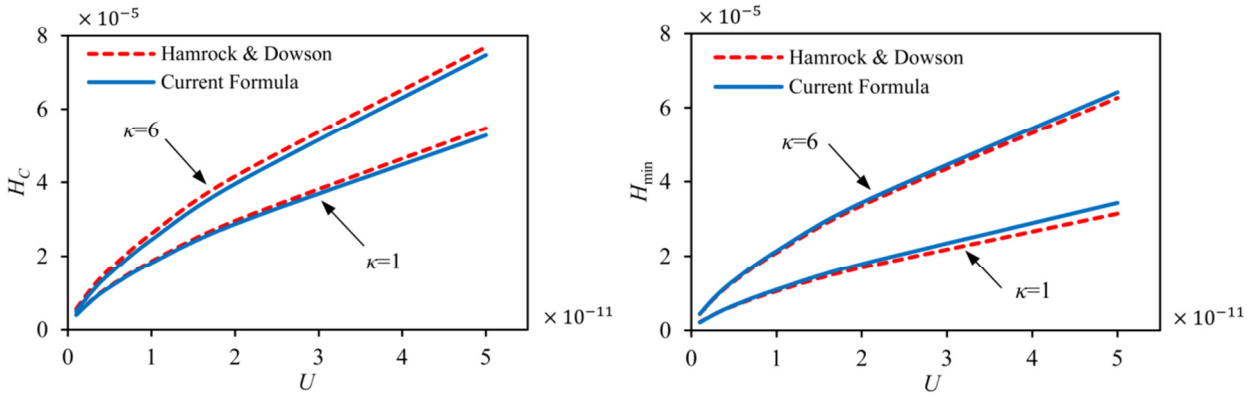

(a) (b)

Fig. 5.8. Comparison between present film thickness formulas for smooth surface and formula by Hamrock & Dowson [3] (W=1×10^{-6}, G=4972)
(a) central film thickness (Eq. (19)) (b) minimum film thickness (Eq. (20))

Comparison with experimental results: Koye & Winer [46] conducted a set of experiments to measure the minimum film thickness in point-contact EHL. They showed that the curve-fit formula by Hamrock & Dowson [3] followed the experimental results well. In Table 5.3, their experimental results are compared with those obtained from the present curve-fit expression for the minimum film thickness (Eq. (20)) as well as those by Hamrock and Dowson's formula [3].

As shown, the current results from the film thickness formula (Eq. (20)) follow the experimental results. In fact, the agreement between Eq. (20) and the experiments is better than that between Hamrock & Dowson's formula and the experiments. In Table 3.5, the average error of Eq. (20) with respect to experimental data is 6.7%, while it is 11.4% for Hamrock & Dowson's formula compared to experiments.

To explore the source of relatively large error of our formula compared to experiments in a few cases of Table 3.5 (12.07% at case #3, 19.46% at case #9, and 11.88% at case #11), these cases were solved numerically. The results of the simulations showed the associated error of 14.8% at case #3, 20% at case #9, and 1.3% at case #11. This implies that the source of error in case #3 & #9 is not due to curve-fitting. However, it seems that the error in case #11 is coming from the expression. It should be mentioned that the experimental tests [46] were conducted under the

dimensionless material number of G=10451 which is larger than the maximum value used in the regression analyses of the current study and those by Hamrock & Dowson. Therefore, the results from the expressions should be taken by caution.

Table 5.3. Comparison between experiments [46], Hamrock & Dowson's formula [3], and current results (Eq. (20))

Case No.	κ	W	U	H_{min} from experiment	H_{min} from Eq. (20)	Error of Eq. (20)	H_{min} by Ref. [3]	Error of Ref. [3]
1	3.7	1.61×10^{-6}	3.53×10^{-11}	6.85×10^{-5}	7.21×10^{-5}	5.33	6.43×10^{-5}	6.16
2	3.7	1.61×10^{-6}	6.33×10^{-11}	1.11×10^{-4}	1.08×10^{-4}	2.92	9.56×10^{-5}	14.01
3	3.7	1.61×10^{-6}	8.80×10^{-11}	1.21×10^{-4}	1.35×10^{-4}	12.07	1.20×10^{-4}	1.05
4	3.7	5.31×10^{-6}	3.53×10^{-11}	7.06×10^{-5}	6.61×10^{-5}	6.44	5.89×10^{-5}	16.54
5	3.7	5.31×10^{-6}	6.33×10^{-11}	1.04×10^{-4}	9.88×10^{-5}	4.70	8.76×10^{-5}	15.48
6	3.7	5.30×10^{-6}	8.80×10^{-11}	1.32×10^{-4}	1.24×10^{-4}	5.80	1.10×10^{-4}	16.73
7	2.4	9.68×10^{-7}	3.48×10^{-11}	6.44×10^{-5}	6.60×10^{-5}	2.54	5.78×10^{-5}	10.21
8	2.4	9.68×10^{-7}	6.25×10^{-11}	9.50×10^{-5}	9.93×10^{-5}	4.54	8.61×10^{-5}	9.36
9	2.4	9.68×10^{-7}	8.69×10^{-11}	1.05×10^{-4}	1.25×10^{-4}	19.46	1.08×10^{-4}	3.00
10	2.4	3.26×10^{-6}	3.48×10^{-11}	6.03×10^{-5}	6.00×10^{-5}	0.50	5.29×10^{-5}	12.25
11	2.4	3.26×10^{-6}	6.25×10^{-11}	1.02×10^{-4}	9.02×10^{-5}	11.88	7.88×10^{-5}	23.05
12	2.4	3.26×10^{-6}	8.69×10^{-11}	1.09×10^{-4}	1.14×10^{-4}	4.44	9.86×10^{-5}	9.30

5.6.2. Rough surfaces

In this section, the results from the present curve-fit formulas for the film thickness and asperity load ratio in rough point-contact EHL are compared with the simulations results by and Zhu & Wang [26] and Zhu & Hu [23] which are both based on deterministic method for characterizing the surface roughness. In deterministic treatment of surface roughness, an actual surface profile (or a randomly-generated surface profile using a given surface roughness value) is directly entered into the deformation equations. As a result, the obtained film thickness profile in such studies has fluctuations and therefore its average value within a specific distance from the contact center is reported as the mean film thickness.

Figure 5.9 (a) shows the comparison between the results of the present curve-fit formula for central film thickness (Eq. (19) & (21)) and those obtained in deterministic simulations by Zhu & Wang [26]. The input is κ=2, maximum Hertzian pressure of 2.277 GPa (equal to W=5.3×10^{-5}), G=2830 and $\bar{\sigma}$=4.7×10^{-5}. In the study by Zhu & Wang, the rolling speed is varied and the rough-to-smooth film thickness ratio is plotted against the ratio of the central film thickness (smooth) to the surface roughness. In their study [26], the rough-to-smooth ratio of the film thickness (vertical axis) is obtained using their simulations while the smooth film thickness in the horizontal axis is obtained by Hamrock & Dowson's formula [3]. In the current study, the results from the present smooth central film thickness formula (Eq. (19)) is used for the horizontal axis

while the results from the present rough and smooth central film thickness formulas (Eq. (19) and (21)) are used for the vertical axis.

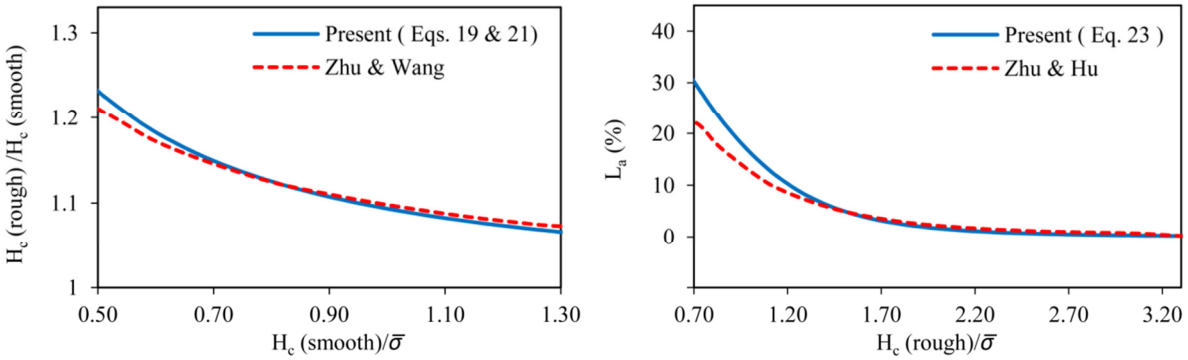

(a) (b)

Fig. 5.9. Verification of present formulas for rough surfaces
(a) results from central film thickness formula (Eq. (21)) and simulations by Zhu & Wang [26] (κ=2, W=5.3×10^{-5}, G=2830, $\bar{\sigma}$=4.7×10^{-5})
(b) results from asperity load ratio formula (Eq. (23)) and simulations by Zhu & Hu [23] (κ=1, W=1.008×10^{-5}, G=4000, $\bar{\sigma}$=2.1×10^{-5})

As shown in Fig. 5.9 (a), the results from the current formulas are in close agreement with the simulation results by Zhu & Wang. At H_c (smooth)/$\bar{\sigma}$ = 0.5 (occurs at U=2.40×10^{-11}), their simulation shows the rough-to-smooth film ratio of 1.21 while the present formulas predict it as 1.23. Also, at H_c (smooth)/$\bar{\sigma}$ = 1.3 (U=1×10^{-10}), both their simulation and current formulas show this ratio is about 1.07.

It should be noted that in Fig. 5.9 (a), the minimum value of horizontal axis is chosen as H_c (smooth)/$\bar{\sigma}$ = 0.5, since at this point the film parameter Λ=H_{min}/$\bar{\sigma}$ (where H_{min} can be obtained from Eq. (22)) is obtained as Λ =0.51. This is close to the critical value of 0.5 below which using the modified Reynolds equation by Patir & Cheng [16] is not recommended.

It is worthwhile to mention that the current film thickness formula (Eq. (21)) gives the central value of the film thickness which is the distance between the mean lines of two rough surfaces at the center of the contact (statistical approach). In Fig. 5.9 (a), this value is compared to the mean value of film thickness in the study by Zhu & Wang which is obtained by averaging the film thickness within the half radius from the center of normalized Hertzian contact zone (deterministic approach).

To verify the obtained asperity load ratio, the results from the current formula (Eq. (23)) are compared to those reported by Zhu & Hu [23]. Figure 5.9 (b) shows this comparison. The input

used in their study is κ=1, W=1.008×10^{-5}, G=4000, and $\bar{\sigma}$=2.10×10^{-5}. Here, the horizontal axis shows the ratio of the average rough film thickness (equivalent to central film thickness in the current study) to the surface roughness.

As shown, the results from the current curve-fit expression (Eq. (23)) are in agreement with the simulation results by Zhu & Hu. However, at lower film thickness values, the present formula predicts a higher asperity load ratio. In Fig. 5.9 (b), the maximum difference between the predicted asperity load ratios is about 8% (at $H_c/\bar{\sigma}$=0.70 occurs at U=7.6×10^{-12}) where their simulation shows L_a=22% and the present formula (Eq. (23)) predicts L_a=30%. This difference becomes less than 3% after $H_c/\bar{\sigma}$=1. Note that in Fig. 5.9 (b), the minimum value of horizontal axis is chosen as H_c (rough)/$\bar{\sigma}$ = 0.70, because the film parameter ($\Lambda = H_{min}/\bar{\sigma}$) at this point reaches the critical value of 0.5.

It should be mentioned that since the surface hardness is not reported in neither of the studies by Zhu & Wang [26] and Zhu & Hu [23], a dimensionless hardness of 0.01 (equal to about 20 Rockwell C) is used as input in the current formulas.

The agreement between the results of the present study and the studies by Zhu & Wang [26] and Zhu & Hu [23] is especially interesting because of the inherently different approach employed. While the current formulas are based on the result of simulations with statistical treatment of the surface asperities, the method used in both studies by Zhu & Wang and Zhu & Hu are based on the deterministic method. However, despite this difference, it is shown that both methods predict close results. While the deterministic approach has the advantage of going through boundary lubrication regime (lower lambda ratios), the main advantage of using the formulas reported in this paper is that the film thickness and asperity load ratio can be readily predicted without the need of going through the numerical simulations.

5.6.3. Comparison with Line-Contact EHL Results

In the study by Hamrock & Dowson [2], it was demonstrated that at the ellipticity of κ=8, the film thickness obtained by point-contact EHL solution becomes close to that obtained from line-contact solution. Here, the results from the present film thickness and asperity load ratio formulas for rough point-contact EHL (Eqs. (21-23)) at κ=8 are compared with those presented by the authors for rough line-contact EHL [33].

In order to be able to compare the point contact and line contact results, an equivalent load should be used since the dimensionless load in line contact ($W_{line}=F/BE'R$) contains the contact length (B). Therefore, for a given point-contact problem with κ=8 and given load, the Hertzian contact length ($2a$) is calculated using Eq. (8) and put as the contact length B. That is:

$$W_{\text{point}} = \frac{F}{E'R_x^{\,2}},\quad W_{\text{line}} = \frac{F}{BE'R_x} = \frac{W_{\text{point}}E'R_x^{\,2}}{2aE'R_x} = \frac{W_{\text{point}}R_x}{2a} = \frac{W_{\text{point}}R_x}{2\kappa b} = \frac{W_{\text{point}}}{2\kappa\gamma} \tag{24}$$

where γ is obtained from Eq. (8) using the given load (W_{point}) and ellipticity (κ=8).

Figure 5.10 illustrate the comparison between the results of the current formulas for point-contact EHL (Eqs. (21-23)) at ellipticity of κ=8 and those for line-contact EHL presented in Ref. [33]. The central and the minimum film thickness as well as the asperity load ratio are compared. The input used is fixed at $W_{\text{point}}=3\times10^{-5}$ (equivalent to $W_{\text{line}}= 9.8\times10^{-5}$), G=4972, $\bar{\sigma}=2\times10^{-5}$, and V=0.01, The dimensionless speed is varied along the horizontal axis between $U=3\times10^{-12}$ (below which the film parameter become smaller than the critical value of 0.5) to $U=5\times10^{-11}$ (beyond which there is almost no effect of surface roughness).

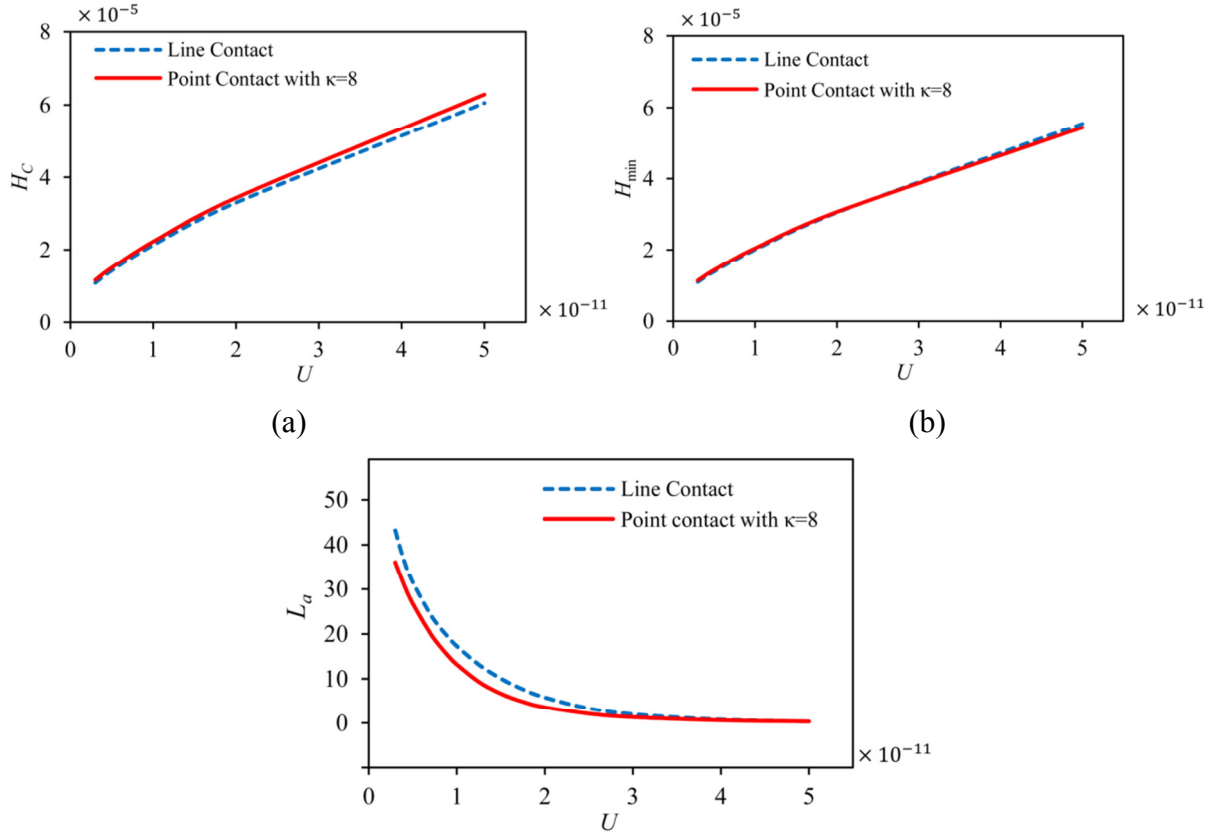

Fig. 5.10. Comparison between point-contact EHL formulas with κ=8 and line-contact EHL formulas [33] ($W_{\text{point}}=3\times10^{-5}$, $W_{\text{line}}=9.8\times10^{-5}$, G=4972, $\bar{\sigma}=2\times10^{-5}$, V=0.01)
(a) central film thickness (b) minimum film thickness (c) asperity load ratio

As depicted in Fig. 5.10, at ellipticity of κ=8, the results obtained from point-contact EHL formulas (Eqs. (21-23)) are in good agreement with those obtained from line-contact EHL

formulas presented in Ref. [33]. Therefore, based on the results of this study, it is suggested that for the ellipticity range of κ=1 (spherical contact) to κ=8, point-contact formulas (Eqs. (21-23)) can be utilized, while for ellipticity values above κ=8 (equivalent to $D=R_y/R_x>25.3$), line-contact formulas [33] can be used.

5.7. Conclusions

In this paper, a model is developed to investigate the effect of surface roughness in elastohydrodynamic lubrication of elliptical contacts. The modified Reynolds, surface deformation and elasto-plastic asperity contact equations are simultaneously solved in dimensionless form. The results of an extensive set of simulations are then used to obtain the following curve-fit expressions for the film thickness and asperity load ratio as:

Central film thickness:

$$H_c = 3.672\, W^{-0.045\kappa^{0.18}} U^{0.663\kappa^{0.025}} G^{0.502\kappa^{0.064}} (1 - 0.573\, e^{-0.74\kappa})(1 + 0.025\, \bar{\sigma}^{1.248} V^{0.119} W^{-0.133} U^{-0.884} G^{-0.977} \kappa^{0.081})$$

Minimum film thickness:

$$H_{\min} = 1.637\, W^{-0.09\kappa^{-0.15}} U^{0.711\kappa^{-0.023}} G^{0.65\kappa^{-0.045}} (1 - 0.974 e^{-0.676\kappa})(1 + 0.141\, \bar{\sigma}^{1.073} V^{0.149} W^{-0.044} U^{-0.828} G^{-0.954} \kappa^{-0.395})$$

Asperity load ratio:

$$L_a = 10\, W^{-0.083} U^{0.143} G^{0.314} [\ln (1 + \bar{\sigma}^{4.689} V^{0.509} W^{-0.501} U^{-2.90} G^{-2.870})]$$

The results from these formulas are shown to be in agreement with the results presented in other publications for both smooth and rough surfaces. It is also shown that at higher ellipticity values, the results of point-contact EHL become close to those of line-contact EHL.

The present formulas have the advantage of being easy-to-use without the need of performing extensive numerical simulations. Using these formulas, one can readily predict the film thickness and therefore the film parameter for various operating conditions. This will determine if the machine elements are working within the safe conditions or they are prone to reach the boundary lubrication regime and ultimate failure. The asperity load ratio equation is also a key factor for calculating the friction and the wear.

Nomenclature

a	half Hertzian length, m
b	half Hertzian width, m
B	line-contact length, m
D	$R_{y/}R_x$
E'	effective modulus of elasticity, $1/E'=0.5[(1-\nu_1^2)/E_1+(1-\nu_2^2)/E_2]$, Pa

F	normal load, N
G	dimensionless material number, $E'\alpha$
h	film thickness, m
h^*	h/σ
h_c	central film thickness, m
h_{min}	minimum film thickness, m
h_T	average gap between two surfaces, m
H	dimensionless film thickness, h/R_x
H_c	dimensionless central film thickness, h_c/R_x
H_{min}	dimensionless minimum film thickness, h_{min}/R_x
H_T	dimensionless average gap between two surfaces, h_T/R_x
L_a	asperity load ratio (percentage)
n	asperity density, m^{-2}
$\bar{n}$	dimensionless asperity density, nR^2
p	total pressure, Pa
p_a	asperity pressure, Pa
p_h	hydrodynamic pressure, Pa
P	dimensionless total pressure
P_a	dimensionless asperity pressure
P_h	dimensionless hydrodynamic pressure
R_x	equivalent contact radius in x direction, $[1/R_{1x}\pm1/R_{2\,x}]^{-1}$, m
R_y	equivalent contact radius in y direction, $[1/R_{1y}\pm1/R_{2\,y}]^{-1}$, m
u	rolling speed, $(u_1+u_2)/2$, m/s
U	dimensionless speed number, $\mu_0 u/E'R_x$
v	Vickers hardness, Pa
V	dimensionless hardness number, v/E'
w_1	critical interference at the point of initial yield, $(0.6\pi.v/E)^2\beta$, m
$\bar{w_1}$	w_1/R_x
w_1^*	w_1/σ
w_2	critical interference at the point of fully plastic flow, $54w_1$, m
$\bar{w_2}$	w_2/R_x
w_2^*	w_2/σ
W	dimensionless load number, $F/E'R_x^2$
x	coordinate in moving direction, m
y	coordinate perpendicular to moving direction, m
X	dimensionless coordinate in moving direction, x/b
Y	dimensionless coordinate perpendicular to moving direction, y/a
y_s	distance between the mean line of the surface and the mean line of its summits, m
$\bar{y}_s$	y_s/R_x
y_s^*	y_s/σ
z	height of asperities measured from the mean line of the summits, m
z^*	z/σ
Z	viscosity-Pressure index
α	pressure-viscosity coefficient, m^2/N

β	asperity radius, m
$\bar{\beta}$	dimensionless asperity radius, β/ R_x
γ	b/ R_x
κ	ellipticity parameter, a/b
Λ	film parameter, h_{min}/σ
μ	lubricant viscosity, Pa.s
μ_0	lubricant viscosity at zero pressure, Pa.s
$\bar{\mu}$	dimensionless viscosity, μ/μ_0
ρ	lubricant density, kg/m^3
ρ_0	lubricant density at zero pressure, kg/m^3
$\bar{\rho}$	dimensionless density, ρ/ρ_0
σ	standard deviation of the surface heights, m
$\bar{\sigma}$	dimensionless surface roughness, σ/R_x
σ_s	standard deviation of the surface summits, m
$\bar{\sigma}_s$	σ_s/R_x
φ_x	pressure flow factor in x direction
φ_y	pressure flow factor in y direction

5.8. References

[1] Hamrock BJ, Dowson D. Isothermal Elastohydrodynamic Lubrication of Point Contacts .1. Theoretical Formulation. J Lubric Tech-T Asme. 1976;98:223-9.

[2] Hamrock BJ, Dowson D. Isothermal Elastohydrodynamic Lubrication of Point Contacts .2. Ellipticity Parameter Results. J Lubric Tech-T Asme. 1976;98:375-83.

[3] Hamrock BJ, Dowson D. Isothermal Elastohydrodynamic Lubrication of Point Contacts .3. Fully Flooded Results. J Lubric Tech-T Asme. 1977;99:264-76.

[4] Hooke CJ. The Elastohydrodynamic Lubrication of Heavily Loaded Point Contacts. J Mech Eng Sci. 1980;22:183-7.

[5] Evans HP, Snidle RW. The Elastohydrodynamic Lubrication of Point Contacts at Heavy Loads. P Roy Soc Lond a Mat. 1982;382:183-99.

[6] Venner CH. Multilevel Solution of the EHL Line and Point Contact Problems. PhD Thesis, University of Twente, Enschede, The Netherland. 1991.

[7] Nijenbanning G, Venner CH, Moes H. Film Thickness in Elastohydrodynamically Lubricated Elliptic Contacts. Wear. 1994;176:217-29.

[8] Venner CH, Lubrecht AA. Multigrid techniques: a fast and efficient method for the numerical simulation of elastohydrodynamically lubricated point contact problems. P I Mech Eng J-J Eng. 2000;214:43-62.

[9] Jalali-Vahid D, Rahnejat H, Jin ZM. Elastohydrodynamic solution for concentrated elliptical point contact of machine elements under combined entraining and squeeze-film motion. P I Mech Eng J-J Eng. 1998;212:401-11.

[10] Liu Y, Wang QJ, Bair S, Vergne P. A quantitative solution for the full shear-thinning EHL point contact problem including traction. Tribol Lett. 2007;28:171-81.

[11] Chapkov AD, Bair S, Cann P, Lubrecht AA. Film thickness in point contacts under generalized Newtonian EHL conditions: Numerical and experimental analysis. Tribol Int. 2007;40:1474-8.

[12] Kumar P, Khonsari MM. EHL circular contact film thickness correction factor for shear-thinning fluids. J Tribol-T Asme. 2008;130.

[13] Kumar P, Khonsari MM. On the role of lubricant rheology and piezo-viscous properties in line and point contact EHL. Tribol Int. 2009;42:1522-30.

[14] Katyal P, Kumar P. Central film thickness formula for shear thinning lubricants in EHL point contacts under pure rolling. Tribol Int. 2012;48:113-21.

[15] Zhu D, Cheng HS. Effect of Surface Roughness on the Point Contact Ehl. J Tribol-T Asme. 1988;110:32-7.

[16] Patir N, Cheng HS. Average Flow Model for Determining Effects of 3-Dimensional Roughness on Partial Hydrodynamic Lubrication. J Lubric Tech-T Asme. 1978;100:12-7.

[17] Greenwood JA, Tripp, J.H. . The Contact of Two Nominally Flat Rough Surfaces. Proc Inst Mech Eng. 1971;185:625–33

[18] Kaneta M, Sakai T, Nishikawa H. Effects of Surface-Roughness on Point-Contact Ehl. Tribol T. 1993;36:605-12.

[19] Kweh CC, Patching MJ, Evans HP, Snidle RW. Simulation of Elastohydrodynamic Contacts between Rough Surfaces. J Tribol-T Asme. 1992;114:412-9.

[20] Chang L. A Deterministic Model for Line-Contact Partial Elastohydrodynamic Lubrication. Tribol Int. 1995;28:75-84.

[21] Jiang XF, Hua DY, Cheng HS, Ai XL, Lee SC. A mixed elastohydrodynamic lubrication model with asperity contact. J Tribol-T Asme. 1999;121:481-91.

[22] Hu YZ, Zhu D. A full numerical solution to the mixed lubrication in point contacts. J Tribol-T Asme. 2000;122:1-9.

[23] Zhu D, Hu YZ. A computer program package for the prediction of EHL and mixed lubrication characteristics, friction, subsurface stresses and flash temperatures based on measured 3-D surface roughness. Tribol T. 2001;44:383-90.

[24] Deolalikar N, Sadeghi F, Marble S. Numerical modeling of mixed lubrication and flash temperature in EHL elliptical contacts. J Tribol-T Asme. 2008;130.

[25] Zhu D, Wang QJ. On the lambda ratio range of mixed lubrication. P I Mech Eng J-J Eng. 2012;226:1010-22.

[26] Zhu D, Wang QJ. Effect of Roughness Orientation on the Elastohydrodynamic Lubrication Film Thickness. J Tribol-T Asme. 2013;135.

[27] Wang QJ, Zhu D, Cheng HS, Yu TH, Jiang XF, Liu SB. Mixed lubrication analyses by a macro-micro approach and a full-scale mixed EHL model. J Tribol-T Asme. 2004;126:81-91.

[28] Lu XB, Khonsari MM, Gelinck ERM. The Stribeck curve: Experimental results and theoretical prediction. J Tribol-T Asme. 2006;128:789-94.

[29] Akbarzadeh S, Khonsari MM. Performance of spur gears considering surface roughness and shear thinning lubricant. J Tribol-T Asme. 2008;130:021503.

[30] Sojoudi H, Khonsari MM. On the Behavior of Friction in Lubricated Point Contact With Provision for Surface Roughness. J Tribol-T Asme. 2010;132.

[31] Johnson KL, Greenwood JA, Poon SY. Simple Theory of Asperity Contact in Elastohydrodynamic Lubrication. Wear. 1972;19:91-108.

[32] Greenwood JA, Tripp JH. Elastic Contact of Rough Spheres. J Appl Mech. 1967;34:153-&.

[33] Masjedi M, Khonsari MM. Film Thickness and Asperity Load Formulas for Line-Contact Elastohydrodynamic Lubrication With Provision for Surface Roughness. J Tribol-T Asme. 2012;134:011503.

[34] Masjedi M, Khonsari MM. Mixed elastohydrodynamic lubrication line-contact formulas with different surface patterns. Proceedings of the Institution of Mechanical Engineers, Part J: Journal of Engineering Tribology. 2014;228:849–59.

[35] Masjedi M, Khonsari MM. Theoretical and experimental investigation of traction coefficient in line-contact EHL of rough surfaces. Tribol Int. 2014;70:179-89.

[36] Zhao YW, Maietta DM, Chang L. An Asperity Microcontact Model Incorporating the Transition from Elastic Deformation to Fully Plastic Flow. J Tribol-T Asme. 2000;122:86-93.

[37] Khonsari MM, Booser ER. *Applied tribology : bearing design and lubrication*. 2nd ed. Chichester, England ; Hoboken, NJ: Wiley; 2008.

[38] Dowson D, Higginson GR. *Elasto-hydrodynamic lubrication*. SI ed. Oxford Eng., New York: Pergamon Press; 1977.

[39] Roelands CJA. *Correctional Aspects of the Viscosity-Temperature- Pressure Relationship of Lubricating Oils*. Druk, V.R.B., Groningen, Netherlands1966.

[40] Hamrock BJ. *Fundamentals of Fluid Film Lubrication*. New York: McGraw-Hill; 1994.

[41] Timoshenko S, Goodier JN. *Theory of Elasticity*. 3d ed. New York,: McGraw-Hill; 1969.

[42] Beheshti A, Khonsari MM. Asperity micro-contact models as applied to the deformation of rough line contact. Tribol Int. 2012;52:61-74.

[43] Serest AE, Akbarzadeh S. Mixed-elastohydrodynamic analysis of helical gears using load-sharing concept. P I Mech Eng J-J Eng. 2014;228:320-31.

[44] Gelinck ERM, Schipper DJ. Deformation of Rough Line Contacts. J Tribol-T Asme. 1999;121:449-54.

[45] Harris TA. Rolling bearing analysis. 4th ed. New York: Wiley; 2001.

[46] Koye KA, Winer WO. An Experimental Evaluation of the Hamrock and Dowson Minimum Film Thickness Equation for Fully Flooded Ehd Point Contacts. J Lubric Tech-T Asme. 1981;103:284-94.

Chapter 6: A Study on the Effect of Starvation in Mixed Elastohydrodynamic Lubrication*

6.1. Introduction

Lubrication regime in many industrial applications is governed by the elastohydrodynamic lubrication (EHL). In such applications, when the lubricant quantity is sufficient to fill the contact's inlet, the lubrication regime is called fully-flooded. However, inadequate lubricant supply at the inlet's conjunction results in a lower flow rate of the lubricant that is necessary and the contact is said to be starved. Starved lubrication directly influences the thickness of the lubricant film and increases the asperity interactions that tend to expedite wear which if excessive can ultimately lead to failure.

One of the earliest studies on the starved EHL was performed by Hamrock and Dowson [1, 2]. Following their approach for solving the point-contact EHL problem [1], they studied the effect of starvation on the film thickness [2]. They simulated the starved condition by moving the contact inlet toward the center and proposed correction factors for the film thickness as a function of the inlet distance. Later, Chevalier et al. [3] related the starvation to the amount of the lubricant available at the inlet and investigated the reduction in the film thickness in the contact area as a function of the decrease in the film thickness at the inlet. This approach was later followed by Damiens et al. [4] and Cann et al. [5] who investigated the effect of operating parameters on the starvation in point contacts. The effect of starvation in line contact is reported by Yang et al. [6] who investigated the variations of the film thickness and traction coefficient due to the change of the inlet distance. Later, Kumar & Khonsari [7] conducted a study on the effect of starvation on line-contact EHL of shear-thinning lubricants. By defining the starvation degree as a function of the reduction in the mass flow rate at the contact center, they proposed correction factors for the film thickness and the traction coefficient as function of the starvation degree. Recently, Ali et al. [8, 9] investigated the traction in the starved point-contact EHL where they conducted experiments to determine the change in the traction coefficient as a function of the quantity of oil at the inlet. Additionally, experimental results are also reported by Svoboda at al. [10] who measured the starved film thickness based on the thickness of the oil at the inlet. A review of the existing literature reveals that the vast majority of the available results on the lubricant starvation are devoted to smooth surfaces. One of the very few studies on the starvation in mixed EHL was performed by Faraon and Schipper [11]. They used the so-called

* Reprinted by permission of *Elsevier* (See Appendix I)

load sharing concept together with an approximate expression for the line-contact film thickness at the inlet to obtain Stribeck-type curves as functions of the film parameter at the inlet.

Despite the importance of the starvation in the elastohydrodynamic lubrication, only a few numbers of studies have been devoted to this topic, especially within the context of the mixed EHL. In the present study, the numerical approach conducted by the authors that includes the effect of surface roughness in line-contact [12] and point-contact EHL [13] is extended to take lubricant starvation into account. As mentioned earlier, the degree of starvation can be stated in terms of the inlet distance for both point contact [2] and line contact [6, 14]. However, this definition does not convey a physical understanding of the phenomenon. For point-contact EHL, the starvation can be described in terms of the thickness of the oil layer at the inlet [3-5]. However, this method does not seem to be suitable for line contact because of the assumption of infinite contact width (See ref. [14]). In the current study, the starvation is treated in terms of the reduction in the mass flow rate as defined in Ref. [7]. This definition has the advantage of being applicable to both the line-contact and point-contact EHL as well as conveying the physical meaning of the phenomenon. Using this definition, the influence of the starvation on the pressure distributions and film profiles is investigated in the mixed EHL regime. Subsequently, by performing regression analyses based on the results of a wide range of simulations, appropriate formulas are presented (for both line contact and point contact) to predict the asperity load ratio as well as the reduction in the central and minimum film thickness in the starved mixed EHL regime.

6.2. Model

The authors developed a model to obtain the film thickness and asperity load in the elastohydrodynamic lubrication of rough surfaces for both line contact [12] and point contact [13]. These models are based on the simultaneous solution to the modified Reynolds equation by Patir & Cheng [15], bulk deformation of the surfaces, load balance, and asperity micro-contact equations suggested by Zhao et al. [16] which considers the elastic, elasto-plastic, and plastic deformation of the asperities. Based on these studies, expressions were developed to predict the film thickness and asperity load ratio where each expression is a function of six dimensionless input parameters: load (W), speed (U), material (G), roughness ($\bar{\sigma}$), hardness (V), and ellipticity (κ). These expressions can be found in Chapter 2 for line contact and Chapter 5 for point contact. For more information about the model, the reader is referred to Refs. [12, 13].

In order to study lubricant starvation, the mass flow must be evaluated. The velocity profile of a Newtonian lubricant across the film can be determined from the following equation:

$$u = \frac{u_2 - u_1}{h} z + u_1 + \frac{1}{2\mu} \frac{\partial p_h}{\partial x} (z^2 - hz) \tag{1}$$

where u_1 and u_2 are the velocities of the contacting surfaces and x and z represent the coordinate along the moving direction and across the film, respectively. Parameter p_h is the hydrodynamic pressure, h is the lubricant film thickness, and μ is the lubricant viscosity.

The mass flow rate in a section can be obtained by integrating the velocity profile as:

$$\dot{m} = \iint \rho u dA = \iint \rho \left(\frac{u_2 - u_1}{h} z + u_1 + \frac{1}{2\mu} \frac{\partial p_h}{\partial x} (z^2 - hz) \right) dz dy \tag{2}$$

where ρ represents the lubricant density and y is the coordinate perpendicular to the moving direction in the contact plane. Assuming that the pressure, viscosity, and density are constant across the film (along z direction), the flow rate can be written as:

$$\dot{m} = u_r \int \rho h dy - \frac{1}{12} \int \frac{\rho h^3}{\mu} \frac{\partial p_h}{\partial x} dy \tag{3}$$

where $u_r=(u_1+u_2)/2$ is the rolling speed. Note that parameters ρ, μ, h, and $\frac{\partial p_h}{\partial x}$ vary along both x and y directions; but at a specific x location, they are only functions of y.

For line-contact EHL where the contact is uniform along the y direction, the mass flow rate per contact length reduces to:

$$\frac{\dot{m}}{B} = \int \rho u dz = u_r \rho h - \frac{\rho h^3}{12\mu} \frac{\partial p_h}{\partial x} \tag{4}$$

where B is the contact length. Here, parameters ρ, μ, h, and $\frac{\partial p_h}{\partial x}$ are functions of x, so they are constant at a specific section.

As mentioned earlier, the starvation occurs due to insufficient filling of the inlet conjunction which affects the lubricant flow rate. Thus the starvation degree ξ can be defined as the fractional reduction in the lubricant mass flow rate as [7]:

$$\zeta = 1 - \frac{\dot{m}_S}{\dot{m}_F} \tag{5}$$

where $\dot{m}_F$ and $\dot{m}_S$ denote the mass flow rate in the fully-flooded and the starved conditions, respectively. The starvation degree is zero in the fully-flooded condition and one in the fully-starved condition. To obtain the starvation degree, in this study, the flow rate in both fully-flooded and starved conditions are calculated at the center of the contact using Eq. (3) for point contact and Eq. (4) for line contact. For point contact, since the flow rate is dependent on the contact length in the y direction (perpendicular to the moving direction), it is assumed that only the points with non-zero hydrodynamic pressure contribute to the flow. This assumption is

fulfilled by calculating the flow rate in a cross domain containing the points with the hydrodynamic pressure of larger than one percent of the pressure at the center.

It was previously shown that the dimensionless inlet of X_{min}=-4 is sufficient for achieving the fully-flooded condition (in both line contact and point contact) within the cases studied [12, 13]. However, for more accuracy, X_{min} =-5 is selected in this study for simulating the fully-flooded contact. The starved conditions are achieved by moving the inlet toward the center of the contact. As the inlet area shrinks, the lubricant flow rate decreases and the starvation degree is simulated based on the reduction in the flow rate. The pressure distributions and the film profiles of the starved lubrication are then obtained and compared to the fully-flooded case.

6.3. Results and discussion

6.3.1. Pressure and film distributions

In this section, we first present the typical pressure distributions and film profiles of fully-flooded and starved regimes to show how the starvation affects the characteristics of the mixed elastohydrodynamic lubrication.

6.3.1.1. Line contact

Figure 6.1 shows the hydrodynamic and asperity pressure distributions and the corresponding film profiles in rough line-contact EHL. In these figure, a fully-flooded case (ξ=0) is compared with two starved regimes: 10% starvation (ξ=0.1) and 20% starvation (ξ=0.2). The dimensionless input parameters are: W=5×10^{-5}, U=1×10^{-11}, G=4972, $\bar{\sigma}$=2×10^{-5}, and V=0.01. The selected dimensionless load causes a maximum Hertzian pressure of about 0.64 GPa (for steel). The selected dimensionless roughness corresponds to the roughness of moderately rough surfaces (equal to the combined roughness of about σ=0.5 μm for the effective radius of one inch).

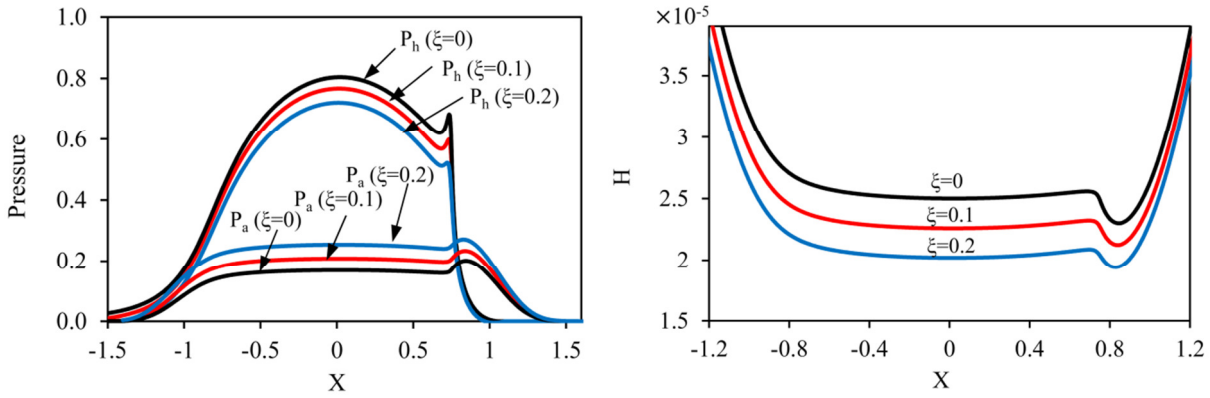

(a) (b)

Fig. 6.1. Fully-flooded and starved regimes in rough line-contact EHL: (a) hydrodynamic and asperity pressure distributions (b) film profiles (W=5×10^{-5}, U=1×10^{-11}, G=4972, $\bar{\sigma}$=2×10^{-5}, and V=0.01)

As shown in Fig. 6.1(a), by starving the inlet, the hydrodynamic part of the pressure, P_h, decreases but the contribution of the asperities to generate contact pressure, P_a, increases. Obviously, this is due to the decrease in the film thickness (shown in Fig. 6.1(b)) which is a direct result of insufficient oil supply in the contact inlet. The simulations show that the asperity load ratio is L_a=23% for the fully-flooded case, while it increases to L_a=28% for the starved regime with ξ=0.1 and L_a=34% for ξ=0.2. Also, the simulations show that the ratio of starved to fully-flooded central film thickness is ϕ_{H_C}=90% for ξ=0.1 and ϕ_{H_C}=81% for ξ=0.2. On the other hand, the ratio of the starved to fully-flooded minimum film thickness is $\phi_{H_{min}}$=92% for ξ=0.1 and $\phi_{H_{min}}$=84% for ξ=0.2.

Due to the reduction of the film thickness in the starved regimes, the film parameter ($\Lambda=h_{min}/\sigma=H_{min}/\bar{\sigma}$) decreases. The simulations show that for the fully-flooded case, the film parameter is Λ=1.15, but it drops to Λ=1.06 for ξ=0.1 and to Λ=0.97 for ξ=0.2. This means that the regime can shift to the boundary lubrication as the degree of starvation increases.

6.3.1.2. Point contact

Figure 6.2 shows the pressure distributions of the fully-flooded and starved regimes and their corresponding film profiles in rough point-contact EHL with the ellipticity of κ=1 (circular contact). The input parameters are W=5×10^{-7} (equal to the maximum Hertzian pressure of 0.66 GPa for steel which is close to the load used above for the line contact), U=1×10^{-11}, G=4972, $\bar{\sigma}$=2×10^{-5}, and V=0.01. As shown in Fig. 6.2(a-b), the asperity pressure increases as the starvation degree increases. The simulations shows that the asperity load ratio is L_a= 43% for the fully-flooded case, while it is L_a= 54% for ξ=0.10 and L_a= 65% for ξ=0.2. As illustrated in Fig. 6.2(c-d), the film thickness decreases as the starvation degree increases. Comparing these results with those in Fig 6.1 reveals that the central film thickness in circular contact is affected more significantly by starvation than that of line contact. The simulations show that the ratio of starved to fully-flooded central film thickness is ϕ_{H_C}=0.80% for ξ=0.10 and ϕ_{H_C}=0.59% for ξ=0.2. However, the minimum film thickness is less affected and the ratio of starved to fully-flooded minimum film thickness is obtained as $\phi_{H_{min}}$=91% for ξ=0.1 and $\phi_{H_{min}}$=0.79% for ξ=0.2.

To have a better understanding of the film distribution, the contour plots of the film thickness in circular contact (κ=1) for a fully-flooded and a starved case (with ξ=0.2) are shown in Fig 6.3. As shown in Fig. 6.3(a), the minimum film thickness in the fully flooded circular contact occurs at the sides (H_{min}=1.73×10^{-5}) which is smaller than the film thickness at the center (H_C=2.21×10^{-5}) as well as the local minimum in Y=0 plane (H=2.04×10^{-5}). On the other hand, in a starved circular contact (ξ=0.2), the film thickness at the center decreases to a level that it becomes the minimum film thickness (H_C=H_{min}=1.36×10^{-5} in Fig 6.3(b)).

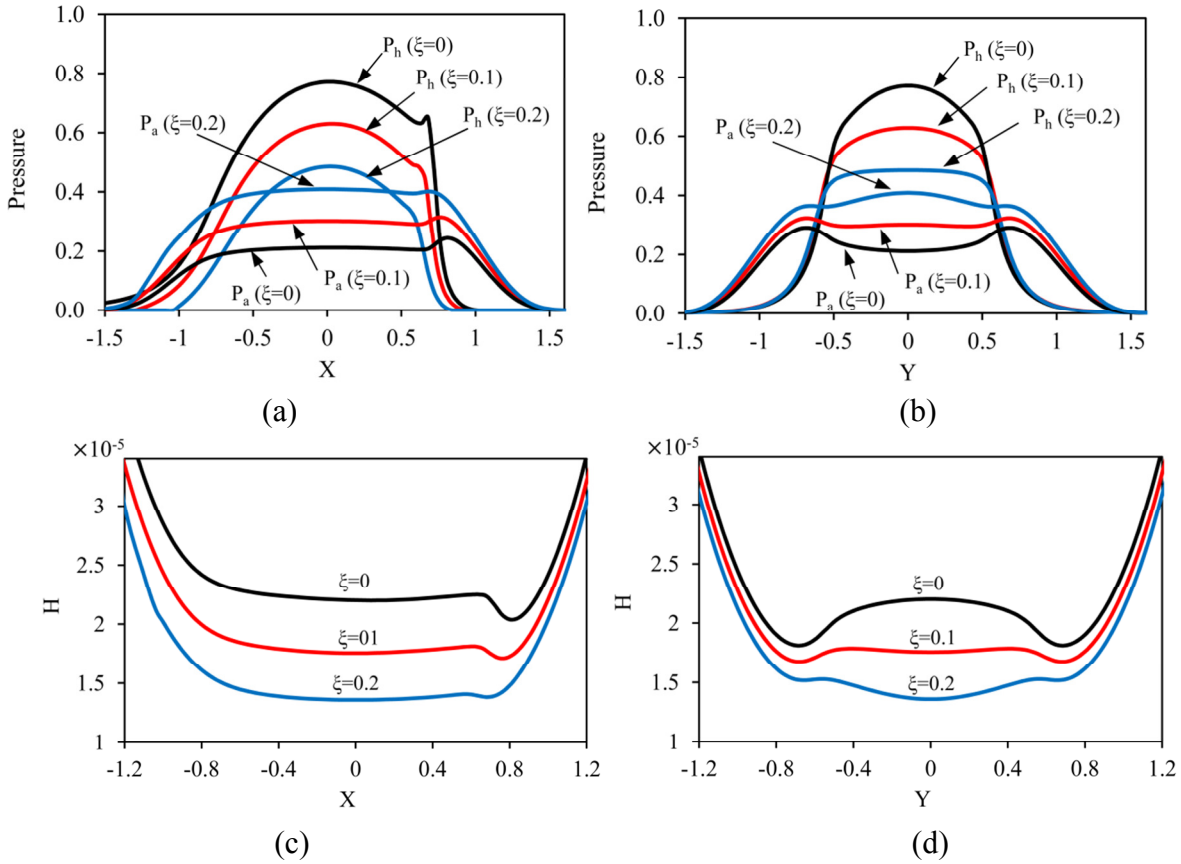

Fig. 6.2. Fully-flooded and starved regimes in rough point-contact EHL with κ=1
pressure profiles: (a) along X in Y=0 plane (b) along Y in X=0 plane
film profiles: (c) along X in Y=0 plane (d) along Y in X=0 plane
(W=5×10^{-7}, U=1×10^{-11}, G=4972, $\bar{\sigma}$=2×10^{-5}, and V=0.01)

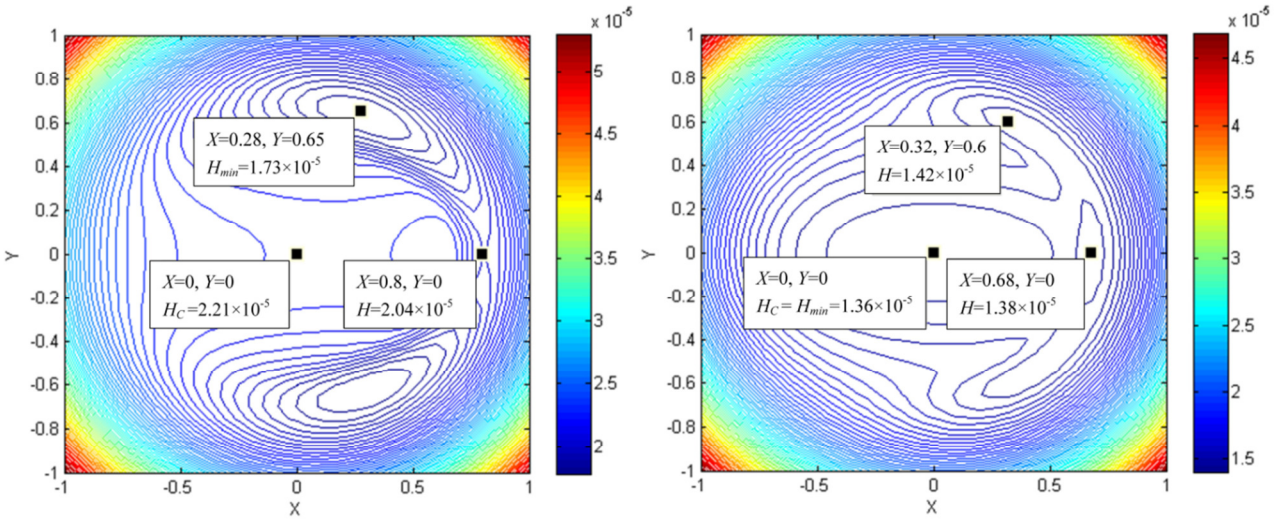

Fig. 6.3. Film thickness contour plot in circular contact (a) fully-flooded (b) starved with ξ=0.2
(κ=1, W=5×10^{-7}, U=1×10^{-11}, G=4972, $\bar{\sigma}$=2×10^{-5}, and V=0.01)

Figures 6.4 shows the pressure distributions and film profiles of fully-flooded and starved regimes in rough point contact with the ellipticity of κ=6. The input parameters are W=5×10^{-6}, U=1×10^{-11}, G=4972, $\bar{\sigma}$=2×10^{-5}, and V=0.01. The load is chosen in a way to yield a similar contact pressure to the previous cases (Figs. 6.1 and 6.2). The simulations show that the asperity load ratio is L_a= 24% for the fully-flooded regime, L_a= 31% for ξ=0.1 and L_a= 39% for ξ=0.2. Also, the ratio of starved to fully-flooded central film thickness is obtained as ϕ_{H_C}=86% for ξ=0.1 and ϕ_{H_C}=0.72% for ξ=0.2. Comparing these results with the previous case (κ=1, Fig. 6.2) reveals that the central film thickness is less affected by the starvation as the ellipticity increases. This can be explained by the fact that for larger ellipticity values, the domain is wider (in the y direction) and the center is less affected by the decrease in the flow rate. (Note that in all figures, the contact domain is normalized by the Hertzian dimensions). This trend is expected since the behavior of the elliptical contact should approach to that of the line contact at high ellipticity values. The simulations also predict the ratio of starved to fully-flooded minimum film thickness is $\phi_{H_{min}}$=88% for ξ=0.1 and $\phi_{H_{min}}$=77% for ξ=0.2.

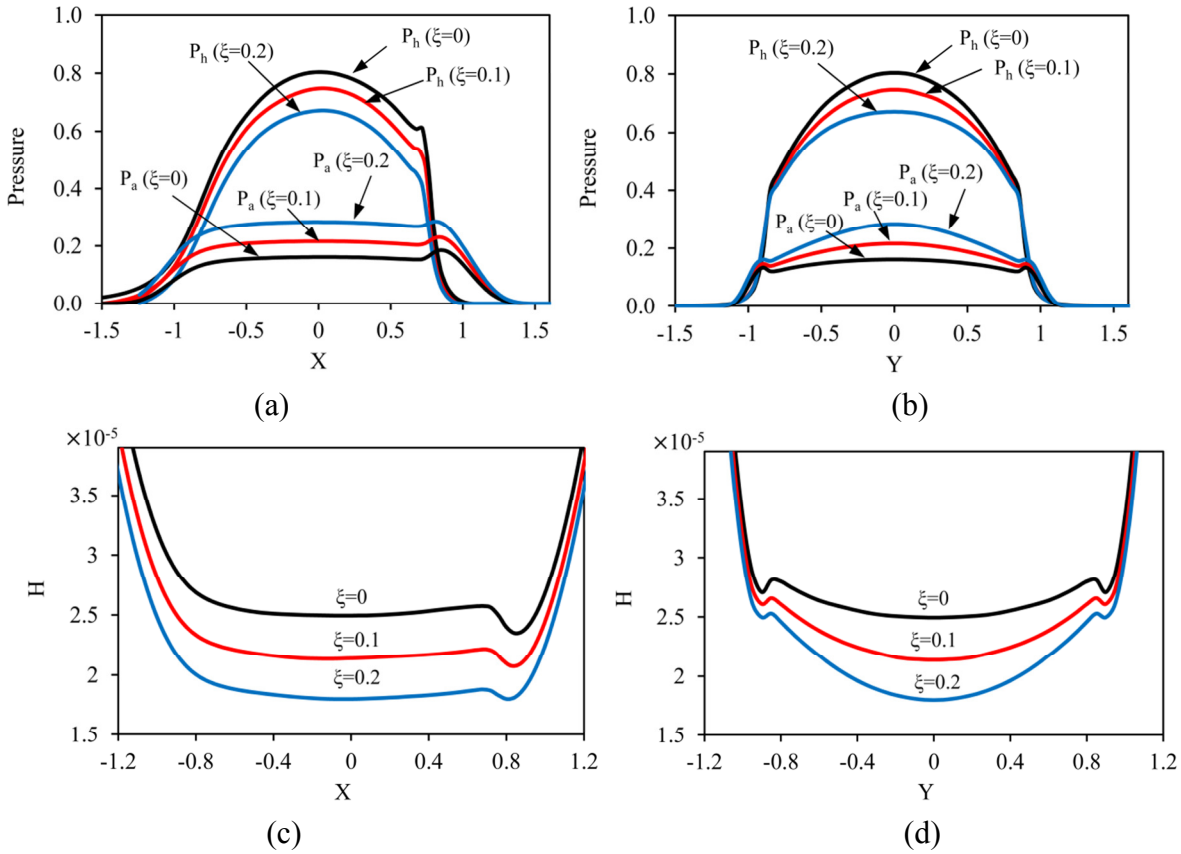

Fig. 6.4. Fully-flooded and starved regimes in rough point-contact EHL with κ=6
pressure profiles: (a) along X in Y=0 plane (b) along Y in X=0 plane
film profiles: (c) along X in Y=0 plane (d) along Y in X=0 plane
(W=5×10^{-6}, U=1×10^{-11}, G=4972, $\bar{\sigma}$=2×10^{-5}, and V=0.01)

The contour plots of the film thickness in elliptical contact (with κ=6) for a fully-flooded and a starved case (with ξ=0.2) are presented in Fig 6.5. As shown, the minimum film thickness in fully-flooded elliptical contact occurs in Y=0 plane right before the outlet (H_{min}=2.34×10^{-5} in Fig. 6.5(a)). By starving the inlet (Fig. 6.5(b)), the central film thickness decreases and gradually approaches the minimum value.

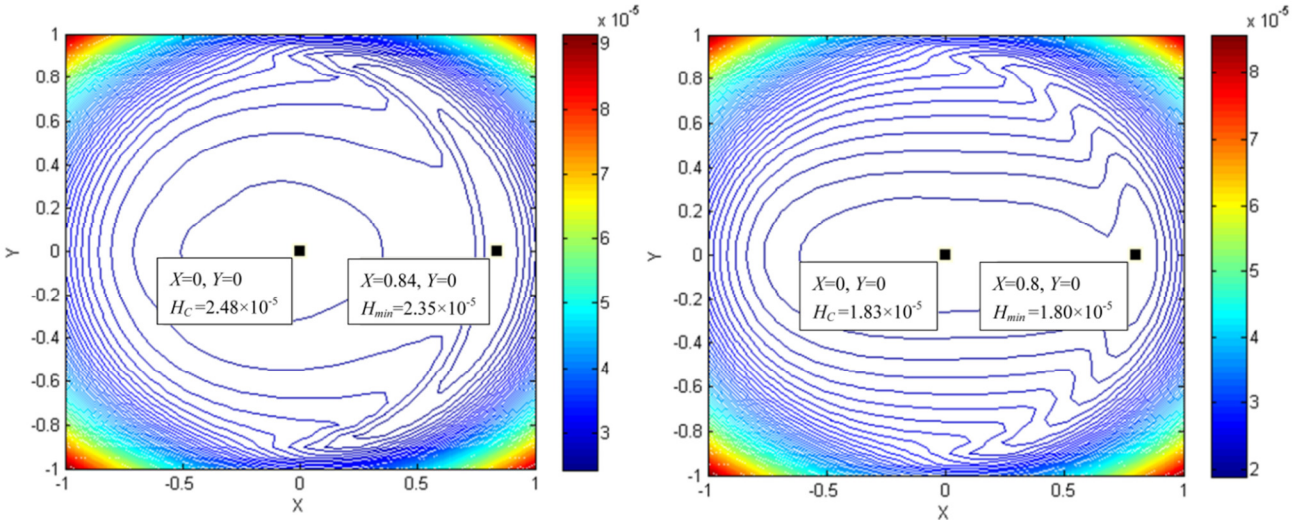

(a) (b)

Fig. 6.5. Film thickness contour plot in elliptical contact (a) fully-flooded (b) starved with ξ=0.2 (κ=6, W=5×10^{-6}, U=1×10^{-11}, G=4972, $\bar{\sigma}$=2×10^{-5}, and V=0.01)

6.3.2. Effect of inlet distance on the film thickness reduction

In this section, the effect of the inlet distance on the starvation degree and the film thickness reduction is investigated. The results are shown for the line contact, but similar pattern can be observed in point contact. As mentioned earlier, starvation is achieved by decreasing the size of the inlet. Since the shape of the pressure and the film profiles vary by changing the operating parameters (such as the load, speed and surface roughness), it is expected that the relationship between the inlet distance and the starvation degree depends on these parameters. To investigate this, the starvation degree is plotted versus the inlet distance (for the line contact) in Fig. 6.6(a) where four different operating conditions are investigated. In Case 1, W=1×10^{-4}, U=1×10^{-11} and $\bar{\sigma}$=2×10^{-5}, G=4972, V=0.01 are used while in the other cases, one input is changed: Case 2 has a lower load (W=2×10^{-5}), Case 3 has a higher speed (U=3×10^{-11}), and Case 4 has smooth surfaces ($\bar{\sigma}$=0).

As Fig. 6.6(a) illustrates, for all cases, the starvation degree ξ tends to zero when X_{min}=-4 is selected and starts to increase as the inlet is narrowed down. It is shown that when the contact is subjected to a lower load, starvation is more severe for the same inlet distance (compare Cases 1 and 2). This can be explained by the fact that at lower loads, the pressure profiles deviate significantly from the Hertzian solution (there is a noticeable pressure at the inlet far from the

contact center), so decreasing the inlet distance affects the flow rate more appreciably. The same pattern can be observed for higher speeds especially at smaller inlet distances (compare Cases 1 and 3). This can be again explained by the shape of the pressure profile at higher speeds. Also, it is observed that the starvation degree for the rough and smooth surfaces are close to each other at larger inlet distances. However, as the inlet becomes smaller, the starvation degree becomes larger for the smooth surface (compare Cases 1 and 4). This is because in rough surfaces, a part of the pressure is carried by the asperities and thus to satisfy the applied load, the hydrodynamic pressure decreases. Consequently, the hydrodynamic pressure profiles shrink toward the center thereby making the flow rate (and therefore the starvation degree) less sensitive to the inlet distance. For the same reasons, the relationship between the film reduction ratio and the inlet distance is affected by different input conditions presented in Figure 6.6(b).

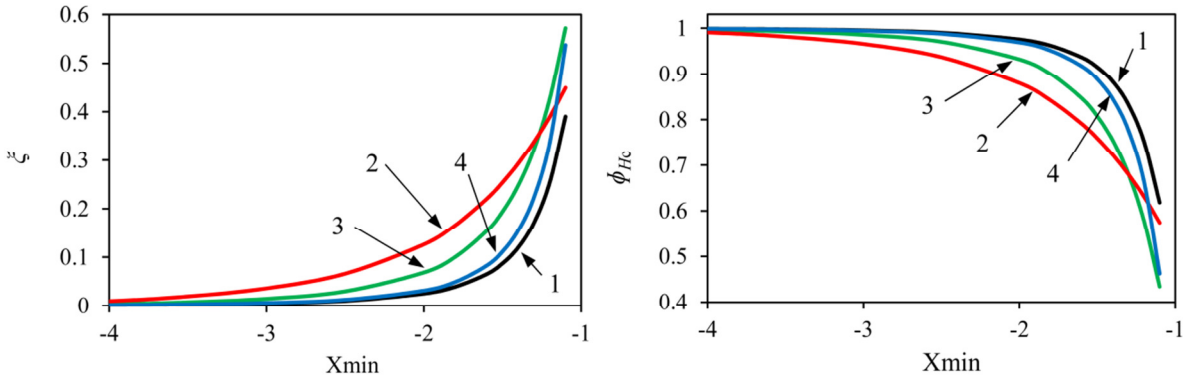

(a) (b)

Fig. 6.6. Effect of inlet distance (a) on starvation degree (b) on film reduction ratio
W=1×10^{-4}, U=1×10^{-11} and $\bar{\sigma}$=2×10^{-5}, G=4972, V=0.01 (Case 1)
W=2×10^{-5} (Case 2), U=3×10^{-11} (Case 3), $\bar{\sigma}$=0 (Case 4)

6.3.3. Effect of starvation degree on film thickness reduction

In this section, the effect of the starvation degree (the reduction in the mass flow rate) on the film thickness is investigated.

6.3.3.1. Line contact

Figure 6.7 shows the effect of the starvation degree on the film thickness reduction in line-contact EHL where the ratio of the starved to fully-flooded film thickness (both central and minimum) versus the starvation degree is compared for four different operating conditions investigated above. From these graphs, it is observed that even though the relationship between the film reduction ratio and the inlet distance varies for different input parameters (Fig. 6(b)), the relationship between the film reduction ratio (both central and minimum) and the starvation degree is nearly independent of the input parameters. Another observation is that the ratio of starved to fully-flooded central film thickness has a linear relationship with the starvation degree in line-contact EHL (Fig. 6.7(a)). It is shown that for example at ξ=0.2 (20% reduction in the

flow rate), the central film thickness drops about 20%. This can be explained by referring to Eq. (4). At the center of the contact, the pressure gradient is nil and therefore the film thickness is linearly related to the flow rate (noting that the starvation does not significantly affect the density, which is only a function of the contact pressure). As shown in Fig 6.7(b), the drop in the minimum film thickness due to the starvation is slightly less than the central film thickness. Note, also, that there is a slight nonlinearity between the minimum film thickness reduction and the starvation degree. This is because the pressure gradient is not zero at the location of minimum film thickness (see Eq. (4)).

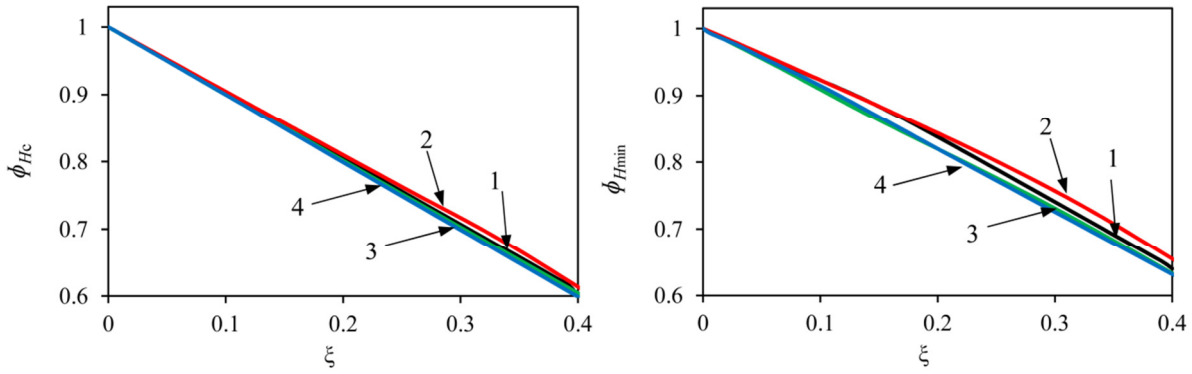

(a) (b)

Fig. 6.7. Effect of starvation degree on film thickness in line-contact EHL
(a) central film thickness (b) minimum film thickness
(W=1×10^{-4}, U=1×10^{-11} and $\bar{\sigma}$=2×10^{-5}, G=4972, V=0.01 (Case 1)
W=2×10^{-5} (Case 2), U=3×10^{-11} (Case 3), $\bar{\sigma}$=0 (Case 4)

6.3.3.2. Point contact

Figure 6.8 shows the effect of the starvation degree on the film thickness reduction ratios in point-contact EHL. The dimensionless load is chosen in a way to yield a similar contact pressure for all cases (maximum Hertzian pressure of about 0.7 GPa). It is observed that in point- contact EHL, the reduction in the film thickness is not only a function of the starvation degree, but also the ellipticity parameter. As shown in Fig. 6.8(a), the reduction in the central film thickness due to the starvation is much larger for the circular contact (κ=1). This can be explained by referring to Fig. 6.2(d) where the starvation significantly changes the film shape. As Fig 6.8(a) shows, the influence of the starvation on the central film thickness decreases by increasing the ellipticity. This is expected, because the behavior of the point-contact EHL at higher ellipticity numbers should become similar to the line-contact EHL (Fig. 6.7). As Fig. 6.8(b) shows, the minimum film thickness is less affected by the starvation. Also, the decrease in the minimum film thickness is slightly larger for the higher ellipticity values.

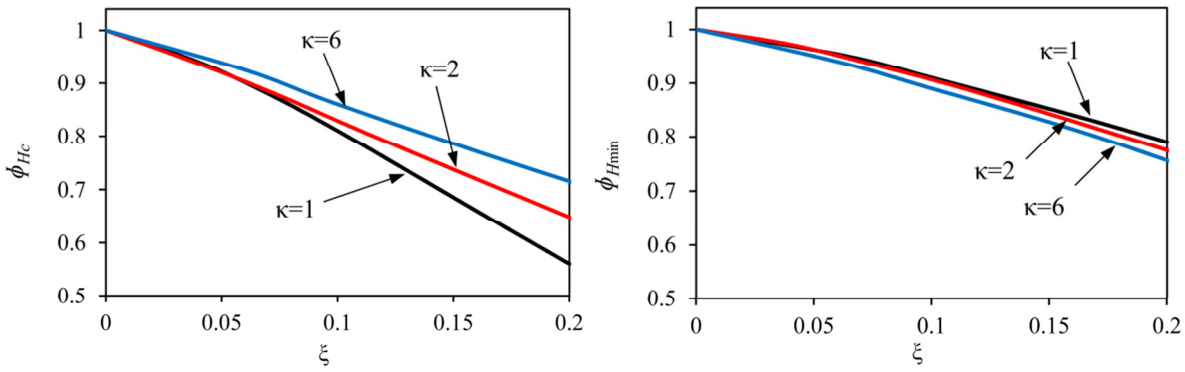

(a) (b)

Fig. 6.8. Effect of starvation degree on film thickness in point-contact EHL
(a) central film thickness (b) minimum film thickness
U=1×10^{-11}, $\bar{\sigma}$=2×10^{-5}, G=4972, V=0.01
W=5×10^{-7} (κ=1), W=1×10^{-6} (κ=2), W=5×10^{-6} (κ=6)

6.4. Predictive Formulas

The authors previously presented curve-fit formulas to predict the film thickness and asperity load ratio for fully-flooded line-contact EHL [12] as well as point-contact EHL [13]. In this study, the results from wide sets of simulations with different input are used to obtain expressions for the film thickness and asperity load in starved lubrication regime.

6.4.1. Line Contact

Simulations are done within the range of input displayed in Table 1. The roughness range covers the theoretically smooth surfaces ($\bar{\sigma}$=0) to the combined roughness of 1.27 μm for equivalent radius of one inch ($\bar{\sigma}$=5×10^{-5}). The hardness range covers the Vickers Hardness of 1.1 GPa to 6.8 GPa for steel.

Table 6.1. Range of input parameters selected for simulation (line contact)

Parameter	ξ	W	U	G	$\bar{\sigma}$	V
min	0	2×10^{-5}	1×10^{-12}	2500	0	0.005
max	0.4	5×10^{-4}	1×10^{-10}	7500	5×10^{-5}	0.03

In each simulation, the ratio of starved to fully-flooded central film thickness (ϕ_{H_C}) and minimum film thickness ($\phi_{H_{min}}$) as well as the asperity load ratio (L_a) are obtained for different degrees of starvation. Regression analyses are performed for the results of more than 200 simulation cases to obtain the ratio of starved to fully-flooded central film thickness and minimum film thickness as:

$$\Phi_{H_C} = 1 - \zeta$$
$$\Phi_{H_{\min}} = 1 - \zeta^{1.08} \quad (6)$$

Notice that the regression analysis verifies the linear relationship between the ratio of starved to fully-flooded central film thickness and the starvation degree explained in the previous section.

The central and the minimum film thickness in starved-lubrication regime can be simply obtained as:

$$H_{C(starved)} = \Phi_{H_C} \times H_{C(fully\ flooded)}$$
$$H_{\min(starved)} = \Phi_{H_{\min}} \times H_{\min(fully\ flooded)} \quad (7)$$

where the fully-flooded equations are given in Chapter 2 for line contact.

The results from the simulations reveal that the asperity load ratio in starved lubrication is not only a function of the starvation degree, but also a function of other operating parameters. Regression analyses predict the following asperity load ratio in the starved regime:

$$L_{a\ (starved)} = 0.005 W^{-0.408} U^{-0.088} G^{0.103} [\ln(1 + 4470 (1-\zeta)^{-8.04} \bar{\sigma}^{6.015} V^{1.168} W^{0.485} U^{-3.741} G^{-2.898})] \quad (8)$$

Note that Eq. (8) is very similar to the fully-flooded equation (see Chapter 2) except that it contains a new term for the starvation degree (ξ). In the case of fully-flooded inlet, $\xi = 0$ and Eq. (8) reverts back to the fully-flooded equation.

Table H.1 in Appendix H presents the results from the simulations and the curve-fit expressions as well as their corresponding errors. The error for the ratios of the film thickness reduction (both central and minimum) is defined as $100 \times |\phi_{H(\text{simulation})} - \phi_{H(\text{curve-fit})}| / \phi_{H(\text{simulation})}$ while the error for the asperity load ratio is defined as $|L_{a(\text{simulation})} - L_{a(\text{curve-fit})}|$. The mean error values for ϕ_{H_C}, $\phi_{H_{min}}$ and L_a are 0.30%, 1.06%, and 2.20%, respectively, while the maximum error values are 2.94%, 4.43%, and 5.64%, respectively.

It should be pointed out that attention should be paid in using the obtained formulas especially for higher values of the starvation degree. Since the starvation decreases the film thickness, the regime may easily fall into boundary lubrication. Therefore, after using the formulas, the starved film parameter ($\Lambda = H_{\min\ (starved)}/\bar{\sigma}$) should be checked. According to the modified Reynolds equation by Patir & Cheng [15], only the results with $\Lambda > 0.5$ are valid. Also, caution should be exercised if the obtained asperities load ratio is very large (generally more than 70%), even if the film parameter is within the valid range [12, 13].

6.4.2. Point Contact

For point-contact EHL, simulations are done within the range of input displayed in Table 6.2.

Table 6.2. Range of input parameters selected for simulation (point contact)

Parameter	ξ	κ	W	U	G	$\bar{\sigma}$	V
min	0	1	1.5×10^{-7}	3×10^{-12}	2500	0	0.005
max	0.3	8	1×10^{-4}	1×10^{-10}	7500	5×10^{-5}	0.03

The regression analyses are done for the results of more than 200 simulations. The results show that in point-contact EHL, the ratio of starved to fully-flooded film thickness is not only a function of the starvation degree, but also the ellipticity parameter. These ratios for the central and minimum film thickness are obtained as:

$$\Phi_{H_C} = 1 - 1.561\zeta^{0.849}\kappa^{-0.214}$$
$$\Phi_{H_{\min}} = 1 - 0.845\zeta^{0.893}\kappa^{0.081} \quad (9)$$

The central and the minimum film thickness in starved-lubrication regime can then be obtained from Eq. (7) where the fully-flooded values are given in Chapter 5 for point contact.

The asperity load ratio in the starved point-contact regime is obtained as:

$$L_{a(starved)} = 10W^{-0.083}U^{0.143}G^{0.314}[\ln(1+(1-\zeta)^{-7.326}\bar{\sigma}^{4.689}V^{0.509}W^{-0.501}U^{-2.90}G^{-2.870})] \quad (10)$$

which is again similar to the fully-flooded form (see Chapter 5) with the difference of containing a term for the starvation degree.

Table H.2 in Appendix H compares the results from the simulations and the curve-fit expressions and shows the corresponding errors. The mean error values for ϕ_{H_C}, $\phi_{H_{min}}$ and L_a are 2.89%, 3.08%, and 1.43%, respectively, while the maximum errors are 8.47%, 8.11%, and 7.34%, respectively. Again, it should be emphasized that if the film parameter falls below 0.5 or the obtained asperity load ratio is very large, the results may not be valid.

6.4.3. Verification of the model

In this section, the validity of the present numerical model is investigated. Unfortunately, no experimental data was found for the starvation in the mixed EHL regime. There are only a few experimental studies for the smooth surfaces (as mentioned in the introduction), but they are not based on the reduction of the mass flow rate. Here, the fully-flooded results from the present study are compared with those from other studies, and it is shown how the starvation changes the results.

Figure 6.9 shows the results from the present formulas for the fully-flooded regime as well as two starved regimes (with ξ=0.2 and ξ=0.3) where the simulation results by Zhu & Wang [17] (for the fully-flooded regime) are also shown. The ratio of the central film thickness to the

surface roughness is plotted against the dimensionless speed for both the line-contact and elliptical contact (with κ=2). The input (as used by Zhu & Wang) are: $\bar{\sigma}=4.7\times10^{-5}$, G=2830, and a maximum Hertzian pressure of 2.277 GPa (which is equal to $W=6.3\times10^{-4}$ for line contact and $W=5.5\times10^{-5}$ for elliptical contact with κ=2). The hardness is not reported in the study Zhu & Wang, therefore a dimensionless hardness of 0.01 (equals to about 20 Rockwell C) is used as input in the current formulas.

As shown in Fig. 6.9, the fully-flooded results from the present formulas are in agreement with the results by Zhu & Wang [17] for both line contact and point contact. The difference between the results can be explained by the fact that the current formulas are based on the statistical treatment of the surface asperities, and the central film thickness (which is the distance between the mean lines of two rough surfaces at the center of the contact) is compared to the mean value of the film thickness in the deterministically-based study by Zhu & Wang.

As shown, the film thickness decreases as the inlet is starved. It is also observed that the decrease in the central film thickness is more significant in point contact compared to line contact (as mentioned earlier). The decrease in the film thickness can shift the regime from mixed into the boundary lubrication regime. As mentioned earlier, the modified Reynolds equation by Patir and Cheng [15] is valid for the film parameter values greater than 0.5. Therefore, the points in which the film parameter falls below 0.5 are marked by dashed lines in Fig. 6.9. It can be seen that the transition between the mixed and the boundary lubrication regimes occurs at higher speeds as the starvation prevails.

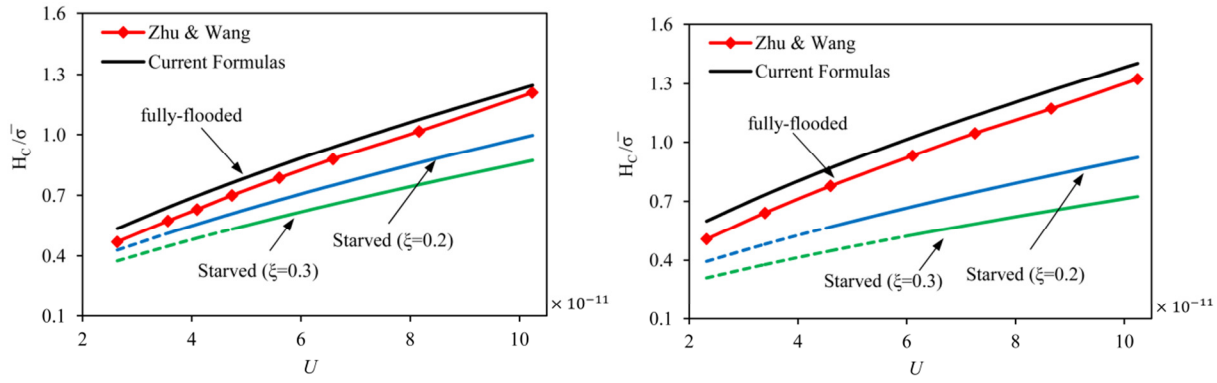

Fig. 6.9. Fully-flooded and starved results compared to results by Zhu & Wang [17]
(a) line contact (b) point contact with κ=2
$\bar{\sigma}=4.7\times10^{-5}$, G=2830, $W=6.3\times10^{-4}$ (line-contact), $W=5.5\times10^{-5}$ (point contact with κ=2)

6.4.4. Illustrative examples

To show the utility of the obtained formulas, three illustrative examples are presented next.

Contact between rollers: consider the contact of two identical steel rollers (with effective Young's modulus of E'=228 GPa) and the radius of 25.4 mm (effective radius of R=12.7 mm). The applied load is 2 KN, and the linear speed of rollers are 1 m/s and 0.5 m/s, so the rolling speed is u_r=.75 m/s. The lubricant used is SAE 20W (μ_0=0.048 Pa.s, α= 2×10^{-8} m^2/N). Both surfaces are ground with σ=0.2 μm, (combined roughness is 0.283 μm) while the Vickers hardness of the surfaces is 240 Kg/mm^2 (2.35 GPa). Therefore, the dimensionless parameters are calculated as W=8.16×10^{-5}, U=1.24×10^{-11}, G=4560, $\bar{\sigma}$=2.23×10^{-5} and V= 0.0103. For the fully-flooded case, Eqs. (19) and (20) in Chapter 2 yield H_C=2.45×10^{-5} and H_{min}=2.27×10^{-5}, so h_c=0.31 μm and $h_{\min}$=0.29 μm. Also, from Eq. (21) in Chapter 2, the asperity load is L_a=18%. The fully-flooded film parameter is calculated as Λ=1.02. Now, consider that the oil supply is 70% of the fully-flooded case (ξ=0.3). From Eq. (6), ϕ_{H_C}=0.7 and $\phi_{H_{\min}}$=0.73, so the starved values of the film thickness are h_c=0.22 μm and $h_{\min}$=0.21 μm. From Eq. (8), the asperity load ratio is L_a=33% which means that the contribution of the asperities has almost doubled. The starved film parameter is calculated as Λ=0.74 which means that the lubrication regime is approaching the boundary lubrication in the starved condition.

Lift-off speed: consider the rollers investigated above. The lift–off speed is defined as the speed in which transition between the mixed and full-film regimes takes place. This is generally assumed to occur at the film parameter of Λ=3. For the dimensionless surface roughness used ($\bar{\sigma}$=2.23×10^{-5}), the dimensionless minimum film thickness should be H_{min}=6.69×10^{-5} in order to achieve this transition. Using Eq. (20) in Chapter 2 for the fully-flooded case, the required dimensionless speed is obtained as U=6.91×10^{-11} which yields the rolling speed of 4.17 m/s as the lift-off speed. Now consider a starved inlet with ξ=0.2. Using Eq. (6), $\phi_{H_{min}}$=0.82, therefore the required dimensionless speed for the lift-off condition is obtained as U=9.28×10^{-11} from Eq. (7). This gives the lift-off speed of 5.6 m/s which shows that a larger speed is required to attain the full-film regime when the inlet is starved.

Ball-on-disk problem: Consider the contact between a 30 mm diameter ball and a flat disk (which yields an effective radius of 15 mm) with the same material and lubricant as above. The applied normal load is 50 N and the ball speed is 1 m/s which yields the rolling speed of 0.5 m/s. The roughness of the surfaces are both σ=0.1 μm, (combined roughness is 0.14 μm). The dimensionless parameters are calculated as κ=1, W=9.75×10^{-7}, U=7.02×10^{-12}, G=4560, $\bar{\sigma}$=9.33×10^{-6} and V= 0.0103. For the fully-flooded case, substituting into Eqs. (21) and (22) in Chapter 5 gives H_C=1.51×10^{-5} and $H_{\min}$=1.05×10^{-5}, so h_c =0.23 μm and $h_{\min}$=0.16 μm and the film parameter is obtained as Λ =1.12. Also, Eq. (23) in Chapter 5 yields L_a=11.7%. Now, consider a starved case with ξ=0.2. From Eq. (9), ϕ_{H_C}=0.6 and $\phi_{H_{\min}}$=0.8, so the starved values of the film thickness are h_c=0.14 μm and $h_{\min}$=0.13 μm and the starved film parameter is obtained to Λ =0.9. Also, from Eq. (10), the asperity load ratio is L_a=28% which is more than twice the fully-flooded case.

6.5. Conclusions

In this paper, an approach is presented to study the effect of starvation in elastohydrodynamic lubrication (EHL) of rough surfaces in both line contact and point contact. By relating the starvation to the reduction of the lubricant mass flow rate, the changes in the pressure distribution (both hydrodynamic and asperity) as well as the film thickness are investigated. It is shown that, in general, the effect of starvation on the central film thickness is more pronounced compared to the minimum film thickness. Also, the reduction of the central film thickness in point contact is greater than that of line contact, especially at smaller ellipticity values. It is also observed that in line contact, the reduction in the film thickness is only a function of the starvation degree; while in point contact, it is a function of the starvation degree as well as the ellipticity.

Regression analyses are performed for the simulation results within a wide range of input to develop expressions for the ratio of the reduction in central and minimum film thickness. These ratios are found to be functions of the starvation degree in line contact while they are functions of the starvation degree and ellipticity in point contact. These ratios can be applied to the film thickness formulas presented in Refs. [12, 13] to extend their availability to the starved regimes. Also presented are the expressions for the asperity load ratio as functions of the starvation degree as well as other input parameters.

Nomenclature

a	half Hertzian length, m
b	half Hertzian width, m
B	line-contact length, m
E'	effective modulus of elasticity, $1/E'=0.5[(1-\nu_1^2)/E_1+(1-\nu_2^2)/E_2]$, Pa
F	normal load, N
G	dimensionless material number, $E'\alpha$
h	film thickness, m
h_c	central film thickness, m
h_{min}	minimum film thickness, m
H	dimensionless film thickness, h/R_x
H_c	dimensionless central film thickness, h_c/R_x
H_{min}	dimensionless minimum film thickness, h_{min}/R_x
L_a	asperity load ratio (percentage)
$\dot{m}$	lubricant mass flow rate, kg/s
$\dot{m}_F$	fully-flooded mass flow rate, kg/s
$\dot{m}_S$	starved mass flow rate, kg/s
p	total pressure, Pa
p_a	asperity pressure, Pa
p_h	hydrodynamic pressure, Pa
P	dimensionless total pressure, p/p_{Hmax}

P_a	dimensionless asperity pressure, p_a/p_{Hmax}
P_h	dimensionless hydrodynamic pressure, p_h/p_{Hmax}
R_x	equivalent contact radius in x direction, $[1/R_{1x}\pm1/R_{2\,x}]^{-1}$, m
R_y	equivalent contact radius in y direction, $[1/R_{1y}\pm1/R_{2\,y}]^{-1}$, m
u	lubricant velocity, m/s
u_r	rolling speed, $(u_1+u_2)/2$, m/s
U	dimensionless speed number, $\mu_0 u/E'R_x$
v	Vickers hardness, Pa
V	dimensionless hardness number, v/E'
W	dimensionless load number, $F/BE'R_x$ in line contact and $F/E'R_x^2$ in point contact
x	coordinate in moving direction, m
y	coordinate perpendicular to moving direction, m
z	coordinate across the film, m
X	dimensionless coordinate in moving direction, x/b
Y	dimensionless coordinate perpendicular to moving direction, y/a
α	pressure-viscosity coefficient, m^2/N
κ	ellipticity parameter, a/b
Λ	film parameter, h_{min}/σ
μ	lubricant viscosity, Pa.s
μ_0	lubricant viscosity at zero pressure, Pa.s
ξ	starvation degree
ρ	lubricant density, kg/m^3
σ	standard deviation of the surface heights, m
$\bar{\sigma}$	dimensionless surface roughness, σ/R_x
ϕ_{H_C}	ratio of starved to fully-flooded central film thickness
$\phi_{H_{min}}$	ratio of starved to fully-flooded minimum film thickness

6.6. References

[1] Hamrock BJ, Dowson D. Isothermal Elastohydrodynamic Lubrication of Point Contacts .1. Theoretical Formulation. J Lubric Tech-T Asme. 1976;98:223-9.

[2] Hamrock BJ, Dowson D. Isothermal Elastohydrodynamic Lubrication of Point Contacts .4. Starvation Results. J Lubric Tech-T Asme. 1977;99:15-23.

[3] Chevalier F, Lubrecht AA, Cann PME, Colin F, Dalmaz G. Film thickness in starved EHL point contacts. J Tribol-T Asme. 1998;120:126-33.

[4] Damiens B, Venner CH, Cann PME, Lubrecht AA. Starved lubrication of elliptical EHD contacts. J Tribol-T Asme. 2004;126:105-11.

[5] Cann PME, Damiens B, Lubrecht AA. The transition between fully flooded and starved regimes in EHL. Tribol Int. 2004;37:859-64.

[6] Yang P, Wang J, Kaneta M. Thermal and non-Newtonian numerical analyses for starved EHL line contacts. J Tribol-T Asme. 2006;128:282-90.

[7] Kumar P, Khonsari MM. Effect of Starvation on Traction and Film Thickness in Thermo-EHL Line Contacts with Shear-Thinning Lubricants. Tribol Lett. 2008;32:171-7.

[8] Ali F, Krupka I, Hartl M. An Approximate Approach to Predict the Degree of Starvation in Ball-Disk Machine Based on the Relative Friction. Tribol T. 2013;56:681-6.

[9] Ali F, Krupka I, Hartl M. Analytical and experimental investigation on friction of non-conformal point contacts under starved lubrication. Meccanica. 2013;48:545-53.

[10] Svoboda P, Kostal D, Krupka I, Hartl M. Experimental study of starved EHL contacts based on thickness of oil layer in the contact inlet. Tribol Int. 2013;67:140-5.

[11] Faraon IC, Schipper DJ. Stribeck curve for starved line contacts. J Tribol-T Asme. 2007;129:181-7.

[12] Masjedi M, Khonsari MM. Film Thickness and Asperity Load Formulas for Line-Contact Elastohydrodynamic Lubrication With Provision for Surface Roughness. J Tribol-T Asme. 2012;134:011503.

[13] Masjedi M, Khonsari MM. On the Effect of Surface Roughness in Point-Contact EHL: Formulas for Film Thickness and Asperity Load. Tribol Int. 2015;82:228–44.

[14] Biboulet N, Colin F, Lubrecht AA. Friction in starved hydrodynamically lubricated line contacts. Tribol Int. 2013;58:1-6.

[15] Patir N, Cheng HS. Average Flow Model for Determining Effects of 3-Dimensional Roughness on Partial Hydrodynamic Lubrication. J Lubric Tech-T Asme. 1978;100:12-7.

[16] Zhao YW, Maietta DM, Chang L. An Asperity Microcontact Model Incorporating the Transition from Elastic Deformation to Fully Plastic Flow. J Tribol-T Asme. 2000;122:86-93.

[17] Zhu D, Wang QJ. Effect of Roughness Orientation on the Elastohydrodynamic Lubrication Film Thickness. J Tribol-T Asme. 2013;135.

Chapter 7: An Engineering Approach for Rapid Evaluation of Traction Coefficient and Wear in Mixed EHL

7.1. Introduction

A model was recently developed by the authors to treat the elastohydrodynamic lubrication of rough surfaces for both line-contact EHL [1] and point-contact EHL [2] by giving solution to the modified Reynolds equation [3] and elasto-plastic asperity micro-contact equations [4]. Based on these studies, expressions were provided to predict the central and minimum film thickness as well as the asperity load ratio in dimensionless form. These formulas are summarized below.

Line-contact EHL [1]:

$$H_c = h_c / R = 2.691 W^{-0.135} U^{0.705} G^{0.556} (1 + 0.2\ \bar{\sigma}^{1.222} V^{0.223} W^{-0.229} U^{-0.748} G^{-0.842})$$

$$H_{\min} = h_{\min} / R = 1.652\, W^{-0.077} U^{0.716} G^{0.695} (1 + 0.026\ \bar{\sigma}^{1.120} V^{0.185} W^{-0.312} U^{-0.809} G^{-0.977}) \quad (1)$$

$$L_a = 0.005 W^{-0.408} U^{-0.088} G^{0.103} [\ln (1 + 4470\ \bar{\sigma}^{6.015} V^{1.168} W^{0.485} U^{-3.741} G^{-2.898})]$$

Point-contact EHL [2]:

$$H_c = h_c / R = 3.672\, W^{-0.045\kappa^{0.18}} U^{0.663\kappa^{0.025}} G^{0.502\kappa^{0.064}} (1 - 0.573 e^{-0.74\kappa})$$
$$\times (1 + 0.025\ \bar{\sigma}^{1.248} V^{0.119} W^{-0.133} U^{-0.884} G^{-0.977} \kappa^{0.081})$$

$$H_{\min} = h_{\min} / R = 1.637\, W^{-0.09\kappa^{-0.15}} U^{0.711\kappa^{-0.023}} G^{0.65\kappa^{-0.045}} (1 - 0.974 e^{-0.676\kappa}) \quad (2)$$
$$\times (1 + 0.141\ \bar{\sigma}^{1.073} V^{0.149} W^{-0.044} U^{-0.828} G^{-0.954} \kappa^{-0.395})$$

$$L_a = 10 W^{-0.083} U^{0.143} G^{0.314} [\ln (1 + \bar{\sigma}^{4.689} V^{0.509} W^{-0.501} U^{-2.90} G^{-2.870})]$$

These expressions offer an easy-to-use procedure for estimating the EHL parameters without the need of performing extensive numerical simulations. Although these formulas are based on isothermal simulations, at moderate rolling velocities, the central film thickness, h_c, and the asperity load ratio, L_a, are not significantly affected by the sliding-induced heat generation. In fact, it is only the minimum value of the film thickness, h_{min}, that experiences a significant drop [5]. Consequently, if the rolling speed is moderate, the formulas for h_c and L_a can still be used at large slide-to-roll ratio values.

Development of a general expression capable of predicting the traction coefficient in EHL applications is a difficult task because it largely depends on the lubricant viscosity which is drastically influenced by both pressure and temperature. Therefore, different lubricants show completely different traction behaviors. In a recent paper, we conducted a full numerical simulation for the mixed thermo-elastohydrodynamic lubrication (mixed TEHL) to predict of the

traction coefficient [5]. Based on extensive set of results, a curve-fit expression was derived for predicting the traction coefficient for a specific type of lubricant (SAE 30).

Deriving an expression for prediction of the wear in the mixed EHL is also a challenging job since it requires the knowledge of the asperity load ratio and the temperature rise [6]. Although the load ratio can be predicted by the curve fit formulas [1, 2], the temperature rise is still an unknown parameter.

In the current study, we report a simple but realistic approach for estimating the traction coefficient and the wear rate in elastohydrodynamic lubrication of rough surfaces without the need of performing extensive numerical simulations. A simplified method is adopted to estimate the temperature rise with the consideration of heat generation by both the solid and the lubricant. The estimated temperature rise is utilized together with the results from the isothermal formulas (Eq. (1)) to evaluate the traction coefficient and the wear rate in the mixed EHL.

7.2. Model

In this section, it is first shown how the temperature rise within the mixed EHL contact can be evaluated. Next, the traction coefficient and the wear rate are approximated using this method.

7.2.1. Temperature rise

To estimate the temperature rise due to the sliding in the mixed EHL regime, the theory by Tian & Kennedy [7] is used here. In their study, the temperature rise within the sliding bodies is analytically obtained. Although the method was originally developed for dry contact, where the asperity friction is the heat source, in the current study the fluid shear heating is treated as a heat source in a similar fashion. The method described here is for line-contact EHL, but it can be extended to point contact.

According to Tian & Kennedy [7], the flash temperature within the contact area of a moving square-shape heat source against a semi-infinite body is obtained as:

$$\Delta T = \frac{2lq}{\sqrt{\pi}\,(k_1\sqrt{(1+Pe_1}+k_2\sqrt{(1+Pe_2})} \tag{3}$$

where q is the average heat flux and l is the half contact length along the sliding direction which is here equal to the Hertzian half width of contact ($b = \sqrt{8RF/\pi BE'}$). Note that for point contact, an expression for the elliptical heat source should be utilized. In Eq. (3), parameters k_1 and k_2 represent the thermal conductivity of the contacting surfaces, and Pe_1 and Pe_2 are their corresponding Peclet numbers.

In the approach by Tian & Kennedy, the average heat flux is:

$$q = f_d.u_s.p \tag{4}$$

where f_d is the dry friction coefficient, u_s is the sliding velocity, and p is the average contact pressure obtained by dividing the normal force by the Hertzian contact area ($p=F/2bB$).

Here, for the mixed EHL regime, it is assumed that the heat flux consists of two parts: surface asperities (q_a) and the hydrodynamic (q_h):

$$q = q_a + q_h \tag{5}$$

The pressure is also the sum of asperity and hydrodynamic parts:

$$p = p_a + p_h \quad : \quad p_a = p(L_a/100) \quad ; \quad p_h = p(1 - L_a/100) \tag{6}$$

where the asperity load ratio, L_a, can be obtained from Eq. (1). The asperity part of the heat flux can be obtained as:

$$q_a = f_c . u_s . p_a = f_c . u_s . p(L_a/100) \tag{7}$$

where f_c is the asperity friction coefficient (also referred to as the boundary friction coefficient in some studies).

The hydrodynamic part of the heat flux (due to shear heating of the lubricant) can be approximated using the average shear stress of the lubricant and the sliding speed as:

$$q_h = \tau_{avg} . u_s \tag{8}$$

Now, the shear stress is directly affected by the lubricant's viscosity which is highly influenced by both pressure and temperature and can quite be different depending on the lubricant. Thus the determination of temperature rise is necessary to evaluate the unknown lubricant viscosity and the shear stress. It is well established that lubricants subjected to EHL operating conditions tend to yield beyond a certain shear rate, known as the limiting shear stress, τ_{lim} [8]. This parameter is utilized here to approximate the heat flux in Eq. (4) by letting

$$q_h = \tau_{\lim} . u_s \tag{9}$$

Note that τ_{lim} is directly related to the lubricant's pressure [9]:

$$\tau_{\lim} = \Lambda_{\lim} . p_h = \Lambda_{\lim} . p(1 - L_a/100) \tag{10}$$

where the limiting shear stress coefficient of the lubricant, $\Lambda_{\lim}$, can be obtained from the its traction curve under a heavy load [5, 9].

The approximate heat flux over the contact in the mixed EHL regime can now be obtained as:

$$q = f_c . u_s . p(L_a/100) + \Lambda_{\lim} . p(1 - L_a/100) \tag{11}$$

Substituting the above equation into Eq. (3) yields an expression for the estimation of the temperature rise.

7.2.2. Traction Coefficient

In order to obtain the traction coefficient, the traction force F_f should first be evaluated. That is [5]:

$$F_f = \left(F_f\right)_a + \left(F_f\right)_h = (F \times \frac{L_a}{100}) f_c + \int \tau_{\lim} (1 - e^{\frac{-\mu . u_s}{\tau_{\lim} h}}) B dx \tag{12}$$

where the first term (asperity traction force) is simply the product of the normal load applied on the asperities ($F.(L_a/100)$) and the asperity friction coefficient f_c. The second term (hydrodynamic traction force) is written based on the formulation proposed by Bair & Winer [8]. Assuming an average viscosity and film thickness within the Hertzian contact area, Eq. (12) is:

$$F_f = \left(F_f\right)_a + \left(F_f\right)_h = (F \times \frac{L_a}{100}) f_c + \tau_{\lim} (1 - \exp(\frac{-\mu_{avg} . u_s}{\tau_{\lim} h_c}))(2bB) \tag{13}$$

Note that the central film thickness, h_c, is used here as the average value within the contact.

The traction coefficient can now be obtained by dividing the traction force by the normal force:

$$f = \frac{F_f}{F} = (\frac{L_a}{100}) f_c + \frac{2bB\tau_{\lim}}{F} (1 - \exp(\frac{-\mu_{avg} . u_s}{\tau_{\lim} h_c})) \tag{14}$$

Note that in Eq. (14), the asperity load ratio L_a and the central film thickness h_c can be readily predicted from the available formulas (Eq. (1)). Also, $\tau_{\lim}$ is obtained from Eq. (10). Therefore, the only unknown is the average viscosity which can be evaluated from the Roelands equation [10] as:

$$\mu_{avg} = \mu_0 \exp\left\{(\ln \mu_0 + 9.67)\left[-1 + \left(1 + 5.1 \times 10^{-9} p_h\right)^Z\right] - K_T \Delta T\right\} \tag{15}$$

where the average hydrodynamic pressure p_h can be obtained from Eq. (6), while the temperature rise ΔT can be approximated by the flash temperature using Eq. (3). Note that Eq. (15) is best suited for moderate pressures.

7.2.3. Wear rate

To evaluate the wear rate in the mixed EHL, the Archard theory [11] for dry condition is extended to lubricated case [6, 12]. The lubricated wear rate is:

$$\Omega_{\text{lub}} = K\psi(\frac{L_a}{100})\frac{F.u_s}{v} \tag{16}$$

In Eq. (16), parameter ψ is the fractional film defect obtained as [13, 14]:

$$\psi = 1 - \exp\left\{-\left[\frac{a_\chi}{u_s t_0} \exp(-\frac{E_a}{R_g T_s})\right]\right\} \tag{17}$$

As Eq. (17) shows, the unknown parameters for determination of the lubricated wear are the asperity load ratio L_a and the surface temperature T_s. Parameter L_a can be predicted by applying Eq. (1), and the surface temperature can be simply estimated as:

$$T_s = T_0 + \Delta T \tag{18}$$

where the temperature rise ΔT can be evaluated from Eq. (3).

7.3. Results and Discussion

7.3.1. Comparison with Experiments

In this section, the results from the present approach are compared with the experimental data provided by Wu & Cheng [15] who used a two-disk machine configuration to measure the traction coefficient and wear volume in the mixed EHL. The input values used in their study are: R=5.4 mm, B=6.35 mm, μ_0=0.0325 Pa.s, T_0=315 K, and u_r=1.83 m/s, and a maximum contact pressure of 2 GPa. The combined surface roughness is about σ=0.34 μm and the surface hardness is 56 Rockwell C (equivalent to Vickers hardness of about v=6 GPa). The lubricant's temperature-viscosity coefficient is calculated as K_T=0.03 based on the data provided in [16]. However, the pressure-viscosity coefficient is not reported, so $\alpha=1.5\times10^{-8}$ m^2/N is assumed. Also, a limiting shear stress of Λ=0.06 (which is suitable for the behavior of the traction curve) is assumed, and a typical asperity friction coefficient of f_c=0.12 is considered [5].The thermal properties of the surfaces are chosen as k=60.5 W/mK and c_p =434 J/kgK for typical carbon steel [16]. For calculation of wear, the fractional film defect parameters (Eq. (17)) are assumed as: $a_\chi=3\times10^{-10}$ m, $E_a=49\times10^3$ J/mole, R_g=8.31 J/mole·K, and $t_0=3\times10^{-12}$ s [15], while a typical value of $K=5\times10^{-4}$ is considered as the dry wear coefficient [15, 17].

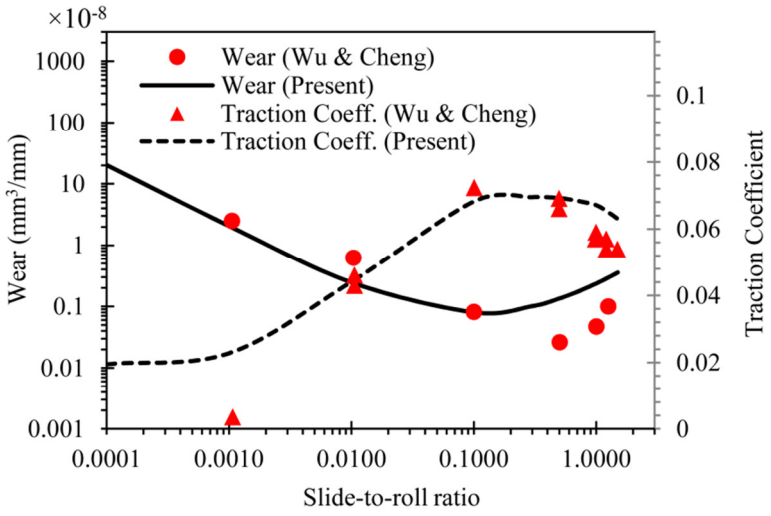

Fig. 7.1. Results from current approach compared to experimental results by Wu & Cheng [15]
$W=4.8\times10^{-11}$, $U=4.8\times10^{-11}$, $\bar{\sigma} = 6.3 \times 10^{-5}$, V=0.01, G=3420

Based on the above data, W=4.8×10^{-4}, U=4.8×10^{-11}, G=3420, $\bar{\sigma}$=6.3×10^{-11}, and V=0.026. Therefore, from Eq. (1), h_c=0.24 μm and L_a=16%. Also, the average contact pressure is: p=1.57 GPa. These values are used to calculate the traction coefficient and the wear based on the method described in the previous section. Figure 7.1 compares these results to the experimental measurements by Wu & Cheng [15]. Note that they reported the wear per sliding distance which is simply obtained by dividing the wear rate Ω_{lub} (Eq. (16)) by the sliding speed, u_s.

As shown, the current approach correctly captures the trend of both the traction coefficient and the wear, while also yields reasonable magnitude for these parameters. The difference between the results (mostly visible in the wear at higher sliding values) is in part due to the lack of accurate properties of the oil used in the experiments. As discussed in Ref. [5], the free-volume rheological properties of the lubricant should be utilized in order to properly predict the results in TEHL. Note also that the largest discrepancy in the traction curve is at the lowest slide-to-roll ratio (S=0.001). This can be explained by the fact that it is not easy to experimentally capture traction at very small sliding. Therefore, the experimental value may correspond to the pure rolling which is theoretically zero (see the next section).

7.3.2. Comparison with the Mixed TEHL Numerical Results

To further investigate the validity of the present approach, the results predicted from this method are compared with those obtained from the full numerical solution of the mixed TEHL presented in Ref. [5]. The traction coefficient and wear rate results obtained from these two approaches are then compared for two different types of lubricant (with significantly different properties), each under two loading conditions.

Two types of lubricants investigated are the engine oil SAE 30 and Poly-α-olefin (PAO) oil. For SAE 30, the inlet viscosity and the limiting shear stress are according to the experiments in Ref. [5] while the pressure-viscosity and temperature-viscosity coefficients are approximated using its free volume properties in Ref. [5]. For PAO oil, a value of Z=0.45 was selected for this type of lubricant [18] while other properties are taken from Ref. [19]. These values are listed in Table 7.1.

Table 7.1. lubricant used for investigation

Lubricant	μ_0 at 20˚C (Pa.s)	Z	α (m^2/N)	K_T (K^{-1})	Λ_{lim}	ρ (Kg/m^3)
SAE 30	0.35	0.57	2.5×10^{-8}	0.045	0.091	888
PAO	0.04	0.45	1.5×10^{-8}	0.027	0.0434	826

Table 7.2 shows the geometry, load, rolling speed, and surface properties used in this study. The rolling speed is chosen in a way to yield the same dimensionless speed for both lubricants. Based on these data, the dimensionless parameters (used for determining h_c and L_a from Eq (1)) are:

W_1=2.2×10^{-5}, W_2=1.1×10^{-4}, U=1×10^{-11}, $\bar{\sigma}$=2×10^{-5}, and V=0.01. Also, for SAE 30 G=5700 and for PAO G=3420. Note that while the rolling velocity is kept constant, the slide-to-roll ratio is varied between S=0 (pure rolling) and S=1.5.

Table 7.2. operating conditions, geometry, and surface properties

E' (GPa)	R (cm)	u_r (m/s)	F (N)	B (cm)	$\bar{\sigma}$ (μm)	v (MPa)	f_c
228	2	0.13 (SAE30) 1.14 (PAO)	F_1=5000 F_2=25000	5	0.4	235	0.13

The thermal properties of the typical carbon steel surface chosen are k=60.5 W/mK and c_p =434 J/kgK [16], while for both lubricants they are assumed as k=0.145 W/mK and c_p=1880 J/kgK [20]. Note that the conductivity and the specific heat of the lubricant are only used for the full numerical solution, and they are not directly needed for the simplified present method. For calculating the wear, the dry wear coefficient is chosen as K =5×10^{-4} [15, 17], while a_χ=3×10^{-10} m, R_g=8.31 J/mole·K, E_a=49×10^3 J/mole, and t_0=3×10^{-12} are used for obtaining the fractional film defect [15].

As shown in the previous section, the central film thickness is a key factor in determining the traction coefficient, while the asperity load ratio is a key factor for both the traction coefficient and the wear rate. Therefore, the results obtained from the isothermal formulas (Eq. (1)) are first compared to those obtained from the thermal mixed EHL solution (Ref. [5]). These comparisons are illustrated in Figures 7.2 and 7.3.

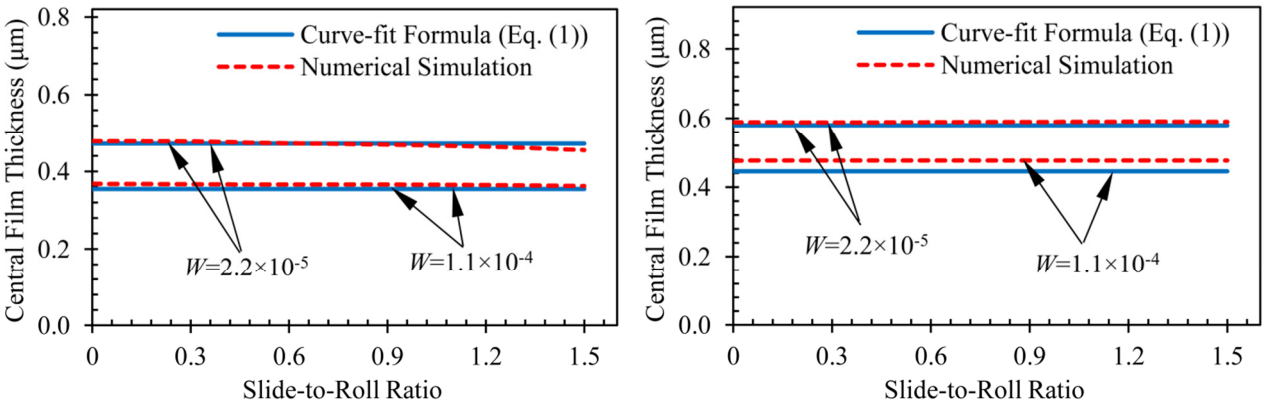

(a) (b)

Fig. 7.2. Central film thickness from isothermal formula (Eq. (1)) compared to those from numerical solution of mixed TEHL (Ref. [5]) (a): PAO (b): SAE30
U=1×10^{-11}, $\bar{\sigma} = 2 \times 10^{-5}$, V=0.01, G=3420(PAO), G=5700 (SAE30)

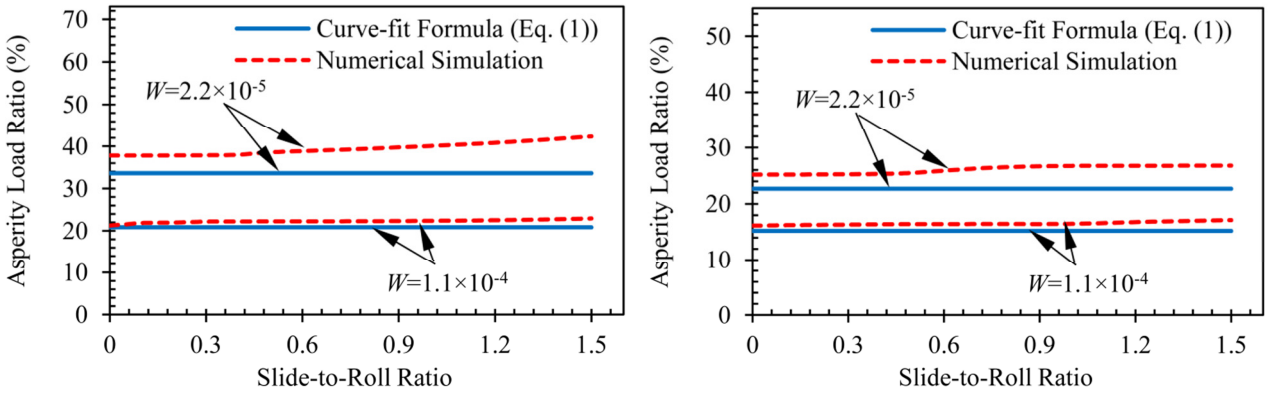

Fig. 7.3. Asperity load ratio from isothermal formula (Eq. (1)) compared to those from numerical solution of mixed TEHL (Ref. [5]) (a): PAO (b): SAE30
U=1×10^{-11}, $\bar{\sigma} = 2 \times 10^{-5}$, V=0.01, G=3420(PAO), G=5700 (SAE30)

From Figs. 7.2 and 7.3, it is observed that the results from the curve-fit expressions are in good agreement with the results from the numerical simulations. It is also noticed that the central film thickness and the asperity load ratio are not significantly affected by the slide-to-roll ratio. In fact, it was shown in Ref. [5] that at moderate rolling velocities, the temperature rise due to sliding does not significantly influence these values.

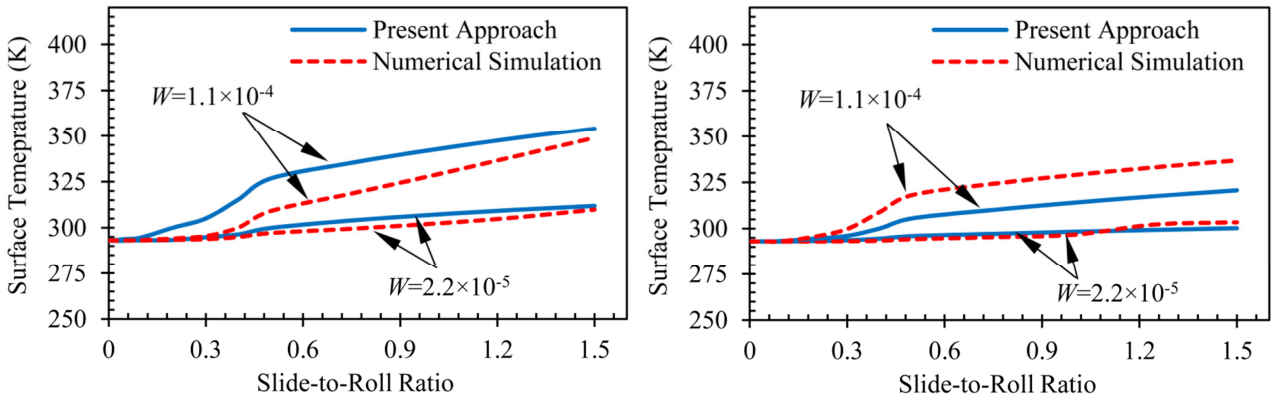

Fig. 7.4. Surface temperature from present method compared to those from numerical solution of mixed TEHL (Ref. [5]) (a): PAO (b): SAE30
U=1×10^{-11}, $\bar{\sigma} = 2 \times 10^{-5}$, V=0.01, G=3420(PAO), G=5700 (SAE30)

Figure 7.4 shows the surface temperatures predicted by the current method compared to those obtained from the full TEHL solution. As shown, there is a difference between the results especially at the higher loads. However, the present approach is able to capture the trend and also estimate reasonable values for the temperate which can later be utilized to predict the traction

coefficient and the wear. Note that in Fig. 7.4, the predicted surface temperatures are higher for PAO compared to SAE 30. This is because the dimensionless speed is equal for both cases, so the rolling speed (and therefore the sliding speed) is higher for the case of PAO (See Table 7.2).

Figure 7.5 compares the traction coefficient results obtained from the present approach with those obtained from the numerical simulation. As shown, the present method is able to predict the traction coefficient with reasonable accuracy compared to the full mixed TEHL solution. For both lubricants, the current approach correctly captures the trend and estimates the value of the traction coefficient. As observed, for PAO lubricant, the traction coefficient values are higher for the lighter load. This is because for this case, the dominant part of the traction coefficient is the asperity part which is larger for the lighter load (note that the traction coefficient is larger and not the traction force). On the other hand, for SAE 30 oil, the traction coefficient values are higher at the heavier load. In fact, because of the large pressure-viscosity coefficient and large limiting shear stress coefficient of this lubricant, the dominant part of the traction is the hydrodynamic part which significantly increases at the higher loads. As observed, the present method is capable of predicting these trends, and that it also gives a reasonable engineering evaluation for the amount of the traction coefficient. Note that in Fig. 7.5, the traction curves start from a non-zero value. This is because of the asperity part of the traction coefficient, which unlike the hydrodynamic part is not directly a function of the slide-to-roll ratio (See Eq. (14)). In fact, this part is theoretically zero at pure sliding (since there is no relative movement), but once there is a small sliding, its value becomes equal to $f_c \times (L_a/100)$.

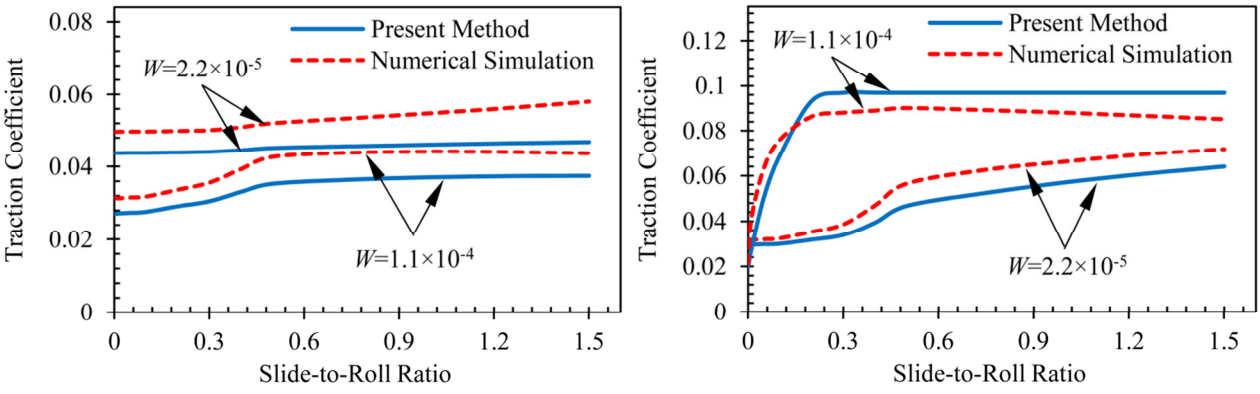

(a) (b)

Fig. 7.5. Traction coefficient from present method compared to those from numerical solution of mixed TEHL (Ref. [5]) (a): PAO (b): SAE30
U=1×10^{-11}, $\bar{\sigma} = 2 \times 10^{-5}$, V=0.01, G=3420(PAO), G=5700 (SAE30)

Figure 7.6 compares the wear rate results obtained from the present approach with those obtained from the numerical simulation where the vertical axis is shown in logarithmic scale. Again, the results reveal that the present method is a useful approach for evaluating the wear rate. As

shown, for both lubricants, the results are in a close agreement at lighter loads where there is smaller temperature rise. For the heavier load, the difference is more visible, but it can still be used as a reasonable approximation for the trend and the value of the wear rate at different sliding conditions.

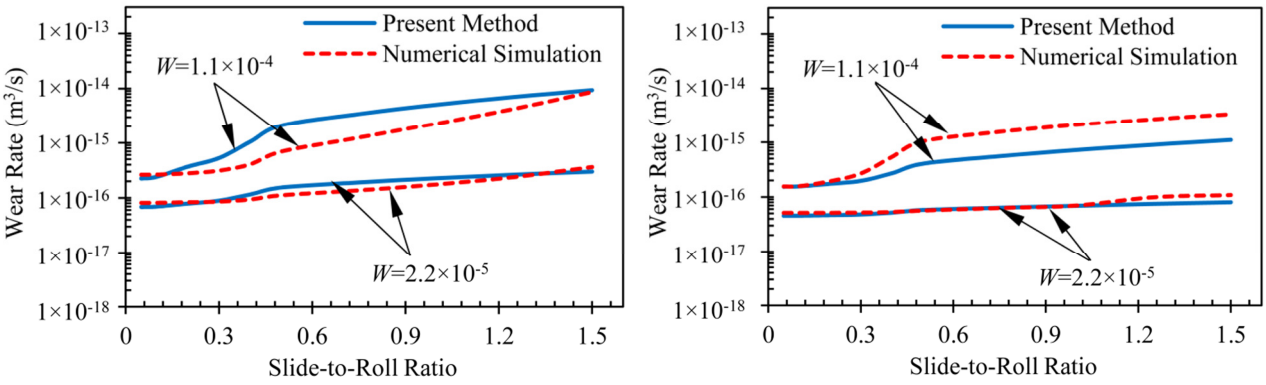

Fig. 7.6. Wear rate from present method compared to those from numerical solution of mixed TEHL (Ref. [5]) (a): PAO (b): SAE30 U=1×10^{-11}, $\bar{\sigma} = 2 \times 10^{-5}$, V=0.01, G=3420(PAO), G=5700 (SAE30)

7.4. Conclusions

An engineering approach is presented for rapid estimation of the traction coefficient and the wear rate in elastohydrodynamic lubrication of rough surfaces. The temperature rise within the mixed EHL contact is evaluated from the theory by Tian & Kennedy. The central film thickness and asperity load ratio obtained from the predictive formulas for the mixed EHL are then utilized together with the estimated surface temperature and the average contact pressure to approximate the traction coefficient and the wear rate. The results from this approach are compared to those from the thermal numerical solution of the mixed EHL (mixed TEHL) for different types of lubricants and different load levels. It is shown that this method can correctly capture the trend and yield reasonable estimation for both the traction coefficient and the wear rate.

Nomenclature:

a_χ	diameter of area associated with an adsorbed molecule, m
b	half Hertzian width, m
B	contact length, m
c_p	specific heat, J/kgK
E'	effective Young's modulus, 1/ E'=0.5[(1-ν_1^2)/E_1+(1-ν_2^2)/E_2], Pa
E_a	heat of oil's adsorption on surface, J/mole
f	traction coefficient
f_c	asperity friction coefficient
f_d	dry friction coefficient

F	total normal load, N
F_f	traction force, N
$(F_f)_a$	asperity traction force, N
$(F_f)_h$	hydrodynamic traction force, N
G	dimensionless material number, $E'\alpha$
h	film thickness, m
h_c	central film thickness, m
h_{min}	minimum film thickness, m
H	dimensionless film thickness, h/R
H_c	dimensionless central film thickness, h_c/R
H_{min}	dimensionless minimum film thickness, h_{min}/R
v	Vickers hardness, Pa
k	thermal conductivity, W/mK
K	dry wear coefficient
K_T	temperature-viscosity coefficient, K^{-1}
L_a	asperity load ratio (percentage)
p	average contact pressure, $F/2bB$, Pa
p_a	average asperity pressure, Pa
p_h	average hydrodynamic pressure, Pa
p_e	Peclet number, $u_s.b.\rho.c_p/2k$
q	total heat flux, W/m^2
q_a	asperity part of heat flux, W/m^2
q_h	hydrodynamic part of heat flux, W/m^2
R	equivalent contact radius, $[1/R_1 \pm 1/R_2]^{-1}$, m
R_g	gas constant, J/mole·K
S	slide-to-roll ratio, u_s/ u_r
t_0	fundamental time of molecule's vibration in the adsorbed state, s
T_s	surface temperature, K
T_0	inlet temperature, K
ΔT	temperature rise, K
u_r	rolling speed, $(u_1+u_2)/2$, m/s
u_s	sliding speed, $\|u_1-u_2\|$, m/s
U	dimensionless speed number, $\mu_0 u_r/E'R$
v	Vickers hardness, Pa
V	dimensionless hardness number, v/E'
w	load per contact length, F/B, N/m
W	dimensionless load number, $F/BE'R$ in line contact and $F/E'R^2$ in point contact
Z	viscosity-pressure index
α	pressure-viscosity coefficient, m^2/N
$\Lambda_{\lim}$	limiting shear stress coefficient
κ	ellipticity parameter
μ	lubricant viscosity, Pa.s
μ_0	inlet viscosity, Pa.s
ρ	density, kg/m^3
σ	standard deviation of the surface heights, m
$\bar{\sigma}$	dimensionless surface roughness number, σ/R
τ_{avg}	average shear stress of the lubricant, Pa
τ_{lim}	limiting shear stress, Pa
Ω_{lub}	lubricated wear volume, m^3/s
ψ	fractional film defect

7.5. References:

[1] Masjedi M, Khonsari MM. Film Thickness and Asperity Load Formulas for Line-Contact Elastohydrodynamic Lubrication With Provision for Surface Roughness. J Tribol-T Asme. 2012;134:011503.

[2] Masjedi M, Khonsari MM. On the Effect of Surface Roughness in Point-Contact EHL: Formulas for Film Thickness and Asperity Load. Tribol Int. 2015;82:228–44.

[3] Patir N, Cheng HS. Average Flow Model for Determining Effects of 3-Dimensional Roughness on Partial Hydrodynamic Lubrication. J Lubric Tech-T Asme. 1978;100:12-7.

[4] Zhao YW, Maietta DM, Chang L. An Asperity Microcontact Model Incorporating the Transition from Elastic Deformation to Fully Plastic Flow. J Tribol-T Asme. 2000;122:86-93.

[5] Masjedi M, Khonsari MM. Theoretical and experimental investigation of traction coefficient in line-contact EHL of rough surfaces. Tribol Int. 2014;70:179-89.

[6] Beheshti A, Khonsari MM. A Thermodynamic Approach for Prediction of Wear Coefficient Under Unlubricated Sliding Condition. Tribol Lett. 2010;38:347-54.

[7] Tian XF, Kennedy FE. Maximum and Average Flash Temperatures in Sliding Contacts. J Tribol-T Asme. 1994;116:167-74.

[8] Bair S, Winer WO. Rheological Model for Elastohydrodynamic Contacts Based on Primary Laboratory Data. J Lubric Tech-T Asme. 1979;101:258-65.

[9] Bair SS, McCabe C. High-pressure rheology for quantitative elastohydrodynamics. 1st ed. Amsterdam ; Boston: Elsevier; 2007.

[10] Roelands CJA. *Correctional Aspects of the Viscosity-Temperature- Pressure Relationship of Lubricating Oils*. Groningen, Netherlands: Druk, V.R.B., ; 1966.

[11] Archard JF. Contact and Rubbing of Flat Surfaces. J Appl Phys. 1953;24:981-8.

[12] Stolarski TA. A Probabilistic Approach to Wear Prediction. J Phys D Appl Phys. 1990;23:1143-9.

[13] Kingsbury EP. Some Aspects of the Thermal Desorption of a Boundary Lubricant. J Appl Phys. 1958;29:888-91.

[14] Rowe CN. Some Aspects of Heat of Adsorption in Function of a Boundary Lubricant. Asle Trans. 1966;9:101-&.

[15] Wu SF, Cheng HS. A Sliding Wear Model for Partial-Ehl Contacts. J Tribol-T Asme. 1991;113:134-41.

[16] Incropera FP, DeWitt DP. Introduction to heat transfer. 4th ed. New York: Wiley; 2002.

[17] Rabinowicz E. Friction and wear of materials. 2nd ed. ed. New York ; Chichester: Wiley; 1995.

[18] Khonsari MM, Booser ER. Applied tribology : bearing design and lubrication. 2nd ed. Chichester, England ; Hoboken, NJ: Wiley; 2008.

[19] Hoglund E. The Relationship between Lubricant Shear-Strength and Chemical-Composition of the Base Oil. Wear. 1989;130:213-24.

[20] Hamrock BJ. *Fundamentals of Fluid Film Lubrication*. New York: McGraw-Hill; 1994.

Chapter 8: Film Thickness, Traction and Wear in Spur Gears: Applications of Mixed EHL Models

8.1. Introduction

Lubrication regime in gears—which are among the key components of many machinery—is governed by the so-called line-contact elastohydrodynamic lubrication (EHL). Considerable research has been conducted to determine the film thickness in line-contact EHL [1-5]. Moreover, numerous studies focused on the thermal effects in such applications considering the significant influence of the temperature rise on the traction coefficient and the wear rate [6-15]. In order to properly predict the lubricant viscosity, the free volume theory [16] was utilized in a number of recent publications [17-23], while the effect of limiting shear stress was also investigated in the literature [17, 18, 24-26].

Because the thickness of the lubricant film between the contacting surfaces is generally small in EHL applications, the surface asperities experience intimate contact where the regime is referred to as the mixed EHL. The surface roughness is treated using two main approaches: statistical and deterministic. Within the context of deterministic rough EHL analysis, some attempts were initially made to incorporate the real surface features like the waviness or irregularities into the EHL equations [27-31]. However, the first comprehensive deterministic modeling of line-contact EHL using a random rough surface was introduced by Chang [32]. Since then, several studies focusing on the deterministic modelling of the rough surfaces have been published. See for example, [33-39]. Studies dealing with statistical rough EHL generally follow the work of Johnson et al. [40] who pioneered the so-called load-sharing concept where they used the Greenwood-Williamson [41] asperity micro-contact model to evaluate the role of the surface roughness. Gelinck & Schipper [42] utilized this method to predict the film thickness in the rough line-contact EHL [43]. Later, other researchers applied this method to study the mixed EHL of journal bearings [44] and gears [45-47].

Another method within the category of statistical treatment of surface roughness is the numerical solution to the modified Reynolds equation [48] along with the asperity deformation equations. This approach was first used by Majumdar & Hamrock [49] and later by other researchers [23, 50, 51]. Most recently, Masjedi & Khonsari used the asperity model by Zhao et al. [52] to derive predictive formulas for the film thickness [53] and later extended that to include different surface patterns [54]. The traction coefficient was also investigated using a similar method which also included the heat generation [55].

Let us now turn our attention to analysis of adhesive wear. Since the publication of what is commonly referred to as the Archard's wear law for dry contact of two bodies undergoing sliding motion [56], there have been numerous attempts to extend the analysis to predict the wear volume in the lubricated contacts. One of the earliest approaches is due to work of Rowe [57] who extended the dry wear to the lubricated condition using Kingsbury's concept of thermal desorption [58]. Later, Stolarski [59, 60] continued Rowe's approach by including the asperity load effect to predict the adhesive wear in the lubricated sliding contacts. Since then, many other studies have been reported that concentrate on the prediction of wear in the boundary or the mixed lubrication regimes [61-70]. Most recently, Beheshti & Khonsari [71] proposed a method to estimate the wear coefficient using continuum damage mechanic approach. They later utilized their achievement along with the load sharing concept [40] and the statistical asperity micro-contact equations [72, 73] to predict the wear rate in the mixed EHL regime [74].

The present study is devoted to the application of statistical rough EHL to analyze the performance spur gears in terms of film thickness, traction, wear rate, and lubricant starvation effect. For this purpose, the model developed in Ref. [55]—which is based on the simultaneous solution of the Reynolds, asperity contact, and energy equations— is utilized to study the performance of spur gears. The film thickness and the asperity load are calculated along the line of action (LoA), and the results are compared to those obtained by the isothermal formulas for the mixed EHL [53]. On the other hand, the predicted traction coefficient and the wear rate along the LoA are compared to those obtained from a simplified engineering approach developed recently [75]. Also studied is the effect of lubricant starvation on the film thickness, asperity load, traction coefficient, and wear rate along the LoA.

8.2. Model

We recently developed an approach to treat the EHL of rough surfaces [53, 76]. Based on extensive set of simulations using that approach, we presented convenient formulas to predict the film thickness and asperity load ratio. These expressions for line contact, which is the topic of the present study, can be found in Chapter 2.

For the investigation of the traction coefficient, since it is highly dependent on the viscosity, we developed another model [55]—hereinafter referred to as the mixed TEHL—which also considers the heat generation within the contact area not only by the shear heating of the lubricant, but also by the friction of surface asperities.

For line contact, the traction coefficient is written as the sum of asperity and hydrodynamic parts as [55]:

$$f = \left(\frac{L_a}{100}\right) f_c + \frac{1}{w}\int \Lambda_{\lim} p_h \left(1 - e^{\frac{-\mu . u_s}{\Lambda_{\lim} \cdot p_h h}}\right) dx \qquad (1)$$

Note that the asperity part is simply the product of the asperity friction coefficient, f_c, and the asperity part of the total load (L_a/100). The hydrodynamic part is written based on the limiting shear stress of the lubricant [19, 77].

For prediction of lubricated wear rate, the extension of Archard theory [56] to the mixed lubrication regime using fractional film defect, ψ, is utilized [57-60]:

$$\Omega_{\text{lub}} = K\psi(\frac{L_a}{100})\frac{F.u_s}{v}; \quad \psi = 1-\exp\left\{-\left[\frac{a_\chi}{u_s t_0}\exp(-\frac{E_a}{R_g T_s})\right]\right\} \tag{2}$$

It is import to mention that for TEHL analysis, the free-volume theory is the preferred method of predicting the changes in the lubricant's density and viscosity with both pressure and temperature [19, 55]. In the absence of lubricant's specific properties, the equation by Dowson and Higginson [1] can be used for the prediction of lubricant's density while the commonly-used Roelands equation [78] is commonly utilized for the prediction of lubricant's viscosity at moderate pressures.

Beside the comprehensive TEHL model, we also developed an engineering approach for the rapid evaluation of the traction coefficient and the wear rate in the mixed EHL [75]. For this purpose, the method developed by Tian & Kennedy for estimation of flash temperature [79] is utilized together with the results from the predictive formulas in Ref. [53] to evaluate the traction coefficient and the wear rate. More details can be found in Chapter 7.

8.3. Verification

Before delving into presenting results for gears, in this section, we present a series of verification where the results of the film thickness, traction coefficient, and wear rate in the mixed EHL are compared with the published data available in the literature.

8.3.1. Film Thickness

Figure 8.1 compares the film thickness obtained from the present TEHL simulations with those predicted by the isothermal formulas for the mixed EHL [53], as well as the results by Zhu & Wang [80] which are based on the deterministic treatment of the surface roughness. The input parameters used by Zhu & Wang are: E'=226 GPa, R=12.7 mm, μ_0=0.026 Pa.s, α=1.25×10^{-8} m^2/N, σ=0.6 μm, and a maximum Hertzian pressure of 2.277 GPa. Since the hardness is not reported in [80], a Vickers hardness of v=2.35 GPa (equals to about 20 Rockwell C) is used as input. For the TEHL simulations, typical thermal properties of k=60.5 W/mK and c_p =434 J/kgK for steel surface [81] and k=0.145 W/mK and c_p=1880 J/kgK for the lubricant [82] are used.

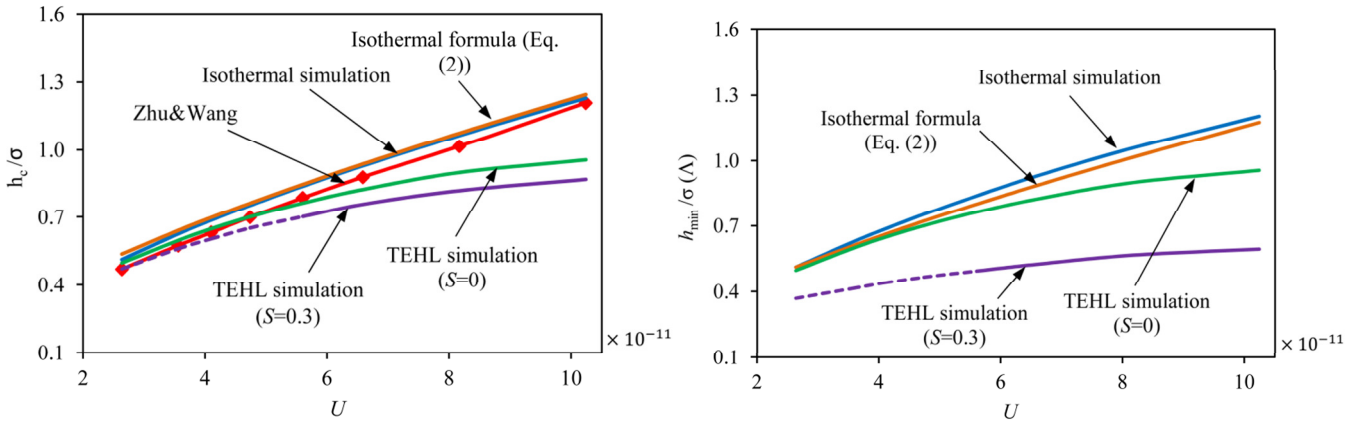

Fig. 8.1. film thickness from isothermal and thermal (TEHL) simulations compared to those from isothermal formulas and simulations by Zhu & Wang [80]
(a) central film thickness (b) minimum film thickness

Figure 8.1(a) shows the ratio of the central film thickness to the surface roughness against the dimensionless speed. As shown, the central film thickness results from the isothermal simulation are very close to those predicted by the curve-fit formula for the mixed EHL (Ref. [53]). These results are also in agreement with mean film thickness values obtained from the deterministically-based model by Zhu & Wang [80]. Also plotted in Fig. 8.1(a) is the thermal results for the slide-to-roll ratio of S=0 (zero sliding) as well as S=0.3. As shown, the thermal results are close to isothermal results at lower speeds, but start to deviate at higher speeds. This is mostly due to the shear heating at the inlet, which is generally negligible at moderate rolling velocities, but becomes significant at higher speeds which highly influences the film thickness [83]. Note that the contact load is very high in this study (over 2 GPa), which signifies this effect.

Figure 8.1(b) shows the ratio of the minimum film thickness to the surface roughness (which is referred to as the film parameter $\Lambda = h_{min}/\sigma = H_{min}/\bar{\sigma}$) against the dimensionless speed. As shown, the minimum film thickness results from the isothermal simulation are in agreement with those predicted by the curve-fit equation [53]. It is also shown that the results from the thermal solution at zero sliding (S=0) are close to those from isothermal solution at lower speeds, but deviates from each other at higher speeds. Again, this is a consequence of the general film thickness drop due to viscous heating at the inlet [83]. On the other hand, unlike the central film thickness, the minimum film thickness significantly drops at the slide-to-roll ratio of S=0.3, even at lower rolling speeds. This accounts for the viscous heating due to sliding, which is shown to affect the minimum film thickness much more significantly than the central film thickness [8, 55]. There are also studies (for example Hsu & Lee [10]) that estimate the drop in the minimum film thickness by the slide-to-roll ratio. Due to the significant decrease in the film thickness at S=0.3, at some points, the film parameter drops below 0.5 which warns the transition into the

boundary lubrication regime where the modified Reynolds equation by Patir and Cheng [48] is not recommended. These points are marked by dashed lines in Fig. 8.1.

8.3.2. Traction Coefficient and Wear

In this section, the results from the TEHL simulations are validated with the experiments by Wu & Cheng [62] who measured the traction coefficient and wear in the mixed elastohydrodynamic lubrication regime. The experiments were performed for a range of slide-to-roll ratio. In their study, these input parameters were used: R=5.4 mm, B=6.35 mm, T_0=315 K, u_r=1.83 m/s, and a maximum Hertzian pressure of 2 GPa. Also, σ=0.34 μm, and v=6 GPa (56 Rockwell C). The lubricant inlet viscosity is μ_0=0.0325 Pa.s and its temperature-viscosity coefficient is estimated as K_T=0.03 K^{-1} based on the data available in [16]. Also, f_c=0.12 (a typical value, [55]), $\alpha=1.5\times10^{-8}$ m^2/N, and Λ_{lim}=0.06 (which well suits the traction curve) are assumed. For estimating wear, the coefficients needed in Eq. (2) are: R_g=8.31 J/mole·K, $a_\chi=3\times10^{-10}$ m, $t_0=3\times10^{-12}$ s, and $E_a=49\times10^3$ J/mole [62], while $K=5\times10^{-4}$ [62, 84]. Also, for steel surface k=60.5 W/mK and c_p =434 J/kgK [81], while for the lubricant k=0.145 W/mK and c_p=1880 J/kgK [82].

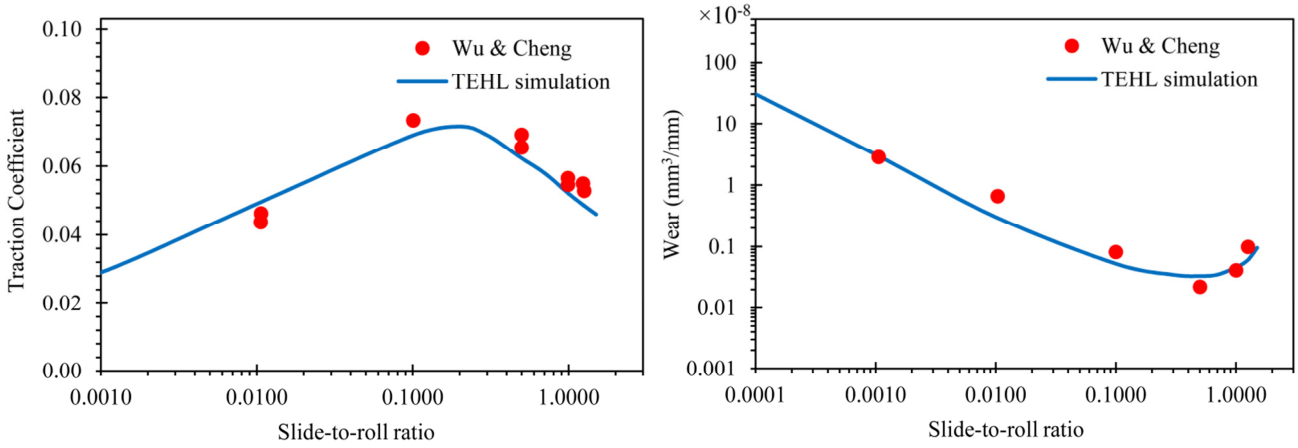

(a) (b)

Fig. 8.2.: Results from current simulation compared to experimental results by Wu & Cheng [62] (a) traction coefficient (b) wear per sliding distance

As shown in Fig. 8.2, the TEHL results are in agreement with the experimental data for both the traction coefficient and the wear. Note that the wear per sliding distance is reported in the experiment data, which

As plotted in Fig. 8.2(a), the traction coefficient goes up as the slide-to-roll ratio increases. However, after a certain point, the decrease in the lubricant's viscosity due to the heat generation causes the traction coefficient to drop. On the other hand, as plotted in Fig 8.2(b), the wear per sliding distance decreases with increasing the slide-to-roll ratio up to a certain point (around S=0.5) after which it begins to increase. This is due to the contribution of the opposing effect of the sliding speed and the surface temperature in the fractional film defect (Eq. (2)), where the

high temperature rise at large slide-to-roll ratios dominates the effect of the sliding speed. Note that the experimental data is based on the wear per sliding distance (obtained by eliminating u_s in Eq. (2)) which means that the specimen at smaller slide-to-roll ratio has undergone more rolling (more cycles of rotations).

8.4. Mixed EHL of Spur Gears

Having verified the validity of the approach, in this section, we proceed to apply the developed model to investigate the performance of a spur gear operating under the mixed line-contact EHL regime.

8.4.1. Variation of input parameters along LoA

The contact between the gear's teeth takes place along the line of action (LoA) where the pinion and gear can be considered as two cylinders with the variable radii of R_1 and R_2.

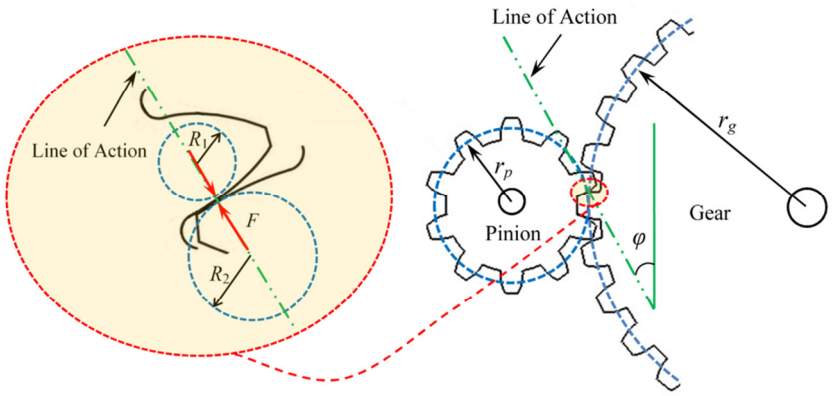

Fig. 8.3. Contact between a pair of gear teeth

As the contact point moves along the tooth, the radius of curvature, speed, and transmitted load vary along the LoA. The pitch radius of the pinion (r_p) and the gear (r_g) are [85]:

$$r_p = \frac{1}{2}(N_p \times m),\ r_g = \frac{1}{2}(N_g \times m) \tag{3}$$

The equivalent radius of curvature along the LoA is [86]:

$$R = (1/R_1 + 1/R_2)^{-1};\ R_1 = r_p \sin\varphi + \varepsilon,\ R_2 = r_g \sin\varphi - \varepsilon \tag{4}$$

where the pressure angle φ is as the angle between the LoA and the line tangent to both pinion and gear pitch circles (See Fig. 8.3).

The rolling and sliding velocities along the LoA are [86]:

$$u_r = (u_1 + u_2)/2,\ u_s = |u_1 - u_2|/2;\quad u_1 = 2\pi n_p R_1,\ u_2 = 2\pi n_g R_2 \tag{5}$$

The contact load carried by each tooth is another varying parameter because the number of teeth involved along the LoA changes. At the initial point of contact, two pairs of teeth are involved where the contact load varies linearly from 1/3 to 2/3 of the total load. The load then jumps to the total load when only one pair is in contact. It again drops to 2/3 when another pair comes into contact, and reduces to 1/3 at the end of the LoA [45, 86].

Figure 8.4 shows the variations of the contact radius, load, rolling and sliding speeds, and the slide-to-roll ratio along the LoA. This is for a pair of pinion-gear with N_p=32 and N_g=96, m=0.005 m, B=0.05 m, and φ=20˚. The contact load is F=25 KN and the pinion speed is 100 RPM. As shown in Fig. 8.4(a), the equivalent contact radius continuously increases along the LoA. Also, the load varies as described above, where the peak belongs to the points where only one pair of teeth is engaged. As shown in Fig. 8.4(b), the rolling speed monotonically increases along the LoA. In contrast, the sliding speed decreases starting from the initial point of contact to the pitch point where it becomes nil (pure rolling). It again increases after the pitch point as the contact point moves toward the contact end. Also plotted in Fig. 8.4(b) is the slide-to-roll ratio which is the ratio of the sliding speed to the rolling speed.

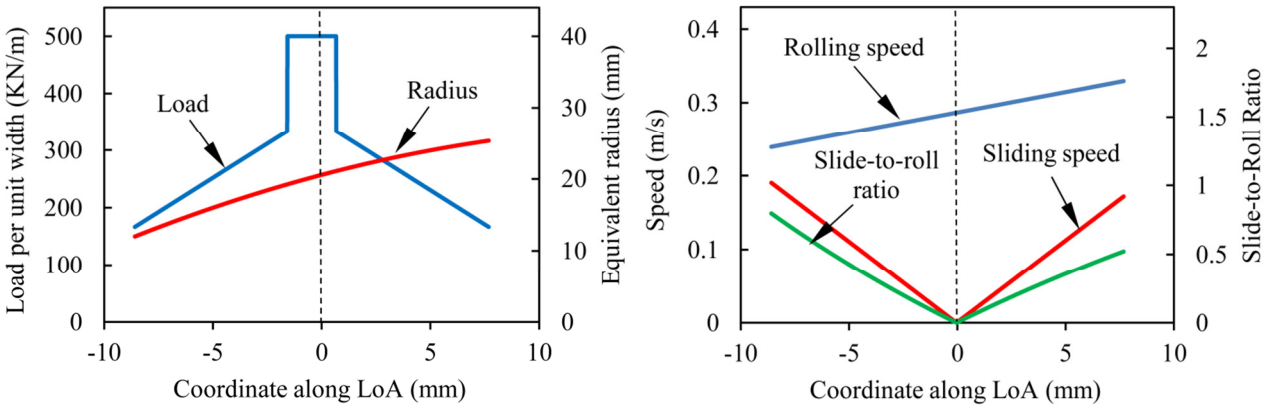

(a) (b)

Fig. 8.4. Variations of gear parameters along LoA
(a): radius and load (b): rolling/sliding speed and slide-to-roll ratio

Based on the loading and geometry of the gears explained in the previous section and the surface and lubricant properties, the dimensionless input parameters can be obtained. Since the load, speed, and contact radius changes along the line of action, the dimensionless load, speed, and roughness also vary along this line. Therefore, each point along the LoA represents a rough EHL problem, and a separate simulation should be performed for each point. This signifies the advantage of using isothermal formulas or engineering estimations which can save considerable amount of time.

For the pair of gears investigated in the previous section (Fig. 8.4), considering the gear surface as steel (E'=228 GPa) and the lubricant as SAE30 (μ_0=0.35 Pa.s at T_0=293 K), the variations of dimensionless load W and speed U along the LoA are plotted in Fig. 8.5(a). Also, the dimensionless roughness is shown in Fig. 8.5(b) for three levels of the surface roughness: slightly rough (σ=0.1 μm), fairly rough (σ=0.5 μm), and considerably rough (σ=1 μm).

For the case of dimensionless load $W=F/(BE'R)$, the two parameters vary along the LoA are: contact load and contact radius (see Fig. 8.4). At the first stage of the contact where two pairs of teeth are involved, both the load and radius are increasing which result in a slight increase in W (Fig. 8.5(a)). At the second stage where only one pair of teeth is in contact, the sudden increase in the load causes a jump in W. During this stage, the load is constant but the radius is increasing, which result in decreasing W. For the last stage, the load decreases and the radius increases, which results in a steep decrease in W. On the other hand, the combination of increasing radius and rolling speed (Fig. 8.4) results in a slight decrease in the dimensionless speed $U= \mu_0 u_r/(E'R)$ along the LoA (Fig. 8.5(a)). Also, the increase in the contact radius along the LoA causes a decrease in the dimensionless surface roughness $\bar{\sigma} = \sigma/R$ as shown in Fig. 8.5(b). Note that for σ=1 μm, at the beginning of the LoA, the dimensionless roughness exceeds the maximum range of the formulas which is $\bar{\sigma} \leq 5\times10^{-5}$ [53]. These points are marked by dotted lines in Fig. 8.5. Caution should be taken while using the formulas for these points (see the next section).

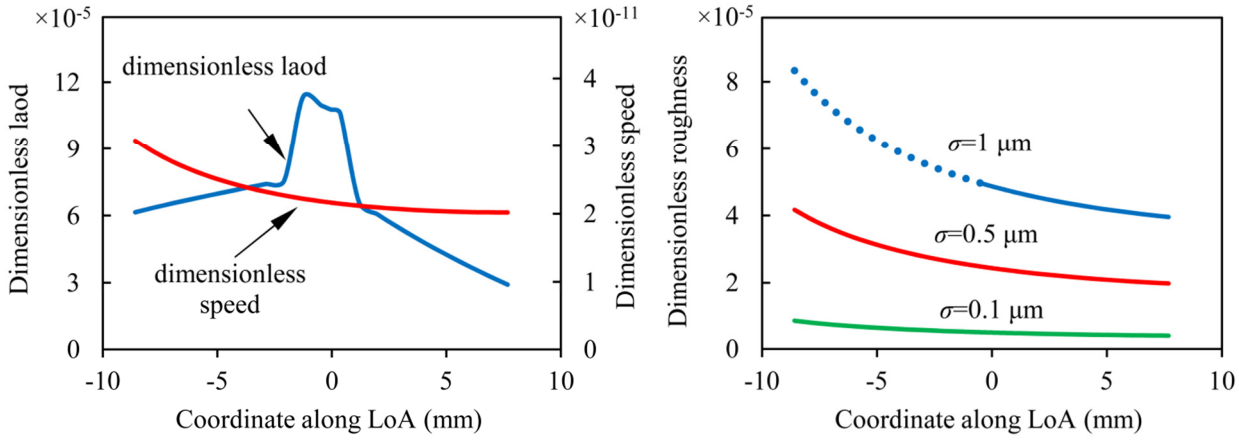

Fig. 8.5. Variations of dimensionless parameters along LoA
(a): load and speed (b): surface roughness

To investigate the film thickness and the asperity load, as well as the traction coefficient and wear rate along the gear's LoA, the thermo-elastohydrodynamic (TEHL) model (described in Section 2) is utilized. The free-volume rheological properties as well as thermal properties of the SAE30 lubricant are taken from Ref. [55]. Also, the limiting shear stress for this lubricant is assumed as Λ_{lim}=0.091 as measured in Ref. [55]. The variations of dimensionless load W and speed U are according to Fig. 8.5(a). For each case, the simulations are done for three levels of

surface roughness (σ=0.1 μm σ=0.5 μm, and σ=1 μm) with the variations of $\bar{\sigma}$ shown in Fig. 8.5(b). The surface hardness is assumed to be 20 Rockwell C (equal to the Vickers hardness of about v=2.35 GPa). This yields a dimensionless hardness of $V=v/E$=0.01. Also, as the experimental data shows according to Ref. [55], the asperity friction coefficient changes with the surface roughness. Therefore, in the current simulations, it is assumed to be f_c=0.12 for the lowest roughness (σ=0.1μm), f_c=0.135 for the medium roughness (σ=0.5) μm, and f_c=0.15 for the largest roughness (σ=1 μm). It should also be mentioned that since the free-volume properties of the lubricant is used in the TEHL simulations, there is no need for the dimensionless material number G. However, for the use in the isothermal formulas, the pressure-viscosity coefficient of α=2.5×10^{-8} m^2/N is used for SAE30 which yields $G= E'\alpha$=5700 [55].

8.4.2. Film Thickness and Asperity Load Ratio

Figure 8.6 shows the changes in the central and minimum film thickness along the LoA. In each case, the results from the simulations are compared to those obtained from the isothermal formulas. As shown, both the central and minimum film thickness have a general ascending trend along the LoA which is attributed to the increasing rolling velocity along this line (See Fig. 8.4).. However, they have a sudden decrease in the middle section which is due to the jump in the contact load (Fig. 8.4).

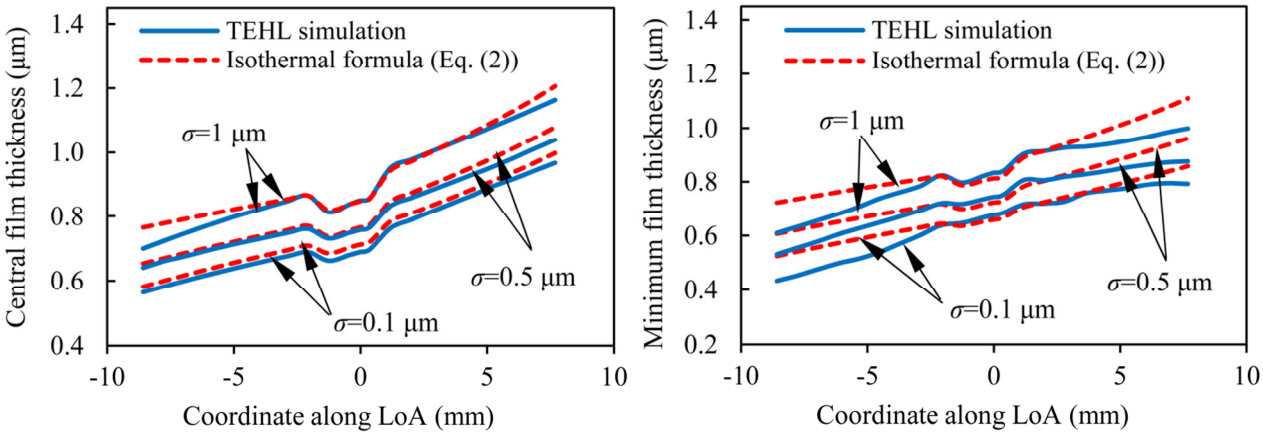

Fig. 8.6. results from TEHL simulations and isothermal formulas along LoA
(a): central film thickness (b): minimum film thickness

As Fig. 8.6(a) shows, for the central film thickness, the results from the current simulations show a very good agreement with those from the isothermal central film thickness formula for the mix EHL [53]. As mentioned in Ref. [55], for the regular rolling speeds, the central film thickness does not appreciably change due to the heat generation caused by the sliding. It should be noticed that for σ=1 μm, the notable difference at the beginning of the contact is due to the large values of dimensionless roughness (see Fig. 8.5(b)) which is out of the maximum range allowed in the isothermal formulas ($\bar{\sigma} = 5 \times 10^{-5}$) [53].

As shown in Fig. 8.6(b), there is a considerable difference between the minimum film thickness values obtained from the current simulations and those predicted by the isothermal minimum film thickness formula [53], especially at the beginning and end of the contact. According to Ref. [55], unlike the central film thickness, the minimum film thickness undergoes a significant drop due to the heat generation caused by the sliding. It is observed form Fig. 8.6(b) that for all roughness values, the difference between the isothermal and thermal results are more noticeable at the beginning and end of the contact. It can be explained by the fact that the slide-to-roll ratio is larger at these points (see Fig. 8.4(b)) which results in a higher contact temperature which affects the minimum film thickness more significantly.

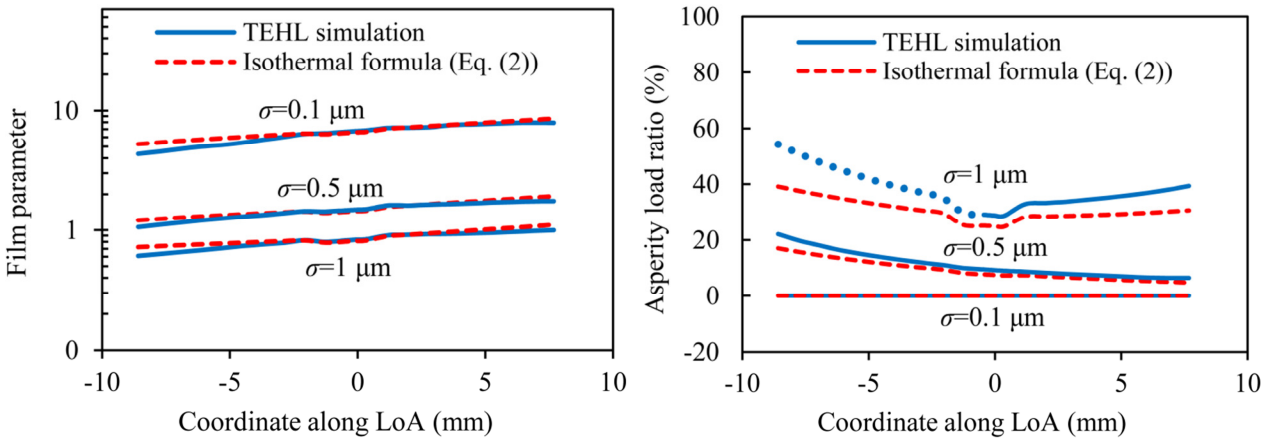

Fig. 8.7. results from TEHL simulations and isothermal formulas along LoA
(a): film parameter (b): asperity load ratio

Although increasing the roughness yields a thicker film as illustrated in Fig. 8.6, it causes a drop in the ratio of the film thickness to the surface roughness. The film parameter Λ which is the ratio of the minimum film thickness to the surface roughness is then plotted in Fig. 8.7(a) where the vertical axis is shown in logarithmic scale. As shown, for the lowest roughness value (σ=0.1 μm), the film parameter varies between about 5 to 9, which implies that there is no asperity contact. By increasing the roughness by 5 fold (σ=0.5 μm), the film parameter drops to the range of about 1.2 ~ 2 which means that the mixed EHL regime prevails. Further, doubling the surface roughness (σ=1μm) decreases the film parameter to about 0.7 to 1 which means that the system is approaching the boundary lubrication regime.

The corresponding asperity load ratios are plotted in Fig 8.7(b). As shown, the asperity load ratio is nil for σ=0.1 μm, while it varies between 6% to 22% for σ=0.5 μm, and 39% to 54% for σ=1 μm. The asperity load has a general decreasing trend along the LoA which is due to the increasing rolling speed along this line. However, it experiences a drop at the middle stage due to the decrease in the contact load (Note that increasing the load increases the asperity load but decreases the asperity load ratio [53]). Moreover, the asperity load ratio may have an increasing

trend at the last stage of the contact (visible for σ=1 μm) where the effect of decreasing load dominates the effect of increasing the rolling speed. It is also shown in Fig. 8.7(b) that there is an agreement between the current results and those obtained from isothermal formula for asperity load [53]. As mentioned in Ref. [55], for moderate rolling speeds, the isothermal asperity load ratio formula can still be used at higher slide-to-roll ratios. It should be mentioned that for σ=1 μm, the noticeable difference between the results of the thermal simulation and isothermal formula at the beginning of the LoA is due to the large values of dimensionless roughness (see Fig. 5(b)) which is out of the valid range for the isothermal formula (See Fig. 5(b)). These points are shown in dotted line in Fig. 7(b).

8.4.3. Traction Coefficient and Wear Rate

Fig. 8(a) shows the variations of the traction coefficient along the LoA. At the first stage of the contact, the load increases but the slide-to-roll ratio decreases (see Fig. 8.4). The combination of these two opposing factors may result in increasing or decreasing the traction coefficient. At the second stage, the load is constant, but the slide-to-roll ratio drops to zero (pure rolling at pitch point) and then increases again. This directly results in the traction coefficient dropping to its minimum at the pitch point and increasing afterwards. At the last stage, the load decreases, but the slide-to-roll ratio increases and the combination of these factors determines the trend.

It is interesting to note that in Fig. 8(a), the average traction coefficient along the LoA is calculated as 0.068 for σ=0.1 μm, 0.072 for σ=0.5 μm, and 0.087 for σ=1 μm. This means that increasing the surface roughness by five fold (from σ=0.1 μm to σ=0.5 μm) has only a mild effect on the traction coefficient, especially at the last stage of the contact as seen in Fig. 8.8(a). This can be explained by Fig. 8.7(b), where the L_a is about 22% at the beginning of the contact, but only 6% at the end. However, for the roughness surface (σ=1 μm), the traction coefficient increases significantly, as a results of notable contributions of the surface asperities. Note that in Fig. 8.8(a), the traction coefficient is non-zero at the pitch point when there is the surface roughness contribution. This is because the sliding does not directly affect the asperity part of the traction coefficient (See Eq. (1)). Theoretically, this part is zero at the pitch point because of no relative motion. However, it becomes equal to $f_c \times (L_a/100)$ once there is a slight sliding.

Plotted in Fig. 8.8(b) is the wear rate along the line of action. These results reveal that surface roughness has a more pronounced effect on the wear rate compared to the traction coefficient. As shown, for σ=0.1 μm, the wear rate is very small compared to the higher roughness values. In fact, the average wear rate along the LoA is about 4.78×10^{-23} m^3/s for σ=0.1 μm which is orders of magnitude smaller than those for the higher roughness values (1.04×10^{-23} m^3/s for σ=0.5 μm and 3.18×10^{-23} m^3/s for σ=1 μm). This is because the asperity load ratio is almost nil at σ=0.1 μm which directly results in a negligible wear rate (Eq. (2)). Increasing the roughness by 5 fold (σ=0.5 μm) yields a much higher wear rate as shown in Fig. 8.8(b). Further increasing the roughness (σ=1 μm) increases the wear rate (because of the higher asperity load), but its order is

comparable with that of σ=0.5 µm. The nonlinear trend of the wear rate along the LoA is due to contribution of multiple factors. While the wear rate is a direct function of the contact load, asperity load ratio, and sliding speed (Eq. (2)), the fractional film defect is also a function of sliding speed and surface temperature, all vary along the LoA. In general, the wear rate is larger at the beginning of the contact compared to the end, mostly due to a larger asperity load ratio (see Fig 8.7(b)). The local maximum in the second stage of the contact is due to the increase in the contact load, while the sliding speed is still large to cause a high wear rate. The wear rate suddenly drops to zero at the pitch point, where theoretically there is no wear at this point (pure rolling).

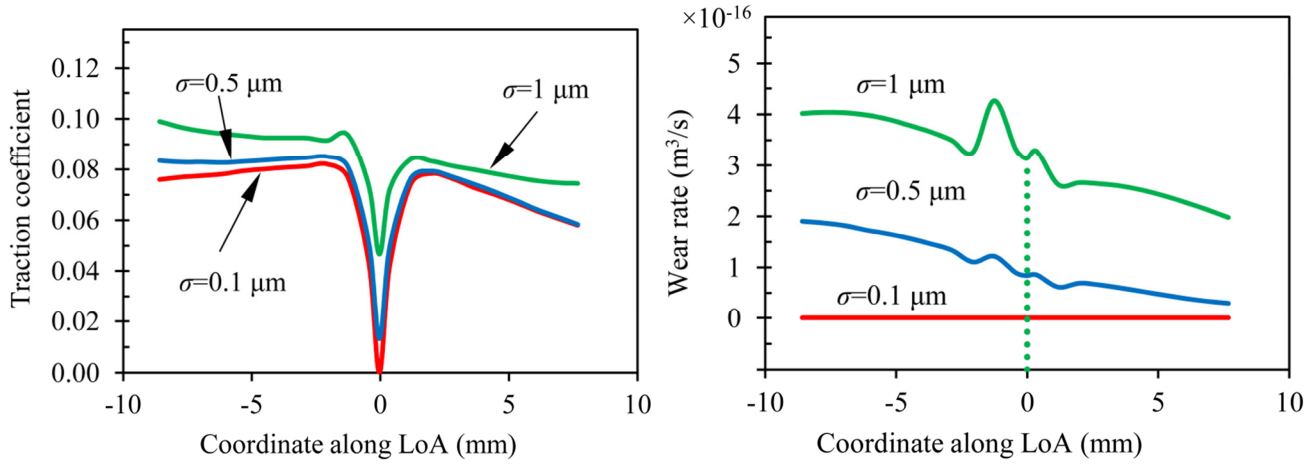

(a) (b)

Fig. 8.8. Results from TEHL simulations along LoA (a): traction coefficient (b): wear rate

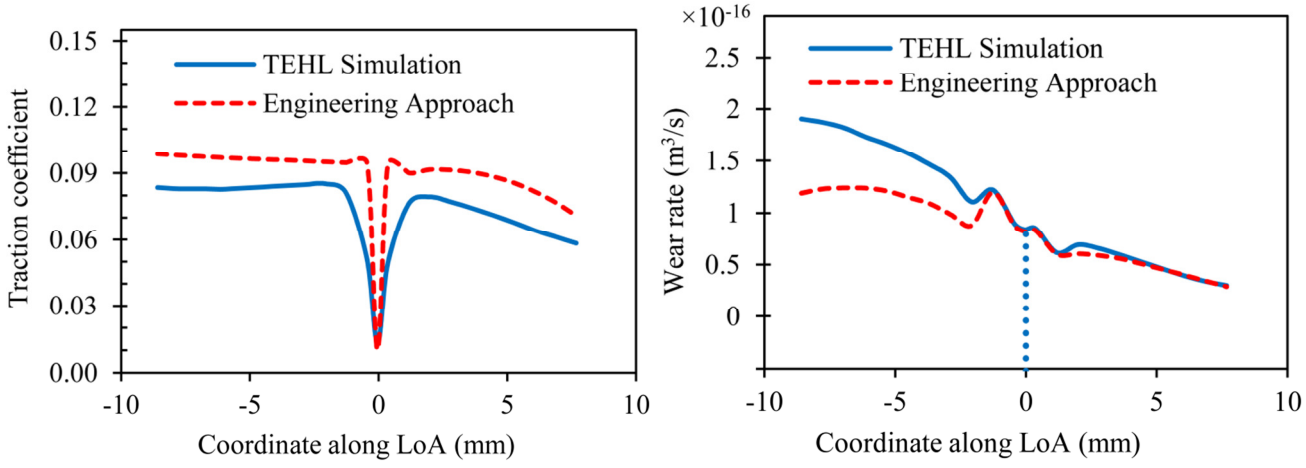

(a) (b)

Fig. 8.9. results from TEHL simulation compared to estimations by the engineering approach [75] (σ=0.5 µm) (a): traction coefficient along LoA (b): wear rate along LoA

Figure 8.9 shows a comparison between the results from the TEHL simulations for the roughness value of σ=0.5 μm and those obtained from a recently-developed simplified approach [75] (See Appendix B). As mentioned before, this approach is based on the results of the isothermal formulas, and an approximate contact flash temperature.

As Fig. 8.9 shows, the engineering approach [75] is able to capture the trend of both the traction coefficient and the wear rate, while also estimates reasonable values for them. Note that the difference between the results is partly because the simplified method is based on using the Roelands equation for prediction of the viscosity, while the TEHL solution is based on the free-volume properties of the lubricant. The advantage of using this engineering method is that there is no need to perform a time-consuming numerical simulation for every point along the LoA.

8.4.4. Effect of Starvation

The results in the previous section were obtained assuming a fully-flooded inlet. Inadequate supply of oil at the inlet results in decreasing the lubricant's flow rate where the regime is referred to as the starved lubrication. Starvation occurs in many practical applications and directly influences the film thickness. Lower film thickness leads into larger asperity contact which also increases the traction coefficient and the wear rate. In theory, the starved condition is achieved by moving the inlet toward the center of the contact which results in decreasing the lubricant's flow rate. The starvation degree, ξ, is defined in terms of the reduction in the mass flow rate at the contact center ($\xi = 1 - \dot{m}_{starved}/\dot{m}_{fully-flooded}$) [87, 88].

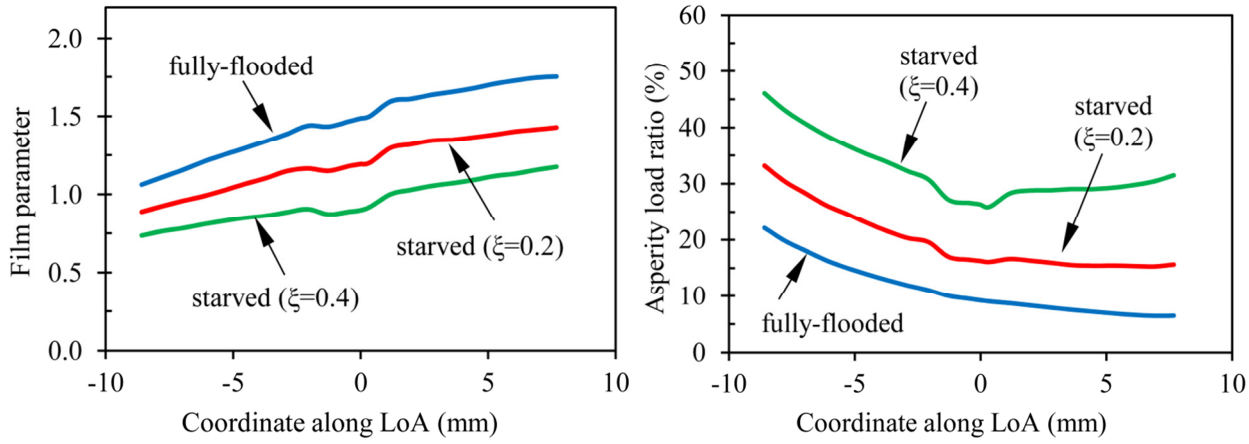

Fig. 8.10. Effect of starvation on (a): film parameter (b): asperity load ratio (σ=0.5 μm)

To understand the effect of starvation, the above problem (for the surface roughness value of σ=0.5 μm) is simulated for two different degrees of starvation: ξ=0.2 and ξ=0.4 which respectively corresponds to 20% and 40% reduction in the lubricant supply. Figure 8.10 shows the changes in the film parameter and asperity load ratio along the LoA for the fully-flooded and starved regimes.

As Fig. 8.10(a) shows, the film parameter undergoes a considerable drop due to the starvation. The simulations predict a fully-flooded film parameter between 1.06 and 1.75, which is within the mixed EHL limits. However, 20% percent reduction in the lubricant's flow rate (ξ=0.2) drops the film parameter to the range of 0.89 and 1.44. Further decrease in the lubricant supply (ξ=0.4) results in a film parameter within the range of 0.73 and 1.18 which warns the onset of the boundary regime. It is evident that the reduction in the film parameter results in more asperity contact. The corresponding asperity load ratios are plotted in Fig. 8.10(b). As shown, while the asperity load ratio varies between 6% to 22% for the fully-flooded case, it increases to 15% ~ 33% for ξ=0.2 and 31% ~ 46% for ξ=0.4.

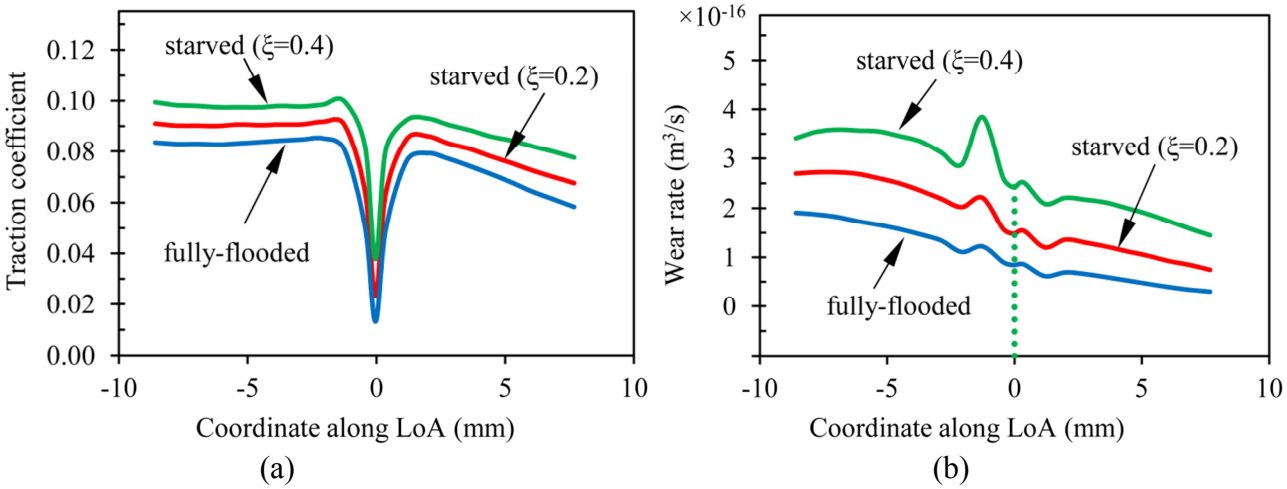

Fig. 8.11. Effect of starvation on: (a) traction coefficient (b): wear rate (σ=0.5 μm)

Plotted in Fig. 8.11 are the traction coefficient and the wear rate along the LoA for the fully-flooded and the starved regimes. As observed above, the starvation increases the asperity contact which leads to an increase in both the traction coefficient and the wear rate.

As Figure 8.11(a) shows, the traction coefficient goes up with as the inlet is starved. In this figure, the average traction coefficient along the LoA is calculated as 0.072 for the fully-flooded case, where it is 0.080 for ξ=0.2 and 0.089 for ξ=0.4. This means that the average traction coefficient increases about 12% for 20% reduction in the flow rate, and 25% for 40% reduction in the flow rate. On the other hand, the corresponding wear rates are plotted in Fig. 8.11(b). While the average wear rate is obtained as 1.04×10^{-16} m^3/s for the fully-flooded regime, it jumps to 1.77×10^{-16} m^3/s for ξ=0.2 and 2.68×10^{-16} m^3/s for ξ=0.4. This means that the average wear rate increases 70% for ξ=0.2 and 158% for ξ=0.4. This implies that the starvation has a huge effect on the wear rate because it is directly affected by the asperity load ratio.

8.5. Conclusions

The performance of the spur gears under the mixed elastohydrodynamic lubrication regime is investigated. By conducting full numerical mixed TEHL simulations using the variable input along the gear's line of action (LoA), the property values are obtained along this line and compared for different roughness values.

The results show that the film thickness experiences a drop at the middle of the LoA due to the sudden increase in the load. However, the lowest film thickness generally occurs at the beginning of LoA, where the rolling speed has its minimum value. For the same reason, the asperity load ratio has its maximum amount at this point. The results are also compared to those obtained by the isothermal formulas [53] where they yield good accuracy for the central film thickness and asperity load ratio. The formulas may however overestimate the minimum film thickness especially at the beginning and end of the LoA which is due to the high heat generation caused by the considerable slide-to-roll ratio.

The results also suggest that the traction coefficient and the wear rate have a nonlinear trend along the line of action which is the results of contributing multiple factors. It is shown that both the traction coefficient and the wear rate increase by increasing the surface roughness, with the wear affected more significantly that the traction coefficient. The traction coefficient and wear results are also compared to those obtained by a simplified approach [75] based on the results of the isothermal formulas and an approximate flash temperature. This approach is shown to be able to reasonably estimate the traction coefficient and wear rate along the LoA.

Also investigated is the effect of a starved inlet, where it is shown that larger contribution of the surface asperities in the starved regime directly results in a smaller film parameter, larger traction coefficient and more significantly a higher wear rate along the line of action.

Nomenclature:

a_χ	diameter of area associated with an adsorb molecule, m
b	half Hertzian width, m
B	line-contact width (gear tooth width), m
c_p	specific heat, J/kgK
E'	Effective Young's modulus, $1/E'=0.5[(1-\nu_1^2)/E_1+(1-\nu_2^2)/E_2]$, Pa
E_a	lubricant adsorption heat, J/mole
f	traction coefficient
f_c	asperity friction coefficient
F	normal load, N
G	dimensionless material number, $E'\alpha$
h	film thickness, m
h_c	central film thickness, m
h_{min}	minimum film thickness, m

H	dimensionless film thickness, h/R
H_c	dimensionless central film thickness, h_c/R
H_{min}	dimensionless minimum film thickness, h_{min}/R
k	thermal conductivity, W/mK
K	dry wear coefficient
K_T	temperature-viscosity coefficient, K^{-1}
L_a	asperity load ratio (percentage)
m	gear module, m
n_g	gear rotational speed, s^{-1}
n_p	pinion rotational speed, s^{-1}
N_g	number of teeth in gear
N_p	number of teeth in pinion
p	total pressure, $F/2bB$, Pa
p_a	asperity pressure, Pa
p_h	hydrodynamic pressure, Pa
p_{avg}	average Hertzian pressure, Pa
p_e	Peclet number
q	average heat flux, W/m^2
r_g	gear's radius, m
r_p	pinion's radius, m
R	equivalent radius, $[1/R_1 \pm 1/R_2]^{-1}$, m
R_g	gas constant, J/mole·K
S	slide-to-roll ratio, u_s/ u_r
t_0	fundamental time of vibration of molecule in adsorbed state, s
T_s	surface temperature, K
T_0	inlet temperature, K
u_r	rolling speed, $(u_1+u_2)/2$, m/s
u_s	sliding speed, $\|u_1-u_2\|$, m/s
U	dimensionless speed, $\mu_0 u_r/E'R$
v	Vickers hardness, Pa
V	dimensionless hardness, v/E'
w	load per contact width, F/B, N/m
W	dimensionless load, $w/E'R$
Z	viscosity-pressure index
α	pressure-viscosity coefficient, m^2/N
ε	coordinate along LoA
φ	gear pressure angle
Λ	film parameter, h_{min}/ σ
Λ_{lim}	limiting shear stress coefficient
μ	viscosity, Pa.s
μ_0	inlet viscosity, Pa.s
σ	surface roughness, m
$\bar{\sigma}$	dimensionless surface roughness, σ/R
Ω_{lub}	lubricated wear rate, m^3/s
ψ	fractional film defect
ξ	starvation degree

8.6. References

[1] Dowson D, Higginson GR. *Elasto-hydrodynamic lubrication*. SI ed. Oxford Eng., New York: Pergamon Press; 1977.

[2] Dowson D, Toyoda S. A Central Film Thickness Formula for Elastohydrodynamic Line Contacts. Proceedings of the 5th Leeds-Lyon Symposium on Tribology, London. 1978:60-5.

[3] Houpert LG, Hamrock BJ. Fast Approach for Calculating Film Thicknesses and Pressures in Elastohydrodynamically Lubricated Contacts at High Loads. J Tribol-T Asme. 1986;108:411-20.

[4] Pan P, Hamrock BJ. Simple Formulas for Performance Parameters Used in Elastohydrodynamically Lubricated Line Contacts. J Tribol-T Asme. 1989;111:246-51.

[5] Moes H. Optimum Similarity Analysis with Applications to Elastohydrodynamic Lubrication. Wear. 1992;159:57-66.

[6] Sadeghi F, Dow TA, Johnson RR. Thermal Effects in Rolling Sliding Contacts .3. Approximate Method for Prediction of Mid-Film Temperature and Sliding Traction. J Tribol-T Asme. 1987;109:519-24.

[7] Sadeghi F, Dow TA. Thermal Effects in Rolling Sliding Contacts .2. Analysis of Thermal Effects in Fluid Film. J Tribol-T Asme. 1987;109:512-8.

[8] Sadeghi F, Sui PC. Thermal Elastohydrodynamic Lubrication of Rolling Sliding Contacts. J Tribol-T Asme. 1990;112:189-95.

[9] Lee RT, Hsu CH. A Fast Method for the Analysis of Thermal Elastohydrodynamic Lubrication of Rolling Sliding Line Contacts. Wear. 1993;166:107-17.

[10] Hsu CH, Lee RT. An Efficient Algorithm for Thermal Elastohydrodynamic Lubrication under Rolling/Sliding Line Contacts. J Tribol-T Asme. 1994;116:762-9.

[11] Wolff R, Kubo A. The Application of Newton-Raphson Method to Thermal Elastohydrodynamic Lubrication of Line Contacts. J Tribol-T Asme. 1994;116:733-40.

[12] Pandey RK, Ghosh MK. Temperature rise due to sliding in rolling/sliding elastohydrodynamic lubrication line contacts: an efficient numerical analysis for contact zone temperatures. Tribol Int. 1998;31:745-52.

[13] Pandey RK, Ghosh MK. A thermal analysis of traction in elastohydrodynamic rolling/sliding line contacts. Wear. 1998;216:106-14.

[14] Kumar P, Khonsari MM. Combined effects of shear thinning and viscous heating on EHL characteristics of rolling/sliding line contacts. J Tribol-T Asme. 2008;130.

[15] Chu LM, Hsu HC, Lin JR, Chang YP. Inverse approach for calculating temperature in EHL of line contacts. Tribol Int. 2009;42:1154-62.

[16] Doolittle AK. Studies in Newtonian Flow .2. The Dependence of the Viscosity of Liquids on Free-Space. J Appl Phys. 1951;22:1471-5.

[17] Bair S, Jarzynski J, Winer WO. The temperature, pressure and time dependence of lubricant viscosity. Tribol Int. 2001;34:461-8.

[18] Bair S, McCabe C, Cummings PT. Calculation of viscous EHL traction for squalane using molecular simulation and rheometry. Tribol Lett. 2002;13:251-4.

[19] Bair SS, McCabe C. High-pressure rheology for quantitative elastohydrodynamics. 1st ed. Amsterdam ; Boston: Elsevier; 2007.

[20] Kumar P, Khonsari MM. Traction in EHL Line Contacts Using Free-Volume Pressure-Viscosity Relationship With Thermal and Shear-Thinning Effects. J Tribol-T Asme. 2009;131.

[21] Kumar P, Anuradha P, Khonsari MM. Some important aspects of thermal elastohydrodynamic lubrication. P I Mech Eng C-J Mec. 2010;224:2588-98.

[22] Habchi W, Vergne P, Bair S, Andersson O, Eyheramendy D, Morales-Espejel GE. Influence of pressure and temperature dependence of thermal properties of a lubricant on the behaviour of circular TEHD contacts. Tribol Int. 2010;43:1842-50.

[23] Jang JY, Khonsari MM. Elastohydrodynamic Line-Contact of Compressible Shear Thinning Fluids With Consideration of the Surface Roughness. J Tribol-T Asme. 2010;132:034501.

[24] Khonsari MM, Hua DY. Thermal Elastohydrodynamic Analysis Using a Generalized Non-Newtonian Formulation with Application to Bair-Winer Constitutive Equation. J Tribol-T Asme. 1994;116:37-46.

[25] Bair S, Khonsari M, Winer WO. High-pressure rheology of lubricants and limitations of the Reynolds equation. Tribol Int. 1998;31:573-86.

[26] Bair S, McCabe C. A study of mechanical shear bands in liquids at high pressure. Tribol Int. 2004;37:783-9.

[27] Goglia PR, Cusano C, Conry TF. The Effects of Surface Irregularities on the Elastohydrodynamic Lubrication of Sliding Line Contacts .2. Wavy Surfaces. J Tribol-T Asme. 1984;106:113-9.

[28] Goglia PR, Conry TF, Cusano C. The Effects of Surface Irregularities on the Elastohydrodynamic Lubrication of Sliding Line Contacts .1. Single Irregularities. J Tribol-T Asme. 1984;106:104-12.

[29] Sadeghi F, Sui PC. Thermal Elastohydrodynamic Lubrication of Rough Surfaces. J Tribol-T Asme. 1990;112:341-6.

[30] Venner CH. Multilevel Solution of the EHL Line and Point Contact Problems. PhD Thesis, University of Twente, Enschede, The Netherland. 1991.

[31] Ai XL, Zheng LQ. A General-Model for Microelastohydrodynamic Lubrication and Its Full Numerical-Solution. J Tribol-T Asme. 1989;111:569-76.

[32] Chang L. A Deterministic Model for Line-Contact Partial Elastohydrodynamic Lubrication. Tribol Int. 1995;28:75-84.

[33] Zhai XJ, Chang L. An engineering approach to deterministic modeling of mixed-film contacts. Tribol T. 1998;41:327-34.

[34] Jiang XF, Hua DY, Cheng HS, Ai XL, Lee SC. A mixed elastohydrodynamic lubrication model with asperity contact. J Tribol-T Asme. 1999;121:481-91.

[35] Wang QJ, Zhu D, Cheng HS, Yu TH, Jiang XF, Liu SB. Mixed lubrication analyses by a macro-micro approach and a full-scale mixed EHL model. J Tribol-T Asme. 2004;126:81-91.

[36] Wang QJ, Zhu D, Zhou RS, Hashimoto F. Investigating the Effect of Surface Finish on Mixed EHL in Rolling and Rolling-Sliding Contacts. Tribol T. 2008;51:748-61.

[37] Ren N, Zhu D, Chen WW, Liu YC, Wang QJ. A Three-Dimensional Deterministic Model for Rough Surface Line-Contact EHL Problems. J Tribol-T Asme. 2009;131.

[38] Zhu D, Wang QJ. On the lambda ratio range of mixed lubrication. P I Mech Eng J-J Eng. 2012;226:1010-22.

[39] Zhu D, Wang QJ. Effect of Roughness Orientation on the Elastohydrodynamic Lubrication Film Thickness. J Tribol-T Asme. 2013;135:031501.

[40] Johnson KL, Greenwood JA, Poon SY. Simple Theory of Asperity Contact in Elastohydrodynamic Lubrication. Wear. 1972;19:91-108.

[41] Greenwood JA, Williamson JB. Contact of Nominally Flat Surfaces. Proc R Soc Lon Ser-A. 1966;295:300-19.

[42] Gelinck ERM, Schipper DJ. Deformation of rough line contacts. J Tribol-T Asme. 1999;121:449-54.

[43] Gelinck ERM, Schipper DJ. Calculation of Stribeck curves for line contacts. Tribol Int. 2000;33:175-81.

[44] Lu XB, Khonsari MM, Gelinck ERM. The Stribeck curve: Experimental results and theoretical prediction. J Tribol-T Asme. 2006;128:789-94.

[45] Akbarzadeh S, Khonsari MM. Performance of spur gears considering surface roughness and shear thinning lubricant. J Tribol-T Asme. 2008;130:021503.

[46] Akbarzadeh S, Khonsari MM. Thermoelastohydrodynamic Analysis of Spur Gears with Consideration of Surface Roughness. Tribol Lett. 2008;32:129-41.

[47] Serest AE, Akbarzadeh S. Mixed-elastohydrodynamic analysis of helical gears using load-sharing concept. P I Mech Eng J-J Eng. 2014;228:320-31.

[48] Patir N, Cheng HS. Average Flow Model for Determining Effects of 3-Dimensional Roughness on Partial Hydrodynamic Lubrication. J Lubric Tech-T Asme. 1978;100:12-7.

[49] Majumdar BC, Hamrock BJ. Effect of Surface-Roughness on Elastohydrodynamic Line Contact. J Lubric Tech-T Asme. 1982;104:401-9.

[50] Sadeghi F, Sui PC. Compressible Elastohydrodynamic Lubrication of Rough Surfaces. J Tribol-T Asme. 1989;111:56-62.

[51] Moraru L, Keith TG, Kahraman A. Aspects Regarding the Use of Probabilistic Models for Isothermal Full Film Rough Line Contacts. Tribol T. 2004;47:386-95.

[52] Zhao YW, Maietta DM, Chang L. An Asperity Microcontact Model Incorporating the Transition from Elastic Deformation to Fully Plastic Flow. J Tribol-T Asme. 2000;122:86-93.

[53] Masjedi M, Khonsari MM. Film Thickness and Asperity Load Formulas for Line-Contact Elastohydrodynamic Lubrication With Provision for Surface Roughness. J Tribol-T Asme. 2012;134:011503.

[54] Masjedi M, Khonsari MM. Mixed elastohydrodynamic lubrication line-contact formulas with different surface patterns. Proceedings of the Institution of Mechanical Engineers, Part J: Journal of Engineering Tribology. 2014;228:849–59.

[55] Masjedi M, Khonsari MM. Theoretical and experimental investigation of traction coefficient in line-contact EHL of rough surfaces. Tribol Int. 2014;70:179-89.

[56] Archard JF. Contact and Rubbing of Flat Surfaces. J Appl Phys. 1953;24:981-8.

[57] Rowe CN. Some Aspects of Heat of Adsorption in Function of a Boundary Lubricant. Asle Trans. 1966;9:101-&.

[58] Kingsbury EP. Some Aspects of the Thermal Desorption of a Boundary Lubricant. J Appl Phys. 1958;29:888-91.

[59] Stolarski TA. Adhesive Wear of Lubricated Contacts. Tribol Int. 1979;12:169-79.

[60] Stolarski TA. A Probabilistic Approach to Wear Prediction. J Phys D Appl Phys. 1990;23:1143-9.

[61] Sastry VRK, Singh DV, Sethuramiah A. Modeling of Wear under Partial Elastohydrodynamic Lubrication Conditions. Wear. 1990;138:259-68.

[62] Wu SF, Cheng HS. A Sliding Wear Model for Partial-Ehl Contacts. J Tribol-T Asme. 1991;113:134-41.

[63] Wu SF, Cheng HS. Sliding Wear Calculation in Spur Gears. J Tribol-T Asme. 1993;115:493-500.

[64] Flodin A, Andersson S. Simulation of mild wear in spur gears. Wear. 1997;207:16-23.

[65] Wang W, Wong PL, Guo F. Application of partial elastohydrodynamic lubrication analysis in dynamic wear study for running-in. Wear. 2004;257:823-32.

[66] Zhu D, Martini A, Wang WZ, Hu YZ, Lisowsky B, Wang QJ. Simulation of sliding wear in mixed lubrication. J Tribol-T Asme. 2007;129:544-52.

[67] Akbarzadeh S, Khonsari MM. Prediction of Steady State Adhesive Wear in Spur Gears Using the EHL Load Sharing Concept. J Tribol-T Asme. 2009;131:-.

[68] Hegadekatte V, Hilgert J, Kraft O, Huber N. Multi time scale simulations for wear prediction in micro-gears. Wear. 2010;268:316-24.

[69] Bosman R, Schipper DJ. Mild Wear Prediction of Boundary-Lubricated Contacts. Tribol Lett. 2011;42:169-78.

[70] Bosman R, Schipper DJ. Mild wear maps for boundary lubricated contacts. Wear. 2012;280:54-62.

[71] Beheshti A, Khonsari MM. A Thermodynamic Approach for Prediction of Wear Coefficient Under Unlubricated Sliding Condition. Tribol Lett. 2010;38:347-54.

[72] Kogut L, Etsion I. A finite element based elastic-plastic model for the contact of rough surfaces. Tribol T. 2003;46:383-90.

[73] Beheshti A, Khonsari MM. Asperity micro-contact models as applied to the deformation of rough line contact. Tribol Int. 2012;52:61-74.

[74] Beheshti A, Khonsari MM. An engineering approach for the prediction of wear in mixed lubricated contacts. Wear. 2013;308:121-31.

[75] Masjedi M, Khonsari MM. An Engineering Approach for Rapid Evaluation of Traction Coefficient and Wear in Mixed EHL Tribology International. 2015: Submitted.

[76] Masjedi M, Khonsari MM. On the Effect of Surface Roughness in Point-Contact EHL: Formulas for Film Thickness and Asperity Load. Tribol Int. 2015;82:228–44.

[77] Bair S, Winer WO. Rheological Model for Elastohydrodynamic Contacts Based on Primary Laboratory Data. J Lubric Tech-T Asme. 1979;101:258-65.

[78] Roelands CJA. *Correctional Aspects of the Viscosity-Temperature- Pressure Relationship of Lubricating Oils*. Groningen, Netherlands: Druk, V.R.B., ; 1966.

[79] Tian XF, Kennedy FE. Maximum and Average Flash Temperatures in Sliding Contacts. J Tribol-T Asme. 1994;116:167-74.

[80] Zhu D, Wang QJ. Effect of Roughness Orientation on the Elastohydrodynamic Lubrication Film Thickness. J Tribol-T Asme. 2013;135.

[81] Incropera FP, DeWitt DP. Introduction to heat transfer. 4th ed. New York: Wiley; 2002.

[82] Hamrock BJ. *Fundamentals of Fluid Film Lubrication*. New York: McGraw-Hill; 1994.

[83] Greenwood JA, Kauzlari JJ. Inlet Shear Heating in Elastohydrodynamic Lubrication. J Lubric Tech-T Asme. 1973;95:417-26.

[84] Rabinowicz E. Friction and wear of materials. 2nd ed. ed. New York ; Chichester: Wiley; 1995.

[85] Budynas RG, Nisbett JK, Shigley JE. Shigley's mechanical engineering design. 8th ed. Boston: McGraw-Hill; 2008.

[86] Hua DY, Khonsari MM. Application of Transient Elastohydrodynamic Lubrication Analysis for Gear Transmissions. Tribol T. 1995;38:905-13.

[87] Kumar P, Khonsari MM. Effect of Starvation on Traction and Film Thickness in Thermo-EHL Line Contacts with Shear-Thinning Lubricants. Tribol Lett. 2008;32:171-7.

[88] Masjedi M, Khonsari MM. A Study on the Effect of Starvation in Mixed Elastohydrodynamic Lubrication. Tribol Int. 2015; 85:26-36.

Chapter 9: Summary and Future Work

9.1. Summary and Conclusions

The main concentration of the present dissertation is the investigation of the effect of surface roughness in the elastohydrodynamic lubrication (EHL) of tribological components. This is of paramount importance as all engineering surfaces are rough to some extent. As a result, a comprehensive study is conducted to realistically simulate the effect of surface roughness in the performance of components operating under the EHL regime. For this purpose, extensive numerical simulations are provided to solve the common EHL equations in conjunction with the deformation of the surface asperities to investigate how the surface roughness influences the results. In all parts, it is tried to express the results of the numerical simulations in terms of some predictive formulas or easy-to-use approaches, so one can evaluate the system performance quickly. A summary of the main results is as follows:

- The lubricant's film thickness and its load-carrying capacity as well as the load carried by the surface asperities in the mixed EHL regime are obtained using isothermal simulations. This is done by giving a systematic solution to the modified Reynolds equation, bulk deformation of the surfaces, and elasto-plastic deformation of the surface asperities. Solutions are provided for both line-contact and point-contact EHL. It is shown how increasing the surface roughness in microscopic level can cause a significant drop in the film parameter and a remarkable increase in the asperity interactions. The results of an extensive set of numerical simulations are then used to derive curve-fit expressions for the central film thickness, minimum film thickness, and asperity load ratio as function of dimensionless input parameters that include geometry, load, speed, lubricant properties, surface material, surface roughness, and surface hardness. By utilizing these formulas, there is no further need for performing extensive numerical simulations.

- The Traction Coefficient in the mixed EHL regime is predicted using thermal EHL (TEHL) simulations. For this purpose, the mixed EHL equations are solved together with the energy equation which takes into account the heat generation by both the lubricant and surface asperities. The lubricant's limiting shear stress and also its free volume properties are considered in the simulations to accurately predict the variations the viscosity at high pressures and temperatures. The results from the simulations are also validated by the experiments conducted using a rolling/sliding test rig. The traction coefficient is shown to consist of hydrodynamic and asperity parts. While the hydrodynamic part is highly dependent on the variation of the viscosity and the sliding velocity, the asperity part depends only on the asperity load ratio. It is also revealed that at moderate rolling velocities, the

central film thickness and the asperity load ratio are not highly influenced by the sliding-induced temperature rise. The developed TEHL model is also used to predict adhesive wear. For this purpose, the knowledge of the asperity load ratio and the surface temperature is required, both of which can be obtained using the present approach. Furthermore, beside the comprehensive TEHL model, a simplified engineering approach is developed for the rapid evaluation of the traction coefficient and the wear rate using the estimated contact flash temperature and the results from the obtained isothermal formulas. The results from this approach are shown to have reasonable accuracy compared to the full numerical solution.

- Since the real engineering surfaces may have different properties in different directions (anisotropy), a study is conducted to investigate the effect of surface pattern (orientation) in rough line-contact EHL. This is done by considering different surface patterns in the modified Reynolds equation. It is shown that the longitudinal pattern makes less resistance against the flow, thus creates a thinner film and more asperity contact. On the other hand, the transverse pattern provides more resistance against the flow, which results in a thicker film and less asperity contact. Moreover, the results yield that changing the pattern from transverse to longitudinal increases the asperity part of the traction coefficient while decreases the hydrodynamic part. The results of simulations are also used to develop curve-fit expressions to quantify the effect of surface pattern in terms of correction factors which can be readily applied to the obtained formulas for the film thickness and asperity load ratio.

- The effect of insufficient lubricant supply at the contact inlet (referred to as the starvation) is also studied. Simulations are performed for both line-contact and point-contact EHL to investigate this effect by relating the starvation to the reduction of the lubricant's flow rate. It is shown that the starvation has a more pronounced effect on the central film thickness compared to the minimum film thickness. Also, the reduction of the central film thickness in point contact is greater than that of line contact, especially at smaller ellipticity values. It is also observed that in line contact, the reduction in the film thickness is only a function of the starvation degree; while in point contact, it is also dependent on the ellipticity. Regression analyses are performed for the simulation results to develop expressions which predict the asperity load ratio, as well as the reduction in both the central and minimum film thickness as functions of the starvation degree and other input parameters.

- To illustrate the application of the developed models, the performance of the spur gears under the mixed EHL regime is investigated. By conducting full numerical simulations along the gear's line of action (LoA), the variations of the film thickness, traction coefficient, and wear rate are investigated along this line. Since the load, speed, and contact radius vary along the LoA, each contact point represents a rough EHL problem which requires a separate simulation. This signifies the advantage of using predictive formulas or engineering estimations which can save considerable amount of time. Thus, the film thickness and

asperity load results are compared to those obtained from the formulas, while the traction coefficient and wear rate are also compared to those obtained from the developed engineering approach. The results are shown to be in agreement with those from simulations by reasonable accuracy.

9.2. Recommendations for Future Work

The following topics are suggested for possible future research:

- The traction coefficient and wear rate can be obtained for the mixed point-contact EHL. Similar to line contact (Chapter 3), a full numerical TEHL solution can be given to the point contact problem (Chapter 5) by simultaneously solving the EHL and energy equations. Moreover, the developed engineering approach (Chapter 7) can be extended to point contact problem as well.

- The effect of surface pattern in point-contact EHL can also be studied. This can be done by following the approach developed in Chapter 4 to consider the effect of surface orientation when solving the point-contact EHL equations (Chapter 5). Similar to the line contact, modification factors can be presented for the film thickness and asperity ratio for point contact of anisotropic surfaces.

- The effect of surface roughness in soft EHL can be studied. For the soft-EHL problem, the governing equations for the bulk deformation of the surfaces are different from the hard-EHL problem. It should also be studied to see which micro-contact model is suitable for predicting the deformation of the surface asperities in soft-EHL.

- The developed model can be extended to include other types of geometry. For example, to study the effect of surface roughness in the performance of artificial hip joints or knee joints, ball-on socket geometry should be considered; while the effect of surface roughness can be applied in a similar fashion.

Appendix A: Simulation and Curve-fit Results (Line-Contact EHL)

Table A.1. Results of the simulation and the curve-fit equation (central film thickness)

Input					H_{min}		Error%	Λ
W	U	G	$\bar{\sigma}$	V	Simulation	Curve Fit		
2.00×10^{-5}	1.00×10^{-11}	4500	2.00×10^{-5}	0.01	2.70×10^{-5}	2.67×10^{-5}	1.17	1.20
7.00×10^{-5}					2.26×10^{-5}	2.15×10^{-5}	4.66	1.05
2.00×10^{-4}					1.91×10^{-5}	1.81×10^{-5}	4.90	0.94
3.00×10^{-4}					1.78×10^{-5}	1.70×10^{-5}	4.36	0.89
5.00×10^{-4}					1.61×10^{-5}	1.57×10^{-5}	2.73	0.81
1.00×10^{-4}	1.00×10^{-12}	4500	0	0.01	3.42×10^{-6}	3.48×10^{-6}	1.70	-
	5.00×10^{-12}		2.00×10^{-5}		1.47×10^{-5}	1.36×10^{-5}	7.41	0.72
	1.00×10^{-11}				2.13×10^{-5}	2.03×10^{-5}	4.84	1.01
	5.00×10^{-11}				5.68×10^{-5}	5.73×10^{-5}	0.82	2.58
	1.00×10^{-10}				9.02×10^{-5}	9.18×10^{-5}	1.72	4.13
2.00×10^{-4}	2.00×10^{-11}	2500	2.00×10^{-5}	0.01	2.26×10^{-5}	2.13×10^{-5}	5.79	1.06
1.00×10^{-4}	1.00×10^{-11}	5000			2.22×10^{-5}	2.13×10^{-5}	4.23	1.06
6.67×10^{-5}	6.67×10^{-12}	7500			2.23×10^{-5}	2.14×10^{-5}	4.03	1.07
1.00×10^{-4}	1.00×10^{-11}	4500	0	0.01	1.77×10^{-5}	1.76×10^{-5}	0.65	-
			1.00×10^{-6}		1.77×10^{-5}	1.77×10^{-5}	0.27	15.54
			1.00×10^{-5}		1.90×10^{-5}	1.88×10^{-5}	0.95	1.74
			3.00×10^{-5}		2.32×10^{-5}	2.20×10^{-5}	5.29	0.75
			5.00×10^{-5}		2.59×10^{-5}	2.58×10^{-5}	0.43	0.51
1.00×10^{-4}	1.00×10^{-11}	4500	4.00×10^{-5}	0.005	2.31×10^{-5}	2.30×10^{-5}	0.36	0.58
				0.0075	2.42×10^{-5}	2.35×10^{-5}	3.17	0.60
				0.015	2.46×10^{-5}	2.44×10^{-5}	0.65	0.60
				0.02	2.48×10^{-5}	2.49×10^{-5}	0.33	0.61
				0.03	2.56×10^{-5}	2.56×10^{-5}	0.20	0.62

Table A.2. Results of the simulation and the curve-fit equation (minimum film thickness)

Input					H_{min}		Error%	Λ
W	U	G	$\bar{\sigma}$	V	Simulation	Curve Fit		
2.00×10^{-5}	1.00×10^{-11}	4500	2.00×10^{-5}	0.01	2.40×10^{-5}	2.41×10^{-5}	0.50	1.20
7.00×10^{-5}					2.11×10^{-5}	1.99×10^{-5}	5.41	1.05
2.00×10^{-4}					1.88×10^{-5}	1.74×10^{-5}	7.55	0.94
3.00×10^{-4}					1.78×10^{-5}	1.65×10^{-5}	7.05	0.89
5.00×10^{-4}					1.61×10^{-5}	1.55×10^{-5}	3.52	0.81
1.00×10^{-4}	1.00×10^{-12}	4500	0	0.01	3.02×10^{-6}	2.97×10^{-6}	1.57	-
	5.00×10^{-12}		2.00×10^{-5}		1.43×10^{-5}	1.32×10^{-5}	7.88	0.72
	1.00×10^{-11}				2.03×10^{-5}	1.90×10^{-5}	6.40	1.01
	5.00×10^{-11}				5.16×10^{-5}	5.20×10^{-5}	0.76	2.58
	1.00×10^{-10}				8.25×10^{-5}	8.32×10^{-5}	0.85	4.13
2.00×10^{-4}	2.00×10^{-11}	2500	2.00×10^{-5}	0.01	2.12×10^{-5}	1.90×10^{-5}	10.41	1.06
1.00×10^{-4}	1.00×10^{-11}	5000			2.12×10^{-5}	2.01×10^{-5}	5.41	1.06
6.67×10^{-5}	6.67×10^{-12}	7500			2.14×10^{-5}	2.08×10^{-5}	2.85	1.07
1.00×10^{-4}	1.00×10^{-11}	4500	0	0.01	1.55×10^{-5}	1.55×10^{-5}	0.26	-
			1.00×10^{-6}		1.55×10^{-5}	1.56×10^{-5}	0.23	15.54
			1.00×10^{-5}		1.74×10^{-5}	1.71×10^{-5}	1.78	1.74
			3.00×10^{-5}		2.25×10^{-5}	2.10×10^{-5}	6.59	0.75
			5.00×10^{-5}		2.57×10^{-5}	2.53×10^{-5}	1.42	0.51
1.00×10^{-4}	1.00×10^{-11}	4500	4.00×10^{-5}	0.005	2.30×10^{-5}	2.22×10^{-5}	3.56	0.58
				0.0075	2.39×10^{-5}	2.27×10^{-5}	4.80	0.60
				0.015	2.42×10^{-5}	2.37×10^{-5}	1.76	0.60
				0.02	2.43×10^{-5}	2.42×10^{-5}	0.46	0.61
				0.03	2.49×10^{-5}	2.49×10^{-5}	0.00	0.62

Table A.3. Results of the simulation and the curve-fit equation (asperity load ratio)

Input					H_{min}		Error%	Λ
W	U	G	$\bar{\sigma}$	V	Simulation	Curve Fit		
2.00×10^{-5}	1.00×10^{-11}	4500	2.00×10^{-5}	0.01	33.08	28.48	4.61	1.20
7.00×10^{-5}					23.155	20.30	2.86	1.05
2.00×10^{-4}					17.632	15.01	2.63	0.94
3.00×10^{-4}					15.85	13.30	2.54	0.89
5.00×10^{-4}					13.71	11.40	2.31	0.81
1.00×10^{-4}	1.00×10^{-12}	4500	0	0.01	0	0	0	-
	5.00×10^{-12}		2.00×10^{-5}		35.37	32.45	2.92	0.72
	1.00×10^{-11}				21.17	18.35	2.82	1.01
	5.00×10^{-11}				0.31	0.45	0.14	2.58
	1.00×10^{-10}				0	0.03	0.03	4.13
2.00×10^{-4}	2.00×10^{-11}	2500	2.00×10^{-5}	0.01	13.134	10.54	2.59	1.06
1.00×10^{-4}	1.00×10^{-11}	5000			19.64	17.12	2.52	1.06
6.67×10^{-5}	6.67×10^{-12}	7500			24.463	22.54	1.92	1.07
1.00×10^{-4}	1.00×10^{-11}	4500	0	0.01	0.00	0.00	0.00	-
			1.00×10^{-6}		0.00	0.00	0.00	15.54
			1.00×10^{-5}		3.923	2.59	1.33	1.74
			3.00×10^{-5}		34.164	29.80	4.36	0.75
			5.00×10^{-5}		50.31	44.34	5.97	0.51
1.00×10^{-4}	1.00×10^{-11}	4500	4.00×10^{-5}	0.005	30.54	34.16	3.62	0.58
				0.0075	39.75	36.40	3.35	0.60
				0.015	42.58	40.23	2.35	0.60
				0.02	43.91	41.82	2.09	0.61
				0.03	49.11	44.06	5.05	0.62

Appendix B: Temperature Equations

The dimensionless mid-film temperature at any point is given as:

$$\overline{T} = \frac{\dfrac{\overline{T}_L + \overline{T}_H}{2} + K_1\left[\dfrac{A_0^2}{240\,\overline{\mu}} + \dfrac{\overline{\mu}S^2}{12}\right] + (K_3 H^2 \overline{\rho}\,\dfrac{\partial \overline{T}}{\partial X})\left[\dfrac{A_0}{120\,\overline{\mu}} - \dfrac{1}{12}\right] + \dfrac{1}{12} K_4 P_a H}{1 + K_2 H^2\,\dfrac{\partial P_h}{\partial X}\left[\dfrac{A_0}{120\,\overline{\mu}} - \dfrac{1}{12}\right]} \tag{B1}$$

where $A_0 = (H^2/4U)\frac{\partial P_h}{\partial X}$, and $\overline{T}_L$ and $\overline{T}_H$ are the dimensionless temperature of lower and upper surfaces, respectively. Equation (B1) is obtained by the method applied in Ref. [14] of Chapter 3. For the simplicity, the viscosity is considered as constant across the film (y direction). The contribution of heat generation due to asperity contact results in the appearance of new term $\frac{1}{12}K_4 P_a H$ since the energy equation (Eq. (11) in Chapter 3) includes a corresponding term for the asperity heat generation.

The boundary (surface) temperatures are:

$$\overline{T}_{L/H} = 1 + D_{L/H}\int_{X_{\min}}^{X} \frac{\left(\overline{T}_H - \overline{T}_L\right) + \chi_{L/H} \pm 0.5 K_4 P_a H}{H\sqrt{X - s}}\,ds \tag{B2}$$

in which

$$\chi_{L/H} = \pm K_1\left[\frac{A_0^2}{24\overline{\mu}} + \frac{1}{2}\overline{\mu}S^2 \mp \frac{SA_0}{6}\right] + (K_3 H^2 \overline{\rho}\,\frac{\partial \overline{T}}{\partial X} - K_2 H^2\,\overline{T}\,\frac{\partial P_h}{\partial X})\left[\mp\frac{1 - S/2}{2} \pm \frac{A_0}{24\overline{\mu}} + \frac{S}{12} \mp \frac{S}{4}\right] \tag{B3}$$

and

$$D_{L/H} = \frac{k\sqrt{\mu_o}}{R\sqrt{\pi \rho_{L/H} c_{L/H} k_{L/H} E' U\left(1 \mp S/2\right)}}\left(\frac{8W}{\pi}\right)^{0.25} \tag{B4}$$

where ρ_L and ρ_H are the density of the lower and upper surfaces; c_L and c_H are the specific heat of the lower and upper surfaces, and k_L and k_H are the thermal conductivity of the lower and upper surfaces. μ_0 is the inlet viscosity of the lubricant.

Appendix C: Finite Difference Scheme for Point-Contact EHL

The Reynolds equation is discretized as:

$$A_{i,j}P_{hi+1,j} + B_{i,j}P_{hi,j-1} + C_{i,j}P_{hi-1,j} + D_{i,j}P_{hi1,j+1} - E_{i,j}P_{hi,j} = F_{i,j} \tag{C1}$$

where:

$$A_{i,j} = 3\Phi_{i+1,j}\eta_{i+1,j}H_{i+1,j}{}^3 + \Phi_{i-1,j}\eta_{i-1,j}H_{i-1,j}{}^3$$

$$B_{i,j} = (\frac{\Delta X}{\kappa\Delta Y})^2\left[\Phi_{i,j+1}\eta_{i,j+1}H_{i,j+1}{}^3 + 3\Phi_{i,j-1}\eta_{i,j-1}H_{i,j-1}{}^3\right]$$

$$C_{i,j} = \Phi_{Xi+1,j}\eta_{i+1,j}H_{i+1,j}{}^3 + 3\Phi_{i-1,j}\eta_{i-1,j}H_{i-1,j}{}^3$$

$$D_{i,j} = (\frac{\Delta X}{\kappa\Delta Y})^2\left[3\Phi_{i,j+1}\eta_{i,j+1}H_{i,j+1}{}^3 + \Phi_{i,j-1}\eta_{i,j-1}H_{i,j-1}{}^3\right] \tag{C2}$$

$$E_{i,j} = 4\left(\Phi_{i+1,j}\eta_{i+1,j}H_{i+1,j}{}^3 + \Phi_{i-1,j}\eta_{i-1,j}H_{i-1,j}{}^3\right)$$
$$+ 4\left((\frac{\Delta X}{\kappa\Delta Y})^2\left[\Phi_{i,j+1}\eta_{i,j+1}H_{i,j+1}{}^3 + \Phi_{i,j-1}\eta_{i,j-1}H_{i,j-1}{}^3\right]\right)$$

$$F_{i,j} = 2K.\Delta X\left(3\overline{\rho}_{i,j}\eta_{i,j}H_{Ti,j} - 4\overline{\rho}_{i-1,j}\eta_{i,j}H_{Ti-1,j} + \overline{\rho}_{i-2,j}\eta_{i,j}H_{Ti-2,j}\right)$$

in which $\eta = \overline{\rho}/\overline{\mu}$, $\Phi = \Phi_X = \Phi_Y$, $K = 8\pi\kappa\gamma^3 U/W$. Note that a combination of central and forward/backward scheme is utilized for the left-hand side, while a second order backward scheme is used for the right-hand side.

Appendix D: Numerical solution procedure for Point-Contact EHL Solution

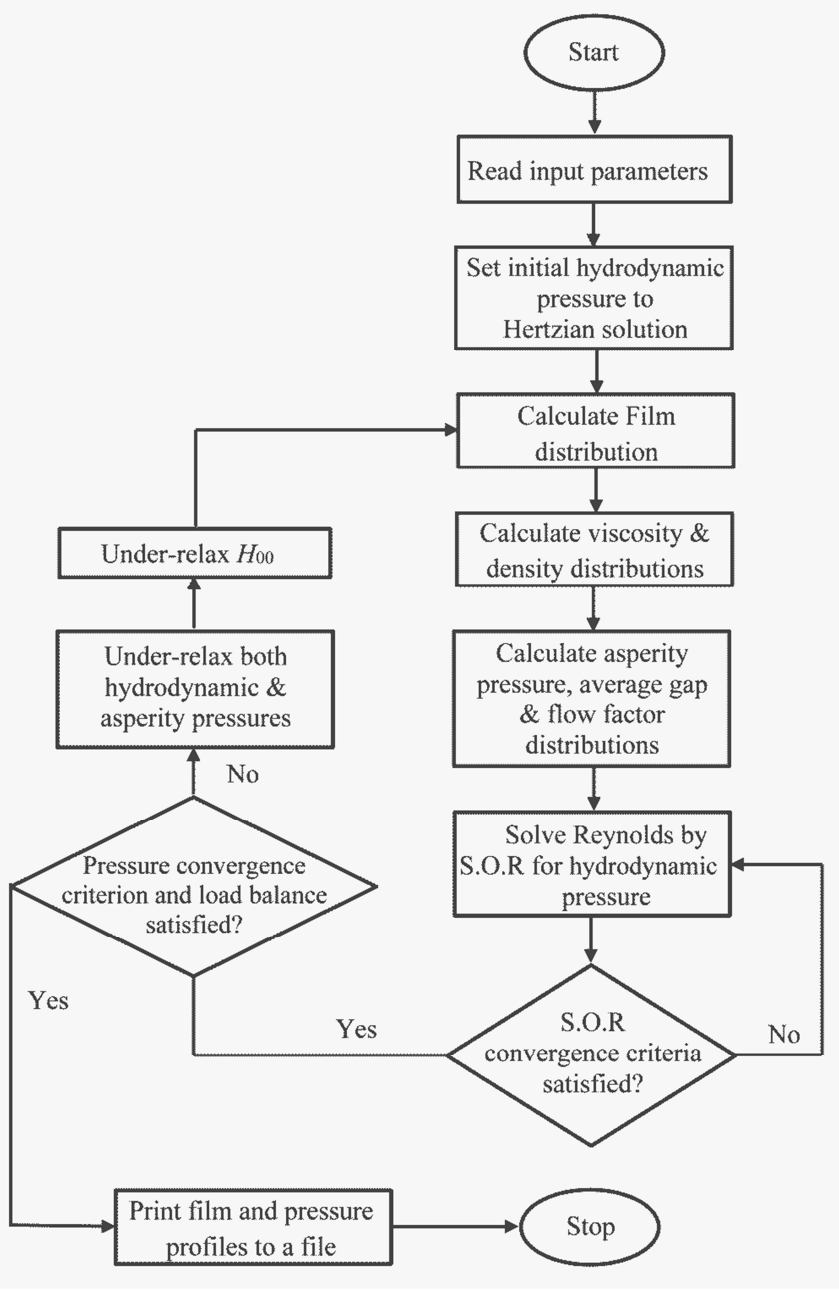

Fig. D.1. Flowchart of Point-Contact EHL Solution by Relaxation Method

Appendix E: Effect of Inlet Distance on Point-Contact EHL Results

Table E.1. Smooth surface, low load (W=1×10^{-6}, U=1×10^{-11}, G=4000, κ=3)

Parameter	X_{min}=-2	X_{min}=-3	X_{min}=-4	X_{min}=-5
H_c	1.879×10^{-5}	2.016×10^{-5}	2.068×10^{-5}	2.074×10^{-5}
(Error)	(-)	(7.29%)	(2.58%)	(0.29%)
$H_{\min}$	1.599×10^{-5}	1.679×10^{-5}	1.698×10^{-5}	1.704×10^{-5}
(Error)	(-)	(5.00%)	(1.13%)	(0.35%)

Table E.2. Smooth surface, high load (W=1×10^{-5}, U=1×10^{-11}, G=4000, κ=3)

Parameter	X_{min}=-2	X_{min}=-3	X_{min}=-4	X_{min}=-5
H_c	1.559×10^{-5}	1.583×10^{-5}	1.593×10^{-5}	1.598×10^{-5}
(Error)	(-)	(1.54%)	(0.61%)	(0.31%)
$H_{\min}$	1.451×10^{-5}	1.441×10^{-5}	1.447×10^{-5}	1.453×10^{-5}
(Error)	(-)	(0.69%)	(0.42%)	(0.41%)

Table E.3. Rough surface, low load ($\bar{\sigma}$=2×10^{-5}, W=1×10^{-6}, U=1×10^{-11}, G=4000, κ=3)

Parameter	X_{min}=-2	X_{min}=-3	X_{min}=-4	X_{min}=-5
H_c	2.297×10^{-5}	2.443×10^{-5}	2.478×10^{-5}	2.488×10^{-5}
(Error)	(-)	(6.35%)	(1.43%)	(0.40%)
$H_{\min}$	2.141×10^{-5}	2.242×10^{-5}	2.267×10^{-5}	2.274×10^{-5}
(Error)	(-)	(4.72%)	(1.11%)	(0.31%)
L_a	42.148	37.833	36.706	36.486
(Error)	(-)	(10.24%)	(2.98%)	(0.60%)

Table E.4. Rough surface, high load ($\bar{\sigma}$=2×10^{-5}, W=1×10^{-5}, U=1×10^{-11}, G=4000, κ=3)

Parameter	X_{min}=-2	X_{min}=-3	X_{min}=-4	X_{min}=-5
H_c	2.042×10^{-5}	2.057×10^{-5}	2.081×10^{-5}	2.085×10^{-5}
(Error)	(-)	(0.73%)	(1.17%)	(0.19%)
$H_{\min}$	1.956×10^{-5}	1.967×10^{-5}	1.976×10^{-5}	1.983×10^{-5}
(Error)	(-)	(0.56%)	(0.46%)	(0.35%)
L_a	22.778	22.390	22.324	22.3397
(Error)	(-)	(1.70%)	(0.29%)	(0.07%)

The errors are calculated with respect to previous inlet distance: (Error=$100\times\left|X_i-X_{i-1}\right|/X_{i-1}$).

Appendix F: Mesh Refinement Study for Point-Contact EHL

Table F.1. Smooth surface, low load (W=1×10^{-6}, U=1×10^{-11}, G=4000, κ=3)

Parameter	Mesh 1	Mesh 2	Mesh 3	Mesh 4
H_c	2.047×10^{-5}	2.058×10^{-5}	2.068×10^{-5}	2.077×10^{-5}
(Error)	(-)	(0.53%)	(0.48%)	(0.43%)
$H_{\min}$	1.710×10^{-5}	1.703×10^{-5}	1.698×10^{-5}	1.695×10^{-5}
(Error)	(-)	(0.41%)	(0.29%)	(0.18%)

Table F.2. Smooth surface, high load (W=1×10^{-5}, U=1×10^{-11}, G=4000, κ=3)

Parameter	Mesh 1	Mesh 2	Mesh 3	Mesh 4
H_c	1.643×10^{-5}	1.607×10^{-5}	1.593×10^{-5}	1.581×10^{-5}
(Error)	(-)	(1.59%)	(0.87%)	(0.75%)
$H_{\min}$	1.481×10^{-5}	1.459×10^{-5}	1.447×10^{-5}	1.438×10^{-5}
(Error)	(-)	(1.49%)	(0.82%)	(0.62%)

Table F.3. Rough surface, low load ($\bar{\sigma}$=2×10^{-5}, W=1×10^{-6}, U=1×10^{-11}, G=4000, κ=3)

Parameter	Mesh 1	Mesh 2	Mesh 3	Mesh 4
H_c	2.474×10^{-5}	2.477×10^{-5}	2.478×10^{-5}	2.479×10^{-5}
(Error)	(-)	(0.12%)	(0.04%)	(0.04%)
$H_{\min}$	2.261×10^{-5}	2.265×10^{-5}	2.267×10^{-5}	2.268×10^{-5}
(Error)	(-)	(0.18%)	(0.09%)	(0.04%)
L_a	36.785	36.733	36.706	36.693
(Error)	(-)	(0.14%)	(0.07%)	(0.04%)

Table F.4. Rough surface, high load ($\bar{\sigma}$=2×10^{-5}, W=1×10^{-5}, U=1×10^{-11}, G=4000, κ=3)

Parameter	Mesh 1	Mesh 2	Mesh 3	Mesh 4
H_c	2.051×10^{-5}	2.079×10^{-5}	2.081×10^{-5}	2.083×10^{-5}
(Error)	(-)	(1.37)	(0.09%)	(0.10%)
$H_{\min}$	1.956×10^{-5}	1.982×10^{-5}	1.976×10^{-5}	1.971×10^{-5}
(Error)	(-)	(1.31)	(0.30%)	(0.25%)
L_a	22.429	22.328	22.324	22.331
(Error)	(-)	(0.45%)	(0.02%)	(0.03%)

Mesh1: 120×20 nodes (20 nodes per unit along X and 10 nodes per unit along Y)
Mesh2: 150×30 nodes (25 nodes per unit along X and 15 nodes per unit along Y)
Mesh3: 180×40 nodes (30 nodes per unit along X and 20 nodes per unit along Y)
Mesh4: 210×50 nodes (35 nodes per unit along X and 25 nodes per unit along Y)
Errors are calculated with respect to previous mesh size: (Error=$100\times\left|X_i-X_{i-1}\right|/X_{i-1}$).

Appendix G: Simulation and Curve-fit Results (Point-Contact EHL)

Table G.1. Results of the simulation and the curve-fit equation for smooth surfaces

Input				H_c (smooth surface)			H_{min} (smooth surface)		
κ	W	U	G	Simulation	Curve-fit	Error (%)	Simulation	Curve-fit	Error (%)
1	1×10^{-6}	1×10^{-11}	4972	1.80×10^{-5}	1.81×10^{-5}	0.56	1.05×10^{-5}	1.09×10^{-5}	3.81
2				2.11×10^{-5}	2.14×10^{-5}	1.42	1.62×10^{-5}	1.61×10^{-5}	0.62
3				2.25×10^{-5}	2.30×10^{-5}	2.22	1.87×10^{-5}	1.88×10^{-5}	0.53
4				2.35×10^{-5}	2.38×10^{-5}	1.28	2.01×10^{-5}	2.02×10^{-5}	0.50
6				2.42×10^{-5}	2.45×10^{-5}	1.24	2.03×10^{-5}	2.14×10^{-5}	5.42
8				2.48×10^{-5}	2.48×10^{-5}	0.00	2.07×10^{-5}	2.19×10^{-5}	5.80
1	1.5×10^{-7}	1×10^{-11}	4972	1.90×10^{-5}	1.98×10^{-5}	4.21	1.33×10^{-5}	1.30×10^{-5}	2.26
	3×10^{-7}			1.88×10^{-5}	1.92×10^{-5}	2.13	1.23×10^{-5}	1.22×10^{-5}	0.81
	2×10^{-6}			1.74×10^{-5}	1.76×10^{-5}	1.15	9.67×10^{-6}	1.03×10^{-5}	6.51
	5×10^{-6}			1.71×10^{-5}	1.69×10^{-5}	1.17	9.42×10^{-6}	9.46×10^{-6}	0.42
	2×10^{-5}			1.74×10^{-5}	1.59×10^{-5}	8.62	8.66×10^{-6}	8.35×10^{-6}	3.58
1	1×10^{-6}	1×10^{-12}	4972	3.69×10^{-6}	3.94×10^{-6}	6.78	1.94×10^{-6}	2.13×10^{-6}	9.79
		5×10^{-12}		1.15×10^{-5}	1.15×10^{-5}	0.00	6.30×10^{-6}	6.68×10^{-6}	6.03
		2×10^{-11}		2.86×10^{-5}	2.87×10^{-5}	0.35	1.79×10^{-5}	1.79×10^{-5}	0.00
		5×10^{-11}		5.21×10^{-5}	5.28×10^{-5}	1.34	3.60×10^{-5}	3.43×10^{-5}	4.72
		1×10^{-10}		8.08×10^{-5}	8.35×10^{-5}	3.34	5.97×10^{-5}	5.62×10^{-5}	5.86
1	1×10^{-6}	1×10^{-11}	2500	1.27×10^{-5}	1.29×10^{-5}	1.57	6.77×10^{-6}	6.99×10^{-6}	3.25
			7500	2.27×10^{-5}	2.23×10^{-5}	1.76	1.44×10^{-5}	1.43×10^{-5}	0.69
	2×10^{-6}	2×10^{-11}	2500	1.87×10^{-5}	1.97×10^{-5}	5.35	1.02×10^{-5}	1.08×10^{-5}	5.88
	6.67×10^{-7}	6.67×10^{-12}	7500	1.75×10^{-5}	1.74×10^{-5}	0.57	1.10×10^{-5}	1.11×10^{-5}	0.91
6	1.5×10^{-6}	1×10^{-11}	4972	2.39×10^{-5}	2.39×10^{-5}	0.00	2.04×10^{-5}	2.08×10^{-5}	1.96
	5×10^{-6}			2.19×10^{-5}	2.21×10^{-5}	0.91	1.94×10^{-5}	1.92×10^{-5}	1.03
	1×10^{-5}			2.04×10^{-5}	2.12×10^{-5}	3.92	1.89×10^{-5}	1.83×10^{-5}	3.17
	5×10^{-5}			1.90×10^{-5}	1.92×10^{-5}	1.05	1.79×10^{-5}	1.64×10^{-5}	8.38
	1×10^{-4}			1.89×10^{-5}	1.84×10^{-5}	2.65	1.71×10^{-5}	1.56×10^{-5}	8.77
6	5×10^{-6}	1×10^{-12}	4972	4.35×10^{-6}	4.49×10^{-6}	3.22	3.91×10^{-6}	3.98×10^{-6}	1.79
		5×10^{-12}		1.36×10^{-5}	1.37×10^{-5}	0.74	1.23×10^{-5}	1.19×10^{-5}	3.25
		2×10^{-11}		3.48×10^{-5}	3.58×10^{-5}	2.87	3.13×10^{-5}	3.08×10^{-5}	1.60
		5×10^{-11}		6.52×10^{-5}	6.76×10^{-5}	3.68	5.92×10^{-5}	5.75×10^{-5}	2.87
		1×10^{-10}		1.03×10^{-4}	1.09×10^{-4}	5.54	9.44×10^{-5}	9.23×10^{-5}	2.22
6	5×10^{-6}	1×10^{-11}	2500	1.52×10^{-5}	1.50×10^{-5}	1.32	1.25×10^{-5}	1.27×10^{-5}	1.60
			7500	2.71×10^{-5}	2.79×10^{-5}	2.95	2.57×10^{-5}	2.45×10^{-5}	4.67
	1×10^{-5}	2×10^{-11}	2500	2.35×10^{-5}	2.33×10^{-5}	0.85	1.94×10^{-5}	1.94×10^{-5}	0.00
	3.33×10^{-6}	6.67×10^{-12}	7500	2.11×10^{-5}	2.16×10^{-5}	2.37	1.96×10^{-5}	1.91×10^{-5}	2.55

Table G.2. Results of the simulation and the curve-fit equation for rough surfaces (central film thickness)

Input						Central film thickness (H_c)			Film parameter (Λ)
κ	W	U	G	$\bar{\sigma}$	V	Simulation	Curve-fit	Error (%)	
1	1×10^{-6}	1×10^{-11}	4972	2×10^{-5}	0.01	2.13×10^{-5}	2.11×10^{-5}	0.94	0.80
2						2.51×10^{-5}	2.50×10^{-5}	0.40	1.08
3						2.63×10^{-5}	2.70×10^{-5}	2.66	1.22
4						2.74×10^{-5}	2.80×10^{-5}	2.19	1.28
6						2.86×10^{-5}	2.90×10^{-5}	1.40	1.31
8						2.93×10^{-5}	2.95×10^{-5}	0.68	1.31
1	1.5×10^{-7}	1×10^{-11}	4972	2×10^{-5}	0.01	2.26×10^{-5}	2.39×10^{-5}	5.75	0.97
	5×10^{-6}					1.91×10^{-5}	1.91×10^{-5}	0.00	0.67
	2×10^{-5}					1.86×10^{-5}	1.76×10^{-5}	5.38	0.59
1	1×10^{-6}	5×10^{-12}	4972	2×10^{-5}	0.01	1.47×10^{-5}	1.49×10^{-5}	1.36	0.60
		3×10^{-11}				3.97×10^{-5}	3.99×10^{-5}	0.50	1.41
		1×10^{-10}				8.16×10^{-5}	8.53×10^{-5}	4.53	3.00
1	2×10^{-6}	2×10^{-11}	2500	2×10^{-5}	0.01	2.24×10^{-5}	2.28×10^{-5}	1.79	0.80
	6.67×10^{-7}	6.67×10^{-12}	7500			2.08×10^{-5}	2.02×10^{-5}	2.88	0.80
	1×10^{-6}	1×10^{-11}	2500			1.66×10^{-5}	1.69×10^{-5}	1.81	0.66
			7500			2.56×10^{-5}	2.47×10^{-5}	3.52	0.93
6	5×10^{-6}	1×10^{-11}	4972	2×10^{-5}	0.01	2.51×10^{-5}	2.55×10^{-5}	1.59	1.16
	1×10^{-5}					2.38×10^{-5}	2.41×10^{-5}	1.26	1.10
	1×10^{-4}					2.01×10^{-5}	2.02×10^{-5}	0.50	0.92
6	5×10^{-6}	5×10^{-12}	4972	2×10^{-5}	0.01	1.76×10^{-5}	1.75×10^{-5}	0.57	0.82
		3×10^{-11}				4.82×10^{-5}	5.01×10^{-5}	3.94	2.20
		1×10^{-10}				1.04×10^{-4}	1.11×10^{-4}	6.73	4.76
6	1×10^{-5}	2×10^{-11}	2500	2×10^{-5}	0.01	2.71×10^{-5}	2.67×10^{-5}	1.48	1.19
	3.33×10^{-6}	6.67×10^{-12}	7500			2.48×10^{-5}	2.49×10^{-5}	0.40	1.15
	5×10^{-6}	1×10^{-11}	2500			1.99×10^{-5}	1.95×10^{-5}	2.01	0.89
			7500			3.01×10^{-5}	3.07×10^{-5}	1.99	1.40
1	1×10^{-6}	1×10^{-11}	4972	1×10^{-6}	0.01	1.80×10^{-5}	1.82×10^{-5}	1.11	11.10
				5×10^{-6}		1.82×10^{-5}	1.87×10^{-5}	2.75	2.40
				1×10^{-5}		1.91×10^{-5}	1.94×10^{-5}	1.57	1.33
				3×10^{-5}		2.31×10^{-5}	2.30×10^{-5}	0.43	0.62
				4×10^{-5}		2.46×10^{-5}	2.51×10^{-5}	2.03	0.53
6	5×10^{-6}	1×10^{-11}	4972	5×10^{-6}	0.01	2.20×10^{-5}	2.27×10^{-5}	3.18	4.02
				1×10^{-5}		2.22×10^{-5}	2.35×10^{-5}	5.86	2.11
				3×10^{-5}		2.79×10^{-5}	2.77×10^{-5}	0.72	0.84
				4×10^{-5}		2.98×10^{-5}	3.00×10^{-5}	0.67	0.69
				5×10^{-5}		3.20×10^{-5}	3.26×10^{-5}	1.88	0.60
1	1×10^{-6}	1×10^{-11}	4972	2×10^{-5}	0.005	2.09×10^{-5}	2.08×10^{-5}	0.48	0.77
					0.02	2.14×10^{-5}	2.13×10^{-5}	0.47	0.82
					0.03	2.15×10^{-5}	2.15×10^{-5}	0.00	0.84
6	5×10^{-6}	1×10^{-11}	4972	2×10^{-5}	0.005	2.46×10^{-5}	2.52×10^{-5}	2.44	1.14
					0.02	2.52×10^{-5}	2.58×10^{-5}	2.38	1.18
					0.03	2.54×10^{-5}	2.59×10^{-5}	1.97	1.20

Table G.3. Results of the simulation and the curve-fit equation for rough surfaces (minimum film thickness)

Input						Minimum film thickness (H_{min})			Film parameter (Λ)
κ	W	U	G	$\bar{\sigma}$	V	Simulation	Curve-fit	Error (%)	
1	1×10^{-6}	1×10^{-11}	4972	2×10^{-5}	0.01	1.58×10^{-5}	1.59×10^{-5}	0.63	0.80
2						2.15×10^{-5}	2.16×10^{-5}	0.47	1.08
3						2.37×10^{-5}	2.43×10^{-5}	2.53	1.22
4						2.43×10^{-5}	2.55×10^{-5}	4.94	1.28
6						2.52×10^{-5}	2.62×10^{-5}	3.97	1.31
8						2.58×10^{-5}	2.62×10^{-5}	1.55	1.31
1	1.5×10^{-7}	1×10^{-11}	4972	2×10^{-5}	0.01	1.93×10^{-5}	1.93×10^{-5}	0.00	0.97
	5×10^{-6}					1.30×10^{-5}	1.34×10^{-5}	3.08	0.67
	2×10^{-5}					1.16×10^{-5}	1.17×10^{-5}	0.86	0.59
1	1×10^{-6}	5×10^{-12}	4972	2×10^{-5}	0.01	1.13×10^{-5}	1.20×10^{-5}	6.19	0.60
		3×10^{-11}				2.86×10^{-5}	2.82×10^{-5}	1.40	1.41
		1×10^{-10}				6.12×10^{-5}	6.00×10^{-5}	1.96	3.00
1	2×10^{-6}	2×10^{-11}	2500	2×10^{-5}	0.01	1.54×10^{-5}	1.59×10^{-5}	3.25	0.80
	6.67×10^{-7}	6.67×10^{-12}	7500			1.62×10^{-5}	1.59×10^{-5}	1.85	0.80
	1×10^{-6}	1×10^{-11}	2500			1.25×10^{-5}	1.31×10^{-5}	4.80	0.66
			7500			1.91×10^{-5}	1.86×10^{-5}	2.62	0.93
6	5×10^{-6}	1×10^{-11}	4972	2×10^{-5}	0.01	2.35×10^{-5}	2.31×10^{-5}	1.70	1.16
	1×10^{-5}					2.31×10^{-5}	2.20×10^{-5}	4.76	1.10
	1×10^{-4}					2.00×10^{-5}	1.84×10^{-5}	8.00	0.92
6	5×10^{-6}	5×10^{-12}	4972	2×10^{-5}	0.01	1.67×10^{-5}	1.63×10^{-5}	2.40	0.82
		3×10^{-11}				4.44×10^{-5}	4.40×10^{-5}	0.90	2.20
		1×10^{-10}				9.55×10^{-5}	9.51×10^{-5}	0.42	4.76
6	1×10^{-5}	2×10^{-11}	2500	2×10^{-5}	0.01	2.42×10^{-5}	2.37×10^{-5}	2.07	1.19
	3.33×10^{-6}	6.67×10^{-12}	7500			2.38×10^{-5}	2.30×10^{-5}	3.36	1.15
	5×10^{-6}	1×10^{-11}	2500			1.78×10^{-5}	1.78×10^{-5}	0.00	0.89
			7500			2.94×10^{-5}	2.80×10^{-5}	4.76	1.40
1	1×10^{-6}	1×10^{-11}	4972	1×10^{-6}	0.01	1.05×10^{-5}	1.11×10^{-5}	5.71	11.10
				5×10^{-6}		1.12×10^{-5}	1.20×10^{-5}	7.14	2.40
				1×10^{-5}		1.28×10^{-5}	1.33×10^{-5}	3.91	1.33
				3×10^{-5}		1.82×10^{-5}	1.86×10^{-5}	2.20	0.62
				4×10^{-5}		2.02×10^{-5}	2.13×10^{-5}	5.45	0.53
6	5×10^{-6}	1×10^{-11}	4972	5×10^{-6}	0.01	1.98×10^{-5}	2.01×10^{-5}	1.52	4.02
				1×10^{-5}		2.06×10^{-5}	2.11×10^{-5}	2.43	2.11
				3×10^{-5}		2.62×10^{-5}	2.53×10^{-5}	3.44	0.84
				4×10^{-5}		2.75×10^{-5}	2.75×10^{-5}	0.00	0.69
				5×10^{-5}		2.96×10^{-5}	2.98×10^{-5}	0.68	0.60
1	1×10^{-6}	1×10^{-11}	4972	2×10^{-5}	0.005	1.50×10^{-5}	1.54×10^{-5}	2.67	0.77
					0.02	1.59×10^{-5}	1.64×10^{-5}	3.14	0.82
					0.03	1.63×10^{-5}	1.67×10^{-5}	2.45	0.84
6	5×10^{-6}	1×10^{-11}	4972	2×10^{-5}	0.005	2.33×10^{-5}	2.28×10^{-5}	2.15	1.14
					0.02	2.35×10^{-5}	2.36×10^{-5}	0.43	1.18
					0.03	2.37×10^{-5}	2.39×10^{-5}	0.84	1.20

Table G.4. Results of the simulation and the curve-fit equation for rough surfaces (asperity load ratio)

Input						Asperity Load Ratio (L_a)			Film parameter (Λ)
κ	W	U	G	$\bar{\sigma}$	V	Simulation	Curve-fit	Error (%)	
1	1×10^{-6}	1×10^{-11}	4972	2×10^{-5}	0.01	34.65	35.61	0.96	0.80
2						31.86	35.61	3.75	1.08
3						32.53	35.61	3.08	1.22
4						34.13	35.61	1.48	1.28
6						35.77	35.61	0.16	1.31
8						37.65	35.61	2.04	1.31
1	1.5×10^{-7}	1×10^{-11}	4972	2×10^{-5}	0.01	63.12	54.76	8.36	0.97
	5×10^{-6}					22.42	23.25	0.83	0.67
	2×10^{-5}					14.78	15.14	0.36	0.59
1	1×10^{-6}	5×10^{-12}	4972	2×10^{-5}	0.01	52.91	53.9	0.99	0.60
		3×10^{-11}				7.09	7.79	0.70	1.41
		1×10^{-10}				0.03	0.37	0.34	3.00
1	2×10^{-6}	2×10^{-11}	2500	2×10^{-5}	0.01	24.34	26.24	1.90	0.80
	6.67×10^{-7}	6.67×10^{-12}	7500			41.84	42.08	0.24	0.80
	1×10^{-6}	1×10^{-11}	2500			47.01	47.6	0.59	0.66
			7500			25.13	25.75	0.62	0.93
6	5×10^{-6}	1×10^{-11}	4972	2×10^{-5}	0.01	23.8	23.25	0.55	1.16
	1×10^{-5}					20.73	18.92	1.81	1.10
	1×10^{-4}					12.62	8.41	4.21	0.92
6	5×10^{-6}	5×10^{-12}	4972	2×10^{-5}	0.01	45.17	39.47	5.70	0.82
		3×10^{-11}				1.65	3.51	1.86	2.20
		1×10^{-10}				0	0.15	0.15	4.76
6	1×10^{-5}	2×10^{-11}	2500	2×10^{-5}	0.01	15.73	16.55	0.82	1.19
	3.33×10^{-6}	6.67×10^{-12}	7500			29.35	27.92	1.43	1.15
	5×10^{-6}	1×10^{-11}	2500			37.66	34.8	2.86	0.89
			7500			14.67	14.89	0.22	1.40
1	1×10^{-6}	1×10^{-11}	4972	1×10^{-6}	0.01	0	0	0.00	11.10
				5×10^{-6}		0.19	0.32	0.13	2.40
				1×10^{-5}		7.81	6.34	1.47	1.33
				3×10^{-5}		54.1	58.2	4.10	0.62
				4×10^{-5}		68.23	74.55	6.32	0.53
6	5×10^{-6}	1×10^{-11}	4972	5×10^{-6}	0.01	0	0.13	0.13	4.02
				1×10^{-5}		2.25	2.83	0.58	2.11
				3×10^{-5}		44.33	42.44	1.89	0.84
				4×10^{-5}		60.56	56.67	3.89	0.69
				5×10^{-5}		71.01	67.79	3.22	0.60
1	1×10^{-6}	1×10^{-11}	4972	2×10^{-5}	0.005	25.53	31.58	6.05	0.77
					0.02	35.73	39.71	3.98	0.82
					0.03	40.4	42.14	1.74	0.84
6	5×10^{-6}	1×10^{-11}	4972	2×10^{-5}	0.005	18.02	19.99	1.97	1.14
					0.02	25	26.65	1.65	1.18
					0.03	28.55	28.68	0.13	1.20

Appendix H: Simulation and Curve-fit Results (Starved Lubrication)

Table H.1. Line Contact EHL

G=4972, V=0.01				ϕ_{H_C} simulation (Curve-Fit)	Error (%)	$\phi_{H_{min}}$ simulation (Curve-Fit)	Error (%)	L_a simulation (Curve-Fit)	Error (%)
W	U	$\bar{\sigma}$	ξ						
2×10^{-5}	1×10^{-11}	2×10^{-5}	0.13	0.88 (0.87)	1.14	0.9 (0.89)	1.11	39.88 (36.20)	3.68
1×10^{-4}	1×10^{-11}	2×10^{-5}	0.03	0.98 (0.97)	1.02	0.98 (0.98)	0.00	20.15 (18.33)	1.82
3×10^{-4}	1×10^{-11}	2×10^{-5}	0.01	0.99 (0.99)	0.00	0.99 (0.99)	0.00	14.78 (12.81)	1.97
1×10^{-4}	5×10^{-12}	2×10^{-5}	0.01	0.99 (0.99)	0.00	0.99 (0.99)	0.00	34.20 (31.73)	2.47
1×10^{-4}	5×10^{-11}	2×10^{-5}	0.10	0.9 (0.9)	0.00	0.9 (0.92)	2.22	0.41 (0.76)	0.35
1×10^{-4}	1×10^{-11}	0	0.03	0.97 (0.97)	0.00	0.98 (0.98)	0.00	0.00 (0.00)	0.00
1×10^{-4}	1×10^{-11}	3×10^{-5}	0.02	0.98 (0.98)	0.00	0.98 (0.99)	1.02	33.28 (29.51)	3.77
1×10^{-4}	1×10^{-11}	5×10^{-5}	0.02	0.98 (0.98)	0.00	0.98 (0.99)	1.02	49.71 (44.19)	5.52
2×10^{-5}	1×10^{-11}	2×10^{-5}	0.17	0.84 (0.83)	1.19	0.87 (0.85)	2.30	43.67 (39.63)	4.04
1×10^{-4}	1×10^{-11}	2×10^{-5}	0.04	0.96 (0.96)	0.00	0.97 (0.97)	0.00	20.69 (18.72)	1.97
3×10^{-4}	1×10^{-11}	2×10^{-5}	0.01	0.99 (0.99)	0.00	0.99 (0.99)	0.00	14.86 (12.81)	2.05
1×10^{-4}	5×10^{-12}	2×10^{-5}	0.02	0.98 (0.98)	0.00	0.98 (0.99)	1.02	34.49 (32.14)	2.35
1×10^{-4}	5×10^{-11}	2×10^{-5}	0.15	0.85 (0.85)	0.00	0.86 (0.87)	1.16	0.61 (1.14)	0.53
1×10^{-4}	1×10^{-11}	0	0.05	0.95 (0.95)	0.00	0.96 (0.96)	0.00	0.00 (0.00)	0.00
1×10^{-4}	1×10^{-11}	3×10^{-5}	0.04	0.96 (0.96)	0.00	0.97 (0.97)	0.00	33.80 (30.30)	3.50
1×10^{-4}	1×10^{-11}	5×10^{-5}	0.04	0.96 (0.96)	0.00	0.97 (0.97)	0.00	50.15 (44.99)	5.16
2×10^{-5}	1×10^{-11}	2×10^{-5}	0.25	0.76 (0.75)	1.32	0.8 (0.78)	2.50	52.72 (47.08)	5.64
1×10^{-4}	1×10^{-11}	2×10^{-5}	0.09	0.91 (0.91)	0.00	0.93 (0.93)	0.00	22.59 (20.74)	1.85
3×10^{-4}	1×10^{-11}	2×10^{-5}	0.03	0.97 (0.97)	0.00	0.97 (0.98)	1.03	15.21 (13.31)	1.90
1×10^{-4}	5×10^{-12}	2×10^{-5}	0.05	0.95 (0.95)	0.00	0.96 (0.96)	0.00	35.55 (33.41)	2.14
1×10^{-4}	5×10^{-11}	2×10^{-5}	0.26	0.74 (0.74)	0.00	0.75 (0.77)	2.67	1.64 (2.81)	1.17
1×10^{-4}	1×10^{-11}	0	0.11	0.89 (0.89)	0.00	0.9 (0.91)	1.11	0.00 (0.00)	0.00
1×10^{-4}	1×10^{-11}	3×10^{-5}	0.08	0.92 (0.92)	0.00	0.94 (0.93)	1.06	35.62 (31.93)	3.69
1×10^{-4}	1×10^{-11}	5×10^{-5}	0.08	0.92 (0.92)	0.00	0.93 (0.93)	0.00	51.64 (46.62)	5.02
2×10^{-5}	1×10^{-11}	2×10^{-5}	0.34	0.68 (0.66)	2.94	0.72 (0.69)	4.17	61.89 (56.52)	5.37
1×10^{-4}	1×10^{-11}	2×10^{-5}	0.17	0.83 (0.83)	0.00	0.87 (0.85)	2.30	26.22 (24.25)	1.97
3×10^{-4}	1×10^{-11}	2×10^{-5}	0.06	0.94 (0.94)	0.00	0.94 (0.95)	1.06	16.08 (14.07)	2.01
1×10^{-4}	5×10^{-12}	2×10^{-5}	0.11	0.9 (0.89)	1.11	0.92 (0.91)	1.09	37.75 (36.08)	1.67
1×10^{-4}	5×10^{-11}	2×10^{-5}	0.40	0.6 (0.6)	0.00	0.63 (0.63)	0.00	4.72 (7.58)	2.86
1×10^{-4}	1×10^{-11}	0	0.22	0.78 (0.78)	0.00	0.8 (0.81)	1.25	0.00 (0.00)	0.00
1×10^{-4}	1×10^{-11}	3×10^{-5}	0.16	0.84 (0.84)	0.00	0.87 (0.86)	1.15	38.92 (35.43)	3.49
1×10^{-4}	1×10^{-11}	5×10^{-5}	0.15	0.85 (0.85)	0.00	0.86 (0.87)	1.16	53.97 (49.67)	4.30
1×10^{-4}	1×10^{-11}	2×10^{-5}	0.39	0.62 (0.61)	1.61	0.65 (0.64)	1.54	37.23 (36.07)	1.16
3×10^{-4}	1×10^{-11}	2×10^{-5}	0.25	0.75 (0.75)	0.00	0.75 (0.78)	4.00	20.96 (19.59)	1.37
5×10^{-4}	1×10^{-11}	2×10^{-5}	0.18	0.82 (0.82)	0.00	0.82 (0.84)	2.44	16.15 (14.74)	1.41
1×10^{-4}	1×10^{-12}	0	0.09	0.91 (0.91)	0.00	0.93 (0.93)	0.00	0.00 (0.00)	0.00
1×10^{-4}	3×10^{-12}	0	0.18	0.82 (0.82)	0.00	0.85 (0.84)	1.18	0.00 (0.00)	0.00
1×10^{-4}	5×10^{-12}	0	0.24	0.76 (0.76)	0.00	0.79 (0.79)	0.00	0.00 (0.00)	0.00
1×10^{-4}	1×10^{-11}	3×10^{-5}	0.36	0.65 (0.64)	1.54	0.67 (0.67)	0.00	47.43 (45.88)	1.55
1×10^{-4}	1×10^{-11}	5×10^{-5}	0.33	0.67 (0.67)	0.00	0.68 (0.7)	2.94	59.17 (58.82)	0.35

Table H.2. Point Contact EHL

G=4972, V=0.01					ϕ_{Hc} simulation (Curve-Fit)	Error (%)	$\phi_{H_{min}}$ simulation (Curve-Fit)	Error (%)	L_a simulation (Curve-Fit)	Error (%)
κ	W	U	$\bar{\sigma}$	ξ						
1	5×10^{-7}	1×10^{-11}	0	0.09	0.81 (0.80)	1.23	0.93 (0.90)	3.23	0.00 (0.00)	0.00
1	5×10^{-7}	1×10^{-11}	1×10^{-5}	0.08	0.84 (0.82)	2.38	0.94 (0.91)	3.19	13.72 (13.19)	0.53
1	5×10^{-7}	1×10^{-11}	2×10^{-5}	0.07	0.88 (0.84)	4.55	0.95 (0.92)	3.16	49.38 (48.65)	0.73
1	5×10^{-7}	1×10^{-11}	0	0.14	0.67 (0.71)	5.97	0.88 (0.85)	3.41	0.00 (0.00)	0.00
1	5×10^{-7}	1×10^{-11}	1×10^{-5}	0.12	0.73 (0.74)	1.37	0.91 (0.87)	4.40	18.31 (16.03)	2.28
1	5×10^{-7}	1×10^{-11}	2×10^{-5}	0.10	0.80 (0.78)	2.50	0.91 (0.89)	2.20	53.99 (51.68)	2.31
1	5×10^{-7}	1×10^{-11}	0	0.29	0.43 (0.45)	4.65	0.68 (0.72)	5.88	0.00 (0.00)	0.00
1	5×10^{-7}	1×10^{-11}	1×10^{-5}	0.21	0.55 (0.59)	7.27	0.77 (0.79)	2.60	29.73 (24.01)	5.72
1	5×10^{-7}	1×10^{-11}	2×10^{-5}	0.16	0.66 (0.67)	1.52	0.84 (0.84)	0.00	61.86 (58.11)	3.75
6	5×10^{-6}	1×10^{-11}	0	0.14	0.81 (0.80)	1.23	0.83 (0.83)	0.00	0.00 (0.00)	0.00
6	5×10^{-6}	1×10^{-11}	1×10^{-5}	0.13	0.82 (0.81)	1.22	0.86 (0.84)	2.33	5.10 (6.53)	1.43
6	5×10^{-6}	1×10^{-11}	2×10^{-5}	0.10	0.86 (0.85)	1.16	0.88 (0.88)	0.00	31.08 (30.81)	0.27
6	5×10^{-6}	1×10^{-11}	3×10^{-5}	0.09	0.87 (0.86)	1.15	0.90 (0.89)	1.11	51.34 (49.70)	1.64
6	5×10^{-6}	1×10^{-11}	4×10^{-5}	0.08	0.88 (0.88)	0.00	0.91 (0.90)	1.10	65.36 (63.15)	2.21
6	5×10^{-6}	1×10^{-11}	0	0.23	0.67 (0.69)	2.99	0.70 (0.74)	5.71	0.00 (0.00)	0.00
6	5×10^{-6}	1×10^{-11}	1×10^{-5}	0.20	0.71 (0.73)	2.82	0.76 (0.77)	1.32	8.29 (10.03)	1.74
6	5×10^{-6}	1×10^{-11}	2×10^{-5}	0.17	0.76 (0.76)	0.00	0.80 (0.80)	0.00	36.18 (36.86)	0.68
6	5×10^{-6}	1×10^{-11}	3×10^{-5}	0.14	0.79 (0.80)	1.27	0.83 (0.83)	0.00	55.61 (54.08)	1.53
6	5×10^{-6}	1×10^{-11}	4×10^{-5}	0.13	0.81 (0.81)	0.00	0.85 (0.84)	1.18	68.59 (67.51)	1.08
6	5×10^{-6}	1×10^{-11}	2×10^{-5}	0.27	0.60 (0.65)	8.33	0.65 (070)	7.69	46.07 (46.68)	0.61
6	5×10^{-6}	1×10^{-11}	3×10^{-5}	0.23	0.65 (0.69)	6.15	0.69 (0.74)	7.25	62.72 (62.68)	0.04
2	5×10^{-6}	1×10^{-11}	2×10^{-5}	0.02	0.97 (0.95)	2.06	0.99 (0.97)	2.02	22.90 (24.66)	1.76
4	5×10^{-6}	1×10^{-11}	2×10^{-5}	0.04	0.95 (0.92)	3.16	0.95 (0.95)	0.00	25.08 (26.12)	1.04
8	5×10^{-6}	1×10^{-11}	2×10^{-5}	0.07	0.92 (0.90)	2.17	0.93 (0.91)	2.15	29.82 (28.41)	1.41
2	5×10^{-6}	1×10^{-11}	2×10^{-5}	0.05	0.93 (0.89)	4.30	0.98 (0.94)	4.08	24.15 (26.87)	2.72
4	5×10^{-6}	1×10^{-11}	2×10^{-5}	0.08	0.89 (0.86)	3.37	0.90 (0.90)	0.00	27.61 (29.20)	1.59
8	5×10^{-6}	1×10^{-11}	2×10^{-5}	0.13	0.84 (0.82)	2.38	0.87 (0.84)	3.45	34.24 (33.32)	0.92
2	5×10^{-6}	1×10^{-11}	2×10^{-5}	0.09	0.85 (0.83)	2.35	0.97 (0.90)	7.22	26.43 (30.00)	3.57
4	5×10^{-6}	1×10^{-11}	2×10^{-5}	0.14	0.80 (0.78)	2.50	0.83 (0.84)	1.20	31.60 (34.19)	2.59
8	5×10^{-6}	1×10^{-11}	2×10^{-5}	0.19	0.75 (0.76)	1.33	0.79 (0.77)	2.53	40.16 (38.71)	1.45
2	5×10^{-6}	1×10^{-11}	2×10^{-5}	0.19	0.64 (0.67)	4.69	0.74 (0.80)	8.11	33.03 (38.71)	5.68
4	5×10^{-6}	1×10^{-11}	2×10^{-5}	0.28	0.62 (0.61)	1.61	0.65 (0.70)	7.69	40.41 (47.75)	7.34
8	5×10^{-6}	1×10^{-11}	2×10^{-5}	0.30	0.59 (0.64)	8.47	0.64 (0.66)	3.13	50.64 (49.92)	0.72
6	5×10^{-6}	1×10^{-12}	0	0.06	0.92 (0.90)	2.17	0.93 (0.92)	1.08	0.00 (0.00)	0.00
6	5×10^{-6}	5×10^{-12}	0	0.08	0.89 (0.88)	1.12	0.91(0.90)	1.10	0.00 (0.00)	0.00
6	5×10^{-6}	5×10^{-11}	0	0.21	0.71 (0.72)	1.41	0.73 (0.76)	4.11	0.00 (0.00)	0.00
6	5×10^{-6}	1×10^{-10}	0	0.29	0.59 (0.63)	6.78	0.64 (0.68)	6.25	0.00 (0.00)	0.00
1	1.5×10^{-7}	1×10^{-11}	0	0.19	0.58 (0.62)	6.90	0.84 (0.81)	3.57	0.00 (0.00)	0.00
6	5×10^{-5}	1×10^{-11}	0	0.12	0.82 (0.82)	0.00	0.83 (0.85)	2.41	0.00 (0.00)	0.00
8	2.5×10^{-4}	1×10^{-11}	0	0.09	0.81 (0.80)	1.23	0.84 (0.90)	7.14	0.00 (0.00)	0.00

Appendix I: Letters of Permission to Use Published Material

The Permissions from publishing companies are presented in the following pages:

It is our pleasure to grant you permission to publish **all or any part of** the ASME paper **"Film Thickness and Asperity Load Formulas for Line-Contact Elastohydrodynamic Lubrication With Provision for Surface Roughness,"** by M. Masjedi; M. M. Khonsari, J. Tribol.. 2012; 134(1), as cited in your letter for inclusion in a PhD dissertation entitled On the Role of Surface Roughness in Elastohydrodynamic Lubrication of Tribological Components to be published by Louisiana State University.

Permission is granted for the specific use as stated herein and does not permit further use of the materials without proper authorization. Proper attribution must be made to the author(s) of the materials. **Please note**: if any or all of the figures and/or Tables are of another source, permission should be granted from that outside source or include the reference of the original source. ASME does not grant permission for outside source material that may be referenced in the ASME works. Paper will be appended only to print series, online (public) version of the thesis includes only the compendium part.

As is customary, we request that you ensure proper acknowledgment of the exact sources of this material, the authors, and ASME as original publisher. Acknowledgment must be retained on all pages printed and distributed.

Many thanks for your interest in ASME publications.

Sincerely,

Beth Darchi
Publishing Administrator
ASME
2 Park Avenue, 6th Floor
New York, NY 10016-5990
Tel 1.212.591.7700
darchib@asme.org

Order Completed

Thank you very much for your order.

This is a License Agreement between Mohammad Masjedi ("You") and Elsevier ("Elsevier"). The license consists of your order details, the terms and conditions provided by Elsevier, and the payment terms and conditions.

Get the printable license.

License Number	3560950728626
License date	Feb 02, 2015
Licensed content publisher	Elsevier
Licensed content publication	Tribology International
Licensed content title	Theoretical and experimental investigation of traction coefficient in line-contact EHL of rough surfaces
Licensed content author	M. Masjedi,M.M. Khonsari
Licensed content date	February 2014
Licensed content volume number	70
Licensed content issue number	n/a
Number of pages	11
Type of Use	reuse in a thesis/dissertation
Portion	full article
Format	both print and electronic
Are you the author of this Elsevier article?	Yes
Will you be translating?	No
Title of your thesis/dissertation	ON THE ROLE OF SURFACE ROUGHNESS IN ELASTOHYDRODYNAMIC LUBRICATION OF TRIBOLOGICAL COMPONENTS
Expected completion date	May 2015
Estimated size (number of pages)	200
Elsevier VAT number	GB 494 6272 12
Permissions price	0.00 USD
VAT/Local Sales Tax	0.00 USD / 0.00 GBP
Total	0.00 USD

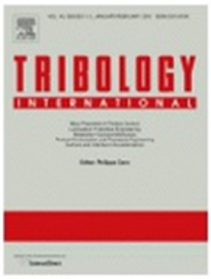

Title: On the effect of surface roughness in point-contact EHL: Formulas for film thickness and asperity load
Publication: Tribology International
Publisher: Elsevier
Date: February 2015

Order Completed

Thank you very much for your order.

This is a License Agreement between Mohammad Masjedi ("You") and Elsevier ("Elsevier"). The license consists of your order details, the terms and conditions provided by Elsevier, and the payment terms and conditions.

Get the printable license.

License Number	3560950959972
License date	Feb 02, 2015
Licensed content publisher	Elsevier
Licensed content publication	Tribology International
Licensed content title	On the effect of surface roughness in point-contact EHL: Formulas for film thickness and asperity load
Licensed content author	None
Licensed content date	February 2015
Licensed content volume number	82
Licensed content issue number	n/a
Number of pages	17
Type of Use	reuse in a thesis/dissertation
Portion	full article
Format	both print and electronic
Are you the author of this Elsevier article?	Yes
Will you be translating?	No
Title of your thesis/dissertation	ON THE ROLE OF SURFACE ROUGHNESS IN ELASTOHYDRODYNAMIC LUBRICATION OF TRIBOLOGICAL COMPONENTS
Expected completion date	May 2015
Estimated size (number of pages)	200
Elsevier VAT number	GB 494 6272 12
Permissions price	0.00 USD
VAT/Local Sales Tax	0.00 USD / 0.00 GBP
Total	0.00 USD

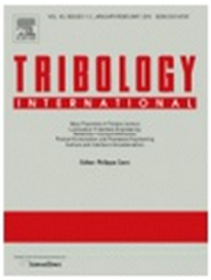

Title: A study on the effect of starvation in mixed elastohydrodynamic lubrication
Publication: Tribology International
Publisher: Elsevier
Date: May 2015

Order Completed

Thank you very much for your order.

This is a License Agreement between Mohammad Masjedi ("You") and Elsevier ("Elsevier"). The license consists of your order details, the terms and conditions provided by Elsevier, and the payment terms and conditions.

Get the printable license.

License Number	3560951073173
License date	Feb 02, 2015
Licensed content publisher	Elsevier
Licensed content publication	Tribology International
Licensed content title	A study on the effect of starvation in mixed elastohydrodynamic lubrication
Licensed content author	None
Licensed content date	May 2015
Licensed content volume number	85
Licensed content issue number	n/a
Number of pages	11
Type of Use	reuse in a thesis/dissertation
Portion	full article
Format	both print and electronic
Are you the author of this Elsevier article?	Yes
Will you be translating?	No
Title of your thesis/dissertation	ON THE ROLE OF SURFACE ROUGHNESS IN ELASTOHYDRODYNAMIC LUBRICATION OF TRIBOLOGICAL COMPONENTS
Expected completion date	May 2015
Estimated size (number of pages)	200
Elsevier VAT number	GB 494 6272 12
Permissions price	0.00 USD
VAT/Local Sales Tax	0.00 USD / 0.00 GBP
Total	0.00 USD

Vita

Mohammad Masjedi received his Bachelor's degree in Mechanical Engineering from Isfahan University of Technology (Isfahan, Iran) in 2003, and his Master's degree in Mechanical Engineering from Sharif University of Technology (Tehran, Iran) in 2006. After graduation, he worked as an engineer in a construction company and then in a design company for a total of about three years.

He came to the United States in 2009 to pursue his PhD in Mechanical Engineering at LSU under the supervision of Prof. Michael M. Khonsari. During his PhD career, he worked as a research assistant at the Center for Rotating Machinery (CeRoM) at Louisiana State University. His research interest is mainly Tribology, Contact Mechanics, Surface Engineering, and numerical analysis. He has authored a number of scientific articles in peer-reviewed journals as the outcome of his PhD. He is expected to receive his PhD degree at the 2015 Spring Commencement.